Non-matching Triangulations of Curvilinear Interfaces Applied to Electro-Mechanics and Elasto-Acoustics

Von der Fakultät Mathematik und Physik der Universität Stuttgart
zur Erlangung der Würde eines Doktors der
Naturwissenschaften (Dr. rer. nat.) genehmigte Abhandlung

Vorgelegt von

Bernd Flemisch

aus Augsburg

Hauptberichter:	Prof. Dr. B. Wohlmuth
Mitberichter:	PD Dr. M. Kaltenbacher
	Prof. Dr. J.M. Melenk
Tag der mündlichen Prüfung:	19. Dezember 2006

Institut für Angewandte Analysis und Numerische Simulation
Universität Stuttgart

2007

D 93 (Diss. Universität Stuttgart)

Acknowledgments

This thesis summarizes the results of my research activities during the years 2001 to 2006 at the chair "Numerische Mathematik für Höchstleistungsrechner" of the Institut für Angewandte Analysis und Numerische Simulation, Universität Stuttgart.

First and foremost, I would like to express my extraordinary gratitude to my supervisor Prof. Dr. Barbara Wohlmuth for her invaluable guidance during the past years. Despite her involvement in countless activities, she has always been willing to offer her advice on professional as well as on more personal topics. Her outstanding dedication to the research activities of our whole group has been truly inspiring for me. I would also like to thank her for putting me in touch with so many international experts, thereby initiating several interesting discussions and most fruitful collaborations.

My special thanks goes to Prof. Dr. Jens Markus Melenk and PD Dr. Manfred Kaltenbacher for sharing with me their deep knowledge of the theoretical and of the practical aspects of numerical analysis, and for their efforts to provide the referee reports for this thesis. I am grateful to Prof. Dr. Christian Rohde for participating in the oral defense. I also would like to thank the other scientists with whom I had the pleasure to co-author several contributions: Franscesca Rapetti, Yvon Maday, Michael A. Puso, and in particular Stefan Kurz who accelerated my mind frame with most stimulating discussions. I am much obliged to the supervisor of my master thesis Michael W. Smiley for arousing my interest in domain decomposition methods.

During my employment at the Institut für Angewandte Analysis und Numerische Simulation, I greatly enjoyed the inspiring and cooperative atmosphere. I would especially like to thank Stephan Brunßen, Corinna Hager, Stefan Hüeber, Andreas Klimke, Bishnu Lamichhane, Michael Mair, Brit Steiner, and Alexander Weiß for always being available and offering help and advice for accomplishing various tasks connected with this thesis.

I am deeply indebted to my parents for always supporting me with all their strength and goodwill, and for providing me with the chance to pursuit the track of an academic career. I would like to remember my father whose life has been taken away too early not only to witness the completion of this work. I am thankful to my brother Frank and his family for exemplifying to me that family life can still be desirable today. Thanks also to my friends for believing in me and for their courage to go out with me.

Finally, I would like to express my deepest gratitude to Lorena whose sincere love illuminates my life every day, managing to direct my thoughts towards a bright future.

Stuttgart, November 2006 Bernd Flemisch

Contents

Abstract

This thesis is concerned with the development of robust and efficient numerical schemes for obtaining approximate solutions of partial differential equations. A most promising tool to develop such schemes is provided by the framework of domain decomposition methods in combination with modern finite element technology. In this context, it is always convenient and sometimes even mandatory to be able to deal with non-matching finite element grids. There are numerous tasks where non-matching grids naturally arise when employing on each subdomain the grid best suited to solve the corresponding subproblem associated with this subdomain. In order to construct the global solution, the stable and inexpensive transmission of data between the grids is of outmost importance. While point-wise coupling procedures usually fail, the framework of mortar finite elements provides a method which is able to deal with non-matching grids both from the mathematical and from the implementational point of view. The method is based on introducing additional degrees of freedom in form of Lagrange multipliers on the interface, thereby replacing the strong continuity requirement of the solution by a weak one.

So far, the theory as well as most of the numerical tests have been restricted to the case of planar interfaces. In this thesis, the mortar method is extended to the case of curvilinear interfaces. For a scalar model equation, a rigorous convergence analysis in the spirit of variational crimes is carried out. In order to derive optimal a priori error estimates, the discrete problem formulation on affine elements is interpreted as a perturbation of a blending element approach, where the curved interfaces are resolved exactly. While the analysis is based on abstract assumptions for the discrete Lagrange multiplier space, dual Lagrange multipliers are introduced as a particular example satisfying these assumptions. They are characterized by the possibility to locally eliminate the multipliers from the system, which substantially increases the efficiency of the approach. Being formerly restricted to simplicial or parallelogram-shaped surface elements, two alternative extensions to arbitrary quadrilateral elements are given. Several numerical examples validate the theoretical results and illustrate the stability of the method with respect to the number of subdomains, as well as with respect to large differences in the subdomain meshsizes and the choice of the discrete Lagrange multiplier space.

Despite the fact that the theory of the scalar case can be extended to the setting of linear elasticity, a preasymptotic misbehavior is encountered for some non-standard Lagrange multipliers if they are used on the coarser interface grid. In order to restore the stability, two alternative modifications for lowest order dual Lagrange multipliers are presented, both preserving the advantages of the dual approach. A priori error estimates are derived, again using perturbation arguments by regarding the discrete problem for-

mulation as a perturbed blending approach. The positive effects of the modifications are illustrated by several numerical tests.

Moreover, the use of non-matching grids for coupled problems in computational acoustics is studied. In particular, the radiation of sound waves due to vibrating structures as well as turbulent flow is investigated. Employing non-matching grids is especially promising here, since the often quite small region occupying the source of the acoustic waves has to be discretized with a much smaller meshsize than the adjacent large domain of propagation. Two settings are examined, the first one considering the wave equation for the acoustic velocity potential in both regions, where a source term is responsible for the development of acoustic waves. The second setting realizes a fluid-structure coupling by considering a displacement based formulation for the elastic structure, and the wave equation for the acoustic fluid. The presented numerical tests range from a point source in two dimensions to the simulation of a three-dimensional piezo-electric loudspeaker, and always exhibit the profit of being able to use non-matching grids. Moreover, a solution method for the case of nonlinear structures is introduced and tested.

Especially for a subdomain in motion, it is natural to use an overlapping decomposition. In addition to the global triangulation, a local region is discretized independently and patched upon the global grid. First, a simple model problem is investigated: inheriting as boundary data the global solution, a corresponding subproblem is solved on the patch with the goal of a better approximation of the exact solution. The a priori error analysis incorporates the use of different meshwidths and finite element spaces on the global domain and the patch. As a particular application, the eddy currents resulting from the motion of a conductor through an electromagnetic field are investigated. The unknown magnetic field is decomposed into the difference of a vectorial component with support restricted to the conductor and the gradient of a scalar potential which is defined everywhere. Inside the conductor, edge elements are used to approximate the vector potential, whereas on the global grid, standard nodal elements are used for the scalar potential. The simulation of an electromagnetic brake is considered as an example which clearly depicts the advantage of using an overlapping decomposition.

Zusammenfassung

Zeitabhängige und stationäre Prozesse in Natur und Technik werden sehr häufig durch partielle Differentialgleichungen modelliert. Da deren analytische Lösungen im Allgemeinen nicht berechenbar sind, ist die Wichtigkeit robuster und effizienter numerischer Algorithmen zur Bestimmung von Näherungslösungen kaum zu überschätzen. Gebietszerlegungsmethoden in Verbindung mit moderner Finite-Elemente-Technologie stellen ein sehr vielversprechendes Werkzeug zur Entwicklung solcher Algorithmen dar. Die allgemeine Idee hinter jeder Gebietszerlegung ist im Wesentlichen reduzierbar auf das Motto "divide et impera"; so wird versucht, ein komplexes und großes globales Problem in mehrere einfachere und/oder kleinere lokale Probleme aufzuspalten. Um daraus eine Lösung des globalen Problems zu konstruieren, ist der stabile und effiziente Informationsaustausch zwischen den Teilproblemen von größter Wichtigkeit. Im Rahmen der numerischen Simulation werden Gebietszerlegungsideen für die optimale Diskretisierung der zugrundeliegenden physikalischen Problemstellungen, für die Entwicklung iterativer Löser, oder für die Parallelisierung bestehender numerischer Algorithmen eingesetzt.

In dieser Arbeit werden wir uns fast immer auf den physikalisch motivierten Diskretisierungsaspekt von Gebietszerlegungsmethoden konzentrieren. Aufgrund ihres breiten Anwendungsspektrums kommen finite Elemente zur Diskretisierung der kontinuierlichen Problemstellungen zum Einsatz. Hierfür ist es immer angenehm und manchmal auch unabdingbar, dass man in der Lage ist, Finite-Elemente-Gitter zu handhaben, die an den Trennflächen der Teilgebiete geometrisch nichtkonform sind. Es gibt eine Vielzahl von Anwendungen, bei denen solche nichtkonformen Gitter aus dem natürlichen Wunsch heraus entstehen, in jedem Teilgebiet das Gitter einzusetzen, welches am besten zur Lösung des entsprechenden Teilproblems geeignet ist. Während Methoden, die eine punktweise Kopplung benutzen, im Allgemeinen scheitern, bieten Mortar-Finite-Elemente einen Ansatz, der nichtkonforme Gitter sowohl aus mathematischer als auch aus implementierungsbezogener Sicht zufriedenstellend handhaben kann. Die Methode basiert auf der Einführung zusätzlicher Freiheitsgrade in Form Lagrangescher Multiplikatoren auf den Trennflächen, wobei starke Stetigkeitsanforderungen durch schwache ersetzt werden. Es hängt von der Qualität des diskreten Lagrange-Multiplikator-Raums ab, ob der resultierende Algorithmus stabil, optimal und effizient ist. Hier bieten sogenannte duale Multiplikatoren, deren zugrundeliegende Basis orthogonal bezüglich der Basis des diskreten Spurraums auf der Trennfläche ist, den entscheidenden Vorteil, dass sie lokal eliminiert werden können und somit die Effizienz des Ansatzes beträchtlich steigern.

Bis jetzt waren sowohl die Theorie als auch die meisten numerischen Tests auf ebene Trennflächen beschränkt. In dieser Arbeit erweitern wir die Mortar-Methode auf den Fall

gekrümmter Trennflächen. Es werden ein rigoroser mathematischer Rahmen im Sinne von "variational crimes" und umfangreiche numerische Beispiele vorgestellt. Für viereckige Oberflächenelemente waren die dualen Basisfunktionen bisher nur für Parallelogramme entwickelt. Wir erweitern duale Lagrange-Multiplikatoren niedrigster Ordnung auf Oberflächengitter bestehend aus beliebigen Drei- und Viereckselementen. Außerdem wird der Einsatz nichtkonformer Gitter für gekoppelte Problemstellungen der Akustik untersucht. Darüber hinaus ist es speziell für bewegte Teilgebiete vorteilhaft, eine überlappende Zerlegung zu verwenden. Wir benutzen die Mortar-Methode zur Handhabung ineinander geschachtelter Gebiete, und untersuchen eine Anwendung in der Elektro-Mechanik. Im Folgenden sind die Inhalte der Arbeit in größerem Detail aufgeführt.

Im einleitenden Kapitel 1 werden im Anschluss an eine Übersicht die in der Arbeit verwendeten Modellprobleme vorgestellt: die Poisson-Gleichung, lineare und nichtlineare Elastizität, sowie ein Kontaktproblem. Wir geben Gründe für die Verwendung dualer Lagrange-Multiplikatoren an und stellen klar, warum der Einsatz einer starken punktweisen Kopplung zwischen den Teilgebieten nicht empfehlenswert ist.

Kapitel 2 errichtet das mathematische Gerüst für das Problem der Handhabung gekrümmter Trennflächen in Mortar-Finite-Elemente-Methoden. Für ein skalares Modellproblem wird eine den Fall vieler Teilgebiete beinhaltende rigorose Konvergenzanalyse durchgeführt. Zur Herleitung optimaler a-priori-Fehlerabschätzungen wird die auf affinen Elementen basierende diskrete Problemformulierung als Störung eines Blending-Elemente-Ansatzes interpretiert, bei welchem die gekrümmten Trennflächen exakt aufgelöst werden. Während die Analysis auf abstrakten Annahmen an den diskreten Lagrange-Multiplikator-Raum beruht, werden duale Multiplikatoren als spezielles diese Annahmen erfüllendes Beispiel eingeführt. Zwei alternative Erweiterungen auf beliebige Viereckselemente werden für die vormals nur auf Dreiecken und Parallelogrammen definierten Multiplikatoren gegeben. Darüber hinaus werden die implementierungsbezogenen Aspekte der Assemblierung der Kopplungsmatrizen adressiert, wobei speziell auf die Schnitterkennung zweier Oberflächenelemente eingegangen wird. Dies führt zu mehreren numerischen Beispielen, welche die Stabilität des Ansatzes zum einen bezüglich der Anzahl der Teilgebiete, als auch bezüglich großer Sprünge in den Maschenweiten der Teilgebietsgitter und der Wahl des Lagrange-Multiplikator-Raumes illustrieren.

Inhalt von Kapitel 3 ist die Behandlung numerischer Instabilitäten, die durch Verwendung dualer Lagrange-Multiplikatoren auf gekrümmten Trennflächen zur Approximation von Oberflächenkräften in der Strukturmechanik entstehen. Obwohl die Theorie des skalaren Falls auf allgemeine elliptische Systeme linearer partieller Differentialgleichungen und damit auch auf den Rahmen linearer Elastizität übertragen werden kann, lässt sich für einige Nicht-Standard-Multiplikatoren ein vorasymptotisches Fehlverhalten beobachten, vorausgesetzt dass die Multiplikatoren auf dem gröberen Oberflächengitter zum Einsatz kommen. Es wird eine Erklärung dieses Fehlverhaltens mittels eines einfachen zwei-dimensionalen Modellproblems gegeben. Um die Stabilität wiederherzustellen, werden zwei Modifikationen für duale Multiplikatoren niedrigster Ordnung vorgestellt, welche beide die Vorteile der dualen Methode erhalten. A-priori-Fehlerabschätzungen werden unter wiederholter Benutzung von Störungsargumenten hergeleitet. Der positive Effekt der Modifikationen wird anhand mehrerer numerischer Tests dokumentiert.

Kapitel 4 ist anwendungsnahen Problemen aus der Akustik gewidmet. Es werden die Entstehung und Ausbreitung von Schallwellen aufgrund vibrierender Strukturen oder aufgrund von Strömungen untersucht. Der Einsatz nichtkonformer Gitter ist hier besonders vielversprechend, da die Quelle der akustischen Wellen häufig in einem verhältnismäßig kleinen Teilgebiet liegt, das mit einer viel kleineren Maschenweite diskretisiert werden muss als das angrenzende große Ausbreitungsgebiet. Wir untersuchen zwei Problemstellungen; bei der ersten wird die Wellengleichung für das akustische Geschwindigkeitspotenzial in beiden Teilgebieten betrachtet, wobei ein nicht-trivialer Quellterm für die Entstehung der Schallwellen verantwortlich ist. Hier erfolgt die Kopplung analog zum stationären Fall der Poisson-Gleichung. Die zweite Problemstellung realisiert eine Fluid-Struktur-Kopplung, indem eine verschiebungsbasierte Formulierung für die elastische Struktur und die Wellengleichung für das akustische Fluid betrachtet werden. Die Kopplungsbedingungen für die vektorwertigen Verschiebungen und das skalare Potenzial können hier in kanonischer Weise in die Variationsformulierung eingearbeitet werden, ohne dass die Einführung Lagrangescher Multiplikatoren erforderlich ist. Die vorgestellten numerischen Tests reichen von einer Punktquelle in zwei Dimensionen bis hin zu einem drei-dimensionalen piezo-elektrischen Lautsprecher. Darüber hinaus wird eine numerische Lösungsmethode für den Fall nichtlinearer Strukturen vorgestellt und getestet.

In Kapitel 5 werden überlappende Zerlegungen geschachtelter Gebiete betrachtet. Zusätzlich zur globalen Triangulierung wird eine lokale Region unabhängig diskretisiert und über das globale Gitter gelegt. Die globale Lösung gibt Dirichlet-Randbedingungen für das Teilgebiet vor, von der daraus resultierenden zusätzlichen Lösung auf dem Teilgebiet wird eine bessere Approximation der exakten Lösung erwartet. Die a-priori-Fehleranalysis schließt die Verwendung unterschiedlicher Maschenweiten und diskreter Ansatzräume auf dem globalen und dem lokalen Gebiet mit ein. Darüber hinaus wird eine äquivalente Formulierung als verallgemeinertes Sattelpunktproblem präsentiert. Die aufgeführten numerischen Resultate beinhalten die Kopplung linearer und quadratischer Elemente sowie die Anwendung auf ein reibungsbehaftetes unilaterales Kontaktproblem.

Kapitel 6 beschäftigt sich mit der Anwendung überlappender Zerlegungen auf die Simulation elektro-mechanischer Probleme. Es werden die aus der Bewegung eines Leiters durch ein Magnetfeld resultierenden Wirbelströme untersucht, die ihrerseits eine auf den Leiter wirkende Lorentzkraft auslösen. Das zu bestimmende Magnetfeld wird in die Differenz eines Vektorpotenzials, das nur auf dem Leiter existiert, und des Gradienten eines skalaren Potenzials, welches im gesamten Gebiet definiert ist, zerlegt. Im Leiter werden Kantenelemente für die Approximation des Vektorpotenzials verwendet, wohingegen auf dem globalen Gitter gewöhnliche nodale Elemente für das skalare Potenzial zum Einsatz kommen. Die Kopplung beider Potenziale wird wieder mittels eines Mortaransatzes realisiert. Als Beispiel wird die Simulation einer Wirbelstrombremse vorgestellt, welches klar den Vorteil des Einsatzes einer überlappenden Zerlegung demonstriert. Schließlich werden in Kapitel 7 die Schlussfolgerungen der Arbeit zusammengefasst.

Die gesamte Arbeit befindet sich im Rahmen herkömmlicher Variationsformulierungen. Im Anhang werden knapp die wichtigsten zugrundeliegenden Konzepte und Resultate aus Funktionalanalysis, schwachen Sattelpunktformulierungen und Finite-Elemente-Ansätzen aufgeführt.

1 Introduction

This introductory chapter first provides an overview of the thesis. After that, several model problems are presented, followed by the derivation of a saddle point problem based on a decomposition of the computational domain. Reasons are given for utilizing dual Lagrange multipliers for the discretization of such problems. Moreover, it is clarified why using a strong point-wise coupling usually fails for non-matching finite element grids.

1.1 Overview

Dynamic and stationary processes in nature and technology are very often modeled by partial differential equations. Since their analytical solutions are not computable in general situations, the importance of robust and efficient numerical schemes for obtaining approximate solutions can hardly be overrated. A most promising tool to develop such schemes is provided by the framework of domain decomposition methods in combination with modern finite element technology. Essentially reducible to the overall slogan "divide et impera", the general idea of domain decomposition is to decompose a complex and large global problem into several simpler and/or smaller local problems. In order to construct the solution to the global problem, the stable and inexpensive transmission of data between the subproblems is of outmost importance. Within the context of numerical simulation, domain decomposition ideas are employed to optimally discretize the underlying physical problems, to develop efficient iterative solvers, or to parallelize numerical algorithms. In order to gain access to the vast literature, the books [100, 113, 115], as well as the proceedings of the annual International Domain Decomposition Meetings can be recommended, [1].

In this thesis, we will almost always focus on the aforementioned physically motivated discretization aspect of domain decomposition methods. Due to their universality and flexibility, finite elements will be used to discretize the continuous problem formulations. When now domain decomposition techniques are applied to discretize partial differential equations by means of finite elements, it is always convenient and sometimes even mandatory to be able to deal with non-matching finite element grids. There are numerous tasks where non-matching grids naturally arise when employing on each subdomain the grid which is best suited to solve the corresponding subproblem associated with this subdomain. Concerning the construction of appropriate transmission operators between the grids, the framework of mortar finite elements provides a method which is able to deal with non-matching grids both from the mathematical and from the implementational point of view. The method is based on introducing additional degrees of freedom in form of Lagrange multipliers on the interface, thereby replacing the strong continuity

requirement of the solution across the interface by a weak one. It depends on the quality of the discrete Lagrange multiplier space whether the resulting numerical scheme is stable, optimal, and efficient.

Originally introduced in [19, 20, 21] for the coupling of spectral and finite element methods, the first choice for the Lagrange multiplier space was the trace of the finite element space on the interface. Soon, the analysis of mortar methods was extended to three-dimensional problems, [15, 24, 77], and to *hp*-finite elements, [16, 110, 111]. The very natural equivalent formulation of the mortar approach by means of a saddle point problem was introduced in [10] and clearly exhibited the important role of the Lagrange multiplier space. The saddle point structure of the linear system arising from mortar discretizations required the development of adjusted iterative solvers, [24, 25, 55, 119, 121]. The advent of dual Lagrange multipliers in [120] opened new perspectives for the construction of iterative solvers by offering the possibility to *locally* eliminate the Lagrange multipliers from the system. In particular, two multigrid methods have been proposed that take advantage of the dual multipliers, one based on the unconstrained product space, [125], and one based on the constrained problem, [126].

Evolving from simple model problems, mortar methods meanwhile have been successfully applied to a wide range of academic and near-to-real-life problem settings. In [11, 12], the Stokes problem was considered, resulting in a stabilized approach with discontinuous multipliers, which got further utilized in [63, 64] for the solution of elastodynamic problems. Applications to flow in porous media were given in [95, 96]. In structural mechanics, a most prominent setting yielding a natural domain decomposition is provided by multi-body contact problems. The urge of being able to deal with non-matching grids led to an extension of mortar methods to this field, [13, 14, 87, 98]. Also here, the use of dual Lagrange multipliers offers an improved numerical efficiency by admitting to construct adjusted active set strategies, [70, 72].

So far, the theory as well as most of the numerical tests have been restricted to the case of planar interfaces. In this thesis, we extend the mortar method to the case of curvilinear interfaces. A rigorous mathematical framework in the spirit of variational crimes is provided, as well as extensive numerical examples. For quadrilateral surface elements, the dual basis functions have only been developed for parallelograms. We extend the lowest order dual Lagrange multipliers to arbitrary quadrilateral or triangular surface grids. Moreover, we study the use of non-matching grids for coupled problems in computational acoustics. Especially for a subdomain in motion, it is natural to use an overlapping decomposition. We employ the mortar framework to deal with nested domains, and investigate an application to electro-mechanics. In the following, the contents of this thesis are presented in more detail.

In the remainder of this introductory chapter, the model problems used throughout the thesis are introduced, including Poisson's equation, linear and nonlinear elasticity, as well as a contact problem. Moreover, we give reasons for using dual Lagrange multipliers, the most important one being the possibility to locally eliminate the multipliers yielding a positive definite system. Additionally, we clarify why it is not advisable to use a strong point-wise coupling between the subdomains.

Chapter 2 sets up the mathematical foundation for the problem of dealing with curvi-

linear interfaces in mortar finite element methods. For a scalar model equation, a rigorous convergence analysis based on [47] is carried out, including the case of many subdomains. In order to derive optimal a priori error estimates, the discrete problem formulation on affine elements is interpreted as a perturbation of a blending element approach, where the curved interfaces are resolved exactly. While the analysis is based on abstract assumptions for the discrete Lagrange multiplier space, dual Lagrange multipliers are introduced as a particular example satisfying these assumptions. Being formerly restricted to simplicial or parallelogram-shaped surface elements, two alternative extensions to arbitrary quadrilateral elements are given, as introduced in [51]. Moreover, the assembly of the coupling matrices is considered from the implementational point of view, focusing on the detection of the intersection area of two surface elements. This leads to several numerical examples validating the theoretical results and illustrating the stability of the method with respect to the number of subdomains, as well as with respect to large differences in the subdomain meshsizes and the choice of the discrete Lagrange multiplier space.

Subject of Chapter 3 is the treatment of numerical instabilities arising from the use of dual Lagrange multipliers on curved interfaces for the approximation of surface tractions within structural mechanics. Despite the fact that the theory of the scalar case can be extended to general elliptic systems of linear partial differential equations and therefore to the setting of linear elasticity, a pre-asymptotic misbehavior is encountered for some non-standard Lagrange multipliers if they are used on the coarser interface grid. An explanation of this misbehavior is given by means of a simple two-dimensional model problem. In order to restore the stability, two alternative modifications for lowest order dual Lagrange multipliers are presented, both preserving the advantages of the dual approach. Unifying the two-dimensional and the three-dimensional case presented in [48] and [51], respectively, a priori error estimates are derived, again using perturbation arguments by regarding the discrete problem formulation as a perturbed blending approach. The positive effects of the modifications are illustrated by several numerical tests.

Chapter 4 is devoted to applied problems arising from computational acoustics. The radiation of sound waves due to vibrating structures as well as turbulent flow is investigated. The use of non-matching grids is especially promising here, since the often quite small region occupying the source of the acoustic waves has to be discretized with a much smaller meshsize than the adjacent large domain of propagation. Setting up on [42], two settings are examined, the first one considering the wave equation for the acoustic velocity potential in both regions, where a non-trivial source term is responsible for the development of acoustic waves. The coupling is managed analogous to the stationary case of Poisson's equation. The second setting realizes a fluid-structure coupling by considering a displacement based formulation for the elastic structure, and the wave equation for the acoustic fluid. The coupling conditions for the vectorial displacement and the scalar potential can be incorporated in a straightforward manner into the variational problem formulation with no need for the introduction of Lagrange multipliers. The coupling matrices remain almost the same. The presented numerical tests range from a point source in two dimensions to the simulation of a three-dimensional piezo-electric loudspeaker, and always exhibit the profit of being able to use non-matching grids. Moreover, a solution method for the case of nonlinear structures is introduced and tested.

In Chapter 5, an overlapping decomposition of nested domains is considered. In addition to the global triangulation, a local region is discretized independently and patched upon the global grid. Inheriting as boundary data the global solution, a corresponding subproblem is solved on the patch with the goal of a better approximation of the exact solution. The a priori error analysis incorporates the use of different meshwidths and finite element spaces on the global domain and the patch, [49]. Moreover, an equivalent formulation as a generalized saddle point problem is presented, [46]. Numerical results including the coupling of linear with quadratic elements, and the application to a frictional unilateral contact-problem complete the chapter.

Chapter 6 deals with the application of an overlapping decomposition to the simulation of an electro-mechanical problem, [44]. In particular, the eddy currents resulting from the motion of a conductor through an electromagnetic field are investigated, causing a Lorentz force acting on the conductor. The unknown magnetic field is decomposed into the difference of a vectorial component with support restricted to the conductor and the gradient of a scalar potential which is defined everywhere. Inside the conductor, edge elements are used to approximate the vector potential, whereas on the global grid, standard nodal elements are used for the approximation of the scalar potential. The coupling between the two potentials is again realized by a mortar approach. As numerical example, the simulation of an electromagnetic brake is considered, [45], which clearly depicts the advantage of using an overlapping decomposition in the case of a moving subdomain. Finally, Chapter 7 draws the conclusions of this thesis.

Throughout the thesis, the standard variational setting is employed. The appendix briefly reviews the most important concepts and results of functional analysis, weak saddle point problems, and finite element spaces. For the numerical results, the software toolbox UG, [8], has been used for the discretization and the solution by multigrid, while PARDISO, [105, 106], has been employed as a direct solver. The visualization in three dimensions has been performed with the help of NETGEN, [108], and GMV, [93].

1.2 Model Problems

We introduce the model equations which are used for the upcoming analysis and the numerical illustrations. Starting with the formulation for a single domain, the strong and the weak form of Poisson's equation and elasticity problems are given. By investigating a simple decomposition into two subdomains, the principles of the coupling via a Lagrange multiplier space are explained, yielding a weak saddle point formulation. Some remarks on the resulting system of equations after discretization conclude the section.

1.2.1 Single Domain Formulation

For scalar problems, we focus on Poisson's equation in $\mathbb{R}^d$, $d = 2, 3$. In particular, given a domain $\Omega \subset \mathbb{R}^d$, we seek a scalar function u as the solution of

$$-\operatorname{div}\operatorname{grad} u = f \text{ in } \Omega. \tag{1.1a}$$

The boundary of Ω is the union of disjoint subsets Γ_N and Γ_D, on which Neumann data, i.e., fluxes, and homogeneous Dirichlet data, i.e., zero solution values, are given, respectively,

$$\partial u/\partial \boldsymbol{n} = g \text{ on } \Gamma_\mathrm{N}, \tag{1.1b}$$
$$u = 0 \text{ on } \Gamma_\mathrm{D}, \tag{1.1c}$$

with $\boldsymbol{n}$ denoting the unit outward normal vector field on $\partial\Omega$. We assume that Γ_D has a nontrivial Lebesgue measure. Starting from the strong problem formulation, the crucial first step in any finite element approach is to proceed to a weak or variational formulation. In case of problem (1.1), this is achieved by choosing appropriate function spaces for the weak solution and for the test functions in accordance with the Dirichlet boundary condition (1.1c), multiplying (1.1a) by a test function v, performing a partial integration by means of Green's formula (A.10), and inserting the Neumann boundary conditions (1.1b). We arrive at the variational problem of finding a function $u \in X = \{v \in H^1(\Omega) : v|_{\Gamma_\mathrm{D}} = 0\}$ such that

$$a(u, v) = l(v), \qquad v \in X, \tag{1.2}$$

where in the definition of X, the restriction of v to Γ_D has to be understood in the sense of traces, see Theorem A.13. Moreover, we set the bilinear form $a(\cdot,\cdot) = (\operatorname{grad}\cdot, \operatorname{grad}\cdot)_\Omega$ with $(\cdot,\cdot)_\Omega$ indicating the L^2-inner product (A.2), and the linear form $l(\cdot) = (f,\cdot)_\Omega + (g,\cdot)_{\Gamma_\mathrm{N}}$. Since the bilinear form $a(\cdot,\cdot)$ is X-elliptic and continuous on $X \times X$, and since the linear form $l(\cdot)$ is continuous on X, the Lax-Milgram Lemma A.21 can be applied yielding the well-posedness of problem (1.2).

Additionally, we consider linear and nonlinear elasticity problems, [32]. For the linear setting, we intend to solve the problem of finding a displacement vector field $\boldsymbol{u}$ such that we have the force balance

$$-\operatorname{div}\sigma(\boldsymbol{u}) = \boldsymbol{f} \text{ in } \Omega, \tag{1.3}$$

supplemented by Hooke's law

$$\sigma = \lambda_\mathrm{L}(\operatorname{tr}\varepsilon)\mathrm{Id} + 2\mu_\mathrm{L}\,\varepsilon, \tag{1.4}$$

with the Lamé constants $\lambda_\mathrm{L}, \mu_\mathrm{L}$, and by the linearized strain tensor

$$\varepsilon(\boldsymbol{u}) = \frac{1}{2}(\operatorname{grad}\boldsymbol{u} + [\operatorname{grad}\boldsymbol{u}]^\mathrm{T}). \tag{1.5}$$

The boundary $\partial\Omega$ is assumed to be partitioned as before, and $\boldsymbol{u}$ has to satisfy the conditions

$$\sigma(\boldsymbol{u})\boldsymbol{n} = \boldsymbol{g} \text{ on } \Gamma_\mathrm{N}, \tag{1.6a}$$
$$\boldsymbol{u} = 0 \text{ on } \Gamma_\mathrm{D}. \tag{1.6b}$$

The term $\sigma(\boldsymbol{u})\boldsymbol{n}$ corresponds to the surface traction on Γ_N. Proceeding like in the scalar case yields the weak formulation (1.2) with X replaced by X^d and $a(\cdot,\cdot) = (\sigma(\cdot), \varepsilon(\cdot))_\Omega$, as well as $l(\cdot) = (\boldsymbol{f},\cdot)_\Omega + (\boldsymbol{g},\cdot)_{\Gamma_\mathrm{N}}$. By Corollary A.20 of Korn's second inequality A.19,

the bilinear form $a(\cdot,\cdot)$ is X^d-elliptic, and again the Lax-Milgram lemma guarantees the unique solvability of (1.2).

However, the validity of the linearized elasticity equations (1.3)-(1.5) is restricted to small strains and small deformations. If the strains remain small but the deformations become large, one has at least to consider the geometrically nonlinear elasticity setting. This amounts to using the full Green–St. Venant tensor

$$E = \frac{1}{2}(F^{\mathrm{T}}F - \mathrm{Id}) = \frac{1}{2}(C - \mathrm{Id}), \tag{1.7}$$

instead of (1.5), with $F = \mathrm{Id} + \operatorname{grad} \boldsymbol{u}$ the deformation gradient and $C = F^{\mathrm{T}}F$ the right Cauchy–Green strain tensor. We keep the constitutive law (1.4) as

$$S = \lambda_{\mathrm{L}}(\operatorname{tr} E)\mathrm{Id} + 2\mu_{\mathrm{L}}\, E = \mathcal{C}E, \tag{1.8}$$

defining the second Piola–Kirchhoff stress tensor S, with $\mathcal{C}$ the Hooke-tensor. We solve

$$-\operatorname{div}(FS) = f, \tag{1.9}$$

complemented by the boundary conditions

$$FS\boldsymbol{n} = \boldsymbol{g} \text{ on } \Gamma_{\mathrm{N}}, \quad \text{and} \quad \boldsymbol{u} = 0 \text{ on } \Gamma_{\mathrm{D}}. \tag{1.10}$$

Transforming to the weak setting, the nonlinearity in (1.7) results in the fact that $a(\cdot,\cdot)$ is nonlinear in the first and linear in the second argument, i.e., we obtain (1.2) with X^d and $l(\cdot)$ as before, and the linear form $a(\boldsymbol{u},\cdot)$ given by $a(\boldsymbol{u},\boldsymbol{v}) = \sum_{i=1}^{4} a_i(\boldsymbol{u},\boldsymbol{v})$, where, cf. [32],

$$a_1(\boldsymbol{u},\boldsymbol{v}) = (\mathcal{C}\varepsilon(\boldsymbol{u}),\varepsilon(\boldsymbol{v}))_\Omega, \qquad a_2(\boldsymbol{u},\boldsymbol{v}) = \frac{1}{2}(\mathcal{C}\left[(\operatorname{grad}\boldsymbol{u})^{\mathrm{T}}\operatorname{grad}\boldsymbol{u}\right],\operatorname{grad}\boldsymbol{v})_\Omega,$$

$$a_3(\boldsymbol{u},\boldsymbol{v}) = (\operatorname{grad}\boldsymbol{u}\mathcal{C}\operatorname{grad}\boldsymbol{u},\operatorname{grad}\boldsymbol{v})_\Omega,\ a_4(\boldsymbol{u},\boldsymbol{v}) = \frac{1}{2}(\operatorname{grad}\boldsymbol{u}\mathcal{C}\left[(\operatorname{grad}\boldsymbol{u})^{\mathrm{T}}\operatorname{grad}\boldsymbol{u}\right],\operatorname{grad}\boldsymbol{v})_\Omega.$$

Under additional assumptions on the data, it is possible to establish the well-posedness of (1.7)–(1.9), [104]. However, the analysis of the nonlinear problem is substantially more involved and not within the scope of this thesis.

Still, the applicability of (1.7)–(1.9) is limited to small strains. In order to extend the model to large strains, we have to introduce another kind of nonlinearity by means of nonlinear material laws, [92]. In particular, to solve (1.9), we employ the neo-Hooke law given by

$$S = \mu_{\mathrm{L}}(\mathrm{Id} - C^{-1}) + \frac{\lambda_{\mathrm{L}}}{2}(J^2 - 1)C^{-1}, \tag{1.11}$$

with $J = \det(F)$ denoting the determinant of the deformation gradient. While in (1.7) the nonlinearity enters in terms of polynomials of $\operatorname{grad}\boldsymbol{u}$, it is given in terms of its inverse in (1.11).

1.2.2 Coupled Formulation

For the ease of notation and to avoid technicalities in this introductory chapter, we restrict ourselves to the case of two non-overlapping open subdomains Ω^{m} and Ω^{s} sharing a common interface Γ, their union giving the global domain Ω, $\overline{\Omega} = \overline{\Omega^{\mathrm{m}} \cup \Omega^{\mathrm{s}}}$. Moreover, we assume that $\Gamma_{\mathrm{D}} = \partial\Omega$. By taking into account the standard modifications at the cross-points or at the wire-basket of more than two subdomains, the following considerations apply analogously to more general situations, especially to decompositions into many subdomains, as will be carried out in Chapter 2.

In the following, we establish a weak formulation of the model problem (1.1) corresponding to the decomposition of the domain Ω. We equivalently can rewrite (1.1a) as

$$
\begin{aligned}
-\operatorname{div}\operatorname{grad} u_k &= f_k, && \text{in } \Omega^k,\ k = \mathrm{m},\mathrm{s}, && (1.12a)\\
u_{\mathrm{m}} &= u_{\mathrm{s}} && \text{on } \Gamma, && (1.12b)\\
\partial u_{\mathrm{m}}/\partial \boldsymbol{n}_{\mathrm{m}} &= -\partial u_{\mathrm{s}}/\partial \boldsymbol{n}_{\mathrm{s}} && \text{on } \Gamma, && (1.12c)
\end{aligned}
$$

denoting by $\boldsymbol{n}_k$ the unit normal vector field on the interface Γ, outward with respect to Ω^{k}, $k = \mathrm{m},\mathrm{s}$. This means that the strong solution $u = (u_{\mathrm{m}}, u_{\mathrm{s}})$ is required to be continuous in its trace as well as in its flux, across the interface Γ. The correct function space to consider now is the product $X = X^{\mathrm{m}} \times X^{\mathrm{s}}$, where $X^k = \{v \in H^1(\Omega^k) : v|_{\Gamma_{\mathrm{D}} \cap \partial\Omega^k} = 0\}$, $k = \mathrm{m},\mathrm{s}$. Multiplying (1.12a) with $v = (v_{\mathrm{m}}, v_{\mathrm{s}}) \in X$ and applying Green's formula (A.10) subdomain-wise yields

$$
\sum_{k=\mathrm{m},\mathrm{s}} (\operatorname{grad} u_k, \operatorname{grad} v_k)_{\Omega^k} - \langle v_{\mathrm{m}}, \partial u_{\mathrm{m}}/\partial \boldsymbol{n}_{\mathrm{m}} \rangle_{H^{-1/2};\Gamma} - \langle v_{\mathrm{s}}, \partial u_{\mathrm{s}}/\partial \boldsymbol{n}_{\mathrm{s}} \rangle_{H^{-1/2};\Gamma} = l(v), \quad (1.13)
$$

where $\langle \cdot, \cdot \rangle_{H^{-1/2};\Gamma}$ indicates the duality product on $H^{1/2}_{00}(\Gamma) \times H^{-1/2}(\Gamma)$. An important step is now the introduction of the Lagrange multiplier $\lambda \in M = H^{-1/2}(\Gamma)$ which is chosen to be the normal flux through the interface Γ, namely, using the coupling condition (1.12c), $\lambda = -\partial u_{\mathrm{s}}/\partial \boldsymbol{n}_{\mathrm{s}} = \partial u_{\mathrm{m}}/\partial \boldsymbol{n}_{\mathrm{m}}$. This simplifies (1.13) to

$$
\sum_{k=\mathrm{m},\mathrm{s}} (\operatorname{grad} u_k, \operatorname{grad} v_k)_{\Omega^k} + \langle v_{\mathrm{s}} - v_{\mathrm{m}}, \lambda \rangle_{H^{-1/2};\Gamma} = l(v). \quad (1.14)
$$

While the introduction of the Lagrange multiplier λ realizes the coupling (1.12c) of the flux in a strong sense, the remaining coupling (1.12b) in the trace is enforced in a weak sense. This is achieved by multiplying (1.12b) by a Lagrange multiplier test function $\mu \in M$ and integrating over Γ, which yields

$$
b(u, \mu) = \langle u_{\mathrm{s}} - u_{\mathrm{m}}, \mu \rangle = 0, \qquad \mu \in M, \quad (1.15)
$$

introducing the coupling bilinear form $b : X \times M \to \mathbb{R}$. With (1.14) and (1.15), we arrive at the typical saddle point problem of the following structure, [27]: find a primal variable $u \in X$ and a Lagrange multiplier $\lambda \in M$ such that

$$
\begin{aligned}
a(u, v) + b(v, \lambda) &= l(v), && v \in X, && (1.16a)\\
b(u, \mu) &= 0, && \mu \in M, && (1.16b)
\end{aligned}
$$

with $a(\cdot,\cdot) = \sum_{k=\mathrm{m,s}} (\operatorname{grad}\cdot, \operatorname{grad}\cdot)_{\Omega^k}$. Problem (1.16) is well-posed, if the well-established conditions (A.15), (A.16) are satisfied.

The above procedure can be applied to the linear elasticity problem (1.3)–(1.6) in a straightforward manner. In the resulting problem formulation (1.16), the spaces X and M consist of vector fields with component functions being in the corresponding spaces for the scalar case. Moreover, the Lagrange multiplier $\boldsymbol{\lambda}$ corresponds to the surface tractions on Γ, namely,

$$\boldsymbol{\lambda} = -\sigma(\boldsymbol{u}_\mathrm{s})\boldsymbol{n}_\mathrm{s}, \tag{1.17}$$

the coupling $b(\cdot,\cdot)$ remains the same with vector fields replacing the scalar functions, and the bilinear form $a(\cdot,\cdot)$ is given analogously to the scalar case as the sum of the corresponding bilinear forms on the subdomains.

By elimination of the Lagrange multiplier, the saddle point problem (1.16) can be recast into a positive definite problem, provided that $a(\cdot,\cdot)$ is elliptic on the constrained space

$$V = \{v \in X : b(v,\mu) = 0,\ \mu \in M\},$$

where in case of the Laplace operator, [54], and of the linear elasticity setting, [61], it is well known that the ellipticity constant does not depend on the number of subdomains. In particular, this yields in analogy to (1.2) the problem of finding $u \in V$ such that

$$a(u,v) = l(v), \qquad v \in V. \tag{1.18}$$

For the nonlinear elasticity problems (1.7)–(1.10) and (1.9)–(1.11), the situation is much more involved. However, the subdomain coupling via Lagrange multipliers remains the same as for linear problems. Physically, $\boldsymbol{\lambda} = -FS\boldsymbol{n}$ is still interpreted as surface traction on Γ.

In addition to the model problems introduced in Section 1.2.1, we consider a two-body nonlinear contact problem as a most natural example where domain decomposition techniques can successfully be applied. The domain Ω is the union of two initially disjoint bodies Ω^s, Ω^m, and its boundary $\partial\Omega = \partial\Omega^\mathrm{s} \cup \partial\Omega^\mathrm{m}$ is subdivided into three disjoint open sets Γ_D, Γ_N, Γ_C. We intend to solve (1.3)-(1.5) with Dirichlet and Neumann boundary conditions on Γ_D and Γ_N, respectively, and frictionless Signorini contact conditions on the possible contact boundary Γ_C, given by

$$\begin{aligned} \boldsymbol{\sigma}_\tau(\boldsymbol{u}_\mathrm{s}) = \boldsymbol{\sigma}_\tau(\boldsymbol{u}_\mathrm{m}) = 0, \quad \sigma_n(\boldsymbol{u}_\mathrm{m})([\boldsymbol{u}\,\boldsymbol{n}] - g) = 0, \\ [\boldsymbol{u}\,\boldsymbol{n}] - g \le 0, \quad \sigma_n(\boldsymbol{u}_\mathrm{m}) = \sigma_n(\boldsymbol{u}_\mathrm{s}) \le 0, \end{aligned} \tag{1.19}$$

where $\boldsymbol{\sigma}_\tau(\boldsymbol{u}_k)$ and $\sigma_n(\boldsymbol{u}_k)$ are the tangential part and the normal component of the surface traction $\sigma(\boldsymbol{u}_k)\boldsymbol{n}$, respectively, $k = \mathrm{m,s}$, $[\boldsymbol{u}\,\boldsymbol{n}]$ stands for the jump of the normal displacement across Γ_C, and g defines the linearized initial gap between the two bodies. We arrive at the problem, [71]: find $(\boldsymbol{u},\boldsymbol{\lambda}) \in X \times M^+$ such that

$$\begin{aligned} a(\boldsymbol{u},\boldsymbol{v}) + b(\boldsymbol{v},\boldsymbol{\lambda}) &= f(\boldsymbol{v}), & \boldsymbol{v} &\in X, \\ b(\boldsymbol{u},\boldsymbol{\mu}-\boldsymbol{\lambda}) &\le \langle g, (\boldsymbol{\mu}-\boldsymbol{\lambda})\,\boldsymbol{n}\rangle_{\Gamma_{\mathrm{C,s}}}, & \boldsymbol{\mu} &\in M^+, \end{aligned} \tag{1.20}$$

with $b(\boldsymbol{v}, \boldsymbol{\mu}) = \langle \boldsymbol{\mu}\,\boldsymbol{n}, [\boldsymbol{v}\,\boldsymbol{n}] \rangle_{\Gamma_{\mathrm{C,s}}}$ and $M^+ = \{\boldsymbol{\mu} \in M : \boldsymbol{\mu}_\tau = 0, \langle \boldsymbol{\mu}\,\boldsymbol{n}, v \rangle_{\Gamma_{\mathrm{C,s}}} \geq 0, v \in W_{\mathrm{C}}, v \geq 0 \text{ on } \Gamma_{\mathrm{C,s}}\}$, where W_{C} denotes the trace space of $H^1(\Omega^{\mathrm{s}})$ restricted to $\Gamma_{\mathrm{C,s}}$, and M is its dual. We discuss an appropriate and efficient solution strategy for the discrete version of (1.20) in Section 3.4.7.

1.2.3 Discretization

In order to numerically solve (1.16), the infinite-dimensional spaces X and M are approximated by a family of finite dimensional spaces $X_h = X_h^{\mathrm{m}} \times X_h^{\mathrm{s}}$ and M_h with a discretization parameter h, and (1.16) yields the discrete problem of finding $(u_h, \lambda_h) \in X_h \times M_h$ such that

$$a(u_h, v_h) + b(v_h, \lambda_h) = f(v_h), \qquad v_h \in X_h, \tag{1.21a}$$

$$b(u_h, \mu_h) = g(\mu_h), \qquad \mu_h \in M_h. \tag{1.21b}$$

If the approximations of X and M by X_h and M_h are conforming, the fulfillment of the discrete analogs (A.19), (A.20) to the conditions (A.15), (A.16) yields a priori error estimates in terms of the best approximation errors. An optimal approximation can only be expected, if the constants involved in (A.19), (A.20) are independent of the discretization parameter h.

In this thesis, the approximations are always chosen to be finite element spaces based on two triangulations $\mathcal{T}_{\mathrm{m}}$ of Ω^{m} and $\mathcal{T}_{\mathrm{s}}$ of Ω^{s}. For the moment, we assume that the triangulations resolve the subdomains (and therefore also Γ) exactly. We emphasize that each triangulation $\mathcal{T}_k$, $k = \mathrm{m,s}$, itself is assumed to be geometrically conforming, while the overall triangulation $\mathcal{T}_{\mathrm{m}} \cup \mathcal{T}_{\mathrm{s}}$ may be non-matching at the interface Γ. Using superscripts, we indicate by $\mathcal{T}^{\mathrm{m}}$ and $\mathcal{T}^{\mathrm{s}}$ the corresponding surface grids meeting the interface Γ. The finite element nodes on $\mathcal{T}^{\mathrm{m}}$ and $\mathcal{T}^{\mathrm{s}}$ are called master and slave nodes, respectively, all remaining nodes are indicated as inner nodes. We associate the discrete Lagrange multiplier space M_h with the mesh $\mathcal{T}^{\mathrm{s}}$ on the slave side. Having chosen a basis for each of the spaces X_h and M_h, the approximate problem (1.21) can be written as

$$\begin{pmatrix} A_{\mathrm{ii}} & A_{\mathrm{im}} & A_{\mathrm{is}} & 0 \\ A_{\mathrm{mi}} & A_{\mathrm{mm}} & 0 & -M^{\mathrm{T}} \\ A_{\mathrm{si}} & 0 & A_{\mathrm{ss}} & D^{\mathrm{T}} \\ 0 & -M & D & 0 \end{pmatrix} \begin{pmatrix} u_h^{\mathrm{i}} \\ u_h^{\mathrm{m}} \\ u_h^{\mathrm{s}} \\ \lambda_h \end{pmatrix} = \begin{pmatrix} f^{\mathrm{i}} \\ f^{\mathrm{m}} \\ f^{\mathrm{s}} \\ 0 \end{pmatrix}, \tag{1.22}$$

where the subscripts i, m, and s represent the inner, master and slave nodes, respectively. The entries of the coupling matrices M and D are assembled from integrals of the form

$$(\phi_p^{\mathrm{m}}, \mu_q)_\Gamma, \quad \text{and} \quad (\phi_p^{\mathrm{s}}, \mu_q)_\Gamma, \tag{1.23}$$

respectively, where ϕ_p^k, $k = \mathrm{m,s}$, denotes the scalar nodal basis function of the trace space $W_h^k = X_h^k|_\Gamma$ of the finite element space on $\mathcal{T}^k$ associated with the node p, and μ_q stands for the scalar basis function of the discrete Lagrange multiplier space M_h associated with the node q.

1.3 Why Dual Lagrange Multipliers?

In the following, we illustrate why dual Lagrange multipliers are an important key to efficiently solve problems discretized by mortar finite elements. We speak of *dual* basis functions μ_q, if they satisfy the biorthogonality relation

$$(\phi_p^{\mathrm{s}}, \mu_q)_\Gamma = \delta_{pq}(1, \phi_p^{\mathrm{s}})_\Gamma. \tag{1.24}$$

The importance of (1.24) comes into play when attempting to solve the discrete problem (1.22). There exist various possibilities for solving the problem efficiently by iterative solvers. The development of positive definite discrete formulations, which are equivalent to (1.22) and for which multigrid schemes can be applied, always involves the elimination of the discrete Lagrange multipliers from the indefinite system (1.22), [124]. This elimination is performed in terms of the discrete projection operator $\widehat{M} = D^{-1}M$, which enters into the positive definite system matrix. The same operator plays an essential role if Dirichlet–Neumann solvers are applied, [62]. Depending on the structure of D, this projection can be carried out locally or it has to be carried out globally, represented by a sparse or a dense matrix $\widehat{M}$, respectively. In particular, if the biorthogonality relation (1.24) is satisfied, the matrix D is diagonal, and therefore, $\widehat{M}$ is sparse and can be easily calculated. We emphasize that the applicability of dual Lagrange multipliers is not restricted to linear stationary problems as (1.16). In more general cases, one has to face a linear system of the structure (1.22) in each iteration step of a time integration and/or nonlinear solution method.

For example, the advantages of the dual approach have been fully exploited for the solution of contact problems like (1.20), [72]. There, the linearized non-penetration condition is formulated as a weak integral inequality constraint $Du_h^{\mathrm{s}} \leq Mu_h^{\mathrm{m}} + g^{\mathrm{s}}$. Only in case of dual Lagrange multipliers, this is equivalent to the point-wise inequality $u_h^{\mathrm{s}} \leq D^{-1}(Mu_h^{\mathrm{m}} + g^{\mathrm{s}})$. Thus, the inequality constraint can be verified for each node separately, and we do not have to apply a global strategy to solve the nonlinear variational inequality.

For the iterative solution of the discretized nonlinear elasticity problems (1.7)–(1.10) and (1.9)–(1.11), it is very useful to eliminate the discrete Lagrange multipliers and apply a Newton iteration to the constrained problem. In particular, the Jacobian of the constrained system is positive definite and admits the use of multigrid solvers for the linear system in each Newton step. As pointed out before, the elimination is especially efficient if the dual basis functions are used for spanning the Lagrange multiplier space.

1.4 Why Not Simply Couple Point-wise?

A very straightforward way to deal with non-matching grids at the interface Γ may seem to perform a strong point-wise coupling in the sense that the nodal values on the slave side have to coincide with the solution on the master side. We investigate this approach by means of an example. As it turns out, this method even yields the celebrated aforementioned possibility of local elimination of the discrete Lagrange multipliers. However, it severely suffers from the fact that it is not optimal.

We consider the model problem (1.12) on $\Omega = (0,2) \times (0,1) \subset \mathbb{R}^2$ with $f_k = 0$, $\Omega^{\mathrm{m}} = (0,1)^2$, $\Omega^{\mathrm{s}} = (1,2) \times (0,1)$, and $\Gamma = \{1\} \times (0,1)$. We assume homogeneous Dirichlet boundary conditions (1.1c) on $\Gamma_l = \{0\} \times (0,1)$, while we require $u = 2$ on $\Gamma_r = \{2\} \times (0,1)$. On $\Gamma_{\mathrm{N}} = \partial\Omega \setminus (\overline{\Gamma_l} \cup \overline{\Gamma_r})$, we set (1.1b) with $g = 0$. Obviously, the exact solution is $u(x,y) = x$. Setting

$$X = \{(v_{\mathrm{m}}, v_{\mathrm{s}}) \in H^1(\Omega^{\mathrm{m}}) \times H^1(\Omega^{\mathrm{s}}) : v_{\mathrm{m}}|_{\Gamma_l} = 0,\ v_{\mathrm{s}}|_{\Gamma_r} = 2\},$$
$$X_0 = \{(v_{\mathrm{m}}, v_{\mathrm{s}}) \in H^1(\Omega^{\mathrm{m}}) \times H^1(\Omega^{\mathrm{s}}) : v_{\mathrm{m}}|_{\Gamma_l} = 0,\ v_{\mathrm{s}}|_{\Gamma_r} = 0\},$$

the saddle point problem (1.16) is derived with the test function space X in the first line (1.16a) replaced by X_0. For the discretization, we choose $X_h = S_h \cap X$ and $X_{0,h} = S_h \cap X_0$ with $S_h = \{(v_{\mathrm{m}}, v_{\mathrm{s}})$ piecewise linear with respect to $\mathcal{T}^{\mathrm{m}} \times \mathcal{T}^{\mathrm{s}}\}$. The point-wise coupling is realized by approximating the Lagrange multiplier space M by Dirac delta distributions $\delta(p)$ associated with the slave nodes p, namely, $M_h = \operatorname{span}\{\delta(p), p \text{ slave node}\}$. An important fact is that this approximation is non-conforming, i.e., $M_h \nsubseteq M$. Proceeding like this, the discrete problem (1.21) reads: find $(u_h, \lambda_h = \sum_p \lambda_p \delta(p)) \in X_h \times M_h$ such that

$$a(u_h, v) \ + \ \textstyle\sum_p \lambda_p (v_{\mathrm{s}}(p) - v_{\mathrm{m}}(p)) = 0, \qquad v \in X_{0,h}, \tag{1.25a}$$
$$\textstyle\sum_p \alpha_p (u_{h,\mathrm{s}}(p) - u_{h,\mathrm{m}}(p)) \qquad = 0, \qquad \mu = \sum_p \alpha_p \delta(p) \in M_h. \tag{1.25b}$$

As pointed out before, this strong coupling means that the solution values at the vertices of the triangulation $\mathcal{T}^{\mathrm{s}}$ on the slave side have to coincide with the solution at the physically same point from the master side (which is in general no vertex of $\mathcal{T}^{\mathrm{m}}$). It is easy to see that the algebraic formulation (1.22) of the discrete problem (1.25) results in D and D^{T} being identity matrices. This yields the fact that also here, the Lagrange multipliers can be locally eliminated from the saddle point system, which is the central advantage of the dual basis functions discussed in the last section. So the question arises why not to choose this simpler coupling procedure.

In order to answer this question, we show that the exact linear solution u is not a solution of the discrete problem (1.25), although it belongs to the space X_h. Since u satisfies the continuity condition (1.25b), it even belongs to the constrained space $V_h = \{v \in X_h : b(v, \mu) = 0,\ \mu \in M_h\}$. However, the equilibrium (1.25a) is in general not satisfied. For this example, we have $\operatorname{grad} u = (1,0)^{\mathrm{T}}$ and (1.25a) amounts to

$$\int_{\Omega^{\mathrm{m}}} \partial_x v_{\mathrm{m}} \, \mathrm{d}\Omega + \int_{\Omega^{\mathrm{s}}} \partial_x v_{\mathrm{s}} \, \mathrm{d}\Omega + \sum_p \lambda_p (v_{\mathrm{s}}(p) - v_{\mathrm{m}}(p)) \ = \ 0, \qquad v \in X_{0,h}. \tag{1.26}$$

We consider the triangulation depicted in Figure 1.1, consisting of four simplicial elements in each subdomain. The three master nodes p_i^{m}, $i = 1,2,3$, are indicated by filled circles, the three slave nodes p_i^{s}, $i = 1,2,3$, by crosses. Indicating by ϕ_i^k the basis function associated with the node p_i^k, $k = \mathrm{m}, \mathrm{s}$, $i = 1,2,3$, we set the test function $v = (\phi_2^{\mathrm{m}}, \phi_2^{\mathrm{s}}/2)$. It is obvious that $v \in X_{0,h}$. Moreover, v is continuous at the slave nodes, i.e., $v_{\mathrm{s}}(p_i^{\mathrm{s}}) = v_{\mathrm{m}}(p_i^{\mathrm{s}})$, $i = 1,2,3$. Thus, v is in the corresponding constrained space $V_{0,h}$

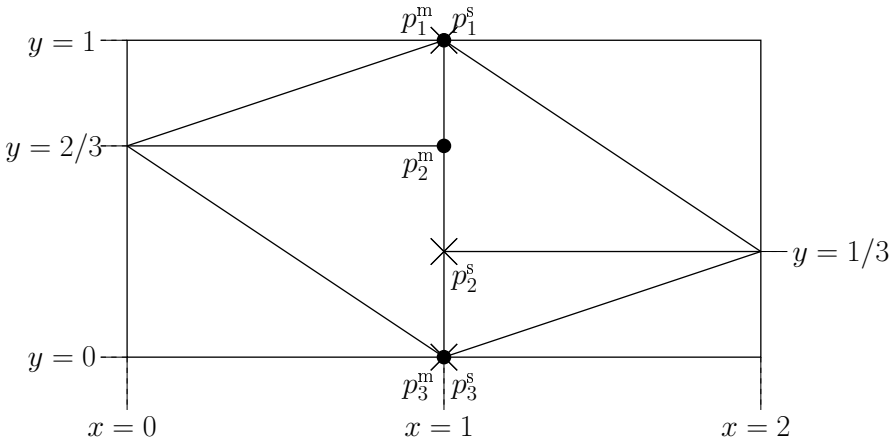

Figure 1.1: Non-matching triangulations $\mathcal{T}_{\mathrm{m}}$, $\mathcal{T}_{\mathrm{s}}$.

and the third term in (1.26) vanishes, so that v should satisfy

$$\int_{\Omega^{\mathrm{m}}} \partial_x v_{\mathrm{m}} \, \mathrm{d}\Omega + \int_{\Omega^{\mathrm{s}}} \partial_x v_{\mathrm{s}} \, \mathrm{d}\Omega \;=\; 0. \tag{1.27}$$

However, we have that

$$\int_{\Omega^{\mathrm{m}}} \partial_x \phi_2^{\mathrm{m}} \, \mathrm{d}\Omega + \frac{1}{2} \int_{\Omega^{\mathrm{s}}} \partial_x \phi_2^{\mathrm{s}} \, \mathrm{d}\Omega \;=\; \frac{1}{2} - \frac{1}{4} = \frac{1}{4} \neq 0,$$

so (1.27) is not satisfied. This means that the strong point-wise coupling is in general not able to yield an exact solution in the discrete space X_h. In other words, the method does not pass a patch test.

This shortcoming of the point-wise coupling would not be that severe, if the method performed well with respect to the error decay. In fact, the weak coupling we are going to use in this thesis only passes a patch test if the triangulations from the master and from the slave side are geometrically conforming, which is always the case for planar interfaces, but in general not true for curvilinear ones. However, a linear solution will be approximated in a superconvergent way. In contrast, the point-wise coupling does not even show an optimal decay of the error. We illustrate this by means of two numerical examples. The first one uses the setting from above. Starting with the initial triangulation from Figure 1.1, we perform a uniform refinement procedure, and record the discretization error measured in the H^1- and in the L^2-norm in each refinement step. The result is visualized in Figure 1.2. We observe that the decay of the error measured in the H^1-norm is only of order $O(h^{1/2})$, while for the L^2-norm, it is of order $O(h)$. This simple example clearly exhibits suboptimal convergence behavior of the point-wise coupling.

The second example, which is taken from [35], is the analog of the one above within the setting of linear elasticity (1.3)–(1.6). The domain $\Omega = (0, 10) \times (0, 10) \subset \mathbb{R}^2$ is decomposed into $\Omega^{\mathrm{m}} = (0, 5) \times (0, 10)$ and $\Omega^{\mathrm{s}} = (5, 10) \times (0, 10)$ sharing the common

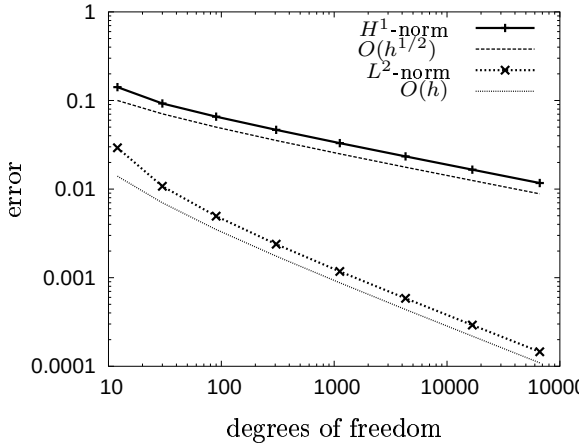

Figure 1.2: Point-wise coupling: error decay.

interface $\Gamma = \{5\} \times (0, 10)$. We assume homogeneous Dirichlet boundary conditions in x-direction on the left boundary $\{0\} \times (0, 10)$, and in y-direction in the node $(0, 0)$. On the right boundary $\{10\} \times (0, 10)$, a constant force of magnitude one is pulling in x-direction. All other boundary parts respect homogeneous Neumann conditions. The model of plane stress is used, with material parameters $E = 10^7$ and $\nu = 0.3$, resulting in the linear exact solution $\boldsymbol{u}(x, y) = E^{-1}(x, -\nu y)^{\mathrm{T}}$. Figure 1.3(a) shows the computational grid, consisting

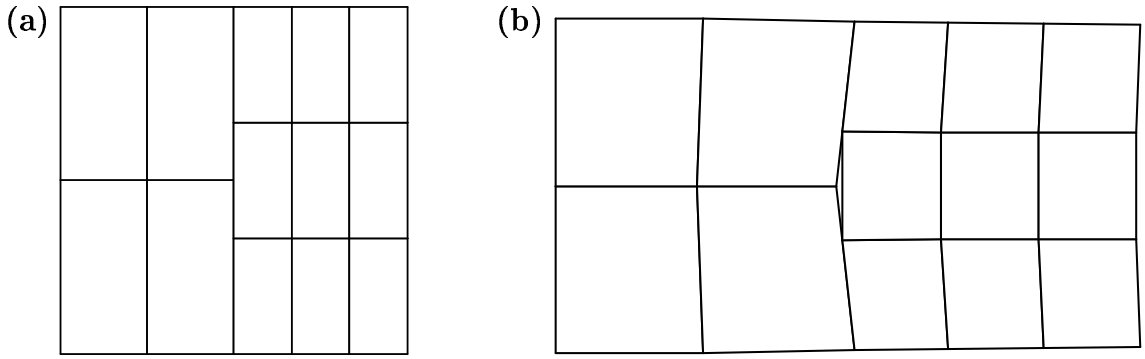

Figure 1.3: Patch test: (a) mesh configuration, (b) deformed geometry (exaggerated) using strong point-wise coupling.

of 2×2 quadrilateral elements on the master side, and 3×3 quadrilateral elements on the slave side. The finite element space consists of piecewise bilinear functions which are able to exactly interpolate the solution $\boldsymbol{u}$. However, the use of point-wise coupling results in a different discrete solution $\boldsymbol{u}_h$. In Figure 1.3(b), the deformed geometry is plotted. Although the displacements are continuous in the slave side nodes, as required by the point-wise coupling, the deformed geometry exhibits a gap around the master node $(5, 5)$. As for the scalar setting, the method exhibits a suboptimal convergence behavior. Figure 1.4(a) shows the decay of the discretization error measured in the energy norm and in the L^2-norm. The same suboptimal convergence rates as for the

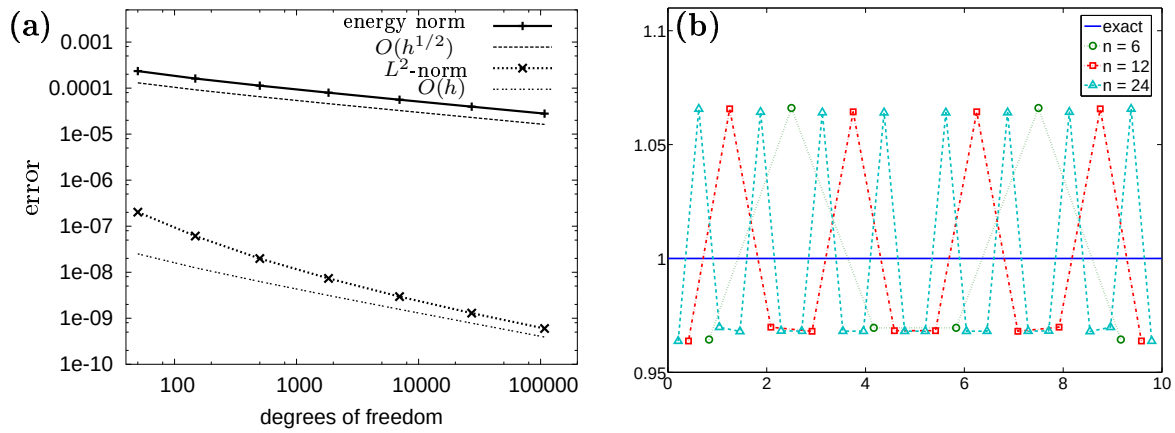

Figure 1.4: Patch test for point-wise coupling: (a) error decay, (b) stresses.

scalar case can be observed, namely, $O(h^{1/2})$ for the energy norm and $O(h)$ for the L^2-norm. In Figure 1.4(b), the stress component σ_{11} at the barycenters of elements with edges on the slave side is plotted versus the y-coordinate for three refinement steps, with $n = 6, 12, 24$ indicating the number of elements on the slave side. It can clearly be seen that σ_{11} oscillates between a minimum and a maximum value. Unfortunately, the difference between the extreme values does not decrease under mesh-refinement, which explains the bad convergence behavior.

The two examples clearly reveal that it is not advisable to use a strong point-wise coupling in the presence of non-matching meshes. The weak coupling used in this thesis is clearly superior with respect to the achieved approximation quality. Moreover, the use of dual Lagrange multipliers exhibits several advantages concerning the solution of the arising systems of equations.

2 The Scalar Case

We consider a non-overlapping decomposition into subdomains with curvilinear boundaries and generalize well-known mortar formulations [20, 21] for non-matching triangulations to this setting. The a priori analysis can be carried out in terms of blending elements [56, 57, 58] and within the abstract mortar setting. Of crucial importance are norm equivalences and uniform inf-sup conditions [10]. A lot of work has been done to analyze mortar settings and the coupling of different model equations. However, most approaches are restricted to straight or planar interfaces. In the special case of two subdomains without cross-points and one curvilinear interface, a first theoretical result can be found in [69]. There, a piecewise constant Lagrange multiplier space is used, which does not guarantee a uniform inf-sup condition. Throughout the whole thesis, we work with discrete Lagrange multiplier spaces for which uniform inf-sup conditions hold and consider many subdomains. We focus on the analysis of the variational crime which enters by using piecewise linear approximations of the curvilinear interfaces. According to these approximations, we use piecewise linear interpolations to map the non-matching meshes on the master and slave sides onto a reference segment, in order to define the jump of a finite element function across the curved interface.

In Section 2.1, we consider the model problem, while in Section 2.2, we discuss the continuous and discrete saddle point formulation. In Section 2.3, we carry out the convergence analysis and provide optimal a priori results for the discretization error in the H^1-norm for the primal variable and in the $H^{-1/2}$-norm for the Lagrange multiplier. Numerical results are given in Section 2.6. In a test series, we show the stability and flexibility of the approach and consider the influence of the number of subdomains on the discretization errors.

2.1 Problem Formulation

We consider the classical model problem (1.1) with $\Omega \subset \mathbb{R}^2$, $\Gamma_{\mathrm{D}} = \partial\Omega$, and $f \in L^2(\Omega)$ piecewise Lipschitz continuous. We assume that Ω is a polygon; this assumption is not necessary and merely done in order to concentrate on the curved interfaces. Let N_Γ smooth (C^2 is sufficient) curves Γ_i, $i = 1, \ldots, N_\Gamma$, be given in terms of the arc length parametrizations

$$\gamma_i \in C^2(\hat{I}_i, \mathbb{R}^2), \qquad \hat{I}_i = [0, \ell_i], \tag{2.1a}$$

such that $\Gamma_i = \gamma_i(\hat{I}_i)$, where ℓ_i denotes the length of Γ_i. We assume furthermore that the parametrizations γ_i are injective and satisfy, for some $c > 0$,

$$|\gamma_i(t) - \gamma_i(t')| \geq c|t - t'|, \qquad t, t' \in \hat{I}_i. \tag{2.1b}$$

We require that the interior of Γ_i is contained in Ω, i.e., no part except possibly the endpoints of Γ_i lies on $\partial\Omega$. We allow these curves to meet at $N_C \in \mathbb{N}_0$ *cross-points*. Without loss of generality, we will assume that the curves Γ_i are selected such that cross-points can only occur at their endpoints. These curves divide the domain Ω into N_Ω subdomains Ω^j, $j = 1, \ldots, N_\Omega$, which we assume to be Lipschitz domains, see Figure 2.1. We require the number of interfaces Γ_i belonging to one subdomain Ω^j to be bounded. Each curve Γ_i is shared by two domains $\Omega^{\mathrm{m}(i)}$, $\Omega^{\mathrm{s}(i)}$, i.e., $\overline{\Gamma_i} \subset \partial\Omega^{\mathrm{m}(i)} \cap \partial\Omega^{\mathrm{s}(i)}$, where $\Omega^{\mathrm{m}(i)}$ is called the *master side* of Γ_i, and $\Omega^{\mathrm{s}(i)}$ is called the *slave side*. In what follows, we will frequently omit the argument i in $\mathrm{m}(i)$ and $\mathrm{s}(i)$. We employ usual Sobolev spaces and norms, see the appendix or the standard work [3], and introduce the space $X = \prod_{j=1}^{N_\Omega} H^1(\Omega^j)$ with the corresponding broken H^1-norm given by

$$\|v\|_X^2 = \sum_{j=1}^{N_\Omega} \|v\|_{1,\Omega^j}^2. \tag{2.2}$$

2.2 Formulation of the Numerical Method

This section is decomposed into two subsections, the first one introducing the continuous and discrete function spaces to be considered in the following, the second one presenting the continuous and discrete problem formulations.

2.2.1 Spaces

We will restrict our attention to piecewise linear discretizations for the domain parts; the Lagrange multiplier can be discretized by means of any of the standard stable spaces, [20, 21, 24, 77, 122]. For each subdomain Ω^j, we have a quasi-uniform, shape-regular triangulation $\mathcal{T}_j$ with mesh size h_j of a domain Ω_h^j that approximates Ω^j in the sense that $\partial\Omega_h^j$ is a piecewise linear interpolation of $\partial\Omega^j$. We insist on the endpoints of the curves Γ_i, $i = 1, \ldots, N_\Gamma$, being interpolation points. For each curve Γ_i, we obtain in this way two piecewise linear approximations that we denote by $\Gamma_{i,h}^{\mathrm{s}}$ and $\Gamma_{i,h}^{\mathrm{m}}$. The superscripts s and m indicate that $\Gamma_{i,h}^{\mathrm{s}}$ and $\Gamma_{i,h}^{\mathrm{m}}$ are parts of $\partial\Omega_h^{\mathrm{s}(i)}$, $\partial\Omega_h^{\mathrm{m}(i)}$, respectively. Since $\Gamma_{i,h}^{\mathrm{s}}$ and $\Gamma_{i,h}^{\mathrm{m}}$ are piecewise linear interpolations of Γ_i, we can parametrize them in the standard way by continuous piecewise linear functions

$$\gamma_{i,h}^{\mathrm{s}}, \gamma_{i,h}^{\mathrm{m}} : \hat{I}_i \to \mathbb{R}^2, \tag{2.3}$$

as illustrated in the right picture of Figure 2.1. In particular, the endpoints of $\hat{I}_i$ are mapped to the same points under these two mappings. The set $\widehat{\mathcal{V}}_i$ of nodes, $\widehat{\mathcal{V}}_i = \{x \in \hat{I}_i : \gamma_{i,h}^{\mathrm{s}}(x) = p,$ where p is an interpolation point on $\Gamma_{i,h}^{\mathrm{s}}\}$, forms a mesh on $\hat{I}_i$. Since the triangulation $\mathcal{T}_{\mathrm{s}(i)}$ is assumed to be shape regular and the parametrizations γ_i satisfy (2.1), the nodes $\widehat{\mathcal{V}}_i$ form a shape regular mesh on $\hat{I}_i$ with mesh size $\widehat{h}$. Moreover, we can find constants C_j such that $C_j^{-1} h_j \leq \widehat{h} \leq C_j h_j$, $j = 1, \ldots, N_\Omega$.

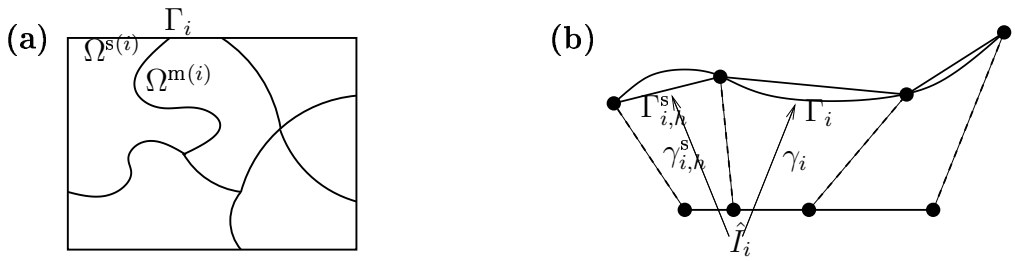

Figure 2.1: (a) decomposition of Ω into six subdomains and three cross-points given by eight curves, (b) interface Γ_i and its piecewise linear interpolation $\Gamma^s_{i,h}$.

We work with two different dual spaces

$$M^0 = \prod_{i=1}^{N_\Gamma} H^{-1/2}(\Gamma_i), \quad H^{-1/2}(\Gamma_i) = \left(H^{1/2}_{00}(\Gamma_i)\right)',$$
$$M = \prod_{i=1}^{N_\Gamma} \left(H^{1/2}(\Gamma_i)\right)'$$

and equip the spaces $H^{1/2}(\Gamma_i)$ and $H^{1/2}_{00}(\Gamma_i)$ with the "intrinsic" norms, i.e., the Slobodecki norms:

$$\|v\|^2_{1/2,\Gamma_i} = \|v\|^2_{0,\Gamma_i} + \int_{\Gamma_i}\int_{\Gamma_i} \frac{|v(x)-v(y)|^2}{|x-y|^2}\,\mathrm{d}x\,\mathrm{d}y, \tag{2.4a}$$
$$\|v\|^2_{00,\Gamma_i} = \|v\|^2_{1/2,\Gamma_i} + \int_{\Gamma_i} \frac{1}{\operatorname{dist}(x,\partial\Gamma_i)}|v(x)|^2\,\mathrm{d}x. \tag{2.4b}$$

The duality pairings for a curve D between $H^{1/2}(D)$ and its dual, and between $H^{1/2}_{00}(D)$ and its dual are denoted by $\langle\cdot,\cdot\rangle_D$ and $\langle\cdot,\cdot\rangle_{H^{-1/2},D}$, respectively. We note that in the case of $v \in H^{1/2}_{00}(D)$, $\mu \in (H^{1/2}(D))'$, the two duality pairings coincide. Moreover, it holds that $(H^{1/2}(\partial\Omega^j))' = H^{-1/2}(\partial\Omega^j)$, $1 \le j \le N_\Omega$. On the spaces M^0 and M, we define the norms $\|\cdot\|_{M^0}$ and $\|\cdot\|_M$ by

$$\|\mu\|^2_{M^0} = \sum_{i=1}^{N_\Gamma} \|\mu\|^2_{-1/2,\Gamma_i}, \ \ \mu \in M^0, \qquad \text{and} \qquad \|\mu\|^2_M = \sum_{i=1}^{N_\Gamma} \|\mu\|^2_{(H^{1/2}(\Gamma_i))'}, \ \ \mu \in M,$$

respectively, where the dual norms are defined in the usual way (A.8). It is easy to see that $M \subset M^0$ and $\|\cdot\|_M$ is the stronger norm, i.e.,

$$\|\mu\|_M \ge \|\mu\|_{M^0}, \qquad \mu \in M. \tag{2.5}$$

By assumption f is in the dual space of $H^1(\Omega^j)$, $1 \le j \le N_\Omega$, and thus the normal flux of the weak solution $u|_{\Omega^j}$ on $\partial\Omega^j$ can be identified with a unique element $\sigma_j \in H^{-1/2}(\partial\Omega^j)$. Let the interface Γ_i be a subset of $\partial\Omega^j$. Then we can define the restriction of σ_j to Γ_i by

$$\langle v, \sigma_j|_{\Gamma_i}\rangle_{H^{-\frac{1}{2}};\Gamma_i} = \langle v, \sigma_j\rangle_{H^{-\frac{1}{2}};\partial\Omega^j}, \quad v \in H^{1/2}_{00}(\Gamma_i),$$

where the trivial extension of v onto $\partial\Omega^j$ is still denoted by v. By definition, we find $\sigma_j|_{\Gamma_i} \in H^{-1/2}(\Gamma_i)$. In what follows, we assume that $\sigma_j|_{\Gamma_i} \in (H^{1/2}(\Gamma_i))' \subset H^{-1/2}(\Gamma_i)$, and that $\sigma_{\mathrm{s}(i)}|_{\Gamma_i} = -\sigma_{\mathrm{m}(i)}|_{\Gamma_i}$, $1 \le i \le N_\Gamma$, in order to define the Lagrange multiplier $\lambda \in M \subset M^0$ by

$$\lambda|_{\Gamma_i} = -\operatorname{grad} u \cdot \boldsymbol{n}_{\mathrm{s}(i)} = -\sigma_{\mathrm{s}(i)}|_{\Gamma_i} = \sigma_{\mathrm{m}(i)}|_{\Gamma_i}, \qquad i = 1, \dots, N_\Gamma, \tag{2.6}$$

where $\boldsymbol{n}_{\mathrm{s}(i)}$ denotes the outer normal vector of $\Omega^{\mathrm{s}(i)}$ on Γ_i.

The nonconforming discretization is based on a saddle point problem, and we have to discretize the spaces X and M^0. The space of piecewise linear functions on $\mathcal{T}_j$ is denoted by

$$X_{j,h} = \{v \in H^1(\Omega_h^j) : v|_T \in \mathbb{P}_1(T),\ T \in \mathcal{T}_j,\ v|_{\partial\Omega} = 0\}, \tag{2.7}$$

where $\mathbb{P}_1(T)$ denotes the classical space of polynomials of degree 1 on the element T. We set $X_h = \prod_{j=1}^{N_\Omega} X_{j,h}$ equipped with the mesh dependent norm $\|\cdot\|_{X_h}$ defined by $\|v\|_{X_h}^2 = \sum_{j=1}^{N_\Omega} \|v\|_{1,\Omega_h^j}^2$. We denote by F_T the element map from the reference element $\widehat{T}$ associated with the element $T \in \mathcal{T}_j$. Additionally, we need to introduce discrete spaces of Lagrange multipliers associated with the curves Γ_i, $i = 1, \dots, N_\Gamma$. Here, we exploit the fact that the curves Γ_i, $\Gamma_{i,h}^{\mathrm{s}}$, and $\Gamma_{i,h}^{\mathrm{m}}$ can be identified with the reference interval $\hat{I}_i$ via the maps γ_i, $\gamma_{i,h}^{\mathrm{s}}$, $\gamma_{i,h}^{\mathrm{m}}$. On $\hat{I}_i$, we take for each i any one of the standard Lagrange multiplier spaces [20, 21, 24, 77, 122], that are based on the mesh on $\hat{I}_i$ determined by the nodes $\widehat{\mathcal{V}}_i$, and we denote this space by $\widehat{M}_{i,h} \subset L^2(\hat{I}_i)$. In particular, the following assumptions are made, which are all satisfied by the spaces proposed in these references.

Assumption 2.1. *The discrete Lagrange multiplier spaces $\widehat{M}_{i,h}$ satisfy:*

(a) *The constant functions are contained in $\widehat{M}_{i,h}$, i.e., $\mathbb{P}_0 \subset \widehat{M}_{i,h}$.*

(b) *It holds that*

$$\inf_{v_h \in \widehat{M}_{i,h}} \|w - v_h\|_{0,\hat{I}_i} \le C\widehat{h}_{s(i)}^{1/2} |w|_{1/2,\hat{I}_i}, \qquad w \in H^{1/2}(\hat{I}_i). \tag{2.8}$$

(c) *There exists a projection $\widehat{\Pi}_{i,h} : H_{00}^{1/2}(\hat{I}_i) \to \widehat{W}_{i,h}$ satisfying*

$$(v, \mu)_{\hat{I}_i} = (\widehat{\Pi}_{i,h} v, \mu)_{\hat{I}_i}, \qquad \mu \in \widehat{M}_{i,h}, \tag{2.9a}$$

$$\|\widehat{\Pi}_{i,h} v\|_{00,\hat{I}_i} \le C_{\widehat{\Pi}} \|v\|_{00,\hat{I}_i}, \quad \|\widehat{\Pi}_{i,h} v\|_{0,\hat{I}_i} \le C_{\widehat{\Pi}} \|v\|_{0,\hat{I}_i}, \quad v \in H_{00}^{1/2}(\hat{I}_i), \tag{2.9b}$$

where $(\cdot,\cdot)_{\hat{I}_i}$ is the L^2-scalar product on $\hat{I}_i$, and $\widehat{W}_{i,h}$ is the pull-back to $\hat{I}_i$ of the trace of $X_{s(i),h}$ on $\Gamma_{i,h}^s$, i.e.,

$$\widehat{W}_{i,h} = \{u|_{\Gamma_{i,h}^s} \circ \gamma_{i,h}^s \,:\, u \in X_{s(i),h}\}, \tag{2.10}$$

and the continuity constant $C_{\widehat{\Pi}}$ of the projections $\widehat{\Pi}_{i,h}$ is assumed to be independent of the discretization parameters.

For a more rigorous axiomatic development of the mortar framework, we refer to [80]. There, the theory is also extended to only *locally* quasi-uniform meshes.

Via $\gamma_{i,h}^{\mathrm{s}}$, we define on $\Gamma_{i,h}^{\mathrm{s}}$ the space

$$M_{i,h} = \widehat{M}_{i,h} \circ (\gamma_{i,h}^{\mathrm{s}})^{-1}, \qquad M_h = \prod_{i=1}^{N_\Gamma} M_{i,h}. \tag{2.11}$$

In order to relate results for the reference interval $\hat{I}_i$ to the exact interface Γ_i, the following norm equivalences will be used.

Lemma 2.2. *Let γ_i satisfy (2.1), $i = 1, \dots, N_\Gamma$. There exists $C > 0$ such that for each $i = 1, \dots, N_\Gamma$*

$$C^{-1}\|v\|_{0,\Gamma_i} \le \|v \circ \gamma_i\|_{0,\hat{I}_i} \le C\|v\|_{0,\Gamma_i}, \qquad v \in L^2(\Gamma_i), \tag{2.12a}$$

$$C^{-1}\|v\|_{00,\Gamma_i} \le \|v \circ \gamma_i\|_{00,\hat{I}_i} \le C\|v\|_{00,\Gamma_i}, \qquad v \in H_{00}^{1/2}(\Gamma_i). \tag{2.12b}$$

Moreover, for a curve Γ and a function $g \in W^{1,\infty}(\Gamma)$ that is bounded away from 0, we obtain

$$C^{-1}\|gv\|_{1/2,\Gamma} \le \|v\|_{1/2,\Gamma} \le C\|v/g\|_{1/2,\Gamma}, \qquad v \in H^{1/2}(\Gamma), \tag{2.12c}$$

$$C^{-1}\|gv\|_{00,\Gamma} \le \|v\|_{00,\Gamma} \le C\|v/g\|_{00,\Gamma}, \qquad v \in H_{00}^{1/2}(\Gamma). \tag{2.12d}$$

Proof. The assumptions (2.1) imply that γ_i and γ_i^{-1} are C^1. A direct calculation with the involved norms yields (2.12a) and (2.12b). We give a detailed proof of (2.12c). Let $g \in W^{1,\infty}(\Gamma)$ and $v \in H^{1/2}(\Gamma)$. For the L^2-norm, it is obvious that

$$\|gv\|_{0,\Gamma}^2 = (gv, gv)_\Gamma \le C\|g\|_{L^\infty(\Gamma)}^2 \|v\|_{0,\Gamma}^2 \le C\|v\|_{0,\Gamma}^2.$$

For the $H^{1/2}$-semi-norm, we observe that

$$\begin{aligned}
|gv|_{1/2,\Gamma}^2 &= \int_\Gamma \int_\Gamma \frac{|g(x)v(x) - g(y)v(y)|^2}{|x-y|^2} \,\mathrm{d}x\,\mathrm{d}y \\
&= \int_\Gamma \int_\Gamma \frac{|(v(x)-v(y))g(x) + (g(x)-g(y))v(x)|^2}{|x-y|^2} \,\mathrm{d}x\,\mathrm{d}y \\
&\le 2\int_\Gamma \int_\Gamma |g(x)|^2 \frac{|v(x)-v(y)|^2}{|x-y|^2} \,\mathrm{d}x\,\mathrm{d}y \;+\; 2\int_\Gamma \int_\Gamma |v(x)|^2 \frac{|g(x)-g(y)|^2}{|x-y|^2} \,\mathrm{d}x\,\mathrm{d}y \\
&\le C\|g\|_{L^\infty(\Gamma)}^2 |v|_{1/2,\Gamma}^2 + C\|\operatorname{grad} g\|_{L^\infty(\Gamma)}^2 \|v\|_{0,\Gamma}^2 \\
&\le C\|v\|_{1/2,\Gamma}^2,
\end{aligned}$$

which proves the first part of (2.12c). The second part follows immediately from the first one by

$$\|v\|_{1/2,\Gamma} = \|(v/g)g\|_{1/2,\Gamma} \le C\|v/g\|_{1/2,\Gamma}.$$

Similar reasoning proves (2.12d). □

Remark 2.3. We note that the constant C in (2.12) depends on the length of the corresponding interface Γ_i. In this particular case, we will not rigorously analyze the dependence of the constant on the decomposition into subdomains. However, in all the following proofs, we will exploit the fact that the number of interfaces Γ_i belonging to one subdomain Ω^j is bounded, and demonstrate that the constants depend on this bound, and not on the total number of subdomains N_Ω. Moreover, in Section 2.6, we provide a numerical example illustrating this independence. ∎

2.2.2 Bilinear Forms and Finite Element Method

To define our saddle point formulation, we also need to define the jump across the interface Γ_i. For a function $v \in X$, the jump across Γ_i is given in the standard way and denoted by $[v]_i = v_{\mathrm{s}(i)} - v_{\mathrm{m}(i)}$. For $v \in X_h$, we exploit the fact that $\Gamma^{\mathrm{s}}_{i,h}$, $\Gamma^{\mathrm{m}}_{i,h}$ can be identified with $\hat{I}_i$ in order to define the discrete jump across $\Gamma^{\mathrm{s}}_{i,h}$ as

$$[v]_{i,h} = v_{\mathrm{s}(i),h} - P_{\mathrm{s}(i)} v_{\mathrm{m}(i),h}, \tag{2.13}$$

where the grid transfer mapping $P_{\mathrm{s}(i)}$ is given as

$$P_{\mathrm{s}(i)} : L^2(\Gamma^{\mathrm{m}}_{i,h}) \to L^2(\Gamma^{\mathrm{s}}_{i,h}), \quad v \mapsto P_{\mathrm{s}(i)} v = v \circ \gamma^{\mathrm{m}}_{i,h} \circ (\gamma^{\mathrm{s}}_{i,h})^{-1}. \tag{2.14}$$

The mapping $P_{\mathrm{s}(i)}$ is responsible for transferring a function on the master side $\Gamma^{\mathrm{m}}_{i,h}$ to the slave side $\Gamma^{\mathrm{s}}_{i,h}$. In Figure 2.2, we illustrate the mappings which are involved in its

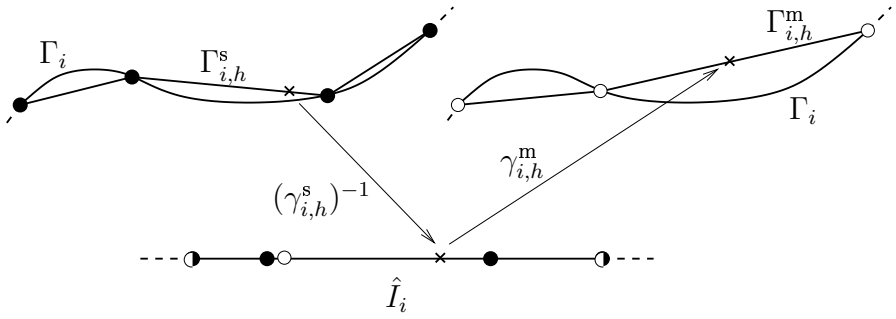

Figure 2.2: The mappings involved in the definition of P_{s}.

definition, and their action on an arbitrary point of the interface Γ_i. Related to the jump across the interfaces Γ_i are the bilinear forms

$$b(v, \mu) = \sum_{i=1}^{N_\Gamma} \langle [v]_i, \mu \rangle_{\Gamma_i}, \quad (v, \mu) \in X \times M, \tag{2.15}$$

$$b_h(v, \mu) = \sum_{i=1}^{N_\Gamma} ([v]_{i,h}, \mu)_{\Gamma^{\mathrm{s}}_{i,h}}, \quad (v, \mu) \in X_h \times M_h. \tag{2.16}$$

Finally defining the domain bilinear forms

$$a(w,v) = \sum_{j=1}^{N_\Omega} (\operatorname{grad} w, \operatorname{grad} v)_{\Omega^j}, \tag{2.17}$$

$$a_h(w,v) = \sum_{j=1}^{N_\Omega} \sum_{T \in \mathcal{T}_j} (\operatorname{grad} w, \operatorname{grad} v)_T, \tag{2.18}$$

it is easy to see that the pair $(u,\lambda) \in X \times M$ satisfies the saddle point problem (1.16) with

$$l(v) = (f,v)_\Omega. \tag{2.19}$$

Correspondingly, the approximate solution $u_h \in X_h$ and the approximation to the Lagrange multiplier, $\lambda_h \in M_h$, are given as the solution of

$$a_h(u_h,v) + b_h(v,\lambda_h) = l_h(v), \qquad v \in X_h, \tag{2.20a}$$

$$b_h(u_h,\mu) \qquad\qquad = 0, \qquad\quad \mu \in M_h. \tag{2.20b}$$

Here, the approximation $l_h(\cdot)$ to the linear functional $l(\cdot)$ is given by

$$l_h(v) = \sum_{j=1}^{N_\Omega} (f_j, v)_{\Omega_h^j}, \tag{2.21}$$

where we assume that f_j is a Lipschitz continuous function on $\Omega^j \cup \Omega_h^j$ such that

$$f_j = f \qquad \text{in } \Omega^j \cap \Omega_h^j, \tag{2.22a}$$

$$\|f_j\|_{W^{1,\infty}(\Omega^j \cup \Omega_h^j)} \leq C_f, \tag{2.22b}$$

and that the constant C_f is independent of mesh parameters.

Remark 2.4. Necessary conditions for the well-posedness of the continuous problem (1.16) and of the discrete problem (2.20) are the continuity of the coupling bilinear forms $b(\cdot,\cdot)$ and $b_h(\cdot,\cdot)$, as well as the fulfillment of the inf-sup conditions (A.16) and (A.20), respectively. It is an important fact that the bilinear form $b(\cdot,\cdot)$ is continuous on $X \times M$ but does not yield an inf-sup condition with respect to the norms $\|\cdot\|_X$ and $\|\cdot\|_M$. This also holds true for the discrete space $X_h \times M_h$ where no uniform inf-sup condition can be shown. In order to overcome this shortcoming, it will be of crucial importance to establish a uniform discrete inf-sup condition for the weaker norm $\|\cdot\|_{M^0}$. ∎

2.3 Convergence Analysis

We do not analyze problem (2.20) directly. To obtain a priori bounds for the discretization error, we proceed in two steps. In the first step, we introduce and analyze a new discrete variational problem based on blending elements, where the curved interfaces are resolved in an exact way. In the second step, we interpret (2.20) as a perturbed blending approach, and estimate the perturbation terms obtained from a modified version of the first Strang lemma.

2.3.1 Error Analysis Using Blending Elements

While problem (2.20) is given in terms of approximations $a_h(\cdot,\cdot)$ and $b_h(\cdot,\cdot)$, respectively, we establish the discrete problem formulation (1.21) based on the exact bilinear forms $a(\cdot,\cdot)$ and $b(\cdot,\cdot)$ as an intermediate step. After the basics of blending elements are introduced, the new discrete problem is established and a rigorous a priori error analysis is carried out.

Blending Elements

Since we intend to approximate the saddle point problem (1.16) by the discrete form (1.21), the subdomains Ω^j, $j = 1,\dots,N_\Omega$ have to be represented exactly by the triangulations. By assumption, Ω is a polygon, and only the elements that have two vertices on one of the interfaces Γ_i, $i = 1,\dots,N_\Gamma$, require a treatment as a *blending element*, [57, 58]. The blending function for an element that has an edge lying on Γ_i results from the parametrization γ_i of Γ_i. The triangulation of Ω^j using blending elements will be denoted by $\widetilde{\mathcal{T}}_j$ with element maps $\widetilde{F}_{\widetilde{T}}$, $\widetilde{T} \in \widetilde{\mathcal{T}}_j$. The triangulations $\mathcal{T}_j$ and $\widetilde{\mathcal{T}}_j$ are illustrated in Figure 2.3. The blending elements are chosen such that there is a one-to-one

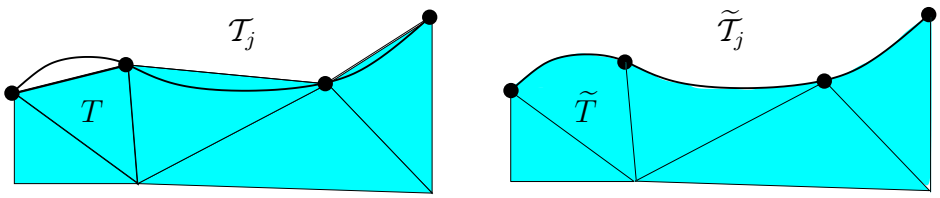

Figure 2.3: Triangulations $\mathcal{T}_j$ and $\widetilde{\mathcal{T}}_j$, corresponding elements T and $\widetilde{T}$.

connection between the elements $T \in \mathcal{T}_j$ and the elements $\widetilde{T} \in \widetilde{\mathcal{T}}_j$, i.e., the vertices of the two triangulations coincide. The particular construction of the blending method implies that the mappings F_T and $\widetilde{F}_{\widetilde{T}}$ of two elements $T \in \mathcal{T}_j$ and $\widetilde{T} \in \widetilde{\mathcal{T}}_j$ corresponding to each other satisfy the following lemma.

Lemma 2.5. *Under Assumption (2.1), the mappings F_T and $\widetilde{F}_{\widetilde{T}}$ of two elements $T \in \mathcal{T}_j$, $\widetilde{T} \in \widetilde{\mathcal{T}}_j$ corresponding to each other satisfy*

$$\widetilde{F}_{\widetilde{T}} = F_T + R_T, \qquad \|R_T\|_{L^\infty(\widehat{T})} + \|R_T'\|_{L^\infty(\widehat{T})} + \|R_T''\|_{L^\infty(\widehat{T})} \le C h_T^2, \tag{2.23}$$

where the constant $C > 0$ depends only on the parametrizations γ_i, $i = 1,\dots,N_\Gamma$. Furthermore, we have that

$$\|\widetilde{F}_{\widetilde{T}}'\|_{L^\infty(\widehat{T})} + h_{\widetilde{T}}^{-1}\|\widetilde{F}_{\widetilde{T}}''\|_{L^\infty(\widehat{T})} + h_{\widetilde{T}}^{2}\|(\widetilde{F}_{\widetilde{T}}')^{-1}\|_{L^\infty(\widetilde{T})} \le C h_{\widetilde{T}}. \tag{2.24}$$

Above, R_T', $\widetilde{F}_{\widetilde{T}}'$ and R_T'', $\widetilde{F}_{\widetilde{T}}''$ denote the Jacobian and the Hessian of R_T, $\widetilde{F}_{\widetilde{T}}$, respectively.

Proof. Without loss of generality, we consider the situation illustrated in Figure 2.4. All other configurations involving one curved edge can be achieved by translations, rota-

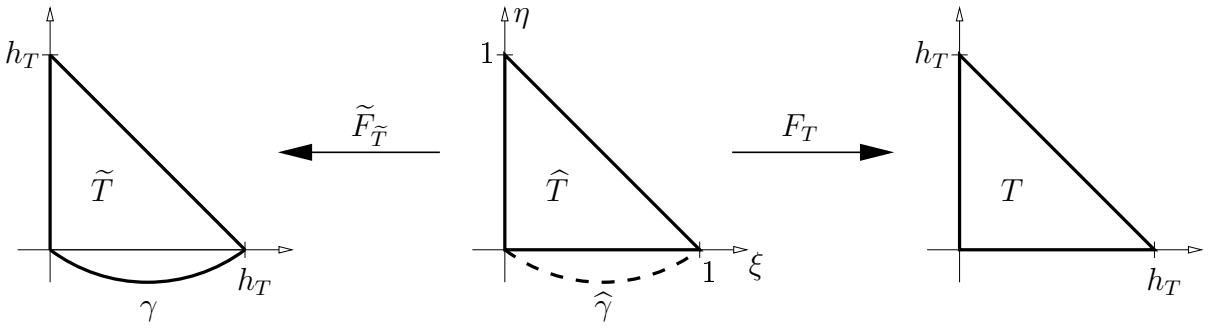

Figure 2.4: Element mappings

tions, and deformations of $\widetilde{T}$ with parameters independent of the diameter h_T. Additional edges can be taken into account by summing up the contributions from each edge. The function $F_T(\xi, \eta) = (h_T\xi, h_T\eta)^{\mathrm{T}}$ maps the reference element $\widehat{T} = ((0,0), (1,0), (0,1))$ onto the element $T = ((0,0), (h_T,0), (0,h_T))$. The blending element $\widetilde{T}$ has one curved edge given by $\gamma \in C^2([0,h_T])$, which is twice continuously differentiable as a consequence of Assumption (2.1) by transforming the subinterval of $\hat{I}_i$ corresponding to the curved edge onto the interval $[0,h_T]$.

We denote the pull-back of γ onto the reference configuration by $\widehat{\gamma} \in C^2([0,1])$, defined by $\widehat{\gamma}(\xi) = \gamma(h_T\xi)$. The element mapping $\widetilde{F}_{\widetilde{T}}$ is given by $\widetilde{F}_{\widetilde{T}} = F_T + R_T$, where

$$R_T = \left(0,\ \frac{1-\xi-\eta}{1-\xi}\widehat{\gamma}(\xi)\right)^{\mathrm{T}}.$$

We note that R_T is well-behaved in $(1,0)$, since on T, η tends to 0 as ξ tends to 1, and $\widehat{\gamma}(1) = 0$. In order to estimate the terms involved in R_T, R_T', R_T'', we develop $\widehat{\gamma}$ into its Taylor series around 1, yielding

$$\widehat{\gamma}(\xi) = \widehat{\gamma}(1) + (\xi-1)\widehat{\gamma}'(1) + r(\xi),$$

with

$$r(\xi) = \int_1^\xi (\xi - t)\widehat{\gamma}''(t)\,dt.$$

By differentiating r, we obtain

$$|r(\xi)| \le (\xi-1)^2\|\widehat{\gamma}''\|_\infty, \quad |r'(\xi)| \le (\xi-1)\|\widehat{\gamma}''\|_\infty, \quad |r''(\xi)| \le \|\widehat{\gamma}''\|_\infty. \tag{2.25}$$

Considering the fact that $\widehat{\gamma}(1) = 0$, we can give R_T as

$$R_T = \left(0,\ (\xi+\eta-1)h_T\gamma'(h_T) + \frac{1-\xi-\eta}{1-\xi}r(\xi)\right)^{\mathrm{T}}.$$

The term $h_T\gamma'(h_T)$ is bounded by Ch_T^2, since $\widehat{\gamma}(0) = \widehat{\gamma}(1) = 0$, and the mean value theorem guarantees the existence of $h_\star \in [0,1]$ such that $\widehat{\gamma}'(h_\star) = 0$. Thus, using (2.25),

we see that $\|R_T\|_{L^\infty(\widehat{T})}$ is bounded by Ch_T^2. For the Jacobian R_T', we obtain

$$R_T' = \begin{pmatrix} 0 & 0 \\ h_T\gamma'(h_T) - \frac{\eta}{(1-\xi)^2}r(\xi) + \frac{1-\xi-\eta}{1-\xi}r'(\xi) & h_T\gamma'(h_T) - \frac{1}{1-\xi}r(\xi) \end{pmatrix},$$

which can be bounded such that $\|R_T'\|_{L^\infty(\widehat{T})} \leq Ch_T^2$. The coefficients of the Hessian R_T'' involve the following terms:

$$\frac{1}{(1-\xi)^2}r(\xi), \quad \frac{1}{1-\xi}r'(\xi), \quad r''(\xi),$$

which can be handled as before, and

$$\frac{2\eta}{(1-\xi)^3}r(\xi), \quad \frac{\eta}{(1-\xi)^2}r'(\xi), \quad \frac{\eta}{1-\xi}r''(\xi).$$

Regarding again the fact that η tends to 0 as ξ tends to 1, since $0 \leq \eta \leq 1-\xi$, these terms also pose no difficulty, so that (2.23) is completed. From (2.23), we deduce (2.24) simply by using the properties of the affine transformation F_T. □

Discrete Problem Formulation

We are now able to state the analog of the discrete problem (2.20) in terms of blending elements. Similar to (2.7) and (2.11), we define the blending element space on a subdomain Ω^j and the blending Lagrange multipliers space on an interface Γ_i as

$$\widetilde{X}_{j,h} = \{v \in H^1(\Omega^j) \,:\, v|_{\widetilde{T}} \circ \widetilde{F}_{\widetilde{T}} \in \mathbb{P}_1(\widehat{T}),\ \widetilde{T} \in \widetilde{\mathcal{T}}_j,\ v|_{\partial\Omega} = 0\}, \tag{2.26}$$

$$\widetilde{M}_{i,h} = \widehat{M}_{i,h} \circ \gamma_i^{-1}, \tag{2.27}$$

respectively, and set $\widetilde{X}_h = \prod_{j=1}^{N_\Omega} \widetilde{X}_{j,h}$ and $\widetilde{M}_h = \prod_{i=1}^{N_\Gamma} \widetilde{M}_{i,h}$. In contrast to the original discretization, we now have conforming approximations $\widetilde{X}_h \subset X$ and $\widetilde{M}_h \subset M$, which admits to introduce the problem: find $(\widetilde{u}_h, \widetilde{\lambda}_h) \in \widetilde{X}_h \times \widetilde{M}_h$ such that

$$a(\widetilde{u}_h, v) + b(v, \widetilde{\lambda}_h) = l(v), \quad v \in \widetilde{X}_h, \tag{2.28a}$$

$$b(\widetilde{u}_h, \mu) = 0, \quad \mu \in \widetilde{M}_h. \tag{2.28b}$$

In order to analyze the error $u - \widetilde{u}_h$ and the error of the Lagrange multiplier $\lambda - \widetilde{\lambda}_h$, we introduce the *constrained* space

$$\widetilde{V}_h = \{v \in \widetilde{X}_h \,:\, b(v, \mu) = 0, \quad \mu \in \widetilde{M}_h\}. \tag{2.29}$$

The constrained space $\widetilde{V}_h$ admits to equivalently reformulate the saddle point problem (2.28) as approximation of (1.18), namely: find $\widetilde{u}_h \in \widetilde{V}_h$ such that

$$a(\widetilde{u}_h, \widetilde{v}_h) = l(\widetilde{v}_h), \quad \widetilde{v}_h \in \widetilde{V}_h. \tag{2.30}$$

Analogous to the continuous setting, the approximate constrained problem (2.30) is positive definite, provided that $a(\cdot,\cdot)$ is coercive on $\widetilde{V}_h$. We emphasize that we have to deal with a nonconforming approximation, i.e., $\widetilde{V}_h \not\subseteq V$.

Of essential use in the upcoming error analysis will be the following observation that stems from using blending elements based on the parametrizations γ_i:

Lemma 2.6. *Let $X_{j,h}$ and $\widehat{W}_{i,h}$ be defined as in (2.7) and (2.10), respectively. Then for each interface Γ_i, $i = 1,\dots,N_\Gamma$, we have*

$$\widetilde{X}_{s(i),h}|_{\Gamma_i} \circ \gamma_i = \widehat{W}_{i,h}.$$

Furthermore, there exists a constant $C > 0$, which depends solely on the parametrizations γ_i, the subdomains Ω^j, and the shape-regularity constant C_γ of (2.24), and there exists a lifting operator $\mathcal{L}_i : \widehat{W}_{i,h} \cap H_{00}^{1/2}(\hat{I}_i) \to \widetilde{X}_{s(i),h}$ such that for all $\widehat{v}_h \in \widehat{W}_{i,h} \cap H_{00}^{1/2}(\hat{I}_i)$

$$\begin{aligned}
&\|\mathcal{L}_i\widehat{v}_h\|_{1,\Omega^{s(i)}} \le C\|\widehat{v}_h\|_{00,\hat{I}_i},\\
&(\mathcal{L}_i\widehat{v}_h)|_{\partial\Omega^{s(i)}\setminus\Gamma_i} = 0,\\
&(\mathcal{L}_i\widehat{v}_h)|_{\Gamma_i} \circ \gamma_i = \widehat{v}_h.
\end{aligned}$$

Proof. Let $\widehat{v}_h \in \widehat{W}_{i,h} \cap H_{00}^{1/2}(\hat{I}_i)$ be given. Define v_h on Γ_i via $v_h = \widehat{v}_h \circ \gamma_i^{-1}$. By (2.12b), we then get $\|v_h\|_{00,\Gamma_i} \le C\|\widehat{v}_h\|_{00,\hat{I}_i}$. Next, we extend v_h to $\partial\Omega^{\mathrm{s}(i)}$ by zero. The thus extended function (still denoted v_h) satisfies $\|v_h\|_{1/2,\partial\Omega^{\mathrm{s}(i)}} \le C\|\widehat{v}_h\|_{00,\hat{I}_i}$ (see, for example, [59, Thms. 1.5.1.3, 1.5.2.3]). By using the generalized discrete harmonic extension $\mathcal{H}^{\mathrm{g}}_{h,\mathrm{s}(i)}$ of v_h into $\Omega^{\mathrm{s}(i)}$ according to (A.24), we set $\mathcal{L}_i\widehat{v}_h = \mathcal{H}^{\mathrm{g}}_{h,\mathrm{s}(i)}v_h$. The equivalence (A.25) yields the assertions of the lemma. □

A Priori Results for Blending Elements

In this subsection, we establish optimal a priori bounds for the discretization errors $u-\widetilde{u}_h$ and $\lambda-\widetilde{\lambda}_h$. Of crucial importance are the best approximation property of the constrained space and a uniform inf-sup condition. We have the following ellipticity result on the space

$$X_\chi = \{u \in X \,:\, b(u,\mu) = 0,\ \ \mu \in \operatorname{span}\{\chi_{\Gamma_i} \mid i = 1,\dots,N_\Gamma\}\}\,, \tag{2.31}$$

where $\chi_{\Gamma_i} \in M^0$ is the function that is identically 1 on Γ_i and vanishes on all other interfaces.

Lemma 2.7. *There exists a constant $\alpha > 0$ such that for all $v \in X_\chi$ there holds*

$$a(v,v) \ge \alpha\|v\|_X^2.$$

Proof. The coercivity assertion is well-known within the framework of mortar methods with straight interfaces, [20]. Moreover, in the case of straight interfaces, the ellipticity constant is independent of the number of subdomains, [54]. □

For the moment, we do not show the existence of a unique solution $(\widetilde{u}_h, \widetilde{\lambda}_h)$ of (2.28). Since (2.28) corresponds to a square system of linear equations, existence follows from

uniqueness. For all standard Lagrange multiplier spaces, we have that $\operatorname{span}\{\chi_{\Gamma_i} \,|\, i = 1, \dots, N_\Gamma\} \subset \widetilde{M}_h$, as required by Assumption 2.1(a), and thus the bilinear form $a(\cdot,\cdot)$ is coercive on the constrained space $\widetilde{V}_h$. To obtain uniqueness of the solution, it is sufficient to establish a suitable uniform inf-sup condition (A.20), see [27], the proof of which will be given in Proposition 2.13. Concerning the approximation, we have the following classical result.

Theorem 2.8. *Let u be the weak solution of (1.1), and assume that $\lambda \in M$ is defined by (2.6). Let $\widetilde{u}_h$ be the solution of (2.28). Then*

$$\|u - \widetilde{u}_h\|_X \le C \inf_{v_h \in \widetilde{V}_h} \|u - v_h\|_X + C \sup_{w_h \in \widetilde{V}_h} \frac{b(w_h, \lambda)}{\|w_h\|_X}, \tag{2.32}$$

for some $C > 0$ that is independent of h. Moreover, if the Lagrange multiplier λ is in $\prod_{i=1}^{N_\Gamma} L^2(\Gamma_i)$, we find

$$\|u - \widetilde{u}_h\|_X \le C \inf_{v_h \in \widetilde{V}_h} \|u - v_h\|_X + C \left\{ \sum_{i=1}^{N_\Gamma} h_{s(i)} \inf_{\mu_h \in \widetilde{M}_{i,h}} \|\lambda - \mu_h\|^2_{0,\Gamma_i} \right\}^{1/2}, \tag{2.33}$$

for some $C > 0$ that is independent of h.

Proof. The first estimate (2.32) is a standard result for mixed finite element methods, as found for example in [101, Thm. 3]. It also follows immediately from the second Strang Lemma A.34 for nonconforming finite elements. We note that the second term measures the consistency error. For the second error bound, (2.33), we employ the approximation property (2.8) of typical Lagrange multiplier spaces, which is transferred to the case of curvilinear interfaces via the equivalence (2.12a),

$$\|w - \Pi_i w\|_{0,\Gamma_i} = \inf_{z \in \widetilde{M}_{i,h}} \|w - z\|_{0,\Gamma_i} \le C h^{1/2}_{\mathrm{s}(i)} |w|_{1/2,\Gamma_i}, \tag{2.34}$$

where Π_i denotes the L^2-projection onto $\widetilde{M}_{i,h}$. Let $w_h \in \widetilde{V}_h$. Using the definition (2.29) of $\widetilde{V}_h$, the assumption that $\lambda \in \prod_{i=1}^{N_\Gamma} L^2(\Gamma_i)$ together with the defining property of the L^2-projection Π_i, as well as (2.34), we can bound the consistency error by

$$\begin{aligned} b(w_h, \lambda) &= \sum_{i=1}^{N_\Gamma} ([w_h]_i, \lambda - \Pi_i \lambda)_{\Gamma_i} = \sum_{i=1}^{N_\Gamma} ([w_h]_i - \Pi_i [w_h]_i, \lambda - \Pi_i \lambda)_{\Gamma_i} \\ &\le C \sum_{i=1}^{N_\Gamma} h^{1/2}_{\mathrm{s}(i)} |[w_h]_i|_{1/2,\Gamma_i} \|\lambda - \Pi_i \lambda_i\|_{0,\Gamma_i}. \end{aligned}$$

The trace theorem A.13 implies

$$\sup_{w_h \in \widetilde{V}_h} \frac{b(w_h, \lambda)}{\|w_h\|_X} \le C \left(\sum_{i=1}^{N_\Gamma} h_{\mathrm{s}(i)} \inf_{\mu_h \in \widetilde{M}_{i,h}} \|\lambda - \mu_h\|^2_{0,\Gamma_i} \right)^{1/2}. \tag{2.35}$$

□

Next, we estimate the infimum and the supremum in the a priori bound (2.32). We first provide an upper bound for the best approximation error in the unconstrained product space $\widetilde{X}_h$, and use the result to establish an upper bound in the constrained space $\widetilde{V}_h$.

Lemma 2.9. *Let $v \in H^2(\Omega^j)$. Then there exists $C > 0$ depending only on C_γ of (2.24), and there exists a unique element $v_h = \widetilde{\mathcal{I}}_j v \in \widetilde{X}_{j,h}$ such that v_h and v coincide in the nodes of $\widetilde{\mathcal{T}}_j$ and*

$$\|v - v_h\|_{1,\Omega^j} \leq C h_j \left(|v|_{2,\Omega^j} + |v|_{1,\Omega^j} \right). \tag{2.36}$$

Moreover, for all i such that $j = \mathrm{s}(i)$ or $j = \mathrm{m}(i)$, it holds that

$$\|(v - v_h)|_{\Omega^j}\|_{00,\Gamma_i} \leq C h_j \left(|u|_{2,\Omega^j} + |u|_{1,\Omega^j} \right). \tag{2.37}$$

Proof. Let $v \in H^2(\Omega^j)$, let $\widetilde{T} \in \widetilde{\mathcal{T}}_j$ be a blending element and consider $w = v|_{\widetilde{T}} \in H^2(\widetilde{T})$. Setting $\widehat{w} = w \circ \widetilde{F}_{\widetilde{T}}$ and denoting by $\mathcal{I}_{\widehat{T}} : C(\widehat{T}) \to \mathbb{P}_1$ the nodal linear interpolant, it is a standard result that

$$\|\widehat{w} - \mathcal{I}_{\widehat{T}} \widehat{w}\|_{1,\widehat{T}} \leq C |\widehat{w}|_{2,\widehat{T}}.$$

We investigate the term $|\widehat{w}|_{2,\widehat{T}}$ more closely. Setting $(x, y) = \widetilde{F}_{\widetilde{T}}(\xi, \eta)$, and applying the chain and the product rule, one obtains for the partial derivatives $\widehat{w}_{rs}$, $r, s \in \{\xi, \eta\}$, that

$$\widehat{w}_{rs}(\xi, \eta) = (\operatorname{grad} w)|^{\mathrm{T}}_{(x,y)} \begin{pmatrix} x_{rs} \\ y_{rs} \end{pmatrix} (\xi, \eta) + Hw|_{(x,y)} : \begin{pmatrix} x_r x_s & x_r y_s \\ x_s y_r & y_r y_s \end{pmatrix} (\xi, \eta), \quad r, s \in \{\xi, \eta\},$$

where Hw denotes the Hessian of w. By transformation to the blending element $\widetilde{T}$, we have

$$|\widehat{w}|_{2,\widehat{T}} \leq C \| \det \widetilde{F}'_{\widetilde{T}} \|^{-1/2}_{L^\infty(\widehat{T})} \left(\|F''_{\widetilde{T}}\|_{L^\infty(\widehat{T})} |w|_{1,\widetilde{T}} + \|F'_{\widetilde{T}}\|^2_{L^\infty(\widehat{T})} |w|_{2,\widetilde{T}} \right).$$

From (2.24), we conclude

$$|\widehat{w}|_{2,\widehat{T}} \leq C h_{\widetilde{T}} \left(|w|_{2,\widetilde{T}} + |w|_{1,\widetilde{T}} \right),$$

yielding

$$\|\widehat{w} - \mathcal{I}_{\widehat{T}} \widehat{w}\|_{1,\widehat{T}} \leq C h_{\widetilde{T}} \left(|w|_{2,\widetilde{T}} + |w|_{1,\widetilde{T}} \right).$$

Transforming the left-hand side back to the element $\widetilde{T}$, and indicating by $\mathcal{I}_{\widetilde{T}}$ the nodal linear interpolant on $\widetilde{T}$, we get

$$h_{\widetilde{T}}^{-1} \|w - \mathcal{I}_{\widetilde{T}} w\|_{0,\widetilde{T}} + |w - \mathcal{I}_{\widetilde{T}} w|_{1,\widetilde{T}} \leq C h_{\widetilde{T}} \left(|w|_{2,\widetilde{T}} + |w|_{1,\widetilde{T}} \right).$$

This proves (2.36), and $\widetilde{\mathcal{I}}_j$ is given element-wise by $\mathcal{I}_{\widetilde{T}}$. We remark that in the bound above, the semi-norms $|\cdot|_1$ and $|\cdot|_2$ are equally scaled.

The bound (2.37) is obtained by similar reasoning. We first exploit that on the reference element $\widehat{T}$, we have by the trace theorem A.13 for the edges $\widehat{e}_i$, $i = 1, \ldots, 3$, of $\widehat{T}$:

$$\|\widehat{w} - \mathcal{I}_{\widehat{T}}\widehat{w}\|_{00,\widehat{e}_i} \leq C|\widehat{w}|_{2,\widehat{T}}, \qquad i = 1, 2, 3.$$

Transforming now to the physical element $\widetilde{T}$ allows us to infer

$$\sum_{e \in \widetilde{\mathcal{E}}_j} \|v - v_h\|_{00,e}^2 \leq C h_j^2 \left(|v|_{2,\Omega^j}^2 + |v|_{1,\Omega^j}^2 \right),$$

where we denote by $\widetilde{\mathcal{E}}_j$ the set of all edges of the triangulation $\widetilde{\mathcal{T}}_j$. Employing the fact that the square of the $H_{00}^{1/2}(\Gamma_i)$-norm is bounded by a constant times the sum of the squares of the $H_{00}^{1/2}$-norms restricted to the edges of Γ_i, we deduce (2.37). □

Theorem 2.10. *Let $u \in H_0^1(\Omega) \cap \prod_{j=1}^{N_\Omega} H^2(\Omega^j)$. Then*

$$\inf_{v_h \in \widetilde{V}_h} \|u - v_h\|_X \leq C \left(\sum_{j=1}^{N_\Omega} h_j^2 \left\{ |u|_{2,\Omega^j}^2 + |u|_{1,\Omega^j}^2 \right\} \right)^{1/2}. \tag{2.38}$$

Proof. The techniques involved in the proof are known from standard mortar element methods, [10]. We note that the assumptions on u guarantee that u is continuous. The construction is done in two steps: first, we define the function $w_h \in \widetilde{X}_h$ subdomain-wise by $w_h|_{\Omega^j} = \widetilde{\mathcal{I}}_j u$, where $\widetilde{\mathcal{I}}_j$ is the piecewise linear interpolant on Ω^j introduced in Lemma 2.9. By (2.36), this leads to

$$\|u - w_h\|_X \leq C \left(\sum_{j=1}^{N_\Omega} h_j^2 \left\{ |u|_{2,\Omega^j}^2 + |u|_{1,\Omega^j}^2 \right\} \right)^{1/2}.$$

Since w_h is not necessarily in $\widetilde{V}_h$, we have to investigate its jump across the interface. The endpoints of the curves Γ_i are nodes, so the jump $\iota_i = [w_h]_i$ across the curve Γ_i satisfies $\iota_i \in H_{00}^{1/2}(\Gamma_i)$, and we obtain from (2.37)

$$\|\iota_i\|_{00,\Gamma_i}^2 = \|(u - w_h)|_{\Omega^{\mathrm{s}(i)}} + (w_h - u)|_{\Omega^{\mathrm{m}(i)}}\|_{00,\Gamma_i}^2 \leq C \sum_{j \in \{\mathrm{s}(i), \mathrm{m}(i)\}} h_j^2 \left\{ |u|_{2,\Omega^j}^2 + |u|_{1,\Omega^j}^2 \right\}.$$

In a second step, we correct this jump using the mortar projection $\widehat{\Pi}_{i,h}$ associated with the curve Γ_i, as given by (2.9). More precisely, we define the pull-back $\widehat{\iota_i} = \iota_i \circ \gamma_i$ and set $z_i = \mathcal{L}_i(\widehat{\Pi}_{i,h}\widehat{\iota_i})$, where the lifting operator $\mathcal{L}_i$ is defined in Lemma 2.6. We may think of z_i as being extended by zero outside of $\Omega^{\mathrm{s}(i)}$. Proceeding in this fashion for each interface Γ_i, we can construct a function $z_h = \sum_{i=1}^{N_\Gamma} z_i \in \widetilde{X}_h$ such that

$$\|z_h\|_X^2 = \sum_{j=1}^{N_\Omega} \left\| \sum_{i=1}^{N_\Gamma} z_i \right\|_{1,\Omega^j}^2 \leq C \sum_{j=1}^{N_\Omega} \sum_{i=1}^{N_\Gamma} \|z_i\|_{1,\Omega^j}^2 = C \sum_{i=1}^{N_\Gamma} \|z_i\|_{1,\Omega^{\mathrm{s}(i)}}^2,$$

with C independent of the number of subdomains. Therefore, by Lemma 2.6, together with (2.9b) and (2.12b),

$$\|z_h\|_X^2 \leq C \sum_{i=1}^{N_\Gamma} \|\iota_i\|_{00,\Gamma_i}^2 \leq C \sum_{j=1}^{N_\Omega} \|u - w_h\|_{1,\Omega^j}^2.$$

We now check that the function $v_h = w_h - z_h$ is an element of $\widetilde{V}_h$. For $\mu \in \widetilde{M}_{i,h}$ we calculate

$$b(v_h, \mu) = \sum_{i=1}^{N_\Gamma} ([\iota_i - z_i]_i, \mu)_{\Gamma_i} = \sum_{i=1}^{N_\Gamma} (\widehat{\iota_i} - \widehat{\Pi}_{i,h}\widehat{\iota_i}, \widehat{\mu})_{\hat{I}_i} = 0$$

by definition of $\widehat{\Pi}_{i,h}$ since $\widehat{\mu} \in \widehat{M}_{i,h}$. For the transformation onto the reference interval $\hat{I}_i$ above, we have used the fact that Γ_i is parametrized by arc length, so that the infinitesimal surface elements coincide and no additional factor appears due to the transformation. □

Remark 2.11. Due to the appearance of $|u|_1$ in (2.38), an affine solution u will in general not be reproduced by the numerical scheme (2.28), which is the essential difference in the a priori results to the case of planar interfaces. However, this term only stems from the blending elements, the number of which is considerably smaller than the total number of elements involved. In typical meshes, curved elements are used only near the boundary so that (2.38) can be sharpened: If $S_j \subset \Omega^j$ denotes the region where blending elements are used (and affine elements are used on $\Omega^j \setminus S_j$), then we obtain the error bound

$$\inf_{v_h \in \widetilde{V}_h} \|u - v_h\|_X \leq C \left(\sum_{j=1}^{N_\Omega} h_j^2 \left(|u|_{2,\Omega^j}^2 + |u|_{1,S_j}^2 \right) \right)^{1/2}. \tag{2.39}$$

If S_j is contained in a strip of width $O(h_j)$ near $\partial\Omega^j$, and if the function u is smooth, then this improved bound yields an error bound $O(\max_{j=1,\ldots,N_\Omega} h_j^{3/2})$; we will illustrate this effect in a numerical example in Section 2.6. ∎

We now turn to estimating the error in the Lagrange multiplier for the blending element formulation (2.28). As already pointed out in Remark 2.4, necessary conditions for deriving optimal estimates are the continuity of the coupling bilinear form $b(\cdot,\cdot)$ and a uniform inf-sup condition (A.20). By definition, the bilinear form $b(\cdot,\cdot)$ is continuous on $X \times M$ with respect to the norms $\|\cdot\|_X$ and $\|\cdot\|_M$ but not on $X \cap X_0 \times M^0 \cap M$ with respect to the norms $\|\cdot\|_X$ and $\|\cdot\|_{M^0}$, where the space X_0 is given by

$$X_0 = \{v \in X \,:\, [v]_i \in H_{00}^{1/2}(\Gamma_i) \quad i = 1, \ldots, N_\Gamma\}. \tag{2.40}$$

On the other hand, we cannot establish a uniform inf-sup condition with respect to the norms $\|\cdot\|_X$ and $\|\cdot\|_M$. A uniform inf-sup condition can be only established with respect to the norms $\|\cdot\|_X$ and $\|\cdot\|_{M^0}$.

Lemma 2.12. *Let $b(\cdot,\cdot)$ be given by (2.15), and equip the space X_0 with the stronger norm $\|v\|_{X_0}^2 = \|v\|_X^2 + \sum_{i=1}^{N_\Gamma} \|[v]_i\|_{00,\Gamma_i}^2$. Then, $b(\cdot,\cdot)$ is continuous on $X_0 \times M^0 \cap M$, i.e., there exists $C_b > 0$ such that*

$$|b(v,\mu)| \le C_b \|v\|_{X_0} \|\mu\|_{M^0}, \qquad v \in X_0, \quad \mu \in M^0 \cap M. \tag{2.41}$$

Moreover, $b(\cdot,\cdot)$ satisfies a discrete inf-sup condition of the following type: There exists a constant $C > 0$ (depending only on the interfaces Γ_i, the stability constants of the mortar projections $\widehat{\Pi}_{i,h}$, and the constant C_γ) such that

$$C\|\widetilde{\mu}_h\|_{M^0} \le \sup_{\widetilde{z}_h \in \widetilde{X}_h \cap X_0} \frac{b(\widetilde{z}_h, \widetilde{\mu}_h)}{\|\widetilde{z}_h\|_{X_0}}, \qquad \widetilde{\mu}_h \in \widetilde{M}_h. \tag{2.42}$$

Proof. The continuity (2.41) follows from the consideration

$$\begin{aligned} |b(v,\mu)| &\le \sum_{i=1}^{N_\Gamma} |\langle [v]_i \,,\, \mu \rangle_{\Gamma_i}| \le \sum_{i=1}^{N_\Gamma} \|[v]_i\|_{00,\Gamma_i} \|\mu\|_{-1/2,\Gamma_i} \\ &\le C \left\{ \sum_{i=1}^{N_\Gamma} \|[v]_i\|_{00,\Gamma_i}^2 \right\}^{1/2} \|\mu\|_{M^0} \le C_b \|v\|_{X_0} \|\mu\|_{M^0}. \end{aligned}$$

In order to see (2.42), let $\widetilde{\mu}_h \in \widetilde{M}_h$. We set $\widetilde{\mu}_i = \widetilde{\mu}_h|_{\Gamma_i}$ and use (2.12) and the fact that γ_i is an arc-length parametrization to obtain

$$\|\widetilde{\mu}_i\|_{-1/2,\Gamma_i} = \sup_{v \in H_{00}^{1/2}(\Gamma_i)} \frac{\langle v, \widetilde{\mu}_i \rangle_{\Gamma_i}}{\|v\|_{00,\Gamma_i}} \le C \sup_{v \in H_{00}^{1/2}(\Gamma_i)} \frac{\langle \widehat{v}, \widehat{\mu}_i \rangle_{\hat{I}_i}}{\|\widehat{v}\|_{00,\hat{I}_i}},$$

where the superscript $\widehat{\ }$ indicates the pull-back to $\hat{I}_i$. Employing the stability properties of mortar projection $\widehat{\Pi}_{i,h}$, we arrive at

$$\begin{aligned} \|\widetilde{\mu}_i\|_{-1/2,\Gamma_i} &\le C \sup_{v \in H_{00}^{1/2}(\Gamma_i)} \frac{\langle \widehat{v} \,,\, \widehat{\mu}_i \rangle_{\hat{I}_i}}{\|\widehat{v}\|_{00,\hat{I}_i}} \le C \sup_{v \in H_{00}^{1/2}(\Gamma_i)} \frac{\langle \widehat{\Pi}_{i,h} \widehat{v} \,,\, \widehat{\mu}_i \rangle_{\hat{I}_i}}{\|\widehat{\Pi}_{i,h} \widehat{v}\|_{00,\hat{I}_i}} \\ &\le C \sup_{z \in \widehat{W}_{i,h} \cap H_{00}^{1/2}(\hat{I}_i)} \frac{\langle z \,,\, \widehat{\mu}_i \rangle_{\hat{I}_i}}{\|z\|_{00,\hat{I}_i}} \le C \langle \widehat{z}_i, \widehat{\mu}_i \rangle_{\hat{I}_i}, \end{aligned} \tag{2.43}$$

for an element $\widehat{z}_i \in \widehat{W}_{i,h} \cap H_{00}^{1/2}(\hat{I}_i)$ with $\|\widehat{z}_i\|_{00,\hat{I}_i} = 1$. We extend $\widehat{z}_i$ to $\widetilde{z}_i \in \widetilde{X}_{\mathrm{s}(i),h}$ by means of the lifting operator from Lemma 2.6, and define $\widetilde{z}_h = \sum_{i=1}^{N_\Gamma} b(\widetilde{z}_i, \widetilde{\mu}_h) \widetilde{z}_i$. Using again the fact that Γ_i is parametrized by arc length, we obtain

$$(\widehat{z}_i \,,\, \widehat{\mu}_i)_{\hat{I}_i} = (\widetilde{z}_i \,,\, \widetilde{\mu}_i)_{\Gamma_i} = b(\widetilde{z}_i, \widetilde{\mu}_i),$$

and, therefore,

$$\|\widetilde{\mu}_h\|_{M^0}^2 = \sum_{i=1}^{N_\Gamma} \|\widetilde{\mu}_i\|_{-1/2,\Gamma_i}^2 \le C \sum_{i=1}^{N_\Gamma} (b(\widetilde{z}_i, \widetilde{\mu}_i))^2 = b(\widetilde{z}_h, \widetilde{\mu}_h) \le C_b \|\widetilde{z}_h\|_{X_0} \|\widetilde{\mu}_h\|_{M^0}, \tag{2.44}$$

where, in the last step, we employed the continuity of $b(\cdot,\cdot)$ stated in (2.41). This allows us to estimate

$$\|\widetilde{z}_h\|_X^2 = \sum_{j=1}^{N_\Omega} \| \sum_{i=1}^{N_\Gamma} b(\widetilde{z}_i, \widetilde{\mu}_h)\widetilde{z}_i\|_{1,\Omega^j}^2 \leq C \sum_{i=1}^{N_\Gamma} b(\widetilde{z}_i, \widetilde{\mu}_h)^2 = Cb(\widetilde{z}_h, \widetilde{\mu}_h),$$

$$\sum_{i=1}^{N_\Gamma} \|[\widetilde{z}_h]_i\|_{00,\Gamma_i}^2 \leq C \sum_{i=1}^{N_\Gamma} b(\widetilde{z}_i, \widetilde{\mu}_h)^2 = Cb(\widetilde{z}_h, \widetilde{\mu}_h).$$

so that we arrive, by summing these last two bounds, at

$$\|\widetilde{z}_h\|_{X_0}^2 \leq Cb(\widetilde{z}_h, \widetilde{\mu}_h). \tag{2.45}$$

From (2.44) we infer $\|\widetilde{\mu}_h\|_{M^0} \leq C\|\widetilde{z}_h\|_{X_0}$; inserting this in (2.45) then allows us to conclude (2.42). □

We are now able to estimate the error in the Lagrange multiplier.

Theorem 2.13. *Let u be the weak solution of (1.1), and assume that $\lambda \in M$ is defined by (2.6). Assume that $(\widetilde{u}_h, \widetilde{\lambda}_h)$ are given by (2.28). Then there exists a constant $C > 0$ depending only on the interfaces Γ_i, the stability constants of the mortar projections $\widehat{\Pi}_{i,h}$, and the constant C_γ of (2.24) such that*

$$\|\lambda - \widetilde{\lambda}_h\|_{M^0} \leq C \left(\inf_{\mu \in \widetilde{M}_h} \|\lambda - \mu\|_{M^0} + \|u - \widetilde{u}_h\|_X \right). \tag{2.46}$$

Proof. Let $\mu_h \in \widetilde{M}_h$ be arbitrary. Then, by the continuity of $b(\cdot,\cdot)$ stated in (2.41), the Galerkin orthogonality, and (2.42), we have

$$\begin{aligned}
\|\mu_h - \widetilde{\lambda}_h\|_{M^0} &\leq C \sup_{\widetilde{z}_h \in \widetilde{X}_h \cap X_0} \frac{b(\widetilde{z}_h, \mu_h - \widetilde{\lambda}_h)}{\|\widetilde{z}_h\|_{X_0}} \\
&\leq C \sup_{\widetilde{z}_h \in \widetilde{X}_h \cap X_0} \frac{b(\widetilde{z}_h, \mu_h - \lambda)}{\|\widetilde{z}_h\|_{X_0}} + \frac{b(\widetilde{z}_h, \lambda - \widetilde{\lambda}_h)}{\|\widetilde{z}_h\|_{X_0}} \\
&\leq C\|\mu_h - \lambda\|_{M^0} + C \sup_{\widetilde{z}_h \in \widetilde{X}_h \cap X_0} \frac{a(u - \widetilde{u}_h, \widetilde{z}_h)}{\|\widetilde{z}_h\|_{X_0}} \\
&\leq C\|\mu_h - \lambda\|_{M^0} + C\|u - \widetilde{u}_h\|_X.
\end{aligned}$$

The standard argument using the triangle inequality then gives the desired result. □

2.3.2 Convergence Analysis on Affine Elements

We now turn to the analysis of the original discrete problem (2.20). Having established a one-to-one connection between the elements of the triangulations $\mathcal{T}_j$ and $\widetilde{\mathcal{T}}_j$, we demonstrate in the following how we can construct one-to-one connections between the elements

of X_h and $\widetilde{X}_h$ and between the elements of M_h and $\widetilde{M}_h$. A function $v_h \in X_h$ corresponds to $\widetilde{v}_h \in \widetilde{X}_h$ if for every element $T \in \mathcal{T}_j$, we have $\widetilde{v}_h \circ \widetilde{F}_{\widetilde{T}} = v_h \circ F_T$. This mapping exists and is denoted by

$$\mathcal{S}_X : X_h \to \widetilde{X}_h, \qquad v_h \mapsto \widetilde{v}_h \tag{2.47}$$

with the inverse map

$$\mathcal{C}_X = \mathcal{S}_X^{-1} : \widetilde{X}_h \to X_h, \qquad \widetilde{v}_h \mapsto v_h. \tag{2.48}$$

In particular, for every element T we have that $v_h|_T$ is the linear nodal interpolant of $\widetilde{v}_h$ on $\widetilde{T}$. Considering the restriction of $\mathcal{C}_X$ onto an element $\widetilde{T} \in \widetilde{\mathcal{T}}$, given by

$$\mathcal{C}_T : \widetilde{T} \to T, \quad \mathcal{C}_T = F_T \circ \widetilde{F}_{\widetilde{T}}^{-1} = \mathrm{Id} + O(h_T^2), \quad \det D\mathcal{C}_T = 1 + O(h_T), \tag{2.49}$$

which follows from property (2.24), it is easy to see that

$$a_h(\mathcal{C}_X\tilde{v}_h, \mathcal{C}_X\tilde{v}_h) \sim a(\tilde{v}_h, \tilde{v}_h), \quad \tilde{v}_h \in \widetilde{X}_h, \tag{2.50}$$

where the constants hidden in the $\sim$-notation are independent of h. On $\widetilde{X}_h \times \widetilde{X}_h$, we define the bilinear form

$$a'_h(w_h, v_h) = a_h(\mathcal{C}_X w_h, \mathcal{C}_X v_h). \tag{2.51}$$

In view of (2.50) and Lemma 2.7, we have ellipticity of the bilinear form a'_h on $\widetilde{X}_h \cap X_\chi$, with the space X_χ defined in (2.31):

$$a'_h(v_h, v_h) \geq \alpha \|v_h\|_X^2, \qquad v_h \in \widetilde{X}_h \cap X_\chi. \tag{2.52}$$

In a similar way, we can uniquely identify a function μ_h of M_h with a function $\widetilde{\mu}_h$ of $\widetilde{M}_h$ by mappings

$$\mathcal{S}_M : M_h \to \widetilde{M}_h, \quad \mu_h \mapsto \widetilde{\mu}_h, \qquad \text{and} \qquad \mathcal{C}_M = \mathcal{S}_M^{-1} : \widetilde{M}_h \to M_h, \quad \widetilde{\mu}_h \mapsto \mu_h. \tag{2.53}$$

For the coupling on $\widetilde{X}_h \times \widetilde{M}_h$, we set

$$b'_h(\widetilde{v}_h, \widetilde{\mu}_h) = b_h(\mathcal{C}_X\widetilde{v}_h, \mathcal{C}_M\widetilde{\mu}_h), \qquad \widetilde{v}_h \in \widetilde{X}_h,\ \widetilde{\mu}_h \in \widetilde{M}_h.$$

Using the bijections $\mathcal{S}_X$ and $\mathcal{S}_M$, we can reformulate the problem (2.20) as a perturbation of a problem of the form analyzed in Section 2.3.1. We set $(u'_h, \lambda'_h) = (\mathcal{S}_X u_h, \mathcal{S}_M \lambda_h)$ for the solution (u_h, λ_h) of (2.20) and rewrite (2.20) as: find $(u'_h, \lambda'_h) \in \widetilde{X}_h \times \widetilde{M}_h$ such that

$$a'_h(u'_h, v) \ + \ b'_h(v, \lambda'_h) \ = \ l_h(\mathcal{C}_X v), \qquad v \in \widetilde{X}_h, \tag{2.54a}$$

$$b'_h(u'_h, \mu) \qquad\qquad = \ 0, \qquad\qquad \mu \in \widetilde{M}_h. \tag{2.54b}$$

In order to assess the error $u - u'_h$, we introduce the corresponding constrained space

$$V'_h = \{\widetilde{v}_h \in \widetilde{X}_h : b'_h(\widetilde{v}_h, \widetilde{\mu}_h) = 0,\ \widetilde{\mu}_h \in \widetilde{M}_h\}. \tag{2.55}$$

As before, the constrained problem is approximated in a nonconforming manner, i.e., $V'_h \not\subseteq V$. However, the second Strang Lemma A.34 cannot be applied directly since the bilinear form $a'_h(\cdot,\cdot)$ is not defined for elements in X. Taking into account the nonconformity, a slight modification of the proof of the first Strang Lemma A.33 admits to derive the following estimate.

Lemma 2.14. *Let u be the weak solution of (1.1), and assume that $\lambda \in M$ is defined by (2.6). Let u_h' be the solution of (2.54). Then*

$$\begin{aligned}\|u-u_h'\|_X \le C \Bigg\{ \inf_{v_h\in V_h'} \Bigg(\|u-v_h\|_X + \sup_{w_h\in V_h'} \frac{a(v_h,w_h)-a_h'(v_h,w_h)}{\|w_h\|_X} \Bigg) \\ + \sup_{w_h\in V_h'} \frac{b(w_h,\lambda)}{\|w_h\|_X} + \sup_{w_h\in V_h'} \frac{l(w_h)-l_h(\mathcal{C}_X w_h)}{\|w_h\|_X} \Bigg\}.\end{aligned} \tag{2.56}$$

Proof. Let $v_h, w_h \in V_h'$. We use the facts that $u_h' \in V_h'$ and that $V_h' \subset X$ to derive from (1.16a) and (2.54a)

$$a_h'(u_h'-v_h,w_h) = l_h(\mathcal{C}_X w_h) - a_h'(v_h,w_h) + a(u-v_h,w_h) + a(v_h,w_h) + b(w_h,\lambda) - l(w_h). \tag{2.57}$$

With the V_h'-ellipticity of $a_h'(\cdot,\cdot)$ following from (2.52), we have

$$\|u_h'-v_h\|_X \le \sup_{w_h\in V_h'} \frac{a_h'(u_h'-v_h,w_h)}{\|w_h\|_X}.$$

Since $v_h, w_h \in V_h'$ are arbitrary in (2.57), the desired result is obtained by using the triangle inequality. □

We are able to conveniently employ the results of the blending approach from the last section by suitably relating the two constrained spaces V_h' and $\widetilde{V}_h$.

Lemma 2.15. *For an arbitrary $v_h' = (v_m', v_s') \in V_h'$, there exists $\widetilde{\Delta} v_h' \in \widetilde{X}_h$ such that*

$$\widetilde{v}_h = v_h' + \widetilde{\Delta} v_h' \in \widetilde{V}_h, \tag{2.58a}$$

$$\|\widetilde{\Delta} v_h'\|_X \le C \left(\sum_{i=1}^{N_\Gamma} h_{\mathrm{s}(i)}^{1+2t} |v_m'|_{t,\Gamma_i}^2 \right)^{1/2}, \quad t \in [0,1], \tag{2.58b}$$

$$\|\widetilde{\Delta} v_h'\|_{0,\Gamma} \le C \left(\sum_{i=1}^{N_\Gamma} h_{\mathrm{s}(i)}^{3} |v_m'|_{1/2,\Gamma_i}^2 \right)^{1/2}, \tag{2.58c}$$

$$\|v_h'\|_X \sim \|\widetilde{v}_h\|_X, \qquad h \text{ small enough.} \tag{2.58d}$$

The analogous statement holds for arbitrary $\widetilde{v}_h \in \widetilde{V}_h$, yielding $v_h' = \widetilde{v}_h + \Delta' \widetilde{v}_h \in V_h'$.

Proof. Given $\widetilde{v}_h \in \widetilde{X}_h$ and $\widetilde{\mu}_h \in \widetilde{M}_h$, it can be observed that

$$\begin{aligned} b_h'(\widetilde{v}_h,\widetilde{\mu}_h) &= b_h(\mathcal{C}_X\widetilde{v}_h, \mathcal{C}_M\widetilde{\mu}_h) = \sum_{i=1}^{N_\Gamma} ([\mathcal{C}_X\widetilde{v}_h]_{i,h},\ \mathcal{C}_M\widetilde{\mu}_h)_{\Gamma_{i,h}^{\mathrm{s}}} \\ &= \sum_{i=1}^{N_\Gamma} \left(\widetilde{v}_{\mathrm{s}} \circ \gamma_i \circ (\gamma_{i,h}^{\mathrm{s}})^{-1} - P_{\mathrm{s}}(\widetilde{v}_{\mathrm{m}} \circ \gamma_i \circ (\gamma_{i,h}^{\mathrm{m}})^{-1}),\ \widetilde{\mu}_h \circ \gamma_i \circ (\gamma_{i,h}^{\mathrm{s}})^{-1} \right)_{\Gamma_{i,h}^{\mathrm{s}}} \\ &= \sum_{i=1}^{N_\Gamma} \left([\widetilde{v}_h]_i \circ \gamma_i \circ (\gamma_{i,h}^{\mathrm{s}})^{-1},\ \widetilde{\mu}_h \circ \gamma_i \circ (\gamma_{i,h}^{\mathrm{s}})^{-1} \right)_{\Gamma_{i,h}^{\mathrm{s}}} = \sum_{i=1}^{N_\Gamma} ([\widetilde{v}_h]_i,\ \omega_i\widetilde{\mu}_h)_{\Gamma_i} \\ &= b(\widetilde{v}_h, \omega\widetilde{\mu}_h), \end{aligned}$$

with a weighting function ω defined interface-wise by $\omega|_{\Gamma_i} = \omega_i = |(\gamma^{\mathrm{s}}_{i,h} \circ \gamma_i^{-1})'|$. Denoting by $\widetilde{W}_{i,h}$ the restriction of the blending element space $\widetilde{X}_{\mathrm{s}(i),h}$ to the interface Γ_i, we employ the mortar-type projections $\widetilde{\Pi}_i, \Pi'_i : L^2(\Gamma_i) \to \widetilde{W}_{i,h}$, given by

$$\begin{aligned}(w - \widetilde{\Pi}_i w,\, \widetilde{\mu}_h)_{\Gamma_i} &= 0, \qquad \widetilde{\mu}_h \in \widetilde{M}_h,\\ (w - \Pi'_i w,\, \omega_i \widetilde{\mu}_h)_{\Gamma_i} &= 0, \qquad \widetilde{\mu}_h \in \widetilde{M}_h.\end{aligned}$$

Given an arbitrary $v'_h \in V'_h$, we define $\widetilde{\Pi}_{i,\Omega^{\mathrm{s}(i)}} v'_h \in X_{\mathrm{s}(i)}$ by

$$(\widetilde{\Pi}_{i,\Omega^{\mathrm{s}(i)}} v'_h)(p_j) = \begin{cases} v'_{\mathrm{s}}(p_j) & \text{for all nodes } p_j \text{ in the interior of } \Omega^{\mathrm{s}(i)},\\ (\widetilde{\Pi}_i v'_{\mathrm{m}}|_{\Gamma_i})(p_j) & \text{for all slave nodes } p_j \text{ on } \Gamma_i.\end{cases}$$

By leaving v'_{m} unchanged and setting subdomain-wise $\widetilde{v}_h = (v'_{\mathrm{m}},\, \widetilde{\Pi}_{i,\Omega^{\mathrm{s}(i)}} v'_h) \in X_{\mathrm{s}(i)}$, it follows immediately that $\widetilde{v}_h \in \widetilde{V}_h$. The difference $\widetilde{\Delta} v'_h = \widetilde{v}_h - v'_h$ is zero on all nodes except the slave side nodes. The restriction of $\widetilde{\Delta} v'_h$ to Γ_i is given by

$$\widetilde{\Delta} v'_h|_{\Gamma_i} = \widetilde{\Pi}_i v'_{\mathrm{m}} - v'_{\mathrm{s}} = (\widetilde{\Pi}_i - \Pi'_i) v'_{\mathrm{m}}, \tag{2.59}$$

since $v'_h \in V'_h$. It follows that

$$\begin{aligned}\|\widetilde{\Delta} v'_h\|_{0,\Gamma_i} &= \|(\widetilde{\Pi}_i - \Pi'_i) v'_{\mathrm{m}}\|_{0,\Gamma_i}\\ &\le \sup_{\|\widetilde{\mu}\|_{0,\Gamma_i}=1} \Big((\widetilde{\Pi}_i - \Pi'_i) v'_{\mathrm{m}},\, \widetilde{\mu}\Big)_{\Gamma_i}\\ &= \sup_{\|\widetilde{\mu}\|_{0,\Gamma_i}=1} \big((v'_{\mathrm{m}}, \widetilde{\mu})_{\Gamma_i} - (\Pi'_i v'_{\mathrm{m}}, \omega_i \widetilde{\mu})_{\Gamma_i} + (\Pi'_i v'_{\mathrm{m}}, (\omega_i - 1)\widetilde{\mu})_{\Gamma_i}\big)\\ &= \sup_{\|\widetilde{\mu}\|_{0,\Gamma_i}=1} \big((v'_{\mathrm{m}}, (1 - \omega_i)\widetilde{\mu})_{\Gamma_i} + (\Pi'_i v'_{\mathrm{m}}, (\omega_i - 1)\widetilde{\mu})_{\Gamma_i}\big)\\ &= \sup_{\|\widetilde{\mu}\|_{0,\Gamma_i}=1} \big((\mathrm{Id} - \Pi'_i) v'_{\mathrm{m}},\, (1 - \omega_i)\widetilde{\mu}\big)_{\Gamma_i} \le C \|1 - \omega_i\|_{\infty,\Gamma_i} \|(\mathrm{Id} - \Pi'_i) v'_{\mathrm{m}}\|_{0,\Gamma_i}\\ &\le C h^{1+t}_{\mathrm{s}(i)} |v'_{\mathrm{m}}|_{t,\Gamma_i}, \qquad t \in [0,1],\end{aligned} \tag{2.60}$$

where we have used the fact that $\omega_i = 1 + O(h_{\mathrm{s}(i)})$ for the last step. Setting $t = 1/2$ gives (2.58c). Using the standard inverse inequality (A.28) and the norm equivalence (A.26) twice, once with $d = 2$ for all finite element nodes, and once with $d = 1$ only for the slave side nodes, we obtain

$$\|\widetilde{\Delta} v'_h\|^2_X \le C \sum_{i=1}^{N_\Gamma} h^{-1}_{\mathrm{s}(i)} \|\widetilde{\Delta} v'_h\|^2_{0,\Gamma_i},$$

since $\widetilde{\Delta} v'_h = \widetilde{v}_h - v'_h$ is zero on all nodes except the slave side nodes. Combining this with (2.60) yields (2.58b). The norm equivalence (2.58d) follows from (2.58b) and the trace theorem by observing that

$$\|v'_h\|_X \begin{cases} \ge \|\widetilde{v}_h\|_X - \|\widetilde{\Delta} v'_h\|_X \ge (1 - C \max\limits_{1 \le i \le N_\Gamma} h_{\mathrm{s}(i)}) \|\widetilde{v}_h\|_X,\\ \le \|\widetilde{v}_h\|_X + \|\widetilde{\Delta} v'_h\|_X \le (1 + C \max\limits_{1 \le i \le N_\Gamma} h_{\mathrm{s}(i)}) \|\widetilde{v}_h\|_X,\end{cases}$$

provided that $\max_{1\le i\le N_\Gamma} h_{\mathrm{s}(i)}$ is small enough. According to (2.59), we observe that $\widetilde{\Delta} v'_h$ only depends on $v'_{\mathrm{m}} = \widetilde{v}_{\mathrm{m}}$. Therefore, it is obvious that the analogous statement of the Lemma has to hold for an arbitrary $\widetilde{v} \in \widetilde{V}_h$. □

In the following, we will estimate each of the terms from the right hand side of (2.56) separately.

Lemma 2.16. *Let $u \in H^1_0(\Omega) \cap \prod_{j=1}^{N_\Omega} H^2(\Omega^j)$ and V'_h be given by (2.55). Then it holds that*

$$\inf_{v'_h \in V'_h} \|u - v'_h\|_X \;\le\; C \max_{1\le j\le N_\Omega} h_j \left(\sum_{j=1}^{N_\Omega} \|u\|^2_{2,\Omega^j} \right)^{1/2}. \tag{2.61}$$

Proof. From (2.38) in Theorem 2.10, we can find $\widetilde{v}_h \in \widetilde{V}_h$ such that

$$\|u - \widetilde{v}_h\|^2_X \le C \sum_{j=1}^{N_\Omega} h_j^2 \|u\|^2_{2,\Omega^j}.$$

We choose $v'_h \in V'_h$ as in Lemma 2.15, and obtain with (2.58b)

$$\begin{aligned} \|u - v'_h\|^2_X \;&\le\; C\|u - \widetilde{v}_h\|^2_X + C\|\Delta' \widetilde{v}_h\|^2_X \\ &\le\; C \sum_{j=1}^{N_\Omega} h_j^2 \|u\|^2_{2,\Omega^j} + C \sum_{i=1}^{N_\Gamma} h^2_{\mathrm{s}(i)} |\widetilde{v}_{\mathrm{m}}|^2_{1/2,\Gamma_i}, \end{aligned}$$

which yields the result by the trace theorem A.13 and the usual coloring argument. □

Lemma 2.17. *Let the bilinear forms $a(\cdot,\cdot)$, $a'(\cdot,\cdot)$, and the blending element space $\widetilde{X}_h$ be given by (2.17), (2.51), and (2.26), respectively. Then*

$$\sup_{v\in\widetilde{X}_h} \sup_{w\in\widetilde{X}_h} \frac{a(v,w) - a'_h(v,w)}{\|v\|_X \|w\|_X} \le C \max_{1\le j\le N_\Omega} h_j.$$

Proof. On each element $\widetilde{T}$, the difference $a(v,w) - a'_h(v,w)$ can be written as

$$(\operatorname{grad} v, (\mathrm{Id} - A_T) \operatorname{grad} w)_{\widetilde{T}}, \tag{2.62}$$

where the matrix A_T is given by

$$A_T = \mathcal{C}'_T{}^{-\mathrm{T}} \mathcal{C}'_T{}^{-1} \det \mathcal{C}'_T,$$

with $\mathcal{C}_T$ defined in (2.49). Hence,

$$\|\mathrm{Id} - A_T\|_{L^\infty(\widetilde{T})} \le C h_T, \qquad T \in \mathcal{T}_j. \tag{2.63}$$

Summation of (2.62) over all involved triangles gives

$$\begin{aligned} a(v,w) - a'_h(v,w) &= \sum_T (\operatorname{grad} v, (\mathrm{Id} - A_T) \operatorname{grad} w)_{\widetilde{T}} \\ &\le \max_T \|\mathrm{Id} - A_T\|_{L^\infty(\widetilde{T})} \sum_T (|\operatorname{grad} v|, |\operatorname{grad} w|)_{\widetilde{T}}, \end{aligned}$$

from which we conclude by (2.63) and the Cauchy-Schwarz inequality

$$\begin{aligned} a(v,w) - a_h'(v,w) &\le C \max_{1\le j\le N_\Omega} h_j \left(\sum_{j=1}^{N_\Omega} \|\operatorname{grad} v\|_{0,\Omega^j}^2\right)^{1/2} \left(\sum_{j=1}^{N_\Omega} \|\operatorname{grad} w\|_{0,\Omega^j}^2\right)^{1/2} \\ &\le C \max_{1\le j\le N_\Omega} h_j \|v\|_X \|w\|_X, \end{aligned}$$

which yields the desired result. □

Lemma 2.18. *Let u be the weak solution of (1.1), and assume that $\lambda \in M$ is defined by (2.6). Let the coupling bilinear form $b(\cdot,\cdot)$ and the constrained space V_h' be defined by* (2.15) *and* (2.55)*, respectively. For h small enough, it holds that*

$$\sup_{v_h' \in V_h'} \frac{b(v_h',\lambda)}{\|v_h'\|_X} \;\le\; C \max_{1\le j\le N_\Omega} h_j \left(\sum_{j=1}^{N_\Omega} \|u\|_{2,\Omega^j}^2\right)^{1/2}. \tag{2.64}$$

Proof. For an arbitrary $v_h' \in V_h'$, we apply Lemma 2.15 to obtain $\widetilde{v}_h \in \widetilde{V}_h$ and $\Delta'\widetilde{v}_h \in X_h$, yielding by (2.58a) and (2.58d)

$$\frac{b(v_h',\lambda)}{\|v_h'\|_X} \;=\; \frac{b(\widetilde{v}_h,\lambda)}{\|v_h'\|_X} + \frac{b(\Delta'\widetilde{v}_h,\lambda)}{\|v_h'\|_X} \;\le\; C\frac{b(\widetilde{v}_h,\lambda)}{\|\widetilde{v}_h\|_X} + C\frac{b(\Delta' v_h,\lambda)}{\|\widetilde{v}_h\|_X}.$$

The first term of the above right hand side can be bounded appropriately by (2.35) and (2.34). For the second term, we use (2.58c), and conclude

$$\frac{b(\Delta'\widetilde{v}_h,\lambda)}{\|\widetilde{v}_h\|_X} \;\le\; \frac{\|\Delta'\widetilde{v}_h\|_{0,\Gamma_h^{\mathrm{s}}}\|\lambda\|_{0,\Gamma}}{\|\widetilde{v}_h\|_X} \;\le\; C \max_{1\le j\le N_\Omega} h_j\|\lambda\|_{0,\Gamma} \;\le\; C \max_{1\le j\le N_\Omega} h_j \left(\sum_{j=1}^{N_\Omega} |u|_{2,\Omega}^2\right)^{1/2},$$

which gives the desired result. □

We now turn to estimating the error introduced by the right hand side $l(\widetilde{w}_h) - l_h(\mathcal{C}_X\widetilde{w}_h)$.

Lemma 2.19. *Let the linear forms $l(\cdot)$, $l_h(\cdot)$, and the blending element space $\widetilde{X}_h$ be given by* (2.19)*,* (2.21)*, and* (2.26)*, respectively. Then*

$$\sup_{\widetilde{w}_h \in \widetilde{X}_h} \frac{|l(\widetilde{w}_h) - l_h(\mathcal{C}_X\widetilde{w}_h)|}{\|\widetilde{w}_h\|_X} \le C \sum_{j=1}^{N_\Omega} h_j^2.$$

Proof. For each element $\widetilde{T} \in \widetilde{\mathcal{T}}_j$, we have

$$\begin{aligned} (f,\widetilde{w}_h)_{\widetilde{T}} - (f_j, \mathcal{C}_X\widetilde{w}_h)_T &= (f,\widetilde{w}_h)_{\widetilde{T}} - (f_j\circ\mathcal{C}_T, \widetilde{w}_h \det\mathcal{C}_T')_{\widetilde{T}} \\ &= (f - f_j\circ\mathcal{C}_T \det\mathcal{C}_T', \widetilde{w}_h)_{\widetilde{T}}. \end{aligned}$$

Our assumptions (2.22) on the choice of the functions f_j together with the fact that $\mathcal{C}_T(x) = x$ for the vertices of the triangle $\widetilde{T}$ give

$$\begin{aligned} \|f - f_j\circ\mathcal{C}_T\|_{L^\infty(\widetilde{T})} &\le \|f - f_j\|_{L^\infty(\widetilde{T})} + \|f_j - f_j\circ\mathcal{C}_T\|_{L^\infty(\widetilde{T})} \\ &\le Ch_{\widetilde{T}} + C\|\mathrm{Id} - \mathcal{C}_T\|_{L^\infty(\widetilde{T})} \le Ch_T, \end{aligned} \tag{2.65}$$

where the constant C is determined by the Lipschitz constant C_f of the functions f, f_j. We therefore have

$$\|f - f_j \circ \mathcal{C}_T \det \mathcal{C}_T'\|_{L^\infty(\widetilde{T})} \leq C h_T.$$

Hence,

$$\left|(f, \widetilde{w}_h)_{\widetilde{T}} - (f_j, \mathcal{C}_X \widetilde{w}_h)_T\right| \leq C h_T \|\widetilde{w}_h\|_{L^1(\widetilde{T})} \leq C h_T^2 \|\widetilde{w}_h\|_{0,\widetilde{T}}.$$

□

The above considerations allow us to conclude

$$\|u - u_h'\|_X \leq C \max_{j=1,\dots,N_\Omega} h_j, \tag{2.66}$$

if the exact solution u satisfies $u \in H_0^1(\Omega) \cap \prod_{j=1}^{N_\Omega} H^2(\Omega^j)$.

It remains to estimate the error in the Lagrange multiplier. Here, we proceed as in Section 2.3.1.

Theorem 2.20. *Let u be the weak solution of (1.1), and assume that $\lambda \in M$ is defined by (2.6). The error of the Lagrange multiplier is bounded by*

$$\|\lambda - \lambda_h'\|_{M^0} \leq C \left(\inf_{\widetilde{\mu}_h \in \widetilde{M}_h} \|\lambda - \widetilde{\mu}_h\|_{M^0} + \|u - u_h'\|_X + (1 + \|u\|_X) \max_{1 \leq j \leq N_\Omega} h_j \right)$$

Proof. The proof follows the lines of the proof of Proposition 2.13. We have the discrete inf-sup condition (2.42). The approximation $u_h' = \mathcal{C}_X u_h$ and the discrete Lagrange multiplier $\lambda_h' = \mathcal{C}_M \lambda_h$ satisfy by (2.54) for arbitrary $\widetilde{\mu}_h \in \widetilde{M}_h$ and $v \in \widetilde{X}_h \cap X_0$

$$\begin{aligned}
b(v, \widetilde{\mu}_h - \lambda_h') &= b(v, \widetilde{\mu}_h - \lambda) + b(v, \lambda - \lambda_h') \\
&= b(v, \widetilde{\mu}_h - \lambda) + l(v) - l_h(\mathcal{C}_X v) + a(u, v) - a_h'(u_h', v) \\
&\leq C \|v\|_{X_0} \left(\max_{1 \leq j \leq N_\Omega} h_j + \|\lambda - \widetilde{\mu}_h\|_{M^0} + \|u - u_h'\|_X \right. \\
&\left. + \frac{a(u_h', v) - a_h'(u_h', v)}{\|v\|_{X_0}} \right) \\
&\leq C \|v\|_{X_0} \left((1 + \|u_h'\|_X) \max_{1 \leq j \leq N_\Omega} h_j + \|\lambda - \widetilde{\mu}_h\|_{M^0} + \|u - u_h'\|_X \right).
\end{aligned}$$

The triangle inequality allows us then to estimate $\|u_h'\|_X \leq \|u - u_h'\|_X + \|u\|_X$. Finally, from the discrete inf-sup condition (2.42), arguments as in the proof of Proposition 2.13, Lemmas 2.17, 2.19 yield the desired result. □

We are now able to provide an a priori estimate for the discretization error of the solution from the original discrete problem (2.20).

Theorem 2.21. *Let $u \in H^2(\Omega)$ be the weak solution of (1.1), and assume that $\lambda \in M$ is defined by (2.6). Assume that (u_h, λ_h) are given by (2.20). Then*

$$\|u - u_h\|_{X_h} + \|\lambda - \mathcal{S}_M \lambda_h\|_{M^0} \leq C(u) \max_{1 \leq j \leq N_\Omega} h_j. \tag{2.67}$$

If u is only subdomain-wise regular, i.e., $u \in \Pi_{j=1}^{N_\Omega} H^2(\Omega^j)$, the first term in (2.67) has to be replaced by $\|u - \mathcal{S}_X u_h\|_X$.

Proof. We first consider the error in the primal variable u. As before, let $\widetilde{\mathcal{I}}_h$ and $\mathcal{I}_h$ indicate the global nodal interpolation operators on $\widetilde{X}_h$ and X_h, respectively. We have

$$\|u - u_h\|_{X_h} \;\leq\; \|u - \mathcal{I}_h u\|_{X_h} \;+\; \|u_h - \mathcal{I}_h u\|_{X_h},$$

where the first term can be bounded appropriately by the right hand side of (2.67). For the second term, we observe that $\widetilde{\mathcal{I}}_h = \mathcal{S}_X \mathcal{I}_h$. Moreover, owing to (2.49), it can be easily seen that $\|v_h\|_{X_h} \sim \|\mathcal{S}_X v_h\|_X$, $v_h \in X_h$. This yields

$$\begin{aligned} \|u_h - \mathcal{I}_h u\|_{X_h} \;&\leq\; C\|\mathcal{S}_X(u_h - \mathcal{I}_h u)\|_X \;=\; C\|u_h' - \widetilde{\mathcal{I}}_h u\|_X \\ &\leq\; C\left(\|u - \widetilde{\mathcal{I}}_h u\|_X + \|u - u_h'\|_X\right). \end{aligned}$$

Again, the first term poses no difficulty. Concerning the second term, we can use Lemmas 2.16–2.19 and obtain the desired bound from (2.56). For the error in the Lagrange multiplier, we observe that $\mathcal{S}_M \lambda_h = \lambda_h'$, and use Proposition 2.20 in combination with the best approximation property (2.34) of $\widetilde{M}_h$. A similar reasoning yields the result for $u \in \Pi_{j=1}^{N_\Omega} H^2(\Omega^j)$. □

2.4 Discrete Lagrange Multiplier Spaces

So far, we have been quite vague about the explicit definition of the discrete Lagrange multiplier space M_h, and only worked with the properties listed in Assumption 2.1. In this section, we introduce concrete spaces for the Lagrange multipliers. Focusing on dual basis functions, we extend this concept to arbitrary quadrilateral surface grids.

2.4.1 Standard and Dual Multipliers

The discrete problem (2.20) can be written as

$$\begin{pmatrix} A_{\mathrm{ii}} & A_{\mathrm{im}} & A_{\mathrm{is}} & 0 \\ A_{\mathrm{mi}} & A_{\mathrm{mm}} & A_{\mathrm{ms}} & -M^{\mathrm{T}} \\ A_{\mathrm{si}} & A_{\mathrm{sm}} & A_{\mathrm{ss}} & D^{\mathrm{T}} \\ 0 & -M & D & 0 \end{pmatrix} \begin{pmatrix} u_h^{\mathrm{i}} \\ u_h^{\mathrm{m}} \\ u_h^{\mathrm{s}} \\ \lambda_h \end{pmatrix} = \begin{pmatrix} f^{\mathrm{i}} \\ f^{\mathrm{m}} \\ f^{\mathrm{s}} \\ 0 \end{pmatrix}, \tag{2.68}$$

where the subscripts i, m, and s represent the inner, master and slave nodes, respectively. We emphasize that the subscript m also includes the degrees of freedom associated with the cross-points of the slave-side mesh, resulting in the possibly non-zero matrices A_{ms} and A_{sm}. According to the definition of the coupling bilinear form $b_h(\cdot,\cdot)$ in (2.16), the entries of the coupling matrices M and D are assembled from integrals of the form

$$(P_{\mathrm{s}(i)}\phi_p^{\mathrm{m}}, \mu_q)_{\Gamma_{i,h}^{\mathrm{s}}}, \quad \text{and} \quad (\phi_p^{\mathrm{s}}, \mu_q)_{\Gamma_{i,h}^{\mathrm{s}}}, \tag{2.69}$$

respectively, where ϕ_p^k, $k = \mathrm{m}, \mathrm{s}$, denotes the scalar nodal basis function of the trace space $W_h^k = X_h^k|_{\Gamma_{i,h}^{\mathrm{s}}}$ of the finite element space on $\mathcal{T}^k$ associated with the node p, and μ_q stands

for the scalar basis function of the discrete Lagrange multiplier space M_h associated with the node q. We speak of *standard* Lagrange multipliers, if $M_h = W_h^{\mathrm{s}}$ and $\mu_q = \phi_q^{\mathrm{s}}$ for all slave nodes q. As already introduced in (1.24), we indicate by *dual* Lagrange multipliers the space $M_h = \operatorname{span}\{\mu_q,\, q \in \mathcal{V}^{\mathrm{s}}\}$ spanned by the basis functions μ_q satisfying the biorthogonality relation

$$(\phi_p^{\mathrm{s}}, \mu_q)_{\Gamma_{i,h}^{\mathrm{s}}} = \delta_{pq}(1, \phi_p^{\mathrm{s}})_{\Gamma_{i,h}^{\mathrm{s}}}. \tag{2.70}$$

From (2.70), it is obvious that the use of dual multipliers results in a diagonal matrix D. As it already has been carried out in Section 1.3, this fact may crucially improve the efficiency of algorithms for the solution of (2.68).

The construction of higher order basis functions with local support satisfying (2.70) may be a tedious or even impossible task, [80]. Throughout this thesis, we focus on the lowest order case. In 2D, as well as in 3D for simplices and parallelograms, the lowest order dual basis functions are well established, [120]. In particular, on a slave edge $[s_1, s_2]$, the basis functions μ_1 and μ_2 associated with the nodes s_1 and s_2, respectively, are given by

$$\mu_1 = 2\phi_1^{\mathrm{s}} - \phi_2^{\mathrm{s}}, \text{ and } \mu_2 = 2\phi_2^{\mathrm{s}} - \phi_1^{\mathrm{s}}. \tag{2.71}$$

On a simplicial slave side element $[s_1, s_2, s_3]$ in three dimensions, the basis functions μ_1, μ_2, and μ_3 associated with the nodes s_1, s_2, and s_3, respectively, are given by

$$\mu_1 = 3\phi_1^{\mathrm{s}} - \phi_2^{\mathrm{s}} - \phi_3^{\mathrm{s}},\ \mu_2 = 3\phi_2^{\mathrm{s}} - \phi_1^{\mathrm{s}} - \phi_3^{\mathrm{s}},\ \text{and } \mu_3 = 3\phi_3^{\mathrm{s}} - \phi_1^{\mathrm{s}} - \phi_2^{\mathrm{s}}.$$

In case of parallelograms, the basis functions can be simply constructed by considering the tensor product of the situation in two dimensions. In particular, if the parallelogram is given by the vertices $[s_1, s_2, s_3, s_4]$, with s_1 and s_3 being opposite, the basis function μ_1 associated the node s_1 can be defined as

$$\mu_1 = 4\phi_1^{\mathrm{s}} - 2\phi_2^{\mathrm{s}} + \phi_3^{\mathrm{s}} - 2\phi_4^{\mathrm{s}},$$

and the remaining ones are constructed in a symmetric manner. However, the situation is more involved in the case of arbitrary quadrilateral surface grids. We address this topic in the following section.

2.4.2 Dual Multipliers on General Quadrilaterals

We extend the lowest order dual Lagrange multipliers to arbitrary quadrilaterals. We focus on planar interfaces and scalar model equations and remark that the extension to curvilinear interfaces and the vectorial case is straightforward. For the moment, we focus on one planar interface Γ, and ignore any potential necessity for modifications on $\partial\Gamma$. However, we allow that the interface grids $\mathcal{T}^{\mathrm{m}}$ and $\mathcal{T}^{\mathrm{s}}$ consist of general non-degenerate convex quadrilaterals or triangles. In case of parallelograms or triangles, the following considerations reduce to the already known standard case. The discrete Lagrange multiplier space M_h is simply defined as the span of all nodal basis functions

μ_p^g, where p is a vertex of the slave side grid. As usual, each basis function μ_p^g is defined element-wise as

$$\mu_p^g = \sum_{T \in \mathcal{T}^p} \mu_{p,T} \tag{2.72}$$

with local supports $\mathcal{T}^p = \{T \in \mathcal{T}^s : p \text{ is a vertex of } T\}$ for μ_p^g and T for $\mu_{p,T}$. Here and in the sequel, we will abuse the notation and indicate by p either a global vertex of the triangulation or a local node number within an element T, depending on the context. Moreover, we will usually write μ_p instead of $\mu_{p,T}$ when there is no ambiguity involved. It is sufficient for the dual approach that the local multiplier functions μ_p satisfy a biorthogonality relation with the element basis functions ϕ_q^s of the trace space $W_h^s = X_h^s|_\Gamma \cap H_0^1(\Gamma)$, namely,

$$(\mu_p, \phi_q^s)_T \;=\; \delta_{pq}(1, \phi_q^s)_T. \tag{2.73}$$

As usual, the integration of the left side of (2.73) is performed via a transformation to the reference element $\widehat{T}$. For a simplex T, the corresponding reference element $\widehat{T}$ is the triangle with vertices $(0,0)$, $(1,0)$, $(0,1)$, while for quadrilaterals, $\widehat{T}$ is set to be the unit square $(0,1)^2$. We remark that, within the considered setting, it is not sufficient to simply choose the Lagrange multiplier μ_p as $\widehat{\mu}_p \circ F_T^{-1}$ with $F_T : \widehat{T} \to T$ the element mapping and $\widehat{\mu}_p$ respecting a biorthogonality relation with the shape functions $\widehat{\phi}_q^s$ on the reference element $\widehat{T}$. This is due to the fact that, for quadrilaterals, F_T is not necessarily an affine, i.e. $\mathbb{P}_1$-mapping, but an isoparametric $\mathbb{Q}_1$-mapping. This yields a surface element $\mathrm{d}T = |\det F_T'|\mathrm{d}\widehat{T}$ with a linear contribution $\det F_T'$, where F_T' indicates the Jacobian of F_T. We note that the expression $\det F_T'$ abuses the notation since F_T maps from $\widehat{T} \subset \mathbb{R}^2$ to $\mathbb{R}^3$, and the Jacobian F_T' is not a square matrix. To be more specific, when F_T is written as $(u,v) \mapsto (x,y,z) = F_T(u,v)$, then we set $\det F_T' = \sqrt{EG - H^2}$, according to [29, (8.152c)], with

$$\begin{aligned} E &= (\partial x/\partial u)^2 + (\partial y/\partial u)^2 + (\partial z/\partial u)^2, \\ G &= (\partial x/\partial v)^2 + (\partial y/\partial v)^2 + (\partial z/\partial v)^2, \\ H &= (\partial x/\partial u)(\partial x/\partial v) + (\partial y/\partial u)(\partial y/\partial v) + (\partial z/\partial u)(\partial z/\partial v). \end{aligned}$$

Transforming the required integral to the reference element, we obtain

$$(\mu_p, \phi_q^s)_T \;=\; (\widehat{\mu}_p, \widehat{\phi}_q^s |\det F_T'|)_{\widehat{T}}, \tag{2.74}$$

from which we obviously cannot expect that (2.73) is satisfied. In what follows, we will provide two alternative ways of defining M_h, both yielding (2.73). The first approach relies on the solution of local subproblems on each element, whereas the second one uses a special transformation to eliminate $|\det F_T'|$ from (2.74).

Local Subproblems

We indicate by D_T and $M_T \in \mathbb{R}^{n_s \times n_s}$ the diagonal matrix and the element mass matrix, respectively, with entries given by

$$d_{pp} = (1, \phi_p^s)_T, \qquad m_{pq} = (\phi_p^s, \phi_q^s)_T. \tag{2.75}$$

With $A_T = D_T M_T^{-1}$, we define

$$\mu_{p,T} = \sum_q a_{pq} \phi_q^{\mathrm{s}}, \tag{2.76}$$

and obtain the biorthogonality (2.73) by

$$(\mu_{p,T}, \phi_q^{\mathrm{s}})_T = \sum_k a_{pk} m_{kq} = (A_T M_T)_{pq} = d_{pq} = \delta_{pq} (1, \phi_q^{\mathrm{s}})_T.$$

Above and in the sequel, we always assume that the summation index runs from 1 to n_{s}, the number of element vertices, unless another index set is given. We especially focus on quadrilateral surface grids, i.e., $n_{\mathrm{s}} = 4$. For simplicial grids, the following considerations are also valid and reduce to already well known results. We continue by showing that the global space M_h constructed above satisfies Assumption 2.1.

Lemma 2.22. *Let M_h be constructed from (2.72) and (2.76). Then M_h satisfies Assumption 2.1(a), i.e., $\mathbb{P}_0 \subset M_h$.*

Proof. Denoting by $\mathcal{V}^{\mathrm{s}}$ the set of vertices of $\mathcal{T}^{\mathrm{s}}$, and by $\mathbf{1} \in \mathbb{R}^{n_{\mathrm{s}}}$ the vector of unity, we observe that

$$\sum_{p \in \mathcal{V}^{\mathrm{s}}} \mu_p^g|_T = \sum_p \mu_p = \sum_{p,q} a_{pq} \phi_q^{\mathrm{s}} = \sum_q (A_T^{\mathrm{T}} \mathbf{1})_q \phi_q^{\mathrm{s}} = \sum_q (M_T^{-1} D_T \mathbf{1})_q \phi_q^{\mathrm{s}}. \tag{2.77}$$

A simple calculation reveals that $M_T^{-1} D_T \mathbf{1} = \mathbf{1}$, namely for $b = M_T^{-1} D_T \mathbf{1} - \mathbf{1}$, we have that

$$(M_T b)_p = (D_T \mathbf{1} - M_T \mathbf{1})_p = (1, \phi_p^{\mathrm{s}})_T - \left(\phi_p^{\mathrm{s}}, \sum_q \phi_q^{\mathrm{s}} \right)_T = 0,$$

thus, $M_T b = 0$ yielding $b = 0$. From (2.77), we get that

$$\sum_{p \in \mathcal{V}^{\mathrm{s}}} \mu_p^g|_T = \sum_q \mathbf{1}_q \phi_q^{\mathrm{s}} = \sum_q \phi_q^{\mathrm{s}} = 1,$$

which concludes the proof. □

By using Lemma 2.22, it can be easily shown that M_h satisfies an approximation property. In fact, if the biorthogonality relation (2.70) is satisfied, the approximation property can be shown to be equivalent to $\mathbb{P}_0 \subset M_h$. For completeness, we repeat a proof here, see [122, Lemma 1.12].

Lemma 2.23. *Let M_h be constructed from (2.72) and (2.76). Then M_h satisfies Assumption 2.1(b), namely, it holds that*

$$\inf_{\mu_h \in M_h} \|v - \mu_h\|_{0,\Gamma} \;\leq\; C h_{\mathrm{s}}^{1/2} |v|_{1/2,\Gamma}, \qquad v \in H^{1/2}(\Gamma).$$

Proof. For any given $v \in H^{1/2}(\Gamma)$, define $\mu_v \in M_h$ by $\mu_v = \sum_{p\in\mathcal{V}^s} \alpha_p(v)\mu_p$ with

$$\alpha_p(v) = \frac{(v,\phi_p^s)_\Gamma}{(1,\phi_p^s)_\Gamma}, \qquad p \in \mathcal{V}^s.$$

By construction, we observe that $\alpha_p^2(v)\|\mu_p\|_{0,\Gamma}^2 \le C\|v\|_{0,\,\mathrm{supp}\,\phi_p^s}^2$. Using the locality of the supports of the basis functions μ_p and ϕ_p^s, we obtain for each surface element $T \in \mathcal{T}^s$

$$\|\mu_v\|_{0,T}^2 \;\le\; C \sum_{p,\; T\cap \mathrm{supp}\,\mu_p\neq\emptyset} \alpha_p^2(v)\|\mu_p\|_{0,\Gamma}^2 \;\le\; C \sum_{p,\; T\cap \mathrm{supp}\,\mu_p\neq\emptyset} \|v\|_{0,\,\mathrm{supp}\,\phi_p^s}^2 \le C\|v\|_{0,\,\omega_T}^2,$$

where ω_T contains a uniformly bounded number of surface elements. By Lemma 2.22, namely by the fact that $\mathbb{P}_0 \subset M_h$, we have that $\mu_v = v$ for $v \in \mathbb{P}_0$. This yields

$$\begin{aligned}\|v-\mu_v\|_{0,T} \;&\le\; \|v-\Pi_0 v\|_{0,T} + \|\mu_{v-\Pi_0 v}\|_{0,T}\\ &\le\; C\|v-\Pi_0 v\|_{0,\omega_T} \;\le\; Ch_{\omega_T}^{1/2}|v|_{1/2,\omega_T},\end{aligned}$$

where Π_0 denotes the locally defined L^2-projection onto $\mathbb{P}_0$. Summing up and using the locality of ω_T gives the desired result. □

The biorthogonality (2.70) is enough to show that the stability assumption (2.9b) is satisfied, which is one of the essential conditions for proving the approximation property of the constrained space (2.38).

Lemma 2.24. *Let $M_h = \mathrm{span}\{\mu_q,\, q \in \mathcal{V}^s\}$ with $\mu_q \in L^2(\Gamma)$ satisfying (2.73), and let the mortar projection Π_h be given by*

$$(v,\mu)_\Gamma = (\Pi_h v,\mu)_\Gamma, \qquad \mu \in M_h.$$

Then, the projection $\Pi_h : L^2(\Gamma) \to W_h^s$ satisfies Assumption 2.1(c), namely, Π_h is uniformly bounded in $L^2(\Gamma)$ as well as in $H_{00}^{1/2}(\Gamma)$.

Proof. We follow the presentation in [80]. First, we prove an inf-sup condition relating the spaces M_h and W_h^s, namely,

$$\inf_{\mu\in M_h}\sup_{v\in W_h^s} \frac{(v,\mu)_\Gamma}{\|v\|_{0,\Gamma}\|\mu\|_{0,\Gamma}} \ge \beta, \tag{2.78}$$

with $\beta > 0$. Given $\mu = \sum_p \alpha_p\mu_p \in M_h$, set $v = \sum_p \alpha_p\phi_p \in W_h^s$. By the norm equivalence (A.26), we have $\|v\|_{0,\Gamma}^2 \sim \|\mu\|_{0,\Gamma}^2 \sim h^{d-1}\sum_p \alpha_p^2$. This yields, together with the biorthogonality (2.73),

$$(v,\mu)_\Gamma = \sum_{T^s}\sum_{p,q} = \alpha_p\alpha_q(\phi_p,\mu_q)_{0,T} = \sum_p \alpha_p^2(1,\phi_p)_{0,T} \ge C\sum_p h^{d-1}\alpha_p^2 \ge \beta\|v\|_{0,\Gamma}\|\mu\|_{0,\Gamma},$$

thus, (2.78) holds. Given $v \in L^2(\Gamma)$, define $(w,\varphi) \in W_h^s \times M_h$ to be the solution of the saddle point problem

$$(w,z)_\Gamma + (\varphi,z)_\Gamma = (v,z)_\Gamma, \quad z \in W_h^s, \tag{2.79a}$$
$$(w,\mu)_\Gamma \qquad\qquad = (v,\mu)_\Gamma, \quad \mu \in M_h. \tag{2.79b}$$

By standard theory as presented in Theorem A.23, problem (2.79) has a unique solution (w, φ) under the condition (2.78), satisfying $\|w\|_{0,\Gamma} \leq (1 + 2\beta^{-1})\|v\|_{0,\Gamma}$. From (2.79b), it follows that $w = \Pi_h v$. Thus, the L^2-stability is proved.

We next show stability in $H_0^1(\Gamma)$. We employ a Scott–Zhang type interpolation operator $P_h : H_0^1(\Gamma) \to W_h^{\mathrm{s}}$, [109], with properties

$$h^{-1}\|v - P_h v\|_{0,\Gamma} \leq C\|w\|_{1,\Gamma}, \quad \text{and} \quad \|P_h\|_{1,\Gamma} \leq C\|w\|_{1,\Gamma}.$$

Using these properties, the fact that Π_h is an L^2-stable projection onto W_h^{s}, and the inverse inequality (A.28), we obtain

$$\begin{aligned}
\|\Pi_h v\|_{1,\Gamma} &\leq \|\Pi_h v - P_h v\|_{1,\Gamma} + \|P_h v\|_{1,\Gamma} \\
&\leq Ch^{-1}\|\Pi_h(v - P_h v)\|_{0,\Gamma} + \|P_h v\|_{1,\Gamma} \\
&\leq Ch^{-1}\|v - P_h v\|_{0,\Gamma} + \|v\|_{1,\Gamma} \\
&\leq C\|v\|_{1,\Gamma}.
\end{aligned}$$

The stability in $H_{00}^{1/2}(\Gamma)$ follows from interpolations arguments, [26, Thm. 12.1.5]. □

We note that the entries of the global coupling matrix M can be easily assembled by the local contributions of $(M_{\mathrm{sm}})_{pq} = (\phi_p^{\mathrm{s}}, \phi_q^{\mathrm{m}})_{T^{\mathrm{sm}}}$, where T^{sm} denotes the intersection of a slave and a master element. Formally, this gives

$$M = \sum_{T^{\mathrm{sm}} = T^{\mathrm{s}} \cap T^{\mathrm{m}}} R_{T^{\mathrm{s}}} D_{T^{\mathrm{s}}} M_{T^{\mathrm{s}}}^{-1} M_{\mathrm{sm}} R_{T^{\mathrm{m}}}^{\mathrm{T}},$$

where R_{T^k} denotes the matrix which maps the local node numbers of the element T^k to the global ones with respect to $\mathcal{T}^k$, $k = \mathrm{m}, \mathrm{s}$.

Special Transformation

In the previous subsection, a local mass matrix has to be inverted on each element for the construction of the dual Lagrange multipliers. Here, we introduce an alternative procedure for deriving them. They are given in terms of a special transformation from the reference element, namely, by

$$\mu_{p,T} = \frac{w_p}{|\det F_T'|} \widehat{\mu}_p \circ F_T^{-1}, \tag{2.80}$$

with a weighting factor $w_p = (1, \phi_p^{\mathrm{s}})_T / (1, \widehat{\phi}_p^{\mathrm{s}})_{\widehat{T}}$. In case of an affine element transformation F_T, the factors $w_p / |\det F_T'|$ are equal to 1, and the approach reduces to the original one. As before, the construction almost immediately implies (2.73) by observing that

$$(\mu_{p,T}, \phi_q^{\mathrm{s}})_T = w_p (\widehat{\mu}_p, \widehat{\phi}_q^{\mathrm{s}})_{\widehat{T}} = \delta_{pq} (1, \phi_p^{\mathrm{s}})_T.$$

Again, we verify the approximation property of M_h by showing that it contains the constants.

Lemma 2.25. *Let M_h be constructed from (2.72) and (2.80). Then $\mathbb{P}_0 \subset M_h$.*

Proof. We take $\mu = \sum_{p\in\mathcal{V}^s} \mu_p^q|_T = \sum_p \mu_p$. We first consider the fact that

$$\mu = 1 \Leftrightarrow \widehat{\mu} = 1 \text{ with } \widehat{\mu} = \mu \circ F_T = \sum_p \frac{w_p}{|\det F_T'|}\widehat{\mu}_p.$$

Moreover, elementary calculations reveal that both $|\det F_T'|\widehat{\mu}$ and $|\det F_T'|$ are $Q1$-functions. We can verify the assertion by showing that $|\det F_T'|\widehat{\mu} = |\det F_T'|$, which is in this case equivalent to the requirement that

$$I = \left(|\det F_T'|\widehat{\mu} - |\det F_T'|,\, \widehat{\phi}_q^{\mathrm{s}}\right)_{\widehat{T}} = 0, \quad q = 1, \ldots, n_{\mathrm{s}}.$$

Using the biorthogonality on $\widehat{T}$ and the definition of the weights w_p, we obtain

$$I \;=\; \sum_p w_p(\widehat{\mu}_p, \widehat{\phi}_q^{\mathrm{s}})_{\widehat{T}} - (\widehat{\phi}_q^{\mathrm{s}}, |\det F_T'|)_{\widehat{T}} = 0,$$

which concludes the proof. □

We remark that the implementation of the coupling matrix M does not require the inverse of a local mass matrix. It can be carried out by transferring μ_p and ϕ_q^{m} onto the reference element, i.e.,

$$(\mu_p, \phi_q^{\mathrm{m}})_{T^{\mathrm{sm}}} = w_p(\widehat{\mu}_p, \phi_q^{\mathrm{m}} \circ F_T)_{\widehat{T}^{\mathrm{sm}}}.$$

2.5 Implementational Details

In what follows, we give a more detailed account of the assembly of the coupling matrices defined in (1.23). Omitting the subscripts p and q in (2.69), we have to evaluate the integral

$$(P_{\mathrm{s}}\phi^{\mathrm{m}},\, \mu^{\mathrm{s}})_{\Gamma_h^{\mathrm{s}}} \tag{2.81}$$

for all basis functions μ^{s} and ϕ^{m} defined on the $(d-1)$-dimensional grids $\mathcal{T}^{\mathrm{s}}$ and $\mathcal{T}^{\mathrm{m}}$ inherited from the grids on Ω^{s} and Ω^{m}, respectively. As usual, the assembly can be performed element-wise. One possible realization is given by Algorithm 1. We remark that the naive implementation of this algorithm for 2D-problems is of order $O(n)$, but for 3D-problems it is of order $O(n^{4/3})$ with n denoting the total number of unknowns. However, it is possible to obtain a better complexity in both cases by incorporating neighborship relations of the surface elements and/or inheritance relations from an underlying geometrical multigrid hierarchy.

The crucial point in Algorithm 1 is the determination of the intersection area of two elements from the different grids. In the remainder of this section, we will address this issue for different situations.

Algorithm 1 Assembly of the coupling matrix

```
for all slave elements T_i^s, i = 1, ..., n_s do
  for all master elements T_j^m, j = 1, ..., n_m do
    determine intersection area T^sm = T_i^s ∩ T_j^m
    if T^sm ≠ ∅ then
      for all basis functions φ^m, μ^s with support ∩ T^sm ≠ ∅ do
        add (φ^m, μ^s)_{T^sm} to M
      end for
    end if
  end for
end for
```

2.5.1 Planar Interfaces

In order to determine whether two surface elements T^{s} and T^{m} intersect, we loop over all vertices p_k^{m}, $k = 1, \ldots, n_v^{\mathrm{m}}$, of T^{m}, where n_v^{m} denotes the corresponding number of vertices. The two elements intersect, if we find at least one vertex p_k^{m} which lies inside T^{s}. An easy way to justify this, is to use the transformation of global to local coordinates, which is usually available in any finite element code. If all local coordinates of p_k^{m} with respect to the element T^{s} are within the correct ranges, the elements T^{s} and T^{m} intersect. Otherwise, it may still be possible that the element T^{s} is completely covered by the element T^{m}. Therefore, one has to repeat the procedure interchanging the roles of T^{s} and T^{m}. If still no appropriate vertex is found, the two elements do not intersect. In the following, we give a more detailed account of how to determine the area of intersection, divided into considerations for two-dimensional problem settings, three-dimensional structured hexahedral grids, and three-dimensional unstructured tetrahedral meshes.

Two-dimensional Problems

We consider the case that the interface Γ is part of the x-axis. The corner coordinates of T^{s} and T^{m} are denoted by x_ℓ^{s} and x_ℓ^{m}, respectively, $\ell = 1, 2$. We assume that $x_1^{\mathrm{s}} < x_2^{\mathrm{s}}$ and $x_1^{\mathrm{m}} < x_2^{\mathrm{m}}$. The possible four situations and resulting intersections are illustrated in Figure 2.5.

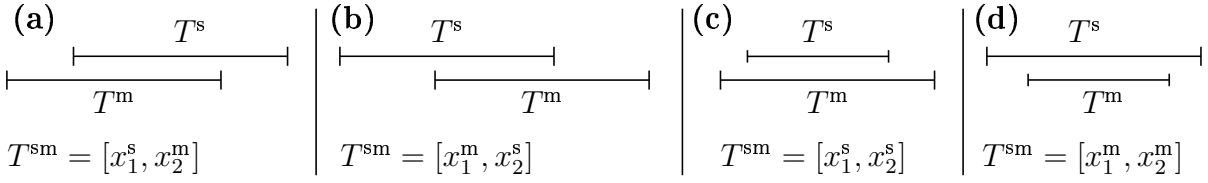

Figure 2.5: 2D: Four situations of intersecting elements T^{s} and T^{m}.

Three-dimensional Structured Hexahedral Grids

We assume that the interface Γ is part of the xy-plane, and that we have axiparallel surface grids $\mathcal{T}_\mathrm{s}$ and $\mathcal{T}_\mathrm{m}$. We describe an axiparallel quadrilateral surface element T^s by its lower left and its upper right corner coordinates as $T^\mathrm{s} = (x^\mathrm{s}_\ell, y^\mathrm{s}_\ell, x^\mathrm{s}_r, y^\mathrm{s}_u)$, analogously for T^m. It is obvious that the intersection of the elements T^s and T^m has to be also an axiparallel quadrilateral. In Figure 2.6, we illustrate two different situations. All other possible situations can be obtained by symmetry observations.

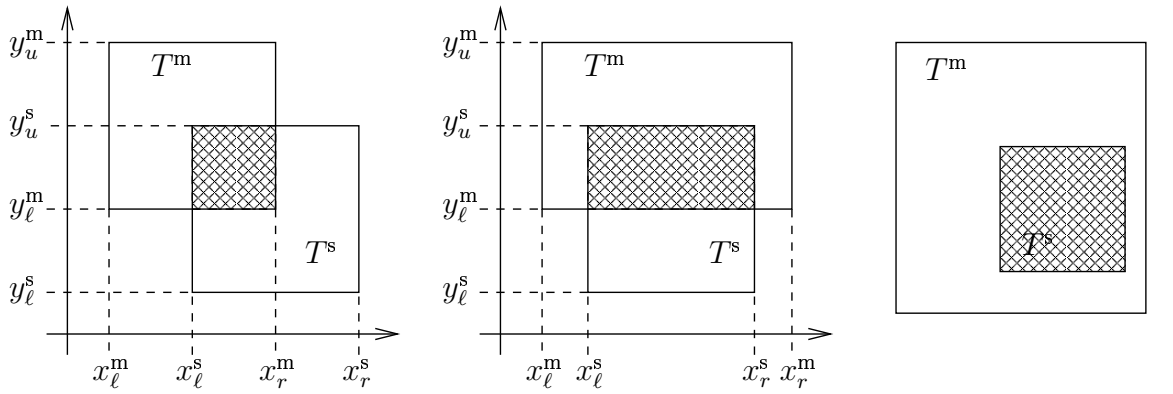

Figure 2.6: 3D structured: Intersecting elements T^s and T^m.

Three-dimensional Tetrahedral Meshes

The intersection of two arbitrary triangles is quite more complex than the situations considered above. In particular, the polygonal intersection T^sm can be anything between a triangle and a 2D-hexahedral, see Figure 2.7. However, the vertices of T^sm can be

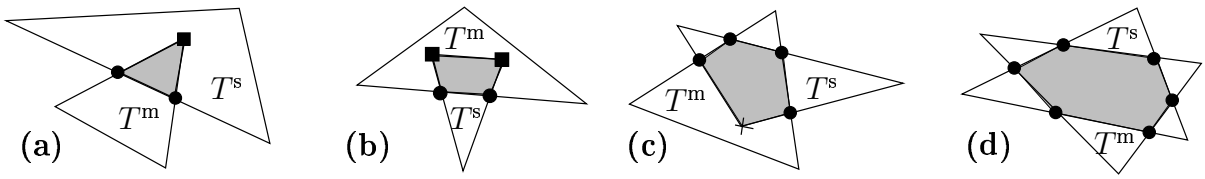

Figure 2.7: 3D unstructured: Intersecting elements T^s and T^m.

determined straightforward by including

- all vertices of T^s lying inside T^m (marked with a cross in Figure 2.7),
- all vertices of T^m lying inside T^s (filled box),
- all intersection points of edges of T^s with edges of T^m (filled circle).

For the evaluation of (2.81), the polygon T^{sm} can be subdivided into triangles by connecting its barycenter with the vertices and applying an appropriate quadrature formula on each subtriangle. Although our presentation focuses on simplices, the above considerations apply for all intersections of convex coplanar polygons.

2.5.2 Curvilinear Interfaces

When dealing with curvilinear interfaces in numerical calculations, often the information about the exact curved interface Γ is lost, and only the computational grids are available. In order to give a meaning to the discrete jump as defined in (2.13), it is important to realize the grid transfer mapping P_{s} by only using the available information from the discrete setting, in contrast to the former definition (2.14). We illustrate possible implementations of P_{s}, first for two and afterwards for three dimensions.

Two Dimensions

The mapping P_{s} can be defined for each slave edge by using the piecewise constant normal projection of the corresponding master edges, as illustrated in Figure 2.8. There, a linear function v_{m} on the master edge $T^{\mathrm{m}} = \{m_1, m_2\}$ is mapped onto the slave edges $T_1^{\mathrm{s}} = \{s_1, s_2\}$ and $T_2^{\mathrm{s}} = \{s_2, s_3\}$. For T_1^{s}, the segment $[m_1, q_1]$ on T^{m} is projected onto $[p_1, s_2]$ (dashed lines), whereas for T_2^{s}, the segment $[q_2, m_2]$ is projected onto $[s_2, p_2]$ (dash-dotted lines). Since $[q_2, q_1]$ is considered twice, the mapped function $P_{\mathrm{s}} v_{\mathrm{m}}$ is discontinuous at the node s_2. Due to this lacking regularity, the a priori results from Section 2.3 cannot be transferred directly. In order to analyze this case, one could decompose P_{s} in a sufficiently smooth part for which the a priori results hold, plus a perturbation, and perform a perturbation analysis in terms of weighted L^2-norms. We will not carry out this analysis in detail, since, for all tested examples, there is only a slight quantitative and no qualitative difference in the error decays compared to using (2.14) for the definition of P_{s}. We provide a numerical comparison of both alternatives in Section 2.6.1.

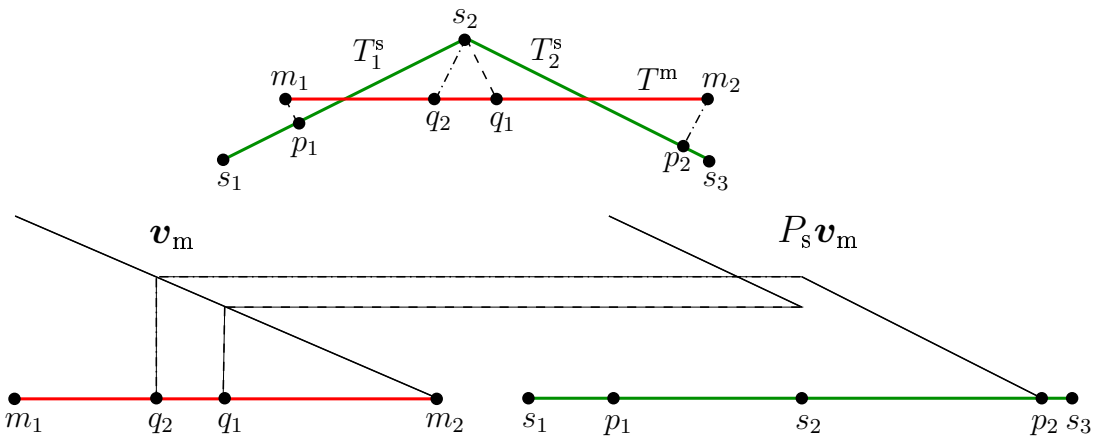

Figure 2.8: Realization of P_{s} via the normal projection onto the slave edges.

Three Dimensions

For curvilinear interior boundaries, the interface grids $\mathcal{T}_s$ and $\mathcal{T}_m$ are both not in any affine hypersurface. In the case of nonconforming grids, this results in the fact that possibly intersecting elements T^s and T^m are not coplanar, see Figure 2.9. One possible way of

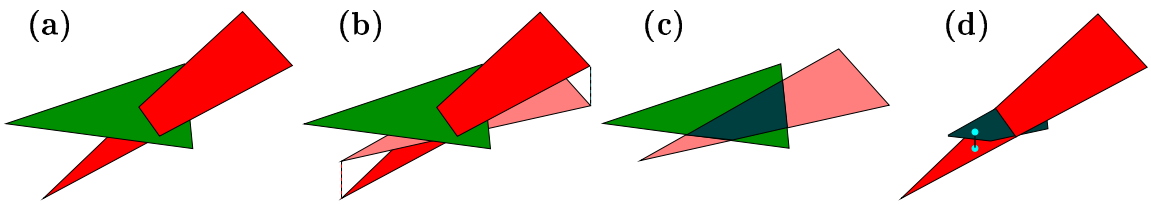

Figure 2.9: 3D curvilinear: Intersecting elements and projection onto one plane.

dealing with this situation in the case of affine-equivalent triangulations is to project the element T^m onto the plane of the element T^s, [97]. Then, the same techniques as described above can be applied in order to determine the intersection T^{sm}. For the evaluation of the basis function ϕ^m, the quadrature points in T^s have to be projected back onto T^s. For more general element transformations, it is possible to perform the intersection by projecting both elements onto an intermediate plane obtained by a least squares approximation.

2.6 Numerical Results

We present various numerical examples. In Subsection 2.6.1, we consider the case of two subdomains sharing one curved interface. In Subsection 2.6.2, a decomposition into eight subdomains with straight as well as curved interfaces is investigated. Moreover, we give numerical evidence of the independence of the constants from the number of subdomains, when we vary the number of subdomains from 4 to 25.

2.6.1 Two Subdomains

In a first test, we consider the case of the domain $\Omega = (0,2) \times (0,1)$ divided into two subdomains Ω^1 and Ω^2 as illustrated in Figure 2.10(a). Dual basis functions with respect to the grid on Ω^2 are used to span the Lagrange multiplier space $\widehat{M}_{1,h}$. We solve the model problem (1.1) with Dirichlet boundary conditions and source term f derived from the exact solution $u(x,y) = x^2 - 2y^2$, starting with the initial triangulation displayed in Figure 2.10(b).

The error decay of the finite element solution u_h, measured in the H^1- and in the L^2-norm, as well as the behavior of the error in the Lagrange multiplier, are plotted in Figure 2.11(a). We note that in order to evaluate the error in the Lagrange multiplier, we substitute the $H^{-1/2}$-norm by $\left(\sum_e h_e \|\lambda - \lambda_h\|_{0,e}^2\right)^{1/2}$, where the sum is taken over all edges e on the slave side of the interfaces, and h_e denotes the length of e. For the H^1-norm, the results are in perfect agreement with the theory presented in Section 2.3.

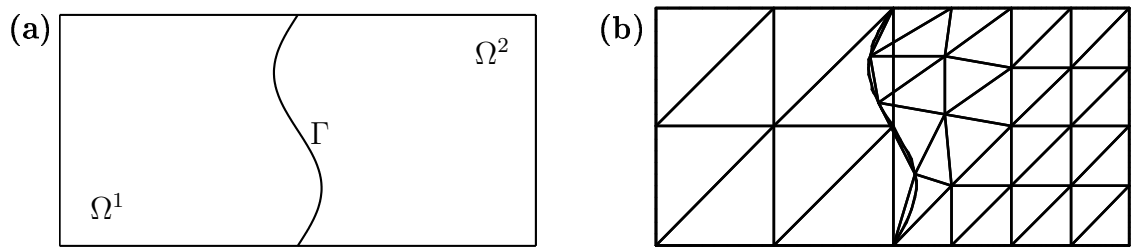

Figure 2.10: (a) decomposition into subdomains Ω^1, Ω^2, (b) initial grid.

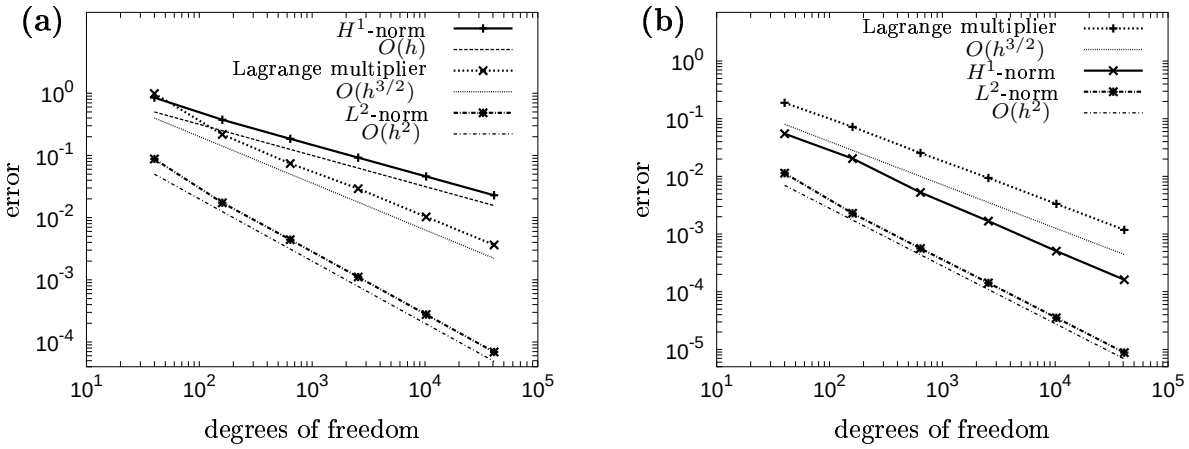

Figure 2.11: Error decays: (a) quadratic solution, (b) linear solution.

Moreover, the numerical convergence order for the Lagrange multiplier is better than predicted from the theory. This can be explained by the following observation. The weighted L^2-norm of the error in the Lagrange multiplier can be bound by the sum of the best approximation error and the discretization error in the H^1-norm restricted to a strip of width h around the interface. Once the solution is $H^{5/2}$-regular, the best approximation error of the Lagrange multiplier space is of order $O(h^{3/2})$. If, moreover, the discretization error can be assumed to be equidistributed over the domain, the overall order $O(h^{3/2})$ can be derived, as is experienced in this example, as well as in the next examples in Section 2.6.2.

An interesting special case is the approximation of a linear solution. In contrast to straight interfaces, the finite element solution does not coincide with the exact one, as pointed out in Remark 2.11. Numerical evidence of this behavior is illustrated in Figure 2.11(b), where the error decays are plotted for the same geometrical setting as before with the exact solution $u(x, y) = y$. The error measured in the H^1-norm is of order $h^{3/2}$ as shown in Remark 2.11.

In a further test, we start from a conforming triangulation consisting of two elements on each subdomain, and refine the right subdomain Ω^2 1 (2, 3) time(s). Thus, a ratio $q_r^l = 2{:}1\,(4{:}1,\ 8{:}1)$ of the number of element edges on the left side of the interface to the number of edges on the right side is obtained. We test the stability of our method choosing first the Lagrange multiplier with respect to the finer (left) grid, and then with respect

to the coarser (right) grid, so that the ratio $q_{\mathrm{m}}^{\mathrm{s}}$ of the number of slave edges to master edges is out of $\{2{:}1, 4{:}1, 8{:}1, 1{:}2, 1{:}4, 1{:}8\}$. In Figure 2.12(a), the error $\lambda - \lambda_h$, measured

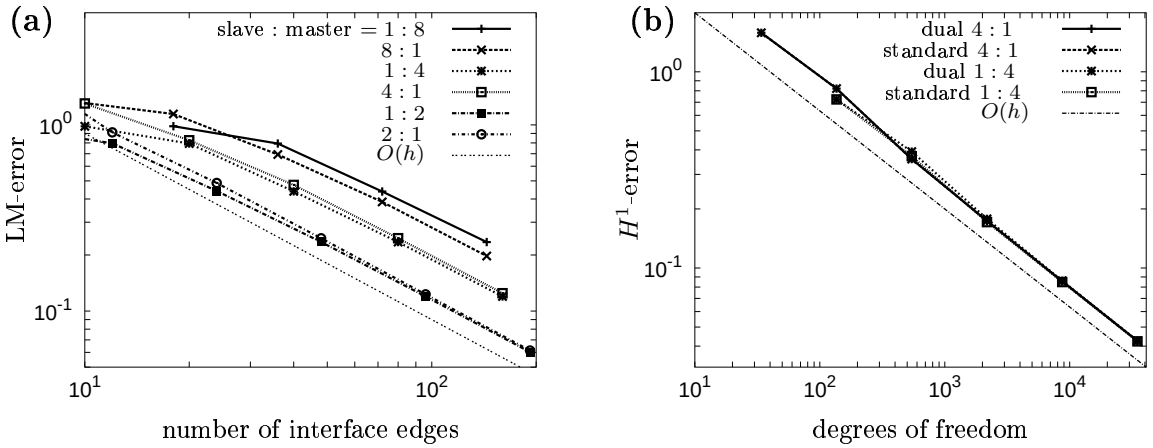

Figure 2.12: Different ratios of the number of slave edges to the number of master edges: (a) error in the Lagrange multiplier λ, (b) error in the solution u.

in the L^2-norm, is plotted against the total number of slave and master edges. Looking at the exact solution, it is not surprising that the error decreases as the ratio $q_{\mathrm{m}}^{\mathrm{s}}$ tends to 1. What is more interesting and demonstrates the stability of our approach, is the very moderate influence of whether to choose the fine grid as master side or the coarse one. Of course, this also depends on the characteristics of the exact solution. Especially in the case of discontinuous coefficients, it might be important to choose the discrete Lagrange multipliers on the correct side. In Figure 2.12(b), we provide a comparison of the H^1-error decays for the ratios $1:4$ and $4:1$, where once, dual Lagrange multipliers are taken, and in the other case, standard Lagrange multipliers are chosen. All approaches yield qualitatively the same and quantitatively almost the same results.

We keep the same setting and test the influence of the projection mapping P_{s} onto our results, once using the exact parametrization and choosing P_{s} as in (2.14), and once realizing P_{s} by projections from the master onto the slave side elements along the slave side normals as discussed in Section 2.5.2. The results for the ratios $q_{\mathrm{m}}^{\mathrm{s}} \in \{1{:}8,\ 8{:}1\}$ are given in Figure 2.13, picture (a) visualizing the decay of the L^2-error in the solution u, and picture (b) depicting the error decay for the Lagrange multiplier λ. For both errors, as well as for the H^1-error in u which is not visualized, the difference between using the exact parametrization or the normal projection is in general negligible. Only for the coarsest grid, the parametrization gives considerably better results for the error in the Lagrange multiplier. We remark that the situation is the same for other ratios $q_{\mathrm{m}}^{\mathrm{s}}$, with even less difference between the two approaches for the other considered cases $q_{\mathrm{m}}^{\mathrm{s}} \in \{1{:}2,\ 2{:}1, 1{:}4,\ 4{:}1\}$.

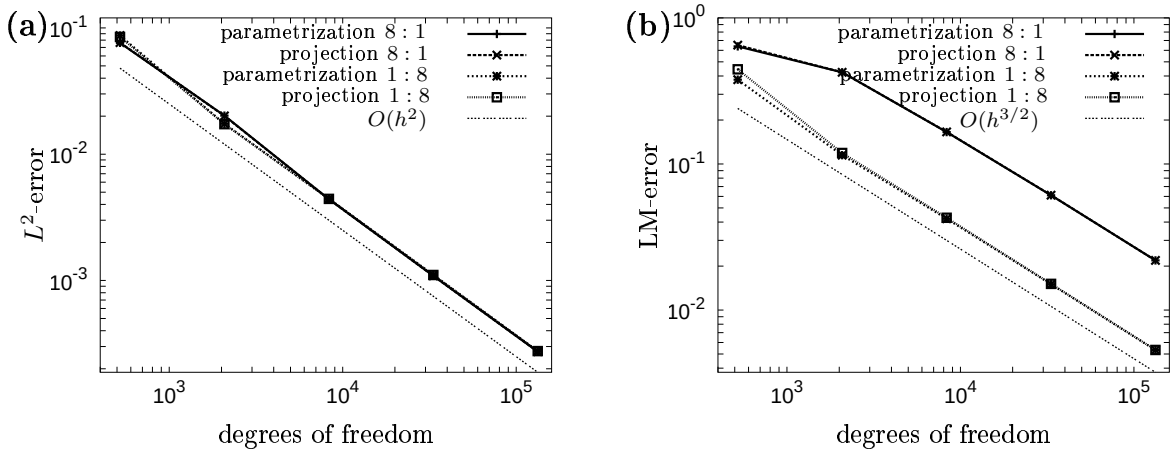

Figure 2.13: Comparing the influence of the mapping P_s: (a) L^2-error in the solution u, (b) error in the Lagrange multiplier λ.

2.6.2 Many Subdomains

We investigate the behavior of our method on the domain $\Omega = (-1, 1)^2$, subdivided into eight subdomains sharing twelve interfaces, four of which are curved, and five cross-points. The exact solution is chosen to be $u(x, y) = (\sin \pi x)(\sin 2\pi y)$. The initial triangulation is displayed in Figure 2.14(a). The Lagrange multiplier spaces are defined with respect to the finer grids, again spanned by the corresponding dual linear basis functions. The various error decays shown in Figure 2.14(b) illustrate the same qualitative behavior as in the case of two subdomains.

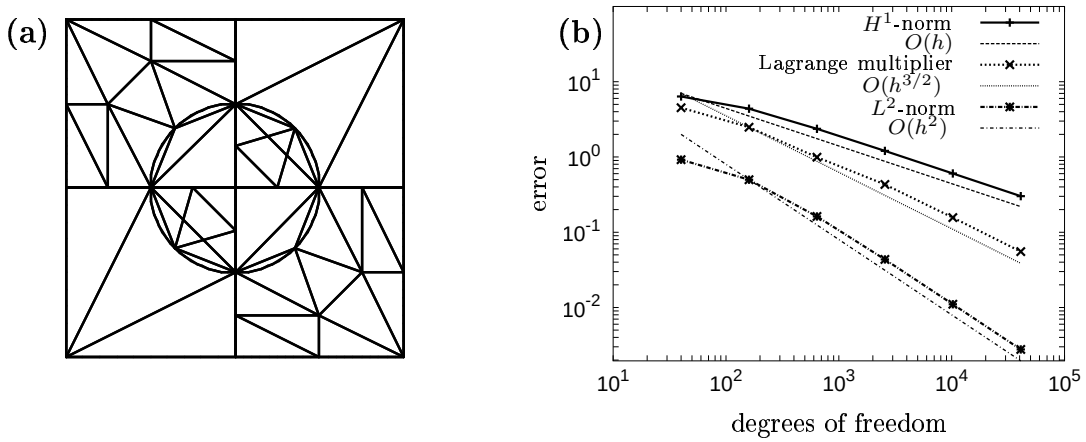

Figure 2.14: Eight subdomains: (a) initial triangulation, (b) error decays.

In the next example, the global domain $\Omega = (0, 1)^2$ is divided into $N_\Omega = 4, 9, 16, 25$ subdomains. Figure 2.15 displays the domain decompositions and the initial triangulations. The discrete Lagrange multiplier spaces are always chosen with respect to the

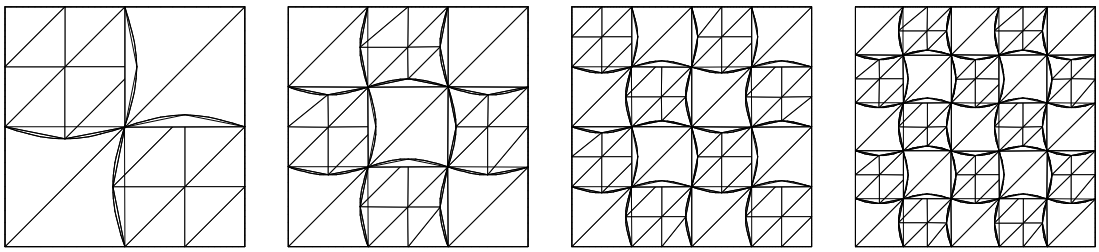

Figure 2.15: Many Subdomains: initial triangulations.

finer triangulations. As exact solution, we use $u(x,y) = \exp(-2((x-0.5)^2+(y-0.5)^2))$. We run a test for each of the decompositions, measuring the error decay under uniform refinement of the triangulations. In Figure 2.16(a), the discretization error measured in the H^1-norm is plotted versus the number of elements. Only very slight differences can be seen between the considered decompositions, which illustrates nicely the independence of the constants appearing in the a priori analysis from the total number of subdomains. In order to achieve comparable results for the error in the Lagrange multiplier, the weighted L^2-norm was divided by the corresponding total length of the interfaces. Also here, it becomes hard to distinguish between the various decompositions, as illustrated in Figure 2.16(b).

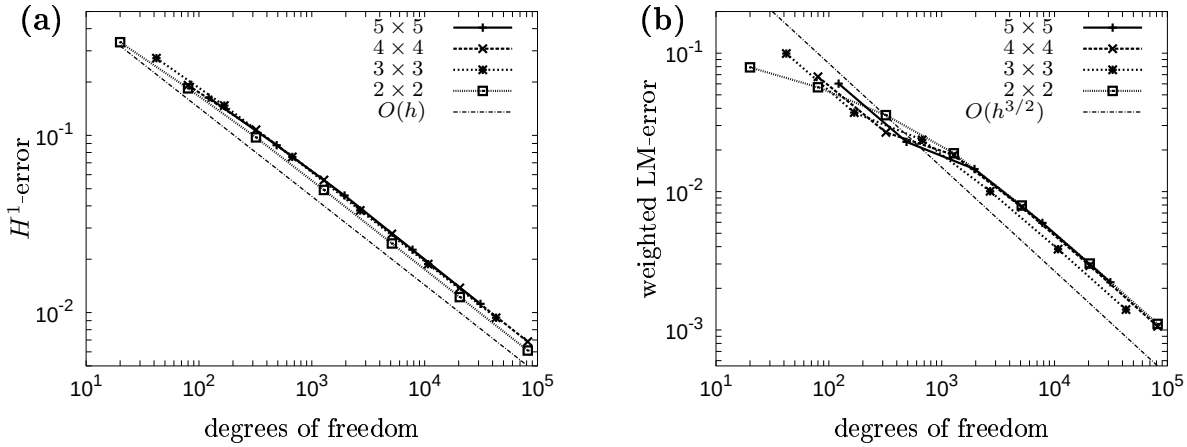

Figure 2.16: Many subdomains: (a) H^1-error, (b) weighted LM-error.

2.6.3 General Quadrilaterals

We now focus on the treatment of interface grids consisting of general quadrilaterals, as discussed in Section 2.4.2. The theoretical results of Section 2.4.2 yield optimal a priori estimates for the error in the broken H^1-norm. Here, we are interested in the quantitative numbers. In addition to the two approaches considered above, we employ two other methods for comparison: one using standard basis functions $\mu_p = \phi_p^s$ not satisfying (2.73), and a "naive" one, where μ_p is chosen as $\widehat{\mu}_p \circ F_T^{-1}$ for the coupling with

the master side, but it is set to be $(|T|/|\det F_T'|)\widehat{\mu}_p \circ F_T^{-1}$ for the coupling with the slave side. We note that the latter approach satisfies (2.73), and coincides with the original dual method for simplices and parallelepipeds. We also point out that by a suitable redefinition of the coupling bilinear form $b(\cdot,\cdot)$, the approach could be reformulated with respect to only one discrete Lagrange multiplier space M_h. The choice is motivated by the fact that nothing has to be modified for the coupling on the master side, and only a minimal modification is necessary for the coupling on the slave side. However, despite its similarity with (2.80), constants are not preserved due to the choice of $|T|$ as weights. Therefore, the approximation property is lost, and optimal convergence cannot be guaranteed anymore.

We consider a simple test example with two cubes Ω^{m} and Ω^{s} of length and width 1 and height 0.2, sharing as interface the unit square of edge length 1 at $z = 0$. We solve (1.1) with right hand side f derived from the exact solution $u(x, y, z) = yz\mathrm{e}^{-x^2}$. On the planes $z = \pm 0.2$, Dirichlet boundary data is considered, while on the remaining part of the boundary, we employ Neumann data. The Lagrange multiplier space M_h is associated with the grid on the lower cube. For the surface meshes $\mathcal{T}^{\mathrm{s}}$ on the slave side, we compare three different sequences as in [6]: square, asymptotically parallelogram, and trapezoidal, see Figure 2.17. For the first two sequences, the initial triangulation is indicated by thick

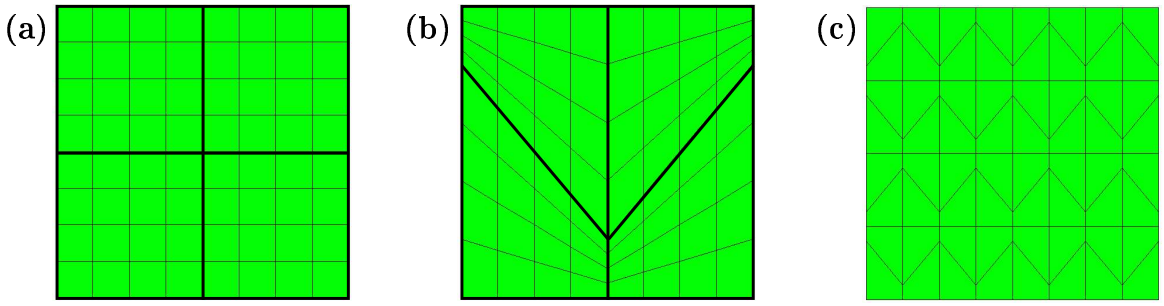

Figure 2.17: Surface grids $\mathcal{T}^{\mathrm{s}}$: (a) square, (b) asymptotically parallelogram, (c) trapezoidal.

lines, and the subsequent grids are simply obtained by uniform refinements. For the trapezoidal grids, the same initial triangulation as for the asymptotically parallelogram grid is used, but instead of employing a standard uniform refinement procedure, the surface is partitioned into congruent trapezoids at each step, all similar to the trapezoid with vertices $(0, 0)$, $(0.5, 0)$, $(0.5, 0.2)$, and $(0, 0.8)$. The thin lines in the pictures of Figure 2.17 indicate the slave side grids after two refinements. On the master side, the meshes $\mathcal{T}^{\mathrm{m}}$ consist of squares twice the size of the elements on the slave side.

In Figure 2.18, the error decays measured in the H^1-norm are plotted for different grid sequences and different Lagrange multipliers. In particular, we compare three approaches: the naive dual one and the ones introduced in Sections 2.4.2 and 2.4.2. For the asymptotically parallelogram grid sequence illustrated in Figure 2.18(a), we choose the results from the uniform square grids as reference. All approaches give qualitatively the same and quantitatively almost the same results. We remark that the same quality is obtained by the use of the standard basis functions. This observation changes drastically

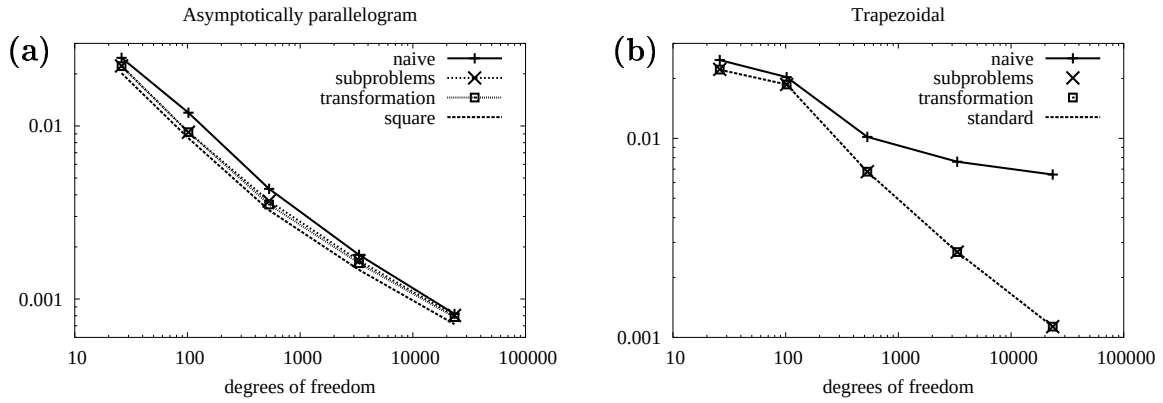

Figure 2.18: Error decays, measured in the H^1-norm: (a) asymptotically parallelogram, (b) trapezoidal.

when employing the sequence of trapezoidal grids, as illustrated in Figure 2.18(b). The naive approach fails completely, the error remains almost static after a few refinement steps. The other two methods behave as predicted by the theory. Moreover, the errors visually coincide with the approach using standard basis functions which is taken as a reference here.

2.6.4 Coupling of Different Model Equations

We consider a global domain consisting of three cylinders $\Omega^{m,1}$, $\Omega^{m,2}$, and Ω^s. Each subdomain is of height 1, the two master subdomains $\Omega^{m,1}$ and $\Omega^{m,2}$ have the unit circle as base, while the slave subdomain Ω^s has as base a circle of radius 0.7 and is placed between the two master subdomains. While Poisson's ratio $\nu = 0.3$ is constant on all subdomains, Young's modulus E is set to be 10^5 on $\Omega^{m,1}$, $\Omega^{m,2}$, and 10^2 on Ω^s. The lowest subdomain $\Omega^{m,1}$ is fixed at its lower face, while on the upper face of the upper subdomain $\Omega^{m,2}$, a rotation of $\pi/4$ parallel to the (x, y)-plane is applied. The material parameters suggest to use a finer grid on the slave subdomain Ω^s, which is easily possible by using non-matching grids. Since it is impossible to mesh a circle purely with parallelograms (apart from a one-element-grid), we have to deal with general quadrilaterals on the subdomain interfaces. In order to use a dual basis for the discrete Lagrange multiplier space, we employ the techniques presented in Section 2.4.2. On each subdomain, individual elasticity model equations can be considered: linearized (1.3)-(1.5), geometrically nonlinear (1.7)-(1.9), and neo-Hooke (1.9)-(1.11).

Figure 2.19 shows the deformed domain on a coarse grid, once using the linear model on all subdomains, and once using the neo-Hooke law everywhere. As was to be expected, the linearized equations do not give a satisfactory result, especially for the upper cube $\Omega^{m,2}$. There, the displacement is almost a pure, but large rotation, which cannot be modeled correctly by (1.3)-(1.5). Visually, the method using the neo-Hooke law everywhere yields correct results. However, the problem setting and the solution suggest that it might not be necessary to use the fully nonlinear and complicated neo-Hooke model on all

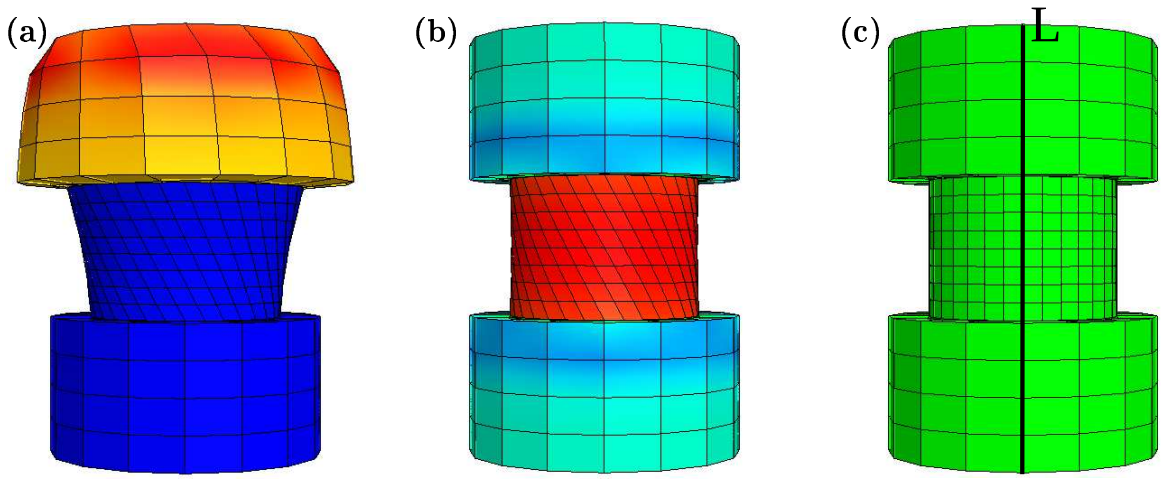

Figure 2.19: Deformed domains for (a) the linearized and (b) the neo-Hooke setting, (c) the broken line L.

three subdomains. On the upper cylinder $\Omega^{\mathrm{m},2}$, it should be enough to consider the geometrically nonlinear setting, because large deformations, but relatively small strains occur. On the lower cylinder $\Omega^{\mathrm{m},1}$, also the deformations remain small, and the linearized model might be sufficient. On the middle subdomain Ω^{s}, both the deformations and the strains are quite large, there, the neo-Hooke law should be mandatory. In Figure 2.20, the displacement in x- and z-direction as well as the effective stress are plotted along the broken line L, which is indicated in Figure 2.19(c). The mesh for the calculation was obtained after one uniform refinement of the mesh from Figure 2.19. The notation ijk, $i, j, k = \mathrm{l}, \mathrm{g}, \mathrm{n}$, in Figure 2.20 indicates that models i, j, and k are used on $\Omega^{\mathrm{m},2}$, Ω^{s}, and $\Omega^{\mathrm{m},1}$, respectively. As suggested by the domain deformations, the fully linear model lll fails almost completely. All considered quantities differ strongly from the reference solution nnn which uses the neo-Hooke law everywhere. It is impossible to reproduce the expected symmetry with respect to $z = 1.5$ in the z-displacement and in the effective stress. Only on the lower cylinder $\Omega^{\mathrm{m},1}$, the solution is quite accurate. The geometrically nonlinear setting ggg still cannot resolve all features. Especially the effective stress on the middle cylinder Ω^{s}, which is due to the relative large strains, is not properly described.

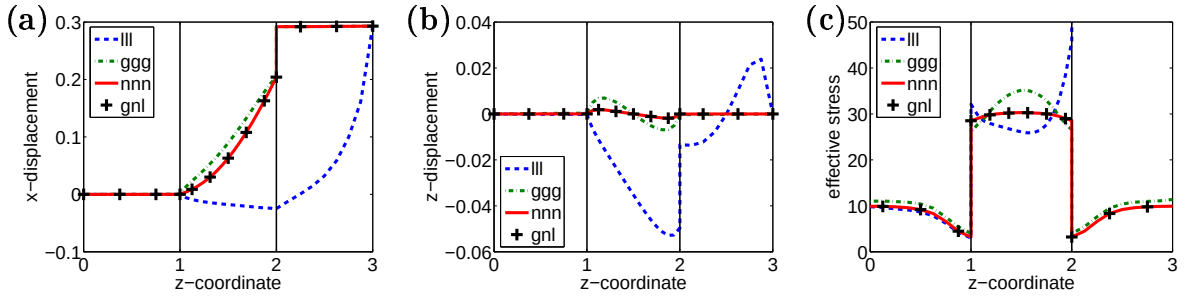

Figure 2.20: Different model equations: displacements in x- and z-direction, effective stress along the line L.

Yet, the quantities on the lower and on the upper subdomain are very close to the reference solution. The combination gnl, as discussed above, uses the "optimal" model on each subdomain. The results cannot be distinguished from the reference solution. We remark that the number of Newton iterations to solve the systems of nonlinear equations was between 4 and 7, starting from the solution of the linear system and using a tolerance of 10^{-10} in the relative difference of two successive iterates as stop criterion.

3 The Vector Field Case

Whether an interface method performs well on curved surfaces should not be taken for granted and may require a modification of the method as will be demonstrated in this chapter. Amongst others, a recent work [97] found that the dual mortar method worked quite well for mesh tying over the range of solid mechanics problems benchmarked in the paper. It was also found that the optimal convergence of the discretization error was attainable for applications where curved surfaces were tied, although it offered no a priori error analysis to validate this claim. After more extensive application, it has since been found that the dual mortar method behaved poorly for elasticity problems with curved boundaries when the slave side was considerably coarser than the master side. On the other hand, the standard mortar method appears to be relatively un-biased to the choice of master and slave sides and works quite well on curved boundaries where the slave side is much coarser than the master side. In this chapter, two modifications to the dual mortar method are proposed for two- and three-dimensional solid mechanics that fix the aforementioned problem. Furthermore, a priori error results demonstrating optimal convergence for this new approach are presented for the curved interface problem. This is achieved by extending the results from Chapter 2.

The following is an outline for this chapter. Section 3.1 introduces basic notation relevant to the proceedings and in particular the mathematical description of the domain decomposition/mesh tying problem. Section 3.2 introduces the model problem of an internally pressurized cylinder. Here, the pathological behavior for the dual formulation is diagnosed. Section 3.3 presents two modifications of the dual approach and uses perturbation arguments analogous to Chapter 2 to provide a priori error results. Section 3.4 shows some numerical examples demonstrating the effectiveness and also the limitations of the new approach.

3.1 Problem Description

We use the standard linear elasticity model (1.3)-(1.6) to investigate the deformation of an elastic body $\Omega \subset \mathbb{R}^d$ under given volume and surface forces. The domain Ω is subdivided into two non-overlapping subdomains Ω^{m} and Ω^{s}, sharing the possibly curved interface $\Gamma = \partial\Omega^{\mathrm{m}} \cap \partial\Omega^{\mathrm{s}}$ with the unit normal vector $\boldsymbol{n} = \boldsymbol{n}_{\mathrm{s}}$. For simplicity, we assume that Γ is a closed surface for $d = 3$ and a closed curve for $d = 2$. For the Neumann and Dirichlet boundary Γ_{N} and Γ_{D}, respectively, we set $\Gamma_{\mathrm{N}}^k = \partial\Omega^k \cap \Gamma_{\mathrm{N}}$ and $\Gamma_{\mathrm{D}}^k = \partial\Omega^k \cap \Gamma_{\mathrm{D}}$, $k = \mathrm{m}, \mathrm{s}$. In order to obtain a weak saddle problem formulation, we introduce the product space $X = (H^1_{\Gamma_{\mathrm{D}}^{\mathrm{m}}}(\Omega^{\mathrm{m}}))^d \times (H^1_{\Gamma_{\mathrm{D}}^{\mathrm{s}}}(\Omega^{\mathrm{s}}))^d$, with $H^1_{\Gamma_{\mathrm{D}}^{\mathrm{k}}}(\Omega^k) = \{v_k \in H^1(\Omega^k) : v_k|_{\Gamma_{\mathrm{D}}^k} = 0\}$, equipped with the broken H^1-norm defined analogously to (2.2). Moreover, the bilinear form $a(\cdot,\cdot)$

and the linear form $l(\cdot)$ acting on X are defined by

$$a(\boldsymbol{u},\boldsymbol{v}) = \sum_{k=\mathrm{m,s}} (\sigma_k(\boldsymbol{u}_k), \operatorname{grad} \boldsymbol{v}_k)_{\Omega^k}, \quad l(\boldsymbol{v}) = \sum_{k=\mathrm{m,s}} (\boldsymbol{f}_k, \boldsymbol{v}_k)_{\Omega^k} + (\boldsymbol{g}_k, \boldsymbol{v}_k)_{\Gamma_{\mathrm{N}}^k}, \tag{3.1}$$

where σ_k is the linearized strain tensor, $\boldsymbol{f}_k$ the given volume force, and $\boldsymbol{g}_k$ the surface traction on the subdomain Ω^k, $k = \mathrm{m,s}$. As for the scalar case, the coupling between the two solution components $\boldsymbol{u}_\mathrm{m}, \boldsymbol{u}_\mathrm{s}$ is realized by establishing a weak transmission condition in terms of the Lagrange multiplier space $M = (H^{-1/2}(\Gamma))^d$, namely the coupling bilinear form b on $X \times M$,

$$b(\boldsymbol{v},\boldsymbol{\mu}) = \langle \boldsymbol{\mu}, [\boldsymbol{v}] \rangle_\Gamma, \quad \boldsymbol{v} \in X, \boldsymbol{\mu} \in M. \tag{3.2}$$

The displacement $\boldsymbol{u} \in X$ and the interface traction $\boldsymbol{\lambda} = -\sigma_\mathrm{s}(\boldsymbol{u}_\mathrm{s})\boldsymbol{n} \in M$ are the solution of the symmetric saddle point problem (1.16).

As in Chapter 2, we discretize (1.16) by means of piecewise linear or bi-(tri-)linear finite elements on quasi-uniform triangulations $\mathcal{T}_k$ with maximum element diameters h_k, $k = \mathrm{m,s}$, and $h = \max(h_\mathrm{s}, h_\mathrm{m})$. The curved interface Γ is replaced by polygons Γ_h^m and Γ_h^s. Analogously to (2.16), the approximate coupling bilinear form b_h acting on $X_h \times M_h$ is defined by

$$b_h(\boldsymbol{v}_h,\boldsymbol{\mu}_h) = (\boldsymbol{\mu}_h, \boldsymbol{v}_\mathrm{s} - P_\mathrm{s}\boldsymbol{v}_\mathrm{m})_{\Gamma_h^\mathrm{s}}, \qquad \boldsymbol{v}_h \in X_h,\ \boldsymbol{\mu}_h \in M_h, \tag{3.3}$$

where $P_\mathrm{s} : (L^2(\Gamma_h^\mathrm{m}))^d \to (L^2(\Gamma_h^\mathrm{s}))^d$ is given component-wise by (2.14). The discrete version of (1.16) is given by (2.20), where the approximate forms $a_h(\cdot,\cdot)$ and $l_h(\cdot)$ are defined element-wise with respect to (3.1). Again, the equivalent algebraic system can be written as (1.22). We repeat the fact that in case of dual Lagrange multipliers [120], D is a diagonal matrix, the interface traction $\boldsymbol{\lambda}_h$ can be locally eliminated, and the resulting system for the displacement is positive definite.

3.2 Dual Lagrange Multipliers: A Drawback?

We consider a simple example in two dimensions. The model domain consists of a ring Ω with inner radius $r_i = 0.9$, outer radius $r_o = 1.1$, and modules $E = 1$, $\nu = 0.3$, as illustrated in Figure 3.1(a). It is fixed at the outer boundary, whereas at the inner boundary, a traction of magnitude one constant in normal direction is applied. The exact solution for the displacement in radial direction is $u_r(r) = c(r - r_o^2/r)$ with $c = 0.5r_i^2/(\lambda_\mathrm{L} r_i^2 + \mu_\mathrm{L}(r_o^2 + r_i^2))$, λ_L and μ_L being the Lamé parameters. The domain Ω is subdivided into two rings Ω^m and Ω^s such that their interface Γ is the unit circle. We choose the inner ring to be Ω^m, and the outer ring to be Ω^s.

A part of the computational grid is shown in Figure 3.1(b). The whole grid consists of 240 elements, constructed in such a way that each element edge on the slave side meets four master edges, thus, the discrete Lagrange multiplier space M_h is defined with respect to the coarse grid on Γ_h^s. For a first test, four different types of Lagrange multipliers (LM) are used: the standard ones coinciding with the trace space W_h^s, the dual ones spanned by piecewise linear discontinuous basis functions given by (2.71), the dual continuous ones

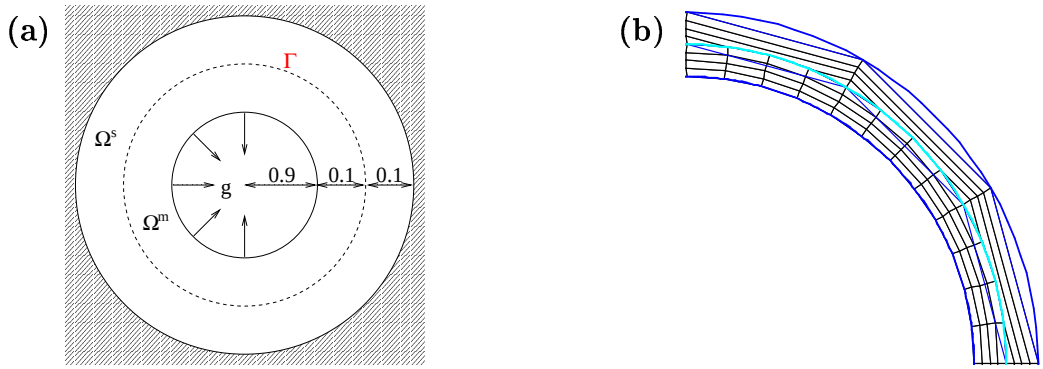

Figure 3.1: (a) problem setting, (b) computational grid.

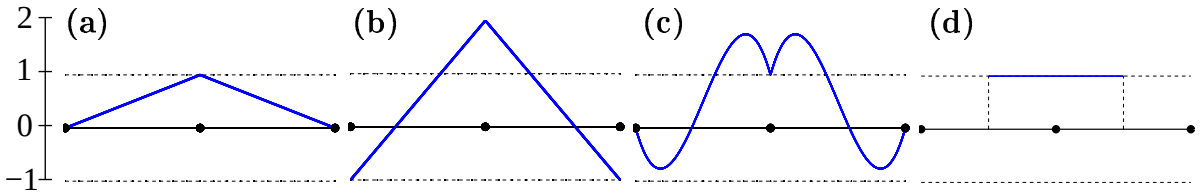

Figure 3.2: Basis functions: (a) standard, (b) discontinuous dual, (c) continuous dual, (d) constant Lagrange multipliers.

where the discontinuous dual basis functions are modified by cubic polynomials [123], and the piecewise constant ones spanned by basis functions which are constant from one edge midpoint to the next [120]. The basis functions associated with each node are illustrated in Figure 3.2.

In Figure 3.3, the isolines of the van Mises stresses of the numerical solutions on the deformed domains are plotted. Whereas the use of standard Lagrange multipliers yields a visually satisfying result, the behavior of all other solutions is dictated by strong oscillations along the master interface Γ_h^{m}.

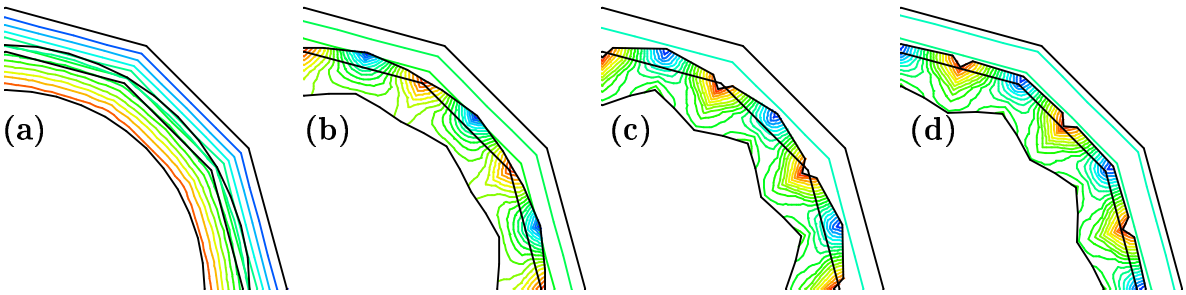

Figure 3.3: van Mises stress: (a) standard, (b) discontinuous dual, (c) continuous dual, (d) constant Lagrange multipliers.

The behavior is also reflected in the error decay for the used methods, documented in Figure 3.4. The ratio of the number of slave edges to the number of master edges is kept constant with 1:4, and starting a uniform refinement procedure from an initial triangu-

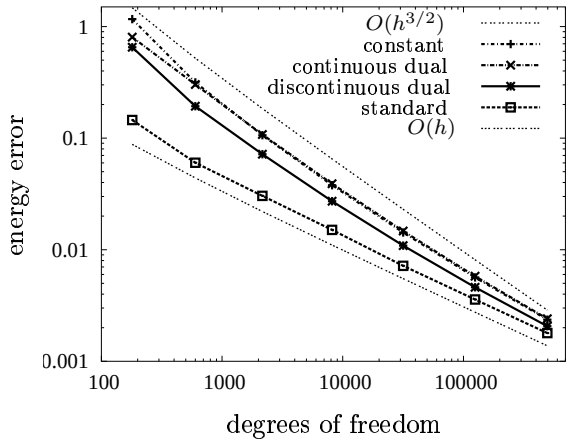

Figure 3.4: Decay of the energy error under uniform refinement.

lation consisting of 60 elements, the error measured in the energy norm is calculated at each refinement step. Comparing the results, the error for the method using the standard multipliers is much less than for the three other methods. We note that, within the plotted range, the decay of these other methods is near $O(h^{3/2})$, and the relative difference to the standard approach decreases as the number of unknowns increases. Asymptotically, the qualitative behavior of all methods is the same as predicted by the theory. So the oscillations can be considered to be a pre-asymptotic misbehavior. We stress that this misbehavior only occurs when the Lagrange multipliers are defined with respect to the coarse grid. When they are chosen corresponding to the fine grid, all four methods behave qualitatively and quantitatively the same. This observation will be addressed in more detail in Section 3.4.

In order to explain the very different behavior of the different discrete Lagrange multipliers, we consider the following situation. Denoting by $\boldsymbol{p}_i^{\mathrm{s}}$, $i = 1, \ldots, n_{\mathrm{s}}$, the finite element nodes on Γ_h^{s}, we associate with each node $\boldsymbol{p}_i^{\mathrm{s}}$ the corresponding unit normal vector $\boldsymbol{n}_i$, the standard piecewise linear scalar basis function ϕ_i^{s}, and the scalar Lagrange multiplier basis function μ_i. In the solution of the above model problem, the interface traction $\boldsymbol{\lambda}$ is given by $\boldsymbol{\lambda} = \beta \boldsymbol{n}$. Here, we set $\beta = -1$ for simplicity. Out of symmetry reasons, we choose the approximation $\boldsymbol{\lambda}_h$ of $\boldsymbol{\lambda}$ to be $\boldsymbol{\lambda}_h = -\sum_{i=1}^{n_{\mathrm{s}}} \boldsymbol{n}_i \mu_i$. Let us neglect for a moment the influence of Γ_h^{s} and P_{s}, and assume that all involved functions and bilinear forms are well-defined on Γ. We first consider the situation on the slave side. Here, (2.20a) yields that

$$(\boldsymbol{\lambda}_h, \boldsymbol{v}_{\mathrm{s}})_\Gamma = \sum_{i,j=1}^{n_{\mathrm{s}}} \boldsymbol{n}_j \boldsymbol{\alpha}_i (\mu_j, \phi_i^{\mathrm{s}})_\Gamma$$

with some coefficients α_{ij}. In the case of dual Lagrange multipliers, we have the biorthogonality $(\mu_j, \phi_i^{\mathrm{s}})_\Gamma = 0$ for $j \neq i$, and the above sum reduces to

$$\sum_{i=1}^{n_{\mathrm{s}}} \boldsymbol{n}_i \boldsymbol{\alpha}_i (1, \phi_i^{\mathrm{s}})_\Gamma.$$

Thus, a virtual displacement at the node $\boldsymbol{p}_i^{\mathrm{s}}$ "sees" only a traction in direction of $\boldsymbol{n}_i$. On the master side, the situation is different. Because of the non-matching structure of the grids, there is no biorthogonality between μ_j and the basis functions ϕ_i^{m} of the master side. Therefore, a virtual displacement at the master node $\boldsymbol{p}_i^{\mathrm{m}}$ "sees" the "full" discrete traction, i.e. $\boldsymbol{\lambda}_h = -\sum \boldsymbol{n}_i \mu_i$.

To get a better feeling on how $\boldsymbol{\lambda}_h$ differs for the different Lagrange multiplier spaces, we focus on the slave edge e_{s} with corner points $\boldsymbol{p}_1^{\mathrm{s}} = (\cos\pi/6, \sin\pi/6)^{\mathrm{T}}$ and $\boldsymbol{p}_2^{\mathrm{s}} = (\cos\pi/3, \sin\pi/3)^{\mathrm{T}}$, i.e., the "middle" slave edge in the pictures of Figure 3.3. For each of the discussed spaces, we choose $\boldsymbol{\lambda}_h = \boldsymbol{p}_1^{\mathrm{s}}\mu_1 + \boldsymbol{p}_2^{\mathrm{s}}\mu_2$ with the corresponding scalar basis functions μ_1, μ_2. The effect of $\boldsymbol{\lambda}_h$ onto the master side is documented in Figure 3.5. The

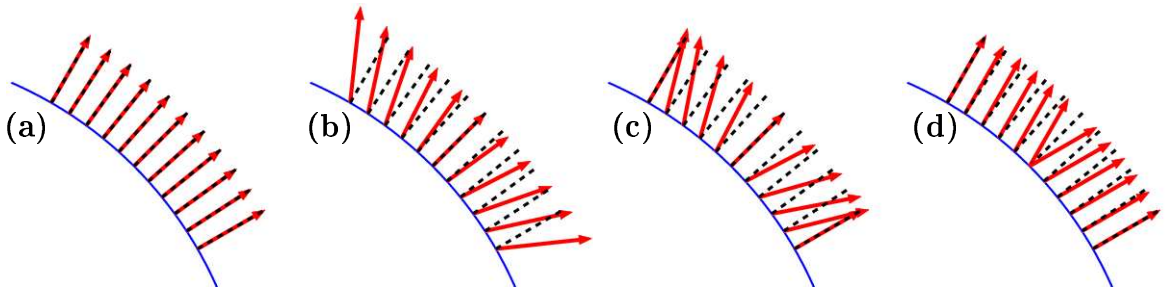

Figure 3.5: The transfer of the discretized normal vector field $-\boldsymbol{n}$ onto the master side: (a) standard, (b) discontinuous dual, (c) continuous dual, (d) constant Lagrange multipliers.

arrows show how $\boldsymbol{\lambda}_h$ transfers to the master side, the dashed lines indicate the correct normal direction. For the standard Lagrange multipliers, the normal field is transferred correctly to the master side. For the two dual LM, the normal vectors get drawn into wrong directions near the endpoints of the slave edges, which can be explained by the negativity of one of the basis functions near these points. For the piecewise constant LM, the problem occurs around the center of the slave edge, reflecting the discontinuity of the corresponding basis functions at this point. The influence of all these behaviors explains the stress plots of Figure 3.3. In particular, the reason for the opposed oscillations of the dual LM compared to the piecewise constant LM becomes clear.

We remark that the problem only seems to occur when working with piecewise linear or bilinear finite elements in combination with non-standard Lagrange multipliers. As an example for higher order elements, we carry out the above test, this time using Serendipity elements and quadratic Lagrange multipliers, once with standard and once with dual basis functions. The left pictures of Figure 3.6 suggest that the transfer of the discretized normal vector field $-\boldsymbol{n}$ onto the master side is performed correctly. The result of the numerical experiment, plotted in the right pictures of Figure 3.6, consequently does not exhibit any significant unwanted oscillations on the master side. The observation that the flow of the isolines is still not optimal occurs for both the standard and the dual multipliers, and is due to the fact that only affine and no isoparametric element transformations have been used.

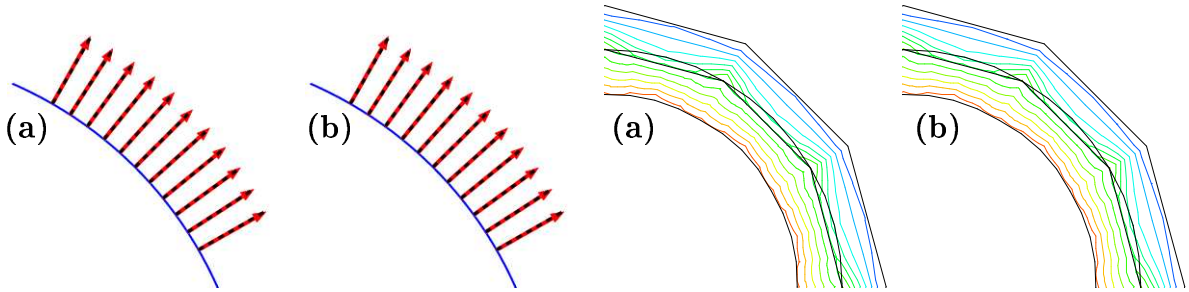

Figure 3.6: The case of Serendipity elements and quadratic Lagrange multipliers: transfer of $-\boldsymbol{n}$ and van Mises stresses using (a) standard, (b) dual basis functions.

3.3 Modifications for Curved Interfaces

Our numerical results above illustrate how sensitive the quality of the mortar approximation depends on the choice of the Lagrange multiplier space, especially for curvilinear interfaces. In this section, we extend our results for the scalar case from Chapter 2 to vector fields in dimension $d \in \{2, 3\}$. In particular, we present two alternative modifications for lowest order dual Lagrange multipliers. Both have in common that only the coupling of the Lagrange multipliers to the master side is changed, namely, $(P_{\mathrm{s}}\boldsymbol{v}_{\mathrm{m}}, \boldsymbol{\mu})_{\Gamma_h^{\mathrm{s}}}$. Formally, the coupling bilinear form $b_h(\cdot,\cdot)$ is replaced by a modification $b_h^{\mathrm{mod}}(\cdot,\cdot)$. In the first alternative to be given, the Lagrange multiplier $\boldsymbol{\mu} \in M_h$ as seen by the master side is replaced by $\boldsymbol{\mu} + \Delta\boldsymbol{\mu}$, whereas for the second one, we replace the L^2-scalar product $(\cdot,\cdot)_{\Gamma_h^{\mathrm{s}}}$ by a discrete one. Both approaches reduce to the original one in the case of a planar interface. For several model problems, they result in a strong improvement of the umodified method. However, the modifications turn out have no positive effect for more general situations, which will be illustrated in Section 3.4.5 by means of an example.

Before we introduce the two modifications, we address some common issues which are needed for deriving them. With each node p on the smooth interface Γ, an orthonormal basis $B_p \in \mathbb{R}^{d\times d}$ is associated, given by $B_p = (\boldsymbol{b}_p^{(1)}, \ldots, \boldsymbol{b}_p^{(d)})$ with $\boldsymbol{b}_p^{(1)} = \boldsymbol{n}_p$ being the unit normal vector on Γ in p, and the remaining columns being corresponding unit tangent vectors. In the following, $\boldsymbol{n}_p$ can be the exact normal on Γ or a weighted sum of the face normals sharing the node p. In the case that Γ is piecewise smooth, we have to decompose Γ into smooth non-overlapping subsets, the boundaries of which have to be regarded as wire-basket edges.

Our modifications will be given in terms of the difference of two bases B_p, B_q, where p refers to a slave node, and, in Section 3.3.1, the nodes p and q are both vertices of one slave side element, whereas in Section 3.3.2, B_q is associated with a master node such that the supports of the corresponding basis functions intersect. For the upcoming analysis in both cases, we assume that

$$\|B_p - B_q\|_\infty = O(h), \tag{3.4}$$

provided that $\|\boldsymbol{p} - \boldsymbol{q}\|_\infty = O(h)$ where $\boldsymbol{p}$ and $\boldsymbol{q}$ are the coordinate vectors of the nodes p and q, respectively. For the first column of B_p and B_q, namely, the difference of the

normal vectors $\boldsymbol{n}_p$ and $\boldsymbol{n}_q$, this is an obvious fact. Whereas in two dimensions, the choice of the tangent vector is unique up to the sign, the construction of two vectors spanning the tangent plane in three dimensions is by no means unique. However, if Γ is not a closed surface, this construction is possible in an unambiguous and continuous way. To this end, we fix one orthonormal system B_* and require that the difference of the first column $\boldsymbol{b}_*^{(1)}$ and any normal vector $\boldsymbol{n}_p$ on Γ is bounded from below by a constant. Then, for each vertex p, the basis B_p can be defined in terms of the unique Householder reflection $H_p \in \mathbb{R}^{d\times d}$ mapping $\boldsymbol{b}_*^{(1)}$ onto $\boldsymbol{n}_p$, namely, $B_p = H_p B_*$. We remark that the choice of $\boldsymbol{b}_*^{(1)}$ avoids any errors due to cancellation. For the sake of clarity, we will indicate by $B_{p,\mathrm{s}}$ or $B_{p,\mathrm{m}}$ whether the node p is associated with the slave or the master side, respectively.

For our a priori analysis, the stability of the grid transfer mapping P_s will be important. We remark that for the use of interpolation arguments in some of the following proofs, we will ignore the fact that the discretized interfaces Γ_h^k depend on the mesh parameter h. Since essentially they can be associated with a fixed surface, our results are still correct.

Lemma 3.1. *For $t \in [0,1]$, we have that $|P_s \boldsymbol{v}|_{t,\Gamma_h^\mathrm{s}} \le C|\boldsymbol{v}|_{t,\Gamma_h^m}$ for all $\boldsymbol{v} \in (H^t(\Gamma_h^m))^d$.*

Proof. Let v be any scalar component of $\boldsymbol{v}$. We obtain

$$\begin{aligned}
\|P_\mathrm{s} v\|_{0,\Gamma_h^\mathrm{s}}^2 &= \int_{\Gamma_h^\mathrm{s}} (P_\mathrm{s} v)^2 \,\mathrm{d}\Gamma_h^\mathrm{s} = \sum_{e_\mathrm{s}} \int_{e_\mathrm{s}} (v \circ \gamma_\mathrm{m} \circ \gamma_\mathrm{s}^{-1})^2 \,\mathrm{d}\Gamma_h^\mathrm{s} \\
&= \sum_{e_\mathrm{s}} \int_{\gamma_\mathrm{s}^{-1}(e_\mathrm{s})} (v \circ \gamma_\mathrm{m})^2 \big|(D\gamma_\mathrm{s})_{|\gamma_\mathrm{s}^{-1}(e_\mathrm{s})}\big| \,\mathrm{d}I \\
&\le \max_{e_\mathrm{s}} \big|(D\gamma_\mathrm{s})_{|\gamma_\mathrm{s}^{-1}(e_\mathrm{s})}\big| \int_I (v \circ \gamma_\mathrm{m})^2 \,\mathrm{d}I \\
&= \max_{e_\mathrm{s}} \big|(D\gamma_\mathrm{s})_{|\gamma_\mathrm{s}^{-1}(e_\mathrm{s})}\big| \sum_{e_\mathrm{m}} \int_{e_\mathrm{m}} v^2 \big|(D\gamma_\mathrm{m}^{-1})_{|e_\mathrm{m}}\big| \,\mathrm{d}\Gamma_h^\mathrm{m} \\
&\le \left(\max_{e_\mathrm{s}} \big|(D\gamma_\mathrm{s})_{|\gamma_\mathrm{s}^{-1}(e_\mathrm{s})}\big|\right) \left(\max_{e_\mathrm{m}} \big|(D\gamma_\mathrm{m}^{-1})_{|e_\mathrm{m}}\big|\right) \|v\|_{0,\Gamma_h^\mathrm{m}}.
\end{aligned}$$

We recall that γ_s and γ_m are piecewise linear interpolations of the smooth parameterization γ. By the mean value theorem, the two maxima above can be estimated by $\max|D\gamma|$ and $\max|D\gamma^{-1}|$, respectively. We remark that a rigorous analysis would involve only local relations of $\max|D\gamma|$ and $\max|D\gamma^{-1}|$. The smoothness of γ implies the assertion for $t = 0$. We follow the same procedure for the H^1-semi-norm:

$$\begin{aligned}
|P_\mathrm{s}\boldsymbol{v}|_{1,\Gamma_h^\mathrm{s}} &= \sum_{e_\mathrm{s}} \int_{e_\mathrm{s}} (\mathrm{grad}_S(P_\mathrm{s} v))^2 \,\mathrm{d}\Gamma_h^\mathrm{s} \\
&= \sum_{e_\mathrm{s}} \int_{\gamma_\mathrm{s}^{-1}(e_\mathrm{s})} (\mathrm{grad}_S(v \circ \gamma_\mathrm{m}))^2 \big|(D\gamma_\mathrm{s}^{-1})_{|e_\mathrm{s}}\big|^2 \big|(D\gamma_\mathrm{s})_{|\gamma_\mathrm{s}^{-1}(e_\mathrm{s})}\big| \,\mathrm{d}I \\
&\le \max_{e_\mathrm{s}} \big|(D\gamma_\mathrm{s}^{-1})_{|e_\mathrm{s}}\big| \int_I (\mathrm{grad}_S(v \circ \gamma_\mathrm{m}))^2 \,\mathrm{d}I \\
&\le \left(\max_{e_\mathrm{s}} \big|(D\gamma_\mathrm{s}^{-1})_{|e_\mathrm{s}}\big|\right) \left(\max_{e_\mathrm{m}} \big|(D\gamma_\mathrm{m})_{|\gamma_\mathrm{m}^{-1}(e_\mathrm{m})}\big|\right) |v|_{1,\Gamma_h^\mathrm{m}}^2,
\end{aligned}$$

which yields the desired result for $t = 1$ by the same observations as above. For $t \in (0, 1)$, the assertion follows from an interpolation argument for operators, given for example in [26, Thm. 12.1.5]. We note that, since the constant C appearing in both estimates for $t = 0$ and $t = 1$ does not depend on h, it also does not for $t \in (0, 1)$. □

3.3.1 Momentum Preserving Modification

In this section, we derive a modification of the approach using linear discontinuous dual Lagrange multipliers. In the sequel, if nothing else is particularly mentioned, the space M_h is always associated with these multipliers. From the viewpoint of efficiency, the modification should preserve all the advantages of the dual approach. From the physical point of view, it is important that the linear momentum is preserved in order to not add any artificial surface tractions. Moreover, the good quantitative behavior of the standard multipliers should be achieved. Therefore, we require that our problem formulation satisfies the following properties:

(P1) a diagonal matrix on the slave side,

(P2) symmetry of the saddle point approach,

(P3) preservation of linear momentum,

(P4) original formulation for straight interfaces,

(P5) preservation of quantities which are constant in normal and tangential direction,

(P6) preservation of the optimal asymptotic behavior of $O(h)$.

The first two requirements suggest leaving the coupling of the slave side to the Lagrange multipliers unchanged, i.e., the matrix D in (1.22), and to symmetrically modify the coupling of the master side to the Lagrange multipliers, i.e., M in (1.22).

Formulation

We focus on a slave element T^{s} of the surface grid $\mathcal{T}^{\mathrm{s}}$ with n_{s} denoting the numbers of its vertices. As in Section 2.4.2, we use the element matrices $D_{T^{\mathrm{s}}}$ and $M_{T^{\mathrm{s}}}$ defined by (2.75). Requiring that the modified Lagrange multipliers still preserve a lowest order momentum, the modification $\Delta\boldsymbol{\mu}$ will be given in terms of

$$\Delta\phi_{pq} = \phi_p^{\mathrm{s}} d_{pp}^{-1} - \phi_q^{\mathrm{s}} d_{qq}^{-1}. \tag{3.5}$$

It is obvious that $(1, \Delta\phi_{pq})_{T^{\mathrm{s}}} = 0$, thus, a linear momentum will be preserved which guarantees (P3). On T^{s}, any given discrete Lagrange multiplier $\boldsymbol{\mu} \in M_h$ can be written as $\boldsymbol{\mu}|_{T^{\mathrm{s}}} = \sum_{p=1}^{n_{\mathrm{s}}} \boldsymbol{\alpha}_p \mu_p$ with coefficients $\boldsymbol{\alpha}_p \in \mathbb{R}^d$, $p = 1, \dots n_{\mathrm{s}}$. Its modification $\Delta\boldsymbol{\mu}$ is defined by

$$\Delta\boldsymbol{\mu}|_{T^{\mathrm{s}}} = \frac{1}{2} \sum_{p,q} \gamma_{pq} \Delta\phi_{pq} \left(\sum_{i=1}^{d} (\boldsymbol{\alpha}_p \cdot \boldsymbol{b}_p^{(i)} + \boldsymbol{\alpha}_q \cdot \boldsymbol{b}_q^{(i)}) \Delta\boldsymbol{b}_{pq}^{(i)} \right), \tag{3.6}$$

yielding the modified multiplier $\boldsymbol{\mu}^{\mathrm{mod}} = \boldsymbol{\mu} + \Delta\boldsymbol{\mu}$. In the formula above, the coefficients γ_{pq} are the elements of a modification matrix $G \in \mathbb{R}^{n_\mathrm{s} \times n_\mathrm{s}}$ which has yet to be defined, and $\Delta \boldsymbol{b}_{pq}^{(i)} = \boldsymbol{b}_p^{(i)} - \boldsymbol{b}_q^{(i)}$, $i = 1, \dots, d$. Since the modification is given in terms of differences of normal vectors at neighboring vertices, the requirement (P4) is met.

In order to motivate our choice for the modification $\Delta\boldsymbol{\mu}$, we introduce the matrix $\boldsymbol{N}_\mathrm{s} \in \mathbb{R}^{d \times n_\mathrm{s}}$ by

$$\boldsymbol{N}_\mathrm{s} = (\boldsymbol{n}_1^\mathrm{s}, \dots, \boldsymbol{n}_{n_\mathrm{s}}^\mathrm{s}),$$

where $\boldsymbol{n}_p^\mathrm{s}$ indicates the unit normal vector on Γ in the slave node p, $p = 1, \dots, n_\mathrm{s}$. Moreover, the symbolic vectors Φ_s and Λ_s of length n_s are given by

$$\Phi_\mathrm{s} = (\phi_1^\mathrm{s}, \dots, \phi_{n_\mathrm{s}}^\mathrm{s})^\mathrm{T}, \quad \Lambda_\mathrm{s} = (\mu_1, \dots, \mu_{n_\mathrm{s}})^\mathrm{T},$$

where, as before, ϕ_p^s and μ_p denote scalar nodal basis functions of the corresponding spaces, $p = 1, \dots, n_\mathrm{s}$. With (P5), we require that the modification guarantees a discrete preservation of quantities which are constant in normal and tangential direction. In particular, we want to preserve these quantities when transferring between the trace space W_h^s and the Lagrange multiplier space M_h. This idea is motivated by the observation that $\sum_p \boldsymbol{n}_p \phi_p^\mathrm{s}$ yields a quite good approximation of the normal field on Γ whereas $\sum_p \boldsymbol{n}_p \mu_p$ gives a bad result as seen in Section 3.2. Because of the duality between μ_p and ϕ_q^s this does not affect the surface traction on the slave side but on the master side. In particular, focusing on the normal direction, this requirement can be expressed elementwise by demanding that $\boldsymbol{N}_\mathrm{s}\Lambda_\mathrm{s} = \boldsymbol{N}_\mathrm{s}\Phi_\mathrm{s}$. However, when usual dual basis functions are used for M_h, this cannot be achieved. But for our modification (3.6) with suitably defined coefficients γ_{pq}, we can show that

$$(\boldsymbol{N}_\mathrm{s}\Lambda_\mathrm{s})^\mathrm{mod} = \boldsymbol{N}_\mathrm{s}\Phi_\mathrm{s}. \tag{3.7}$$

Lemma 3.2. *Let the scalar dual basis functions be defined as in Section 2.4.2, namely,* $\Lambda_s = D_{T^s} M_{T^s}^{-1} \Phi_s$. *Then, the choice*

$$G = \frac{1}{2} D_{T^s} M_{T^s}^{-1} D_{T^s} \tag{3.8}$$

yields (3.7).

Proof. From (3.6), we observe that

$$(\mu_p \boldsymbol{n}_p)^\mathrm{mod} = \mu_p \boldsymbol{n}_p + \sum_q \gamma_{pq} \Delta\phi_{pq} (\boldsymbol{n}_p - \boldsymbol{n}_q), \quad p = 1, \dots, n_\mathrm{s},$$

which yields, using the symmetry of G, that

$$(\boldsymbol{N}_\mathrm{s}\Lambda_\mathrm{s})^\mathrm{mod} = \boldsymbol{N}_\mathrm{s}\Lambda_\mathrm{s} - 2\boldsymbol{N}_\mathrm{s}(G - D_G) D_{T^\mathrm{s}}^{-1} \Phi_\mathrm{s}$$

with a diagonal matrix D_G defined by $(D_G)_{pp} = \sum_q \gamma_{pq}$. The definitions $\Lambda_\mathrm{s} = D_{T^\mathrm{s}} M_{T^\mathrm{s}}^{-1} \Phi_\mathrm{s}$ and (3.8) imply

$$(\boldsymbol{N}_\mathrm{s}\Lambda_\mathrm{s})^\mathrm{mod} = \boldsymbol{N}_\mathrm{s}(D_{T^\mathrm{s}} M_{T^\mathrm{s}}^{-1} - 2G D_{T^\mathrm{s}}^{-1} + 2 D_G D_{T^\mathrm{s}}^{-1}) \Phi_\mathrm{s} = \boldsymbol{N}_\mathrm{s}(2 D_G D_{T^\mathrm{s}}^{-1}) \Phi_\mathrm{s}.$$

We note that the row sums of D_{T^s} and M_{T^s} are equal,

$$(D_{T^\mathrm{s}}\mathbf{1})_p = (1, \phi_p^\mathrm{s})_{T^\mathrm{s}} = \sum_q (\phi_p^\mathrm{s}, \phi_q^\mathrm{s})_{T^\mathrm{s}} = (M_{T^\mathrm{s}}\mathbf{1})_p, \qquad p = 1, \dots, n_\mathrm{s},$$

yielding $D_{T^\mathrm{s}} M_{T^\mathrm{s}}^{-1} D_{T^\mathrm{s}} \mathbf{1} = D_{T^\mathrm{s}}\mathbf{1}$, from which it becomes obvious that $2D_G D_{T^\mathrm{s}}^{-1} = \mathrm{Id}$, which concludes the proof. □

We remark that for $d = 2$ and $B_p = (\boldsymbol{n}_p, \boldsymbol{t}_p)$, the choice $G = \frac{1}{2} D_{T^\mathrm{s}} M_{T^\mathrm{s}}^{-1} D_{T^\mathrm{s}}$ yields the modification

$$\Delta\boldsymbol{\mu}_h|_{T^\mathrm{s}} = -\frac{1}{2}\phi_{pq}\left((\boldsymbol{\alpha}_p \cdot \boldsymbol{n}_p + \boldsymbol{\alpha}_q \cdot \boldsymbol{n}_q)\Delta\boldsymbol{n}_{pq} + (\boldsymbol{\alpha}_p \cdot \boldsymbol{t}_p + \boldsymbol{\alpha}_q \cdot \boldsymbol{t}_q)\Delta\boldsymbol{t}_{pq}\right) \tag{3.9}$$

on the slave edge T^s with endpoints p, q.

Analysis

The modification given in (3.6) yields the saddle point problem

$$a_h(\boldsymbol{u}_h^\mathrm{mod}, \boldsymbol{v}_h) + b_h^\mathrm{mod}(\boldsymbol{v}_h, \boldsymbol{\lambda}_h^\mathrm{mod}) = l_h(\boldsymbol{v}_h), \quad \boldsymbol{v}_h \in X_h, \tag{3.10a}$$

$$b_h^\mathrm{mod}(\boldsymbol{u}_h^\mathrm{mod}, \boldsymbol{\mu}_h) = 0, \qquad \boldsymbol{\mu}_h \in M_h. \tag{3.10b}$$

where $b_h^\mathrm{mod}(\cdot,\cdot)$ indicates the modified coupling bilinear form, namely

$$b_h^\mathrm{mod}(\boldsymbol{v}_h, \boldsymbol{\mu}_h) = (\boldsymbol{\mu}_h, \boldsymbol{v}_\mathrm{s})_{\Gamma_h^\mathrm{s}} - (\boldsymbol{\mu}_h^\mathrm{mod}, P_\mathrm{s}\boldsymbol{v}_\mathrm{m})_{\Gamma_h^\mathrm{s}}, \qquad \boldsymbol{v}_h \in X_h,\ \boldsymbol{\mu}_h \in M_h. \tag{3.11}$$

As with the original approach described in Section 2.3.2, we analyze (3.10) as a perturbation of a problem of the form analyzed in Section 2.3.1. By employing again the isomorphisms $\mathcal{S}_X$ given in (2.47) and $\mathcal{S}_M$ given in (2.53), together with their inverses $\mathcal{C}_X$ and $\mathcal{C}_M$, respectively, and by setting

$$b_h'^{,\mathrm{mod}}(\widetilde{v}_h, \widetilde{\mu}_h) = b_h^\mathrm{mod}(\mathcal{C}_X\widetilde{v}_h, \mathcal{C}_M\widetilde{\mu}_h), \quad \widetilde{v}_h \in \widetilde{X}_h,\ \widetilde{\mu}_h \in \widetilde{M}_h,$$

we can equivalently reformulate (3.10) as the problem of finding $(u_h'^{,\mathrm{mod}}, \lambda_h'^{,\mathrm{mod}}) \in (\widetilde{X}_h, \widetilde{M}_h)$ such that

$$a_h(\boldsymbol{u}_h'^{,\mathrm{mod}}, \widetilde{\boldsymbol{v}}_h) + b_h'^{,\mathrm{mod}}(\widetilde{\boldsymbol{v}}_h, \boldsymbol{\lambda}_h'^{,\mathrm{mod}}) = l_h(\widetilde{\boldsymbol{v}}_h), \quad \widetilde{\boldsymbol{v}}_h \in \widetilde{X}_h, \tag{3.12a}$$

$$b_h'^{,\mathrm{mod}}(\boldsymbol{u}_h'^{,\mathrm{mod}}, \widetilde{\boldsymbol{\mu}}_h) = 0, \qquad \widetilde{\boldsymbol{\mu}}_h \in \widetilde{M}_h. \tag{3.12b}$$

Again considering the first Strang lemma (2.56), we observe that the consistency errors in the stiffness bilinear form $a(\cdot,\cdot)$ and the right hand side $l(\cdot)$ are already handled by Lemmas 2.17 and 2.19, respectively. In order to provide a proof for the optimality of the approximation property and of the consistency error in the coupling bilinear form $b(\cdot,\cdot)$, we aim to relate the two constrained spaces $\widetilde{V}_h$ and

$$V_h'^{,\mathrm{mod}} = \{\boldsymbol{v}_h \in X_h \ :\ b_h'^{,\mathrm{mod}}(\boldsymbol{v}, \widetilde{\boldsymbol{\mu}}) = 0,\ \widetilde{\boldsymbol{\mu}} \in \widetilde{M}_h\} \tag{3.13}$$

in the same way as we relate $\widetilde{V}_h$ and $\widetilde{V}_h'$ in Lemma 2.15. To this end, we proceed along the following chain:

$$\widetilde{V}_h \xrightarrow{\text{Lemma 2.15}} V_h' \xrightarrow{\mathcal{C}_X} V_h \xrightarrow{\text{Lemma 3.3}} V_h^{\text{mod}} \xrightarrow{\mathcal{S}_X} V_h^{\prime,\text{mod}}, \tag{3.14}$$

where the constrained spaces V_h, V_h^{mod} are defined by

$$\begin{aligned} V_h &= \{\boldsymbol{v}_h \in X_h \ : \ b_h(\boldsymbol{v}, \boldsymbol{\mu}) = 0, \ \boldsymbol{\mu} \in M_h\}, \\ V_h^{\text{mod}} &= \{\boldsymbol{v}_h \in X_h \ : \ b_h^{\text{mod}}(\boldsymbol{v}, \boldsymbol{\mu}) = 0, \ \boldsymbol{\mu} \in M_h\}. \end{aligned}$$

In particular, we work on

$$V_h^{\text{mod}} = \left\{ \boldsymbol{v} \in X_h : \left(\boldsymbol{\mu}_p^i, \boldsymbol{v}_{\text{s}}\right)_{\Gamma_h^{\text{s}}} - \left(\boldsymbol{\mu}_p^i + \Delta\boldsymbol{\mu}_p^i, \ P_{\text{s}}\boldsymbol{v}_{\text{m}}\right)_{\Gamma_h^{\text{s}}} = 0, \ p \in \mathcal{V}^{\text{s}}, \ i = 1, \dots, d \right\},$$

where $\mathcal{V}^{\text{s}}$ indicates the set of vertices of the slave side grid $\mathcal{T}^{\text{s}}$. Moreover, $\boldsymbol{\mu}_p^i = \mu_p \boldsymbol{e}_i$ denotes the vectorial basis function of the Lagrange multiplier space M_h in direction x_i associated with the slave node p, and $\Delta\boldsymbol{\mu}_p^i$ stands for its modification according to (3.6).

Lemma 3.3. *Let the modification be given by* (3.6) *and* (3.8). *Then, for an arbitrary* $\boldsymbol{v} = (\boldsymbol{v}_m, \boldsymbol{v}_s) \in V_h$, *there exists* $\Delta\boldsymbol{v} \in X_h$ *such that*

$$\boldsymbol{v}^{\text{mod}} = \boldsymbol{v} + \Delta\boldsymbol{v} \in V_h^{\text{mod}}, \tag{3.15a}$$

$$\|\Delta\boldsymbol{v}\|_{X_h} \leq Ch^{t+1/2}|\boldsymbol{v}_m|_{t,\Gamma_h^m}, \qquad t \in [0,1], \tag{3.15b}$$

$$\|\Delta\boldsymbol{v}\|_{0,\Gamma_h^{\text{s}}} \leq Ch^{3/2}|\boldsymbol{v}_m|_{1/2,\Gamma_h^m}, \tag{3.15c}$$

$$\|\boldsymbol{v}\|_{X_h} \sim \|\boldsymbol{v}^{\text{mod}}\|_{X_h}, \qquad h \text{ small enough.} \tag{3.15d}$$

The analogous statement holds for arbitrary $\boldsymbol{v}^{\text{mod}} \in V_h^{\text{mod}}$.

Proof. Let $\Delta\boldsymbol{v} \in X_h$ be defined by

$$\Delta\boldsymbol{v} = \left(0 \, , \sum_{p \in \mathcal{V}^{\text{s}}} \phi_p^{\text{s}} \boldsymbol{\beta}_p\right), \ \boldsymbol{\beta}_p \in \mathbb{R}^d \text{ with components } \beta_p^i = \frac{(\Delta\boldsymbol{\mu}_p^i, \ P_{\text{s}}\boldsymbol{v}_{\text{m}})_{\Gamma_h^{\text{s}}}}{(\mu_p, \ \phi_p^{\text{s}})_{\Gamma_h^{\text{s}}}}. \tag{3.16}$$

By the norm equivalence (A.26) and the inverse inequality (A.28), it follows that

$$\boldsymbol{v}^{\text{mod}} = \boldsymbol{v} + \Delta\boldsymbol{v} \in V_h^{\text{mod}} \tag{3.17a}$$

$$\|\Delta\boldsymbol{v}\|_{X_h}^2 \leq Ch^{d-2} \sum_{p \in \mathcal{V}^{\text{s}}, i=1,\dots,d} (\beta_p^i)^2, \tag{3.17b}$$

$$\|\Delta\boldsymbol{v}\|_{0,\Gamma_h^{\text{s}}}^2 \leq Ch^{d-1} \sum_{p \in \mathcal{V}^{\text{s}}, i=1,\dots,d} (\beta_p^i)^2. \tag{3.17c}$$

It remains to estimate the coefficients β_p^i. On a slave element $T^{\text{s}} \in \mathcal{T}^{\text{s}}$, we obtain from (3.6) for the Lagrange multiplier basis function $\Delta\boldsymbol{\mu}_p^i$, $i \in \{1, \dots, d\}$, associated with the node p, that

$$\Delta\boldsymbol{\mu}_p^i|_{T^{\text{s}}} = \sum_q \gamma_{pq} \Delta\phi_{pq} \left(\sum_{k=1}^{d} (\boldsymbol{e}_i \cdot \boldsymbol{b}_p^{(k)}) \Delta\boldsymbol{b}_{pq}^{(k)} \right). \tag{3.18}$$

Due to the proper scaling of the difference $\Delta\phi_{pq}$ given by (3.5), we can use the piecewise constant L^2-projection onto the slave elements, indicated by Π_0, and obtain, considering the fact that the area of the support of μ_p and ϕ_p^{s} is $O(h^{d-1})$, that

$$\begin{aligned}(\beta_p^i)^2 &= \left(\frac{\left(\Delta\boldsymbol{\mu}_p^i,\ P_{\mathrm{s}}\boldsymbol{v}_{\mathrm{m}} - \Pi_0 P_{\mathrm{s}}\boldsymbol{v}_{\mathrm{m}}\right)_{\Gamma_h^{\mathrm{s}}}}{\left(\mu_p,\ \phi_p^{\mathrm{s}}\right)_{\Gamma_h^{\mathrm{s}}}}\right)^2 \\ &\leq \frac{C}{(h^{d-1})^2}\left(\Delta\boldsymbol{\mu}_p^i,\ P_{\mathrm{s}}\boldsymbol{v}_{\mathrm{m}} - \Pi_0 P_{\mathrm{s}}\boldsymbol{v}_{\mathrm{m}}\right)_{0,\Gamma_h^{\mathrm{s}}}^2 .\end{aligned}$$

Setting $\Gamma_h^p = \operatorname{supp}\mu_p$, we denote by $\mathcal{T}^p \subset \mathcal{T}^{\mathrm{s}}$ the set of all slave elements T^{s} such that $\Gamma_h^p \cap T^{\mathrm{s}}$ has a positive $(d-1)$-dimensional measure, and remark that $|\mathcal{T}^p| < C$. By using the Cauchy-Schwarz inequality, it follows that, for $t \in [0,1]$,

$$\begin{aligned}(\beta_p^i)^2 &\leq C(h^{1-d})^2 \sum_{T^{\mathrm{s}}\in\mathcal{T}^p} \|\Delta\boldsymbol{\mu}_p^i\|_{0,T^{\mathrm{s}}}^2 \|P_{\mathrm{s}}\boldsymbol{v}_{\mathrm{m}} - \Pi_0 P_{\mathrm{s}}\boldsymbol{v}_{\mathrm{m}}\|_{0,T^{\mathrm{s}}}^2 \\ &\leq C(h^{t+1-d})^2 |P_{\mathrm{s}}\boldsymbol{v}_{\mathrm{m}}|_{t,\Gamma_h^p}^2 \|\Delta\boldsymbol{\mu}_p^i\|_{0,\Gamma_h^p}^2.\end{aligned}$$

Considering (3.4), (3.5), and the definition of G in (3.8), an investigation of the terms appearing in (3.18) yields $\|\Delta\boldsymbol{\mu}_p^i\|_{0,\Gamma_h^p}^2 = O(h^{d+1})$, and, therefore,

$$(\beta_p^i)^2 \leq Ch^{2t+3-d}|P_{\mathrm{s}}\boldsymbol{v}_{\mathrm{m}}|_{t,\Gamma_h^p}^2.$$

Summing up, the stability of the projection P_{s} and (3.17b) imply (3.15b), and, choosing $t = 1/2$, (3.17c) yields (3.15c). The norm equivalence (3.15d) and the analogous statement of the Lemma follow by the same reasoning as in the proof of Lemma 2.15. □

With the following lemma, we complete the chain (3.14).

Lemma 3.4. *For an arbitrary $\widetilde{\boldsymbol{v}}_h = (\widetilde{\boldsymbol{v}}_m, \widetilde{\boldsymbol{v}}_s) \in \widetilde{V}_h$, there exists $\Delta'^{,\mathrm{mod}}\widetilde{\boldsymbol{v}}_h \in \widetilde{X}_h$ such that*

$$\boldsymbol{v}_h'^{,\mathrm{mod}} = \widetilde{\boldsymbol{v}}_h + \Delta'^{,\mathrm{mod}}\widetilde{\boldsymbol{v}}_h \in V_h'^{,\mathrm{mod}}, \tag{3.19a}$$

$$\|\Delta'^{,\mathrm{mod}}\widetilde{\boldsymbol{v}}_h\|_X \leq Ch^{t+1/2}|\widetilde{\boldsymbol{v}}_m|_{t,\Gamma}, \qquad t \in [0,1], \tag{3.19b}$$

$$\|(\Delta'^{,\mathrm{mod}}\widetilde{\boldsymbol{v}}_h)_s\|_{0,\Gamma} \leq Ch^{3/2}|\widetilde{\boldsymbol{v}}_m|_{1/2,\Gamma}, \tag{3.19c}$$

$$\|\widetilde{\boldsymbol{v}}_h\|_X \sim \|\boldsymbol{v}_h'^{,\mathrm{mod}}\|_X, \qquad h \text{ small enough.} \tag{3.19d}$$

The analogous statement holds for arbitrary $\boldsymbol{v}_h'^{,\mathrm{mod}} \in V_h'^{,\mathrm{mod}}$.

Proof. Owing to the observation (2.49), it can be easily seen that

$$\|\boldsymbol{v}_h\|_{X_h} \sim \|\mathcal{S}_X\boldsymbol{v}_h\|_X, \quad |\boldsymbol{v}_k|_{t,\Gamma_h^k} \sim |(\mathcal{S}_X\boldsymbol{v}_h)_k|_{t,\Gamma}, \quad \boldsymbol{v}_h \in X_h,\ t \in [0,1],\ k = \mathrm{m},\mathrm{s}, \tag{3.20a}$$

$$\|\widetilde{\boldsymbol{v}}_h\|_X \sim \|\mathcal{C}_X\widetilde{\boldsymbol{v}}_h\|_{X_h}, \quad |\widetilde{\boldsymbol{v}}_k|_{t,\Gamma} \sim |(\mathcal{C}_X\widetilde{\boldsymbol{v}})_k|_{t,\Gamma_h^k}, \quad \widetilde{\boldsymbol{v}}_h \in \widetilde{X}_h,\ t \in [0,1],\ k = \mathrm{m},\mathrm{s}. \tag{3.20b}$$

For the investigation of the last three connecting arrows in the chain (3.14), we start with $\boldsymbol{v}_h' \in V_h'$ and obtain by using Lemma 3.3 and the isomorphisms $\mathcal{S}_X$, $\mathcal{C}_X$ that

$$\boldsymbol{v}_h' \;\to\; \boldsymbol{v}_h = \mathcal{C}_X \boldsymbol{v}_h' \;\to\; \boldsymbol{v}_h^{\mathrm{mod}} = \mathcal{C}_X \boldsymbol{v}_h' + \Delta \mathcal{C}_X \boldsymbol{v}_h' \;\to\; \boldsymbol{v}_h'^{,\mathrm{mod}} = \boldsymbol{v}_h' + \mathcal{S}_X \Delta \mathcal{C}_X \boldsymbol{v}_h',$$

defining $\Delta^{\mathrm{mod}} = \mathcal{S}_X \Delta \mathcal{C}_X$, which gives

$$\|\Delta^{\mathrm{mod}} \boldsymbol{v}_h'\|_X \;\le\; C \|\Delta \mathcal{C}_X \boldsymbol{v}_h'\|_X \;\le\; C h^{t+1/2} |(\mathcal{C}_X \boldsymbol{v}_h')_{\mathrm{m}}|_{t,\Gamma_h^{\mathrm{m}}} \;\le\; C h^{t+1/2} |\boldsymbol{v}_{\mathrm{m}}'|_{t,\Gamma},$$

as well as

$$\|(\Delta^{\mathrm{mod}} \boldsymbol{v}_h')_{\mathrm{s}}\|_{0,\Gamma} \;\le\; C \|(\Delta \mathcal{C}_X \boldsymbol{v}_h')_{\mathrm{s}}\|_{0,\Gamma_h^{\mathrm{s}}} \;\le\; C h^{3/2} |(\mathcal{C}_X \boldsymbol{v}_h')_{\mathrm{m}}|_{1/2,\Gamma_h^{\mathrm{m}}} \;\le\; C h^{3/2} |\boldsymbol{v}_{\mathrm{m}}'|_{1/2,\Gamma}.$$

Incorporating the first connecting arrow in the chain (3.14), we now start with $\widetilde{\boldsymbol{v}}_h \in \widetilde{V}_h$ and set by using Lemma 2.15

$$\boldsymbol{v}_h'^{,\mathrm{mod}} \;=\; \boldsymbol{v}_h' + \Delta^{\mathrm{mod}} \boldsymbol{v}_h' \;=\; \widetilde{\boldsymbol{v}}_h + \Delta' \widetilde{\boldsymbol{v}}_h + \Delta^{\mathrm{mod}} \boldsymbol{v}_h' \;=\; \widetilde{\boldsymbol{v}}_h + (\Delta' + \Delta^{\mathrm{mod}}(\mathrm{Id} + \Delta')) \widetilde{\boldsymbol{v}}_h,$$

defining $\Delta'^{,\mathrm{mod}} = \Delta' + \Delta^{\mathrm{mod}}(\mathrm{Id} + \Delta')$. With Lemmas 2.15 and 3.3, this gives (3.19b) by

$$\begin{aligned} \|\Delta'^{,\mathrm{mod}} \widetilde{\boldsymbol{v}}_h\|_X \;&\le\; \|\Delta' \widetilde{\boldsymbol{v}}_h\|_X + \|\Delta^{\mathrm{mod}}(\mathrm{Id} + \Delta') \widetilde{\boldsymbol{v}}_h\|_X \\ &\le\; C h^{t+1/2} \left(|\widetilde{\boldsymbol{v}}_{\mathrm{m}}|_{t,\Gamma} + |(\Delta' \widetilde{\boldsymbol{v}}_h)_{\mathrm{m}}|_{t,\Gamma} \right) \;\le\; C h^{t+1/2} |\widetilde{\boldsymbol{v}}_{\mathrm{m}}|_{t,\Gamma}, \end{aligned}$$

since $(\Delta' \widetilde{\boldsymbol{v}}_h)_{\mathrm{m}} = 0$. Relation (3.19c) is obtained the same way. Starting from (3.19b) and following the same lines as in the proof of Lemma 3.3, we arrive at(3.19d). □

Lemma 3.5. *Let $a(\cdot,\cdot)$ and $V_h'^{,\mathrm{mod}}$ be given by* (3.1) *and* (3.13)*, respectively. There exists $\alpha'^{,\mathrm{mod}} > 0$ such that for h small enough*

$$a(\boldsymbol{v}_h'^{,\mathrm{mod}}, \boldsymbol{v}_h'^{,\mathrm{mod}}) \;\ge\; \alpha'^{,\mathrm{mod}} \|\boldsymbol{v}_h'^{,\mathrm{mod}}\|_X^2, \qquad \boldsymbol{v}_h'^{,\mathrm{mod}} \in V_h'^{,\mathrm{mod}}. \tag{3.21}$$

Proof. For an arbitrary $\boldsymbol{v}_h'^{,\mathrm{mod}} \in V_h'^{,\mathrm{mod}}$, we choose $\widetilde{\boldsymbol{v}}_h \in \widetilde{V}_h$ as in Lemma 3.4, and observe, by using the continuity of $a(\cdot,\cdot)$ and (3.19b), that

$$\left| a(\widetilde{\boldsymbol{v}}_h, \Delta'^{,\mathrm{mod}} \widetilde{\boldsymbol{v}}_h) \right| \le C \|\widetilde{\boldsymbol{v}}_h\|_X \|\Delta'^{,\mathrm{mod}} \widetilde{\boldsymbol{v}}_h\|_X \le C h \|\widetilde{\boldsymbol{v}}_h\|_X^2.$$

With the fact that $a(\cdot,\cdot)$ is coercive on $\widetilde{V}_h$, which is a consequence of Lemma 2.7 and Assumption 2.1(b), and with (3.19d), this gives for h small enough

$$a(\boldsymbol{v}_h'^{,\mathrm{mod}}, \boldsymbol{v}_h'^{,\mathrm{mod}}) \ge (\alpha - C h) \|\widetilde{\boldsymbol{v}}_h\|_X^2 \ge \alpha'^{,\mathrm{mod}} \|\boldsymbol{v}_h'^{,\mathrm{mod}}\|_X^2,$$

which is the desired result. □

Lemma 3.6. *Let $\boldsymbol{u} \in (H^1_{\Gamma_{\mathrm{D}}}(\Omega))^d \cap \prod_{k=\mathrm{m,s}} (H^2(\Omega^k))^d$ and $V_h'^{,\mathrm{mod}}$ be given by* (3.13)*. Then it holds that*

$$\inf_{\boldsymbol{v}_h'^{,\mathrm{mod}} \in V_h'^{,\mathrm{mod}}} \|\boldsymbol{u} - \boldsymbol{v}_h'^{,\mathrm{mod}}\|_X \;\le\; C h \left(\sum_{k=\mathrm{m,s}} \|\boldsymbol{u}\|_{2,\Omega^k}^2 \right)^{1/2}. \tag{3.22}$$

Proof. Follows the lines of the proof of Lemma 2.16. □

Lemma 3.7. *Let $\boldsymbol{u} \in (H^1_{\Gamma_\mathrm{D}}(\Omega))^d \cap \prod_{k=\mathrm{m,s}} (H^2(\Omega^k))^d$ be the weak solution of (1.3)-(1.6), and assume that $\boldsymbol{\lambda} \in M$ is defined by (1.17). Let the coupling bilinear form $b(\cdot,\cdot)$ and the constrained space $V_h'^{,\mathrm{mod}}$ be defined by (3.2) and (3.13), respectively. For h small enough, it holds that*

$$\sup_{\boldsymbol{v}_h'^{,\mathrm{mod}} \in V_h'^{,\mathrm{mod}}} \frac{b(\boldsymbol{v}_h'^{,\mathrm{mod}}, \boldsymbol{\lambda})}{\|\boldsymbol{v}_h'^{,\mathrm{mod}}\|_X} \leq Ch \left(\sum_{k=\mathrm{m,s}} \|\boldsymbol{u}\|^2_{2,\Omega^k} \right)^{1/2}. \tag{3.23}$$

Proof. Follows the lines of the proof of Lemma 2.18. □

The same reasoning as in Chapter 2 yields the following theorem.

Theorem 3.8. *Let $\boldsymbol{u} \in (H^1_{\Gamma_\mathrm{D}}(\Omega))^d \cap \prod_{k=\mathrm{m,s}} (H^2(\Omega^k))^d$ be the weak solution of (1.3)-(1.6), and assume that $\boldsymbol{\lambda} \in M$ is defined by (1.17). Then the solution $\boldsymbol{u}_h^{\mathrm{mod}}$ of (3.12) satisfies for h small enough:*

$$\|\boldsymbol{u} - \boldsymbol{u}_h^{\mathrm{mod}}\|_{X_h} \leq C(\boldsymbol{u})h.$$

Assembly of the Coupling Matrices

We provide a detailed account of how the modification (3.9) affects the assembly of the matrix M from (2.68) in two dimensions. We focus on a slave edge e_s and a master edge e_m. The basis functions $\boldsymbol{\mu}_j^i = \mu_j \boldsymbol{e}_i$ associated with the node $\boldsymbol{p}_j^\mathrm{s}$ are modified by

$$\Delta\boldsymbol{\mu}_j^i|_{e_\mathrm{s}} = (\boldsymbol{\mu}_j^i)^{\mathrm{mod}} - \boldsymbol{\mu}_j^i = -\frac{1}{2}\phi_{12}^\mathrm{s} \left(n_j^i \Delta\boldsymbol{n} + t_j^i \Delta\boldsymbol{t} \right), \qquad i = x, y, \quad j = 1, 2.$$

With the endpoints $\boldsymbol{p}_k^\mathrm{m}$ of the master edge e_m, we associate the basis functions $\boldsymbol{\phi}_k^\ell = \phi_k^\mathrm{m} \boldsymbol{e}_\ell|_{e_\mathrm{m}}$, $k = 1, 2$, $\ell = x, y$, which are extended by zero outside e_m. In addition to the unmodified approach, one has to evaluate the integral

$$-(\Delta\boldsymbol{\mu}_j^i, P_\mathrm{s}\boldsymbol{\phi}_k^\ell)_{e_\mathrm{s}}$$

for the coupling of $(\boldsymbol{\mu}_j^i)^{\mathrm{mod}}$ with $\boldsymbol{\phi}_k^\ell$. Consequently, setting $m_k = \frac{1}{2}(\phi_{12}^\mathrm{s}, P_\mathrm{s}\phi_k^\mathrm{m})_{e_\mathrm{s}}$, the following entries have to be added to the matrix M for the coupling of the node $\boldsymbol{p}_k^\mathrm{m}$ to the nodes $\boldsymbol{p}_1^\mathrm{s}$ and $\boldsymbol{p}_2^\mathrm{s}$:

$$\left(\begin{array}{c|cccc} & (\boldsymbol{\mu}_1^x)^{\mathrm{mod}} & (\boldsymbol{\mu}_1^y)^{\mathrm{mod}} & (\boldsymbol{\mu}_2^x)^{\mathrm{mod}} & (\boldsymbol{\mu}_2^y)^{\mathrm{mod}} \\ \hline \boldsymbol{\phi}_k^x & (1 - \boldsymbol{n}_1 \cdot \boldsymbol{n}_2)m_k & (\boldsymbol{n}_1 \times \boldsymbol{n}_2)m_k & (\boldsymbol{n}_1 \cdot \boldsymbol{n}_2 - 1)m_k & (\boldsymbol{n}_1 \times \boldsymbol{n}_2)m_k \\ \boldsymbol{\phi}_k^y & -(\boldsymbol{n}_1 \times \boldsymbol{n}_2)m_k & (1 - \boldsymbol{n}_1 \cdot \boldsymbol{n}_2)m_k & -(\boldsymbol{n}_1 \times \boldsymbol{n}_2)m_k & (\boldsymbol{n}_1 \cdot \boldsymbol{n}_2 - 1)m_k \end{array}\right).$$

We note that $\phi_{12}^\mathrm{s} = \frac{1}{3}(\mu_1 - \mu_2)$, thus, m_k can easily be obtained reusing the information from the original assembly process. Moreover, it is obvious that in case of a straight interface, i.e., $\boldsymbol{n}_1 = \boldsymbol{n}_2$, the modification vanishes.

3.3.2 Point-wise Algebraic Modification

In order to motivate our choice for the point-wise modification, we note that the discrete system (1.22) is for $\lambda_\mathrm{s} = \lambda_h$ and $D_\mathrm{s} = D$ equivalent to

$$\begin{pmatrix} A_\mathrm{ii} & A_\mathrm{im} & A_\mathrm{is} & 0 & 0 \\ A_\mathrm{mi} & A_\mathrm{mm} & 0 & 0 & D_\mathrm{m}^\mathrm{T} \\ A_\mathrm{si} & 0 & A_\mathrm{ss} & D_\mathrm{s}^\mathrm{T} & 0 \\ 0 & -M & D_\mathrm{s} & 0 & 0 \\ 0 & 0 & 0 & M^\mathrm{T} & D_\mathrm{m} \end{pmatrix} \begin{pmatrix} u_h^\mathrm{i} \\ u_h^\mathrm{m} \\ u_h^\mathrm{s} \\ \lambda_\mathrm{s} \\ \lambda_\mathrm{m} \end{pmatrix} = \begin{pmatrix} f^\mathrm{i} \\ f^\mathrm{m} \\ f^\mathrm{s} \\ 0 \\ 0 \end{pmatrix}. \tag{3.24}$$

The system above admits the definition of a discrete dual Lagrange multiplier on the master side by

$$\lambda_\mathrm{m} = -D_\mathrm{m}^{-1} M^\mathrm{T} \lambda_\mathrm{s}, \tag{3.25}$$

where the entries of the diagonal matrix D_m are given by $(1, \phi_q^\mathrm{m})_{\Gamma_h^\mathrm{m}}$. Formally, (3.24) corresponds to a three field approach. The fluxes λ_m and λ_s satisfy a weak continuity condition. We refer to [28] for more details. From (3.25), it can be seen that a Lagrange multiplier λ_s on the slave side which is constant in normal direction, yields a multiplier λ_m on the master side which does not necessarily possess this property. In Section 3.2, this lack of preservation has been identified as the reason for the misbehavior of the dual Lagrange multipliers. Our modification will replace M in (3.25) by a matrix M^mod, such that quantities constant in normal direction are preserved.

Formulation

In the case of curvilinear interfaces, we cannot preserve quantities being constant in normal direction and at the same time quantities being constant with respect to a fixed coordinate system. This observation motivates our choice that we work with a non-symmetric Petrov–Galerkin scheme, where we replace M in the last line of (3.24) by the modified matrix

$$M^\mathrm{mod} = B_\mathrm{s} M B_\mathrm{m}^\mathrm{T}, \tag{3.26}$$

where $B_\mathrm{s} \in \mathbb{R}^{N_\mathrm{s} d \times N_\mathrm{s} d}$ and $B_\mathrm{m} \in \mathbb{R}^{N_\mathrm{m} d \times N_\mathrm{m} d}$ are the block diagonal matrices with entries $B_{p,\mathrm{s}}$ and $B_{q,\mathrm{m}}$, respectively, i.e., each block consists of an orthonormal basis with one basis vector being the unit normal vector associated with the corresponding node. By N_k, we indicate the total number of finite element nodes on $\mathcal{T}^k$, $k = \mathrm{m}, \mathrm{s}$. We note that D_m has the same block structure as B_m with $(d \times d)$-blocks of the form $s\mathrm{Id}$, $s \in \mathbb{R}$. Therefore, we have that $D_\mathrm{m}^{-1} B_\mathrm{m} = B_\mathrm{m} D_\mathrm{m}^{-1}$, yielding

$$\lambda_\mathrm{m} = -D_\mathrm{m}^{-1} (B_\mathrm{s} M B_\mathrm{m}^\mathrm{T})^\mathrm{T} \lambda_\mathrm{s} = -B_\mathrm{m} D_\mathrm{m}^{-1} M^\mathrm{T} B_\mathrm{s}^\mathrm{T} \lambda_\mathrm{s},$$

which gives

$$B_\mathrm{m}^\mathrm{T} \lambda_\mathrm{m} = -D_\mathrm{m}^{-1} M^\mathrm{T} B_\mathrm{s}^\mathrm{T} \lambda_\mathrm{s}.$$

We note that the application of the rotation B_s^T to the coefficient vector λ_s yields the components in normal direction and with respect to the tangent plane in each node.

Thus, if λ_s is constant in a discrete way in normal direction and with respect to the tangent planes, we have that $B_\mathrm{s}^\mathrm{T}\lambda_\mathrm{s} \in \mathbb{R}^{N_\mathrm{s}d}$ can be written as $c_\mathrm{s} = (\boldsymbol{a}^\mathrm{T}, \dots, \boldsymbol{a}^\mathrm{T})^\mathrm{T}$ with $\boldsymbol{a} \in \mathbb{R}^d$. Additionally observing that $D_\mathrm{m}c_\mathrm{m} = M^\mathrm{T}c_\mathrm{s} \in \mathbb{R}^{N_\mathrm{m}d}$ with $c_\mathrm{m} = (\boldsymbol{a}^\mathrm{T}, \dots, \boldsymbol{a}^\mathrm{T})^\mathrm{T}$, we conclude with

$$B_\mathrm{s}^\mathrm{T}\lambda_\mathrm{s} = c_\mathrm{s} \quad \Leftrightarrow \quad B_\mathrm{m}^\mathrm{T}\lambda_\mathrm{m} = c_\mathrm{m} \tag{3.27}$$

Thus, the modification (3.26) guarantees that the normal and tangential components of a vector field are transferred correctly between the master and the slave side in the sense of (3.27). We note that the mass matrix M in the fourth line of (3.24) is kept. Thus, for the primal variable, we preserve constants with respect to a fixed coordinate system whereas for the dual variable constants with respect to the normal direction are preserved across the interface.

Analysis

Proceeding like in Section 3.3.1, we arrive at (3.10),(3.12), and have to relate the constrained spaces $\widetilde{V}_h$ and $V_h^{\prime,\mathrm{mod}}$. If we proceed along the chain (3.14), it is sufficient to show the third arrow analogous to Lemma 3.3. The remaining arrows follow by the same reasoning as in the proof of Lemma 3.4.

Lemma 3.9. *Let the modification be given by* (3.26). *Then, for an arbitrary* $\boldsymbol{v} = (\boldsymbol{v}_m, \boldsymbol{v}_s) \in V_h$, *there exists* $\Delta\boldsymbol{v} \in X_h$ *such that*

$$\boldsymbol{v}^\mathrm{mod} = \boldsymbol{v} + \Delta\boldsymbol{v} \in V_h^\mathrm{mod}, \tag{3.28a}$$

$$\|\Delta\boldsymbol{v}\|_{X_h} \leq Ch^{1/2}\|\boldsymbol{v}_m\|_{X_h}, \tag{3.28b}$$

$$\|\Delta\boldsymbol{v}\|_{0,\Gamma_h^\mathrm{s}} \leq Ch|\boldsymbol{v}_m|_{0,\Gamma_h^m}, \tag{3.28c}$$

$$\|\boldsymbol{v}\|_{X_h} \sim \|\boldsymbol{v}^\mathrm{mod}\|_{X_h}, \qquad h \text{ small enough.} \tag{3.28d}$$

The analogous statement holds for arbitrary $\boldsymbol{v}^\mathrm{mod} \in V_h^\mathrm{mod}$.

Proof. In terms of the scalar basis functions μ_p, the space V_h can be written as

$$V_h \;=\; \{\boldsymbol{v} \in X_h : (\mu_p, [\boldsymbol{v}]_h)_{\Gamma_h^\mathrm{s}} = \boldsymbol{0},\ p \in \mathcal{V}^\mathrm{s}\}$$

For $\boldsymbol{v} = (\boldsymbol{v}_\mathrm{m}, \boldsymbol{v}_\mathrm{s}) \in X_h$ with $\boldsymbol{v}_\mathrm{m} = \sum_{q\in\mathcal{V}^\mathrm{m}} \boldsymbol{\alpha}_q^\mathrm{m}\phi_q^\mathrm{m}$, $\boldsymbol{v}_\mathrm{s} = \sum_{q\in\mathcal{V}^\mathrm{s}} \boldsymbol{\beta}_q^\mathrm{s}\phi_q^\mathrm{s}$, we deduce from (3.26) that

$$V_h^\mathrm{mod} \;=\; \left\{ \boldsymbol{v} \in X_h : \left(\mu_p, \boldsymbol{v}_\mathrm{s} - \sum_{q\in\mathcal{V}^\mathrm{m}} Q_{pq}\boldsymbol{\alpha}_q^\mathrm{m} P_\mathrm{s}\phi_q^\mathrm{m}\right)_{\Gamma_h^\mathrm{s}} = \boldsymbol{0},\ p \in \mathcal{V}^\mathrm{s} \right\}$$

with $Q_{pq} = B_{p,\mathrm{s}}B_{q,\mathrm{m}}^\mathrm{T}$. We note that, in terms of the reference orthonormal basis B_* and the Householder reflections H_p and H_q introduced above, we have that

$$Q_{pq} = B_{p,\mathrm{s}}B_{q,\mathrm{m}}^\mathrm{T} = H_pB_*B_*^\mathrm{T}H_q^\mathrm{T} = H_pH_q, \tag{3.29}$$

thus, Q_{pq} is the rotation matrix which maps the orthonormal system $B_{q,\mathrm{m}}$ to the system $B_{p,\mathrm{s}}$. In the special case of a planar interface, Q_{pq} is the identity for all nodes and thus $V_h = V_h^{\mathrm{mod}}$. For $\boldsymbol{v} \in V_h$, we define $\Delta\boldsymbol{v} \in X_h$ by

$$\Delta\boldsymbol{v} \;=\; \left(0\,,\,\sum_{p\in\mathcal{V}^{\mathrm{s}}}\boldsymbol{\gamma}_p\phi_p^{\mathrm{s}}\right), \quad \boldsymbol{\gamma}_p = \frac{\left(\mu_p,\; P_{\mathrm{s}}\left(\sum_{q\in\mathcal{V}^{\mathrm{m}}}(Q_{pq}-\mathrm{Id})\boldsymbol{\alpha}_q^{\mathrm{m}}\phi_q^{\mathrm{m}}\right)\right)_{\Gamma_h^{\mathrm{s}}}}{(\phi_p^{\mathrm{s}},\;\mu_p)_{\Gamma_h^{\mathrm{s}}}}. \tag{3.30}$$

Using the duality (1.24), it is easy to see that $\boldsymbol{v}^{\mathrm{mod}} = \boldsymbol{v} + \Delta\boldsymbol{v} \in V_h^{\mathrm{mod}}$. In particular,

$$\begin{aligned}
&\left(\mu_p, \sum_{q\in\mathcal{V}^{\mathrm{s}}}(\boldsymbol{\beta}_q^{\mathrm{s}}+\boldsymbol{\gamma}_q^{\mathrm{s}})\phi_q^{\mathrm{s}} - P_{\mathrm{s}}\left(\sum_{q\in\mathcal{V}^{\mathrm{m}}}Q_{pq}\boldsymbol{\alpha}_q^{\mathrm{m}}\phi_q^{\mathrm{m}}\right)\right)_{\Gamma_h^{\mathrm{s}}}\\
&= \boldsymbol{\gamma}_p(\mu_p,\,\phi_p^{\mathrm{s}})_{\Gamma_h^{\mathrm{s}}} \;+\; \left(\mu_p, \boldsymbol{v}_{\mathrm{s}} - P_{\mathrm{s}}\left(\sum_{q\in\mathcal{V}^{\mathrm{m}}}Q_{pq}\boldsymbol{\alpha}_q^{\mathrm{m}}\phi_q^{\mathrm{m}}\right)\right)_{\Gamma_h^{\mathrm{s}}}\\
&= (\mu_p, \boldsymbol{v}_{\mathrm{s}} - P_{\mathrm{s}}\boldsymbol{v}_{\mathrm{m}})_{\Gamma_h^{\mathrm{s}}} \;=\; 0.
\end{aligned}$$

Using the equivalence of discrete norms (A.26) and scaling arguments (A.28), the construction of $\Delta\boldsymbol{v}$ by (3.30) implies that

$$\|\Delta\boldsymbol{v}\|_{X_h}^2 \le Ch^{d-2}\sum_{p\in\mathcal{V}^{\mathrm{s}}}|\boldsymbol{\gamma}_p|^2, \qquad \|\Delta\boldsymbol{v}\|_{0,\Gamma_h^{\mathrm{s}}}^2 \le Ch^{d-1}\sum_{p\in\mathcal{V}^{\mathrm{s}}}|\boldsymbol{\gamma}_p|^2. \tag{3.31}$$

An estimation of the coefficients $\boldsymbol{\gamma}_p$ gives

$$|\boldsymbol{\gamma}_p|^2 \;\le\; C\sum_{q\in\mathcal{V}^{p,\mathrm{m}}}|\boldsymbol{\alpha}_q^{\mathrm{m}}|^2\|Q_{pq}-\mathrm{Id}\|_\infty^2,$$

where $\mathcal{V}^{p,\mathrm{m}}$ denotes the set of all master nodes q such that $\operatorname{supp}\mu_p \cap \operatorname{supp}\phi_q^{\mathrm{m}}$ has positive $(d-1)$-dimensional measure. Considering (3.29) and the fact that $B_{p,\mathrm{s}} = O(1)$, together with applying assumption (3.4), yield

$$\|Q_{pq}-\mathrm{Id}\|_\infty^2 = \|B_{p,\mathrm{s}}B_{q,\mathrm{m}}^{\mathrm{T}} - \mathrm{Id}\|_\infty^2 = \|B_{p,\mathrm{s}}(B_{q,\mathrm{m}}^{\mathrm{T}} - B_{p,\mathrm{s}}^{\mathrm{T}})\|_\infty^2 = O(h^2).$$

Summing up, we obtain

$$\sum_{p\in\mathcal{V}^{\mathrm{s}}}|\boldsymbol{\gamma}_p|^2 \;\le\; Ch^2\sum_{q\in\mathcal{V}^{\mathrm{m}}}|\boldsymbol{\alpha}_q^m|^2.$$

By the same considerations as above, we have

$$\sum_{q\in\mathcal{V}^{\mathrm{m}}}|\boldsymbol{\alpha}_q^m|^2 \;\le\; Ch^{1-d}\|\boldsymbol{v}_{\mathrm{m}}\|_{0,\Gamma_h^{\mathrm{m}}}^2,$$

and, therefore, taking into account (3.31),

$$\|\Delta\boldsymbol{v}\|_{X_h}^2 \le Ch\|\boldsymbol{v}_{\mathrm{m}}\|_{X_h}^2, \quad \text{and} \quad \|\Delta\boldsymbol{v}\|_{0,\Gamma_h^{\mathrm{s}}}^2 \le Ch^2\|\boldsymbol{v}_{\mathrm{m}}\|_{0,\Gamma_h^{\mathrm{m}}}^2,$$

yielding (3.28b) and (3.28c). The norm equivalence (3.28d) follows from (3.28b) by the same reasoning as in the proof of Lemma 3.3, as well as the analogous statements for arbitrary $\boldsymbol{v}^{\mathrm{mod}} \in V_h^{\mathrm{mod}}$. □

Unfortunately, Lemma 3.9 only admits a suboptimal approximation property for the constrained space V_h^{mod}. We recall that a translation which is a rigid body motion in linear elasticity is not in V_h^{mod}. The main difference between Lemma 3.9 and Lemma 3.3 is that we can exploit the fact that $\Delta\boldsymbol{\mu}$ is orthogonal on a constant with respect to the L^2-scalar product. Thus the upper bounds (3.15b) and (3.15c) provide a higher order than the bounds (3.28b) and (3.28c), respectively. However, it is possible to derive optimal a priori estimates by considering the non-symmetric Petrov–Galerkin approach, namely, to find $\boldsymbol{u}_h \in V_h$ such that

$$a_h(\boldsymbol{u}_h, \boldsymbol{v}) = f_h(\boldsymbol{v}), \qquad \boldsymbol{v} \in V_h^{\mathrm{mod}}.$$

For the above formulation, the approximation property is a standard result. It remains to prove the wellposedness and to estimate the consistency error. We remark that Lemma 3.9 implies that $\dim V_h^{\mathrm{mod}} = \dim V_h$, and, therefore, it is sufficient to prove the following lemma for showing wellposedness, [39].

Lemma 3.10. *Provided that h is small enough, there exists α such that*

$$\inf_{\boldsymbol{w}\in V_h} \sup_{\boldsymbol{v}\in V_h^{mod}} \frac{a_h(\boldsymbol{w}, \boldsymbol{v})}{\|\boldsymbol{w}\|_{X_h}\|\boldsymbol{v}\|_{X_h}} \geq \alpha.$$

Proof. For $\boldsymbol{w} \in V_h$, set $\boldsymbol{v} = \boldsymbol{w} + \Delta\boldsymbol{w} \in V_h^{\mathrm{mod}}$ with $\Delta\boldsymbol{w}$ given by Lemma 3.9. This yields

$$\begin{aligned} a_h(\boldsymbol{w}, \boldsymbol{v}) &= a_h(\boldsymbol{w}, \boldsymbol{w}) + a_h(\boldsymbol{w}, \Delta\boldsymbol{w}) \\ &\geq \alpha\|\boldsymbol{w}\|_{X_h}^2 - C\|\boldsymbol{w}\|_{X_h}\|\Delta\boldsymbol{w}\|_{X_h} \\ &\geq (\alpha - Ch^{1/2})\|\boldsymbol{w}\|_{X_h}^2, \end{aligned}$$

which gives the desired condition provided that h is small enough. □

We note that the implementation of this modification can be easily carried out. In addition to M, we only have to compute for each node q on the slave and on the master side the local matrices B_q. Working with a symmetric formulation, we cannot preserve translations. Moreover for the symmetric approach only sub-optimal a priori estimates can be shown. This results from the fact that we use a point-wise modification which does not show L^2-stability. The modification $b_h^{\mathrm{mod}}(\cdot,\cdot)$ can be also interpreted by replacing $\boldsymbol{\mu}$ on the master side by $\boldsymbol{\mu} + \Delta\boldsymbol{\mu}$, where $\Delta\boldsymbol{\mu}$ is the sum of Dirac distributions.

3.4 Numerical Results

In the following, we present several numerical examples. First, we illustrate the effect of the two modifications, where it turns out that they lead to almost the same results

as the method using standard Lagrange multipliers. We also show the robustness of the modifications with respect to rotations of the grid and to the choice of the slave side. Moreover, an example is considered where the surface tractions are constant in tangential direction. We also present an analogous example in three dimensions. Finally, an application to a two-body contact problem is investigated.

3.4.1 Effect of the Modification

As a first example, the effect of the modification is illustrated in Figure 3.7. The two pictures in the left part show that, for the example considered in Section 3.2, the modified approach yields a visually satisfying result in contrast to the unmodified method. This

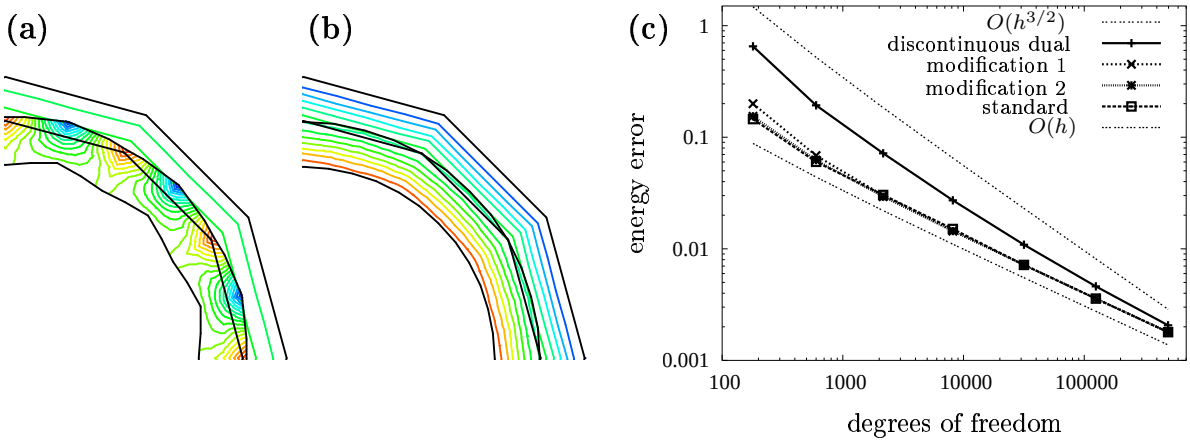

Figure 3.7: Van Mises stress with (a) unmodified, (b) modified dual LM; (c) decay of the energy error using standard, dual, and modified dual LM.

impression gets confirmed by the error decay shown in the right part of Figure 3.7, which was derived in the same way as Figure 3.3. The two modifications already improve the results significantly for a very moderate number of unknowns. The measured errors are for very coarse grids at most slightly worse than the ones from the method using the standard LM. Apart from the coarsest grid, both modifications yield almost equal results. We point out that all the benefits of the dual approach are preserved by the modifications. As expected from the fact that the modification only enters with $O(h^{3/2})$ in the a priori estimates, the relative differences in the errors of the unmodified and the modified approaches decrease as the number of unknowns increases.

3.4.2 Rotation of the Grid

In our second test, we investigate the behavior of the modified method under rotations of the grid on the inner ring. The meshsize on the inner ring corresponds to an angle of $\pi/24$, and we rotate the inner mesh by an angle of $k\pi/144$, $k = 0, \ldots, 6$, corresponding to $k/6$ of the meshsize on the inner ring. In contrast to the above setting, the grid on the master side is now not just a refinement of the one on the slave side for $k = 1, \ldots, 5$.

The resulting deformed grids for $k = 1, 2, 3$, are plotted in Figure 3.8, and a table is given which documents the error measured in the energy norm. The modified method handles

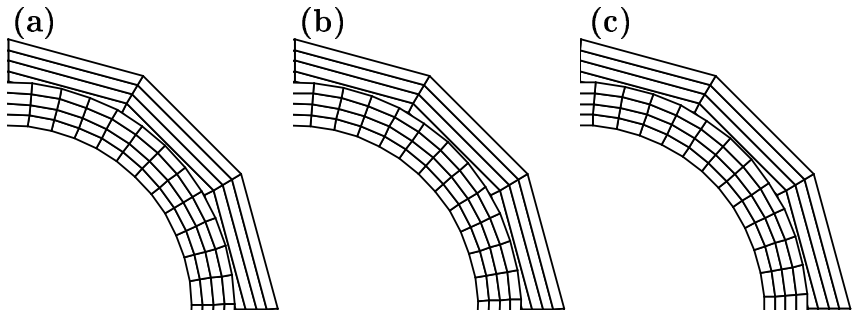

angle	error
0	$6.848 \cdot 10^{-2}$
$\pi/144$	$6.847 \cdot 10^{-2}$
$2\pi/144$	$6.845 \cdot 10^{-2}$
$3\pi/144$	$6.844 \cdot 10^{-2}$
$4\pi/144$	$6.845 \cdot 10^{-2}$
$5\pi/144$	$6.847 \cdot 10^{-2}$
$\pi/24$	$6.848 \cdot 10^{-2}$

Figure 3.8: Rotation of the grid on the inner ring by an angle of (a) $\pi/144$, (b) $2\pi/144$, (c) $3\pi/144$.

the situation very well and yields convincing results. As expected from symmetry, the results for $k = 0, 1, 2$, coincide with the ones for $k = 6, 5, 4$, respectively. Our approach is not at all sensitive to the applied rotation, the errors differ only in the fourth significant digit.

3.4.3 Choice of the Slave Side

We carry out another test where the ratio of the number of edges on the inner ring to the number of edges on the outer ring is out of $\{2{:}1, 4{:}1, 8{:}1\}$. In each case, once the Lagrange multipliers are chosen with respect to the coarse (outer) grid, and once with respect to the fine (inner) grid. For a robust method, we expect that this choice should only moderately influence the numerical results. However, for the unmodified approach which is illustrated in Figure 3.9(a), it results in a huge difference. In contrast, the modification

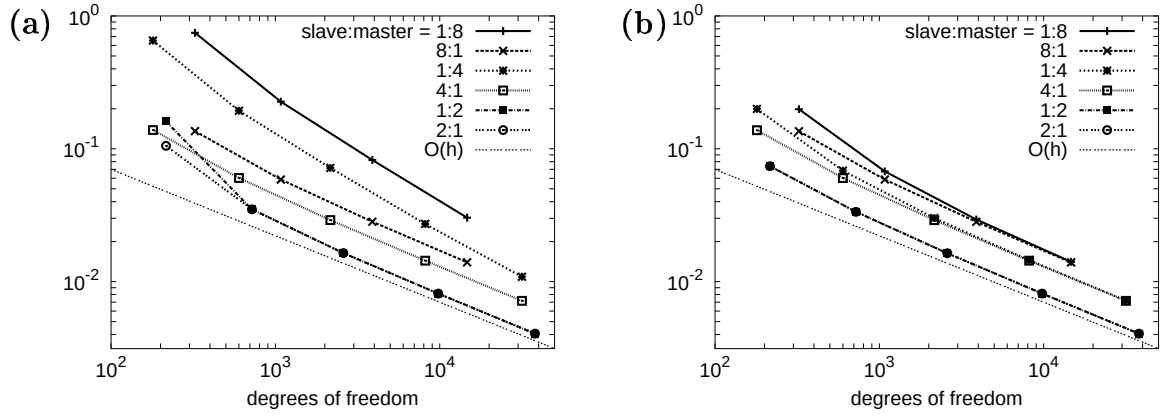

Figure 3.9: Different ratios of the mesh sizes: (a) unmodified dual, (b) modified dual Lagrange multipliers.

yields a satisfying result, as shown in Figure 3.9(b). Only for the very coarse grids, there

is a noteworthy difference, which illustrates the stability of the modified approach. This observation becomes especially important in the context of adaptive methods where it is a priori not clear which side of the interface becomes the coarse (fine) one during the adaptation process.

3.4.4 Tangential Surface Traction

In our last test, the surface traction on the inner boundary of ring Ω is chosen to be constant in tangential direction, namely, $\boldsymbol{g}(x, y) = 0.5(-y, x)^{\mathrm{T}}$. The computational grid is again the same as in Section 3.2, and the Lagrange multipliers are chosen with respect to the coarse grid. In Figure 3.10, the deformed grids and the corresponding van Mises

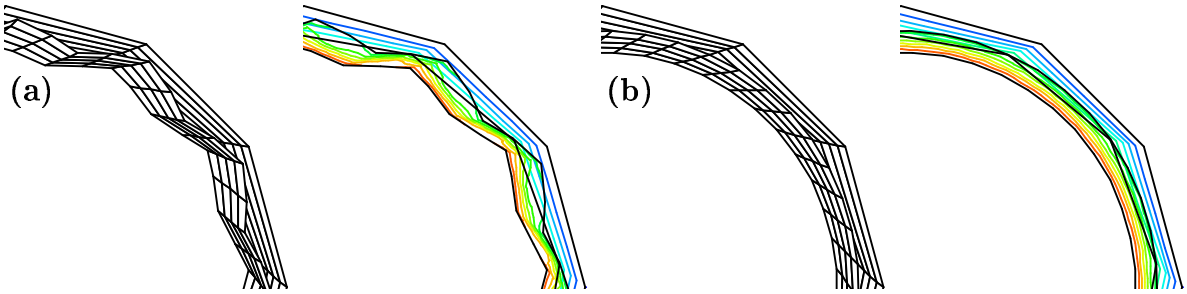

Figure 3.10: Surface traction constant in tangential direction: (a) unmodified dual LM, (b) modified dual Lagrange multipliers.

stresses are plotted for the unmodified and the modified approach. As in the preceding examples, the original approach fails, whereas the modification yields visually a satisfying and physically correct result.

3.4.5 Limitations of the Approach

Unfortunately, the positive effect of the modifications seems to be restricted to model problems where the surface tractions on the interface are a linear combination of components constant in normal and tangential direction. For more general situations, the modifications yield no improvement. As an example, we employ the same setting as for the patch test in Section 1.4, namely, as boundary conditions for the domain $\Omega = (0, 10)^2$, we assume homogeneous Dirichlet conditions in x-direction on the left boundary $\{0\}\times(0, 10)$, and in y-direction in the node $(0, 0)$. On the right boundary $\{10\} \times (0, 10)$, a constant force of magnitude one is pulling in x-direction. All other boundary parts respect homogeneous Neumann conditions. The model of plane stress is used, with material parameters $E = 10^7$ and $\nu = 0.3$, resulting in the linear exact solution $\boldsymbol{u}(x, y) = E^{-1}(x, -\nu y)^{\mathrm{T}}$. This time, we use a decomposition of Ω into the circular disk Ω^{s} of radius 2.5 centered at $(5, 5)^{\mathrm{T}}$, and the rest $\Omega^{\mathrm{m}} = \Omega \setminus \overline{\Omega^{\mathrm{s}}}$. The triangulation is chosen in such a way that the ratio $q^{\mathrm{s}}_{\mathrm{m}}$ of slave edges to master edges is 1:4, as depicted in Figure 3.11(a). The isolines of the x-component of the finite element solution $\boldsymbol{u}_h$ using standard, dual, and modified dual Lagrange multipliers are shown in Figure 3.11(b)–(d), respectively. While

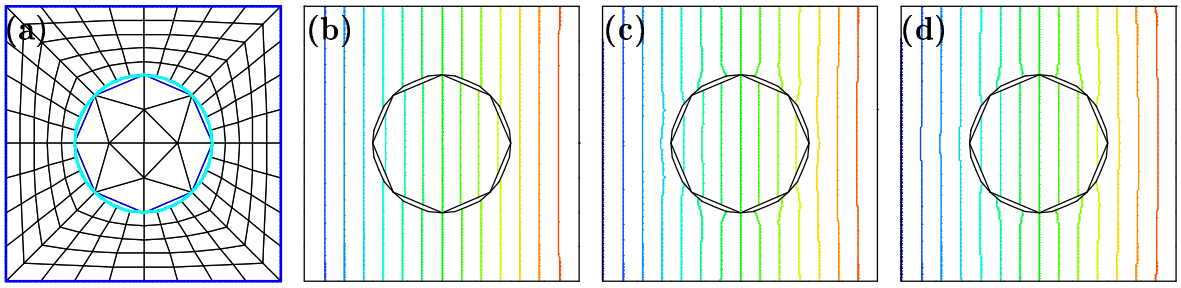

Figure 3.11: Patch test with a curved interface: (a) triangulation, isolines of u_x using (b) standard, (c) dual, (d) modified dual Lagrange multipliers.

they are crossing the interface in a quite nice way in the first case, they are obviously perturbed for the two other cases, and the modification does not improve this behavior. This gets confirmed by the energy error, which is measured to be $6.9{\cdot}10^{-5}$ for the standard approach, while it is $1.9{\cdot}10^{-4}$ and $2.3{\cdot}10^{-4}$ for the unmodified and the modified dual approach, respectively. We note that for all three approaches, the energy error decays as $O(h^{3/2})$. Moreover, it the Lagrange multipliers are chosen with respect to the fine grid, all methods give results of equal quality.

3.4.6 Extension to 3D

In order to present the effect of our modifications, we investigate a 3D example which is analogous to the 2D example given in Section 3.2. The global domain is a spherical shell with inner radius $r_i = 0.9$ and outer radius $r_o = 1.1$, its material data given by $E = 1.0$ and $\nu = 0.3$. The outer boundary $\{\boldsymbol{x} \in \mathbb{R}^3 : |\boldsymbol{x}| = 1.1\}$ is fixed by enforcing homogeneous Dirichlet boundary conditions, whereas on the inner boundary $\{\boldsymbol{x} \in \mathbb{R}^3 : |\boldsymbol{x}| = 0.9\}$, a uniform radial pressure of magnitude -1 is applied. The symmetry of the domain and the problem data yields the exact solution $u(r) = a/r^2 + br$, depending only on $r(\boldsymbol{x}) = |\boldsymbol{x}|$, with $b = 1/(3\lambda_{\mathrm{L}}+2\mu_{\mathrm{L}}+4\mu_{\mathrm{L}}r_o^3/r_i^3)$ and $a = -br_o^3$. In order to keep a full three-dimensional setting, we exploit the radial symmetry only partially for the numerical simulation of the problem, namely, by considering only the octant $O_1 = \{\boldsymbol{x} \in \mathbb{R}^3 : x_i > 0,\ i = 1,2,3\}$. The interface Γ is set to be the unit sphere intersected by O_1, yielding the subdomains $\Omega^{\mathrm{m}} = \{\boldsymbol{x} \in O_1 : |\boldsymbol{x}| \in (r_i, 1)\}$ and $\Omega^{\mathrm{s}} = \{\boldsymbol{x} \in O_1 : |\boldsymbol{x}| \in (1, r_o)\}$. The additional boundary conditions on the symmetry boundaries $\Sigma_i = (\overline{\Omega^{\mathrm{m}} \cup \Omega^{\mathrm{s}}}) \cap \{\boldsymbol{x} \in \mathbb{R}^3 : x_i = 0\}$, $i = 1, \ldots, 3$, are given by $\boldsymbol{u}{\cdot}\boldsymbol{n}_i = 0$ and $\sigma_t = 0$, where $\boldsymbol{n}_i = -\boldsymbol{e}_i$ is the corresponding normal vector and σ_t indicates the tangential part of the surface traction $\sigma(\boldsymbol{u})\boldsymbol{n}_i$. For a detailed account on handling the Lagrange multiplier nodes on $\Sigma_i \cap \overline{\Gamma}$, we refer to [50].

Visible but undesired oscillations occur only when the surface grid $\mathcal{T}^{\mathrm{s}}$ on the slave side is considerably coarser than the grid $\mathcal{T}^{\mathrm{m}}$ on the master side. To this end, we first take a ratio of $h_{\mathrm{s}}/h_{\mathrm{m}} = 4/1$, and the corresponding surface grids consist of 12 and 192 elements for $\mathcal{T}^{\mathrm{s}}$ and $\mathcal{T}^{\mathrm{m}}$, respectively. In radial direction, we take two elements for each subdomain, giving a total of 408 volume elements. In Figure 3.12, the deformed domain is visualized for four different approaches: the unmodified dual one, the modified ones

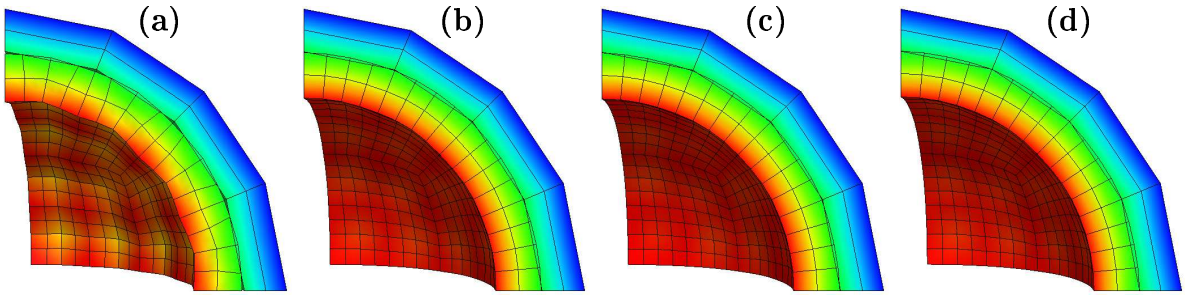

Figure 3.12: Ratio $h_s/h_m = 4/1$, distorted domains: (a) unmodified dual, (b) modification 1, (c) modification 2, (d) standard Lagrange multipliers.

as introduced in Sections 3.3.2 and 3.3.1, and, as a reference, the one taking standard basis functions. The solution of the unmodified dual method is subject to oscillations. The two modifications give equally good results, the surface tractions and the displacements, which are both constant in normal direction, are interchanged between the grids in the expected correct way. We increase the ratio h_s/h_m further to 8/1, taking 768 elements for $\mathcal{T}^m$, and four elements in radial direction, giving 3120 volume elements. The corresponding deformed domains are visualized in Figure 3.13. For the unmodified

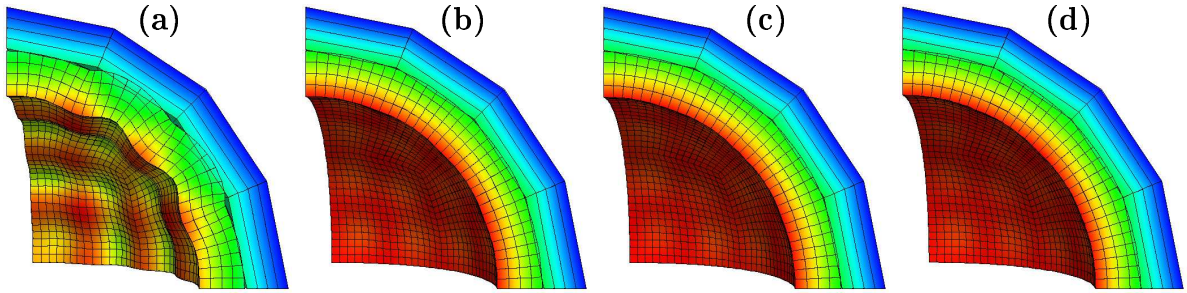

Figure 3.13: Ratio $h_s/h_m = 8/1$, distorted domains: (a) unmodified dual, (b) modification 1, (c) modification 2, (d) standard Lagrange multipliers.

dual approach, the oscillations become worse, while the other three considered methods remain stable. We remark that, although it is not backed up by our theory, also the symmetric version of the first modification presented in 3.3.2 yields good results, and, like all other methods, exhibits an optimal error decay. For all examples that we have tested so far, we could not experience any substantial quantitative difference between the symmetric and unsymmetric variants of Section 3.3.2, as well as the approach considered in Section 3.3.1. All modified approaches are in reasonable agreement with the method using standard Lagrange multipliers. For the current example, these observations are documented in Table 3.1 where we provide the concrete numbers for the errors measured in the energy norm. As suggested by the oscillating deformations, the error for the dual discontinuous multipliers is very large compared to all other methods which are in good agreement with each other. If the Lagrange multipliers are chosen with respect to the finer side, also the dual multipliers yield a good result in comparison with the standard

h_s/h_m	standard	dual	3.3.1	3.3.2 nonsym.	3.3.2 sym.
4/1	3.44e-02	7.76e-02	3.89e-02	3.72e-02	3.69e-02
1/4	3.29e-02	3.29e-02	3.28e-02	3.57e-02	3.46e-02
8/1	3.27e-02	9.30e-02	3.78e-02	3.61e-02	3.57e-02
1/8	3.22e-02	3.22e-02	3.22e-02	3.54e-02	3.41e-02

Table 3.1: Errors measured in the energy norm.

ones. For the first modification presented in Section 3.3.1, we illustrate the error decay in the energy norm in Figure 3.14, compared with the standard and with the original dual multipliers. The decays exhibit the same behavior as in the two-dimensional setting. The

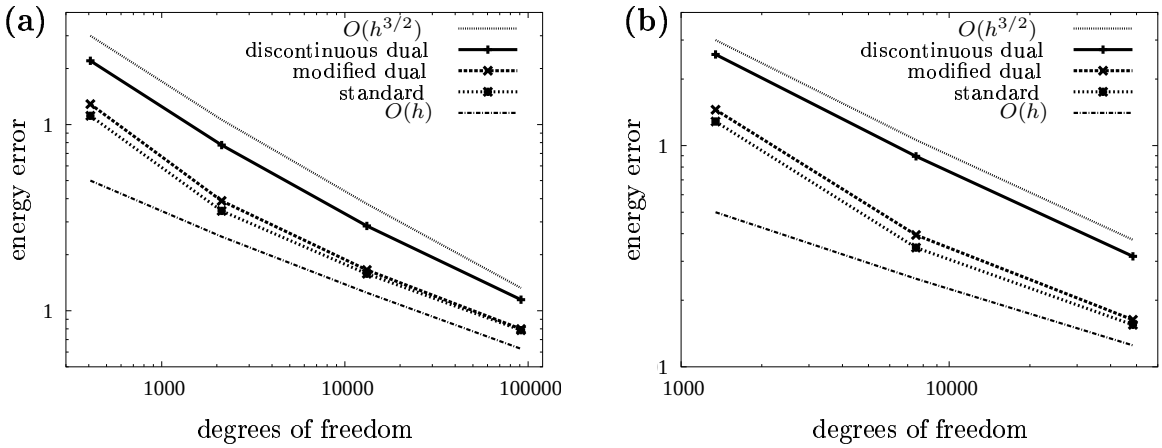

Figure 3.14: Extension to 3D: decay of the energy error using standard, dual, and modified dual LM, (a) $h_s/h_m = 4/1$, (b) $h_s/h_m = 8/1$.

original dual multipliers result in a higher error which decays at a faster rate of $O(h^{3/2})$ in the beginning. The modification yields the desired effect, and the error decay almost coincides with the one resulting from the use of standard multipliers. We emphasize that the effect of numerical oscillations only occurs when the Lagrange multipliers are chosen with respect to the coarse side. Thus, in this simple example, one could avoid any complications by choosing the multipliers on the finer grid. However, in more general settings, the ratio h_{T^s}/h_{T^m} for two intersecting elements from the master and slave side can vary drastically over the global interface Γ. Moreover, the choice of the grid for the Lagrange multipliers may be dictated by the problem formulation. Our modifications introduced in Sections 3.3.1 and 3.3.2 admit the possibility to stay flexible and still keep all the advantages of the dual approach.

3.4.7 An Efficient Solution Strategy for Contact Problems

In the following, we deal with the solution of problem (1.20). The setting is similar to that of the example treated in Section 3.4.6. The two bodies in contact are half-spherical

shells, where the first one, Ω^{m}, with inner radius 1 and outer radius 1.3 is centered around the origin $(0,0,0)$, while the second one, Ω^{s}, with inner radius 0.5 and outer radius 0.8 is centered around the point $(0,0,-0.2)$. Thus, the two bodies initially meet in the point $(0,0,-1)$. The material data is given by $\nu = 0.3$ everywhere, $E = 200$ for Ω^{m}, and $E = 600$ for Ω^{s}. The outer boundary $\{\boldsymbol{x} \in \partial\Omega^{\mathrm{m}} : |\boldsymbol{x}| = 1.3\}$ of Ω^{m} is fixed by enforcing homogeneous Dirichlet boundary conditions, whereas on the inner boundary $\{\boldsymbol{x} \in \partial\Omega^{\mathrm{s}} : |\boldsymbol{x} - (0,0,-0.2)^{\mathrm{T}}| = 0.5\}$ of Ω^{s}, a surface traction $\sigma(\boldsymbol{u})\boldsymbol{n}(\boldsymbol{x}) = (0,0,-500\exp(-20(x_1^2 + x_2^2)))$ is applied. The symmetry of the domain and the problem data is exploited by considering only the octant $\{\boldsymbol{x} \in \mathbb{R}^3 : x_i < 0,\ i = 1,2,3\}$. In Figure 3.15, the distorted domains as well as the contact pressure are visualized. The considered method using

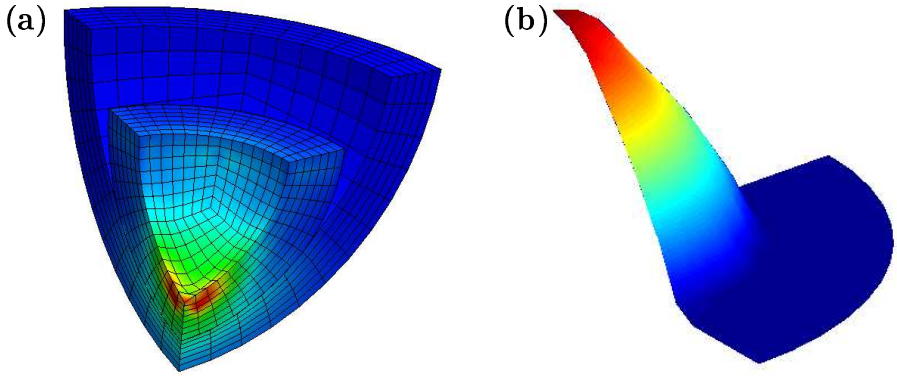

Figure 3.15: Two-body contact problem: (a) distorted domains, (b) contact pressure.

dual Lagrange multipliers yields reasonable results. No noticeable differences between the two alternatives presented in Sections 3.3.2 and 3.3.1 could be observed.

The employed numerical solution process deserves special attention. We employ a primal-dual active set strategy (PDASS), [72], in order to deal with the nonlinearity of the contact condition (1.19). Starting from an initial active set, the PDASS checks in each step the sign of the normal stress component for an active node to determine whether the node stays active, and for an inactive node the non-penetration condition to determine whether the node stays inactive. Proceeding like this, a new active set is calculated, and the active nodes provide Dirichlet conditions and the inactive nodes give homogeneous Neumann conditions for the linear system to be solved. The biorthogonality of the dual basis functions spanning M_h^+ is of crucial importance for the realization of the PDASS. In particular, the weak formulation of the non-penetration condition, i.e., the third equation of (1.19), naturally reduces to a point-wise relation which is easy to handle. Moreover, the Lagrange multiplier can be efficiently eliminated yielding a positive definite linear system for the remaining unknowns in each iteration step of the PDASS. Thus, suitable multigrid solvers can be applied. Limiting the maximum number of multigrid iterations per PDASS step yields an inexact strategy.

4 Application to Acoustic Problems

In many technical applications a sensor or/and actuator is immersed in an acoustic fluid, e.g., ultrasound transducers for non-destructive testing as well as medical diagnostic and therapy, ultrasound cleaning, electrodynamic loudspeakers, capacitive microphones, etc. Very often, the numerical simulation of the actuator mechanism within the structure is quite complex, since in most cases we have to deal with a nonlinear coupled problem (e.g., the electrostatic-mechanical principle used in many micro-electro-mechanical systems), where in addition to the nonlinear coupling terms each single field is nonlinear (e.g., geometric nonlinearity in mechanics, moving body problem in the electrostatic field), [74]. Moreover, in most cases the discretization within the structure has to be much finer than the one we need for the acoustic wave propagation in the fluid. A very similar problem arises in computational aero-acoustics, when solving the inhomogeneous wave equation according to Lighthill's analogy, [82]. The inhomogeneous term of the wave equation is calculated by the fluid flow data within the fluid region, and to obtain reliable results, the discretization of the wave equation within this domain has to be very fine (up to 1000 linear finite elements per wavelength). However, outside the flow region, the homogeneous wave equation is solved, and one could have a relatively coarse mesh (about 20 linear finite elements per wavelength), [7, 75]. The same situation also occurs for the direct simulation of aero-acoustics, [107].

In this chapter, we face one common feature of these problems, namely that the computational grid in one subdomain can be considerably coarser than in the other subdomain. In order to keep as much flexibility as possible, we intend to employ the framework established in the previous chapters, namely to use independently generated grids which are well suited for approximating the solution of decoupled local subproblems in each subdomain. The analysis of numerical methods for the problems under consideration is also subject of many research papers. In [17], the authors analyze a purely displacement-based problem formulation for the elasto-acoustic setting. A time dependent linearized fluid-structure interaction problem involving a very viscous fluid and an elastic shell in small displacements is examined in [81]. In [60], a method is proposed for handling the interface in finite element fluid-structure interaction based on Nitsche's method. Concerning both the acoustic and the elastic wave equation, iterative procedures based on a decomposition into many subdomains and their discretization by means of finite differences are investigated in [99]. The coupling of spectral elements and finite elements on non-matching grids for the solution of wave propagation problems is examined in [79]. A suitable general functional framework for domain decomposition methods for the acoustic wave equation is presented in [7], where, in addition, 2D algorithmic considerations and numerical results restricted to the use of regular grids with a special mesh-size ratio of $1/2$ are given. Moreover, a FEM-BEM coupling on non-matching grids in the context of

structural-acoustic simulations is presented and tested in [41].

The rest of this chapter is organized as follows. Mainly to settle our notation, we present the single field models for elasto-dynamics and acoustics in Section 4.1. In Section 4.2, we derive the coupled problem formulations. Numerical results are provided in Section 4.3, while in Section 4.4, we investigate an extension to the case of nonlinear structures and present a corresponding solution algorithm.

4.1 Single Fields

We introduce the single field problems of elasto-dynamics and of linear acoustics. They constitute the extensions to the transient regime of the corresponding stationary problems treated in the preceding chapters. We provide the strong and weak continuous formulations, the semi-discrete formulations obtained after space discretization, and the totally discrete formulations after additional time discretization.

4.1.1 Elasto-dynamics

We investigate the deformation of an elastic body $\Omega^{\mathrm{e}} \subset \mathbb{R}^d$ with density $\rho_{\mathrm{e}} : \Omega^{\mathrm{e}} \to \mathbb{R}$ under given time dependent volume and surface forces $\boldsymbol{f}$ and $\boldsymbol{g}$, respectively, yielding an extension of the stationary boundary value problem (1.3)-(1.6) to a second order hyperbolic initial boundary value problem. The boundary of Ω^{e} with unit normal vector $\boldsymbol{n}_{\mathrm{e}}$ is the union of disjoint subsets $\Gamma^{\mathrm{e}}_{\mathrm{N}}$ and $\Gamma^{\mathrm{e}}_{\mathrm{D}}$, on which natural and essential data are given, respectively. The strong formulation for linear elasto-dynamic problems then reads as follows: given $\boldsymbol{u}_0, \boldsymbol{u}_1, \boldsymbol{f} : \Omega^{\mathrm{e}} \to \mathbb{R}^d$, find $\boldsymbol{u} : \Omega^{\mathrm{e}} \times (0,T) \to \mathbb{R}^d$ such that

$$\rho_{\mathrm{e}} \ddot{\boldsymbol{u}} - \operatorname{div} \sigma(\boldsymbol{u}) = \boldsymbol{f} \quad \text{in } \Omega^{\mathrm{e}} \times (0,T), \tag{4.1a}$$

with (1.4), (1.5), boundary conditions analogous to (1.6), namely,

$$\boldsymbol{u} = 0 \ \text{ on } \Gamma^{\mathrm{e}}_{\mathrm{D}} \ \times \ (0,T), \quad \sigma(\boldsymbol{u})\boldsymbol{n}_{\mathrm{e}} = \boldsymbol{g} \ \text{ on } \Gamma^{\mathrm{e}}_{\mathrm{N}} \ \times \ (0,T), \tag{4.1b}$$

and initial conditions

$$\boldsymbol{u}(\cdot,0) = \boldsymbol{u}_0, \ \dot{\boldsymbol{u}}(\cdot,0) = \boldsymbol{u}_1 \quad \text{in } \Omega^{\mathrm{e}}. \tag{4.1c}$$

For the weak formulation, it is natural to use the space $X^{\mathrm{e}} = (H^1_{\Gamma^{\mathrm{e}}_{\mathrm{D}}}(\Omega^{\mathrm{e}}))^d$, and the resulting variational problem reads: find $\boldsymbol{u} \in L^2(0,T;X^{\mathrm{e}})$, $\dot{\boldsymbol{u}} \in L^2(0,T;L^2(\Omega^{\mathrm{e}}))$, and $\ddot{\boldsymbol{u}} \in L^2(0,T;H^{-1}(\Omega^{\mathrm{e}}))$ such that for all times $t \in (0,T)$

$$\langle \rho_{\mathrm{e}} \boldsymbol{v}, \ddot{\boldsymbol{u}}(t) \rangle_{\Omega^{\mathrm{e}}} + a_{\mathrm{e}}(\boldsymbol{u}(t), \boldsymbol{v}) = l_t(\boldsymbol{v}) = (\boldsymbol{f}(t), \boldsymbol{v})_{\Omega^{\mathrm{e}}} + (\boldsymbol{g}(t), \boldsymbol{v})_{\Gamma^{\mathrm{e}}_{\mathrm{N}}}, \quad \boldsymbol{v} \in X^{\mathrm{e}}, \tag{4.2}$$

together with initial conditions (4.1c). We employ the standard setting of Sobolev spaces for evolution problems, the space $L^2(0,T;X^{\mathrm{e}})$ is introduced in Definition A.22. In (4.2), $\langle \cdot, \cdot \rangle_{\Omega^{\mathrm{e}}}$ indicates the duality product on $X^{\mathrm{e}} \times (X^{\mathrm{e}})'$, and the bilinear form $a_e(\cdot,\cdot)$ is defined analogous to (3.1). The analysis of the variational form of second order evolution equations like (4.2) is subject of many textbooks, [34, 40, 83, 102]. The main condition

for guaranteeing the wellposedness of the problem formulation is that the bilinear form $a_{\mathrm{e}}(\cdot,\cdot)$ satisfies a Garding inequality,

$$a_{\mathrm{e}}(\boldsymbol{v},\boldsymbol{v}) \geq \alpha \|\boldsymbol{v}\|^2_{1,\Omega^{\mathrm{e}}} - \lambda \|\boldsymbol{v}\|^2_{0,\Omega^{\mathrm{e}}},$$

with constants $\alpha > 0$ and $\lambda \geq 0$. It can be shown that the weak solution $\boldsymbol{u}$ is indeed more regular with respect to time, namely,

$$\boldsymbol{u} \in C^0([0,T]; X^{\mathrm{e}}) \cap C^1([0,T]; L^2(\Omega^{\mathrm{e}})).$$

Performing a spatial discretization with standard nodal finite elements, we approximate X^{e} by X^{e}_h. Given approximations $\boldsymbol{u}_{0,h}, \boldsymbol{u}_{1,h} \in X^{\mathrm{e}}_h$ of the initial data $\boldsymbol{u}_0, \boldsymbol{u}_1$, we seek a spatially discrete solution $\boldsymbol{u}_h : t \mapsto \boldsymbol{u}_h(t) \in X^{\mathrm{e}}_h$ such that

$$\langle \rho_{\mathrm{e}} \boldsymbol{v}_h,\, \ddot{\boldsymbol{u}}_h(t) \rangle_{\Omega^{\mathrm{e}}} + a_{\mathrm{e}}(\boldsymbol{u}_h(t),\, \boldsymbol{v}_h) = l_t(\boldsymbol{v}_h), \quad \boldsymbol{v}_h \in X^{\mathrm{e}}_h. \tag{4.3}$$

Following [102], an a priori estimate can be given, assuming that $\boldsymbol{u} \in C^2(0,T; X^{\mathrm{e}})$ and under the simplifying condition that the bilinear form $a_{\mathrm{e}}(\cdot,\cdot)$ is elliptic on X^{e}. In particular, the discretization error $\boldsymbol{e}_h(t) = \boldsymbol{u}(t) - \boldsymbol{u}_h(t)$ at time t satisfies

$$\begin{aligned}
&\|\boldsymbol{e}_h(t)\|_{1,\Omega^{\mathrm{e}}} + \|\dot{\boldsymbol{e}}_h(t)\|_{0,\Omega^{\mathrm{e}}} \\
&\qquad \lesssim \ \|\boldsymbol{u}_{0,h} - \Psi_h \boldsymbol{u}_0\|_{1,\Omega^{\mathrm{e}}} + \|\boldsymbol{u}_{1,h} - \Psi_h \boldsymbol{u}_1\|_{0,\Omega^{\mathrm{e}}} \\
&\qquad + \ \|\boldsymbol{u}(t) - \Psi_h \boldsymbol{u}(t)\|_{1,\Omega^{\mathrm{e}}} + \|\dot{\boldsymbol{u}}(t) - \Psi_h \dot{\boldsymbol{u}}(t)\|_{0,\Omega^{\mathrm{e}}} + \int_0^t \|\ddot{\boldsymbol{u}}(s) - \Psi_h \ddot{\boldsymbol{u}}(s)\|_{0,\Omega^{\mathrm{e}}}\, \mathrm{d}s,
\end{aligned}$$

with the elliptic projection operator Ψ_h associated with $a_{\mathrm{e}}(\cdot,\cdot)$. Thus, the error can be bounded in terms of the error in the initial data approximation and of the projection error. Under further assumptions on the spatial regularity of the solution $\boldsymbol{u}$ and its time derivatives, each single error term above can be further estimated in the standard way, employing the approximation property of the operator Ψ_h associated with the Galerkin approximation of X^{e} by X^{e}_h.

After introducing a basis of X^{e}_h, we may write (4.3) in matrix form as

$$M_u \ddot{\boldsymbol{u}}_h(t) + K_u \boldsymbol{u}_h(t) = \boldsymbol{f}_h(t), \tag{4.4}$$

or, more generally, as

$$M_u \ddot{\boldsymbol{u}}_h(t) + C_u \dot{\boldsymbol{u}}_h(t) + K_u \boldsymbol{u}_h(t) = \boldsymbol{f}_h(t), \tag{4.5}$$

with a damping matrix C_u. Above and in the sequel, we use the same symbol for a finite element function and its corresponding coefficient vector. Starting with (4.5), one can employ a suitable ODE integration scheme, as for example Newmark's method, [90, 73]. For the time discretization, we decompose the interval $[0,T]$ into subintervals $[t_n, t_{n+1}]$, $n = 0, \ldots, N_t - 1$, with $t_n = n\Delta t$, $\Delta t = T/N_t$. In the time step corresponding to the time t_{n+1}, an equilibrium equation has to be satisfied, namely,

$$M_u \ddot{\boldsymbol{u}}_{n+1} + C_u \dot{\boldsymbol{u}}_{n+1} + K_u \boldsymbol{u}_{n+1} = \boldsymbol{f}_{n+1}, \tag{4.6}$$

where $\boldsymbol{u}_{n+1}$, $\dot{\boldsymbol{u}}_{n+1}$, and $\ddot{\boldsymbol{u}}_{n+1}$ denote approximations of $\boldsymbol{u}_h(t_{n+1})$, $\dot{\boldsymbol{u}}_h(t_{n+1})$, and $\ddot{\boldsymbol{u}}_h(t_{n+1})$, respectively. Given two parameters β and γ, the defining feature of Newmark's method is to compute the approximations $\dot{\boldsymbol{u}}_{n+1}$ and $\ddot{\boldsymbol{u}}_{n+1}$ as functions of the displacements $\boldsymbol{u}_{n+1}$,

$$\dot{\boldsymbol{u}}_{n+1}(\boldsymbol{u}_{n+1}) = a_1 \boldsymbol{u}_{n+1} - \widehat{\dot{\boldsymbol{u}}}_n, \tag{4.7a}$$

$$\widehat{\dot{\boldsymbol{u}}}_n = a_1 \boldsymbol{u}_n + \frac{\gamma-\beta}{\beta}\dot{\boldsymbol{u}}_n + \frac{\gamma-2\beta}{2\beta}\Delta t \ddot{\boldsymbol{u}}_n, \tag{4.7b}$$

$$\ddot{\boldsymbol{u}}_{n+1}(\boldsymbol{u}_{n+1}) = a_2 \boldsymbol{u}_{n+1} - \widehat{\ddot{\boldsymbol{u}}}_n, \tag{4.7c}$$

$$\widehat{\ddot{\boldsymbol{u}}}_n = a_2 \boldsymbol{u}_n + \frac{1}{\beta\Delta t}\dot{\boldsymbol{u}}_n + \frac{1-2\beta}{2\beta}\ddot{\boldsymbol{u}}_n, \tag{4.7d}$$

with $a_1 = \gamma/(\beta\Delta t)$ and $a_2 = 1/(\beta\Delta t^2)$. This admits to express (4.6) as a system of linear equations in the remaining unknowns $\boldsymbol{u}_{n+1}$,

$$K_u^* \boldsymbol{u}_{n+1} = \boldsymbol{f}_{n+1} - C_u \widehat{\dot{\boldsymbol{u}}}_n - M_u \widehat{\ddot{\boldsymbol{u}}}_n, \tag{4.8}$$

with the effective stiffness matrix

$$K_u^* = K_u + a_1 C_u + a_2 M_u. \tag{4.9}$$

Thus, in each time step a linear system of the form (4.8) has to be solved. An appropriate analysis is again carried out in [102]. For the choice of parameters $\beta = 1/4$, $\gamma = 1/2$, it is well known that the Newmark scheme is unconditionally stable and of quadratic order with respect to time. In more detail, assuming $\boldsymbol{u} \in C^2(0,T;X^{\mathrm{e}}) \cap C^4(0,T;L^2(\Omega^{\mathrm{e}}))$, we have for the discrete solution $\boldsymbol{u}_n$ at time t_n that

$$\begin{aligned}\|\boldsymbol{u}_n - \boldsymbol{u}(t_n)\|_{0,\Omega^{\mathrm{e}}} \lesssim\ & \|\boldsymbol{u}_{0,h} - \Psi_h \boldsymbol{u}_0\|_{0,\Omega^{\mathrm{e}}} + \|\boldsymbol{u}_{1,h} - \Psi_h \boldsymbol{u}_1\|_{0,\Omega^{\mathrm{e}}} + \ \|\boldsymbol{u}(t_n) - \Psi_h \boldsymbol{u}(t_n)\|_{0,\Omega^{\mathrm{e}}} \\ & + \int_0^{t_n} \|\ddot{\boldsymbol{u}}(s) - \Psi_h \ddot{\boldsymbol{u}}(s)\|_{0,\Omega^{\mathrm{e}}} + \Delta t^2 \|\boldsymbol{u}^{(4)}(s)\|_{0,\Omega^{\mathrm{e}}}\,\mathrm{d}s,\end{aligned}$$

where the superscript (4) indicates the fourth time derivative. If the approximation of the initial data is performed well enough and if finite elements of order k are used, we therefore expect a convergence order $O(h^{k+1} + \Delta t^2)$ for the L^2-norm of the discretization error.

4.1.2 Computational Acoustics

For the description of the acoustic wave propagation within a domain $\Omega^{\mathrm{a}} \subset \mathbb{R}^d$, we use the wave equation for the velocity potential ψ, i.e., $\boldsymbol{v}_{\mathrm{a}} = -\operatorname{grad}\psi$ with $\boldsymbol{v}_{\mathrm{a}}$ denoting the acoustic velocity field. The acoustic pressure p_{a} is then related to the acoustic velocity potential ψ by

$$p_{\mathrm{a}} = \rho_{\mathrm{a}} \dot{\psi} \tag{4.10}$$

with $\rho_{\mathrm{a}} : \Omega^{\mathrm{a}} \to \mathbb{R}$ the mean density of the fluid. Analogous to the elasticity setting, the strong formulation for linear acoustics is an extension of (1.1) towards an hyperbolic

problem. Indicating with $c : \Omega^{\mathrm{a}} \to \mathbb{R}$ the speed of sound, it reads as follows: given f, ψ_0, $\psi_1 : \Omega^{\mathrm{a}} \to \mathbb{R}$, find $\psi : \Omega^{\mathrm{a}} \times (0,T) \to \mathbb{R}$ such that

$$c^{-2}\,\ddot{\psi} - \operatorname{div}\operatorname{grad}\psi = f \quad \text{in } \Omega^{\mathrm{a}} \times (0,T), \tag{4.11a}$$

with boundary conditions

$$\psi = 0 \ \text{ on } \Gamma^{\mathrm{a}}_{\mathrm{D}} \ \times \ (0,T), \quad \partial\psi/\partial\boldsymbol{n}_{\mathrm{a}} = g \ \text{ on } \Gamma^{\mathrm{a}}_{\mathrm{N}} \ \times \ (0,T), \tag{4.11b}$$

and initial conditions

$$\psi(\cdot,0) = \psi_0,\ \dot{\psi}(\cdot,0) = \psi_1 \quad \text{in } \Omega^{\mathrm{a}}. \tag{4.11c}$$

In (4.11a), we denote by f any excitation function for generating the acoustic wave. Setting $X^{\mathrm{a}} = H^1_{\Gamma^{\mathrm{a}}_{\mathrm{D}}}(\Omega^{\mathrm{a}})$, the weak form of (4.11) reads: Find $\psi \in L^2(0,T;X^{\mathrm{a}})$, $\dot{\psi} \in L^2(0,T;L^2(\Omega^{\mathrm{a}}))$, and $\ddot{\psi} \in L^2(0,T;H^{-1}(\Omega^{\mathrm{a}}))$ such that for all times $t \in (0,T)$

$$\langle c^{-2}w,\, \ddot{\psi}(t)\rangle_{\Omega^{\mathrm{a}}} + (\operatorname{grad}\psi(t),\, \operatorname{grad} w)_{\Omega^{\mathrm{a}}} = (f(t),w)_{\Omega^{\mathrm{a}}} + (g(t),w)_{\Gamma^{\mathrm{a}}_{\mathrm{N}}}, \quad w \in X^{\mathrm{a}}, \tag{4.12}$$

together with (4.11c). Spatial discretization by means of standard nodal finite elements yields in matrix form

$$M_\psi \ddot{\psi}_h + K_\psi \psi_h = f_h. \tag{4.13}$$

Many applications within computational acoustics are open-domain problems, i.e., the bounded domain Ω^{a} was obtained from an unbounded domain by introducing an artificial boundary Γ^{a} in addition to $\Gamma^{\mathrm{a}}_{\mathrm{D}}$ and $\Gamma^{\mathrm{a}}_{\mathrm{N}}$. In order to correctly solve such problems with the finite element method, we have to define appropriate boundary conditions on Γ^{a}. Simply using homogeneous Dirichlet or Neumann boundary conditions would result in a total reflection of the outgoing waves at the boundary. Therefore, special boundary conditions have to be applied for absorbing the waves impinging on the artificial boundary imposed on the acoustic domain. Here, we employ a widely used locally absorbing boundary condition of first order (see [33, 38]),

$$(\partial/\partial t - c\,\partial/\partial\boldsymbol{n}_{\mathrm{a}})\,\psi = 0, \tag{4.14}$$

where $\boldsymbol{n}_{\mathrm{a}}$ denotes the unit normal vector on Γ^{a}. We note that an extension of this method to waves in solids (especially piezo-electric materials) can be found in [67].

To derive the correct formulation including the absorbing boundary condition as given in (4.14), we start from the weak form (see (4.12)) without setting the boundary integral on Γ^{a} to zero

$$\langle c^{-2}w,\, \ddot{\psi}(t)\rangle_{\Omega^{\mathrm{a}}} + (\operatorname{grad}\psi(t),\, \operatorname{grad} w)_{\Omega^{\mathrm{a}}} - \langle w, \operatorname{grad}\psi(t)\cdot\boldsymbol{n}_{\mathrm{a}}\rangle_{\Gamma^{\mathrm{a}}} = l_t(w), \quad w \in X^{\mathrm{a}}, \tag{4.15}$$

where we set $l_t(w) = (f(t),w)_{\Omega^{\mathrm{a}}} + (g(t),w)_{\Gamma^{\mathrm{a}}_{\mathrm{N}}}$. Substituting (4.14) into (4.15) results in

$$\langle c^{-2}w,\, \ddot{\psi}(t)\rangle_{\Omega^{\mathrm{a}}} + (\operatorname{grad} w,\, \operatorname{grad}\psi(t))_{\Omega^{\mathrm{a}}} - \langle c^{-1}w, \dot{\overbrace{\gamma_0\psi(t)}}\rangle_{\Gamma^{\mathrm{a}}} = l_t(w), \quad w \in X^{\mathrm{a}}, \tag{4.16}$$

where $\gamma_0 : H^1(\Omega^{\mathrm{a}}) \to H^{1/2}(\partial\Omega^{\mathrm{a}})$ denotes the usual trace operator, see Theorem A.13. We remark that one may not change the order of taking the trace and of differentiating with

respect to time, since $\dot{\psi}(t)$ is an L^2-function in general which does not allow for a trace in the usual sense. The additional surface integral may be seen as a damping term acting only on the surface of the computational domain. The character of the acoustic problem (4.16) is the same as the one of the elasto-dynamic problem (4.2). Besides having to take into account the additional surface integral, its analysis is completely analogous. In [7], it is shown that

$$\psi \in C^0(0,T;X^{\mathrm{a}}) \cap C^1(0,T;L^2(\Omega^{\mathrm{a}})), \qquad \dot{\overbrace{\gamma_0\psi}} \in L^2(0,T;L^2(\Gamma^{\mathrm{a}})), \tag{4.17}$$

and that ψ depends continuously on the data f, g, ψ_0, ψ_1 with respect to the appropriate norms.

The spatial discretization of (4.16) leads to

$$M_\psi \ddot{\psi}_h + C_\psi \dot{\psi}_h + K_\psi \psi_h = f_h\,, \tag{4.18}$$

and for the time discretization one can also apply a Newmark scheme. In analogy to (4.8), one obtains

$$K_\psi^* \psi_{n+1} = f_{n+1} - C_\psi \widehat{\dot{\psi}}_n - M_\psi \widehat{\ddot{\psi}}_n,$$

where $\widehat{\dot{\psi}}_n$, $\widehat{\ddot{\psi}}_n$, and K_ψ^* are given analogous to (4.7b), (4.7d), and (4.9), respectively.

4.2 Coupled Systems

In the following, the coupled problems of elasto-acoustics and of acoustics-acoustics are presented. For each system, we first focus on the interface conditions. They are quite different from each other: for the mechanical-acoustic system, the time derivative of the Dirichlet data from one side is coupled with the Neumann data from the other side, while for the acoustic-acoustic coupling, the Dirichlet data from both sides as well as the Neumann data from both sides are coupled in the usual way. After presenting the interface conditions, we observe how they enter into the variational formulations. The just mentioned difference results in the fact that for the purely acoustic system, the coupling is performed via a Lagrange multiplier space exactly as in the preceding chapters, while for the fluid-structure problem, there is no need for introducing additional unknowns. Subsequent to the continuous weak formulation, the semi-discrete problem obtained after spatial discretization is presented for each system.

4.2.1 Coupled Mechanical-Acoustic Systems

In general, we distinguish between two situations concerning mechanical-acoustic systems. In the first case, a *strong coupling* between the mechanical and the acoustic field occurs, requiring that the corresponding equations including their couplings have to be solved simultaneously. A typical example is a piezo-electric ultrasound array immersed in water. If, however, the pressure forces of the fluid on the solid are negligible, a sequential computation can be performed, leading to a *weak coupling*. Thus, in a first simulation

the mechanical surface vibrations are calculated, which are then used as the input for an acoustic field computation. For example, the acoustic noise of an electric transformer, generated by the vibration of the windings, can be obtained in this way. In our case, we will concentrate on the strong coupling.

Solid-Fluid Interface

At a solid-fluid interface Γ, as depicted in Figure 4.1(a), the continuity requires that the normal component of the mechanical surface velocity of the solid must coincide with the normal component of the acoustic velocity of the fluid. Thus, the following relation between the velocity $\boldsymbol{v}_\mathrm{e}$ of the solid expressed by the mechanical displacement $\boldsymbol{u}$ and the acoustic particle velocity $\boldsymbol{v}_\mathrm{a}$ expressed by the acoustic scalar potential ψ arises:

$$0 \;=\; \boldsymbol{n}\cdot(\boldsymbol{v}_\mathrm{e} - \boldsymbol{v}_\mathrm{a}) \;=\; \boldsymbol{n}\cdot\dot{\boldsymbol{u}} \;+\; \boldsymbol{n}\cdot\operatorname{grad}\psi \quad \text{on } \Gamma\times(0,T), \tag{4.19}$$

where $\boldsymbol{n}$ is the unit normal vector field on Γ. In addition, one has to consider the fact that the ambient fluid causes a surface force $\boldsymbol{f}_\Gamma = -\boldsymbol{n}p_\mathrm{a} = -\rho_\mathrm{a}\boldsymbol{n}\dot{\psi}$, see (4.10), which acts like a pressure load on the solid. Therefore, a second coupling condition is given by

$$\sigma(\boldsymbol{u})\boldsymbol{n} \;+\; \rho_\mathrm{a}\boldsymbol{n}\dot{\psi} \;=\; 0 \quad \text{on } \Gamma\times(0,T). \tag{4.20}$$

Coupled Field Formulation

Let us consider a setup of a coupled mechanical-acoustic problem as shown in Figure 4.1(b), where at the interface Γ we have to consider the solid-fluid coupling. Now, within

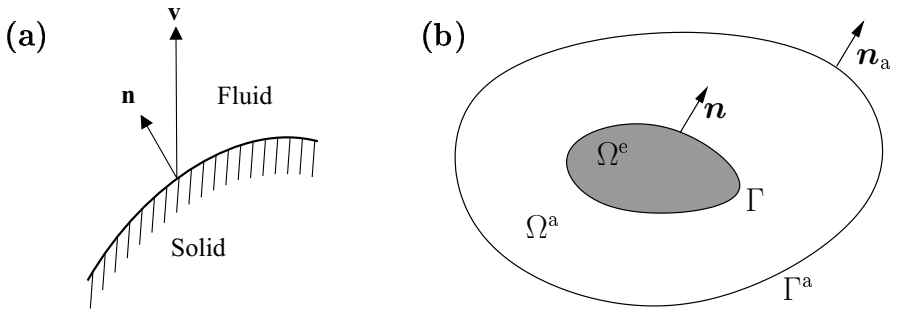

Figure 4.1: (a) solid-fluid interface, (b) setup of the coupled elasto-acoustic problem.

the domain Ω^e the initial boundary value problem (4.1) for the mechanical field, within the domain Ω^a the initial boundary value problem (4.11) for the acoustic field, and along the interface Γ the coupling conditions according to (4.19) and (4.20) have to be satisfied. Transforming to the weak form, assuming for the moment that homogeneous Neumann data is given on Γ^a, we obtain for the mechanical system

$$\langle\rho_\mathrm{e}\boldsymbol{v},\, \ddot{\boldsymbol{u}}(t)\rangle_{\Omega^\mathrm{e}} + a_\mathrm{e}(\boldsymbol{v},\boldsymbol{u}(t)) - \langle\boldsymbol{v},\, \sigma(\boldsymbol{u}(t))\boldsymbol{n}\rangle_\Gamma = l_t(\boldsymbol{v}), \tag{4.21}$$

and for the acoustic system

$$\langle c^{-2}w,\, \ddot{\psi}(t)\rangle_{\Omega^\mathrm{a}} + (\operatorname{grad} w,\, \operatorname{grad}\psi(t))_{\Omega^\mathrm{a}} + \langle w, \operatorname{grad}\psi(t)\cdot\boldsymbol{n}\rangle_\Gamma = 0. \tag{4.22}$$

In (4.22), we have set the excitation f inside Ω^{a} to be zero, since in the coupled case the mechanical vibration of the surface acts as an excitation for the acoustic field. It should be noted that the plus sign in (4.22) in front of the first boundary integral over Γ is due to the choice of $\boldsymbol{n}$ to point outward with respect to the structure Ω^{e}, see Figure 4.1(b). Incorporating the coupling conditions (4.19) and (4.20), we arrive at the following coupled system of equations

$$\langle \rho_{\mathrm{e}} \boldsymbol{v}, \ddot{\boldsymbol{u}}(t) \rangle_{\Omega^{\mathrm{e}}} + a_{\mathrm{e}}(\boldsymbol{u}(t), \boldsymbol{v}) + \langle \rho_{\mathrm{a}} \boldsymbol{v} \cdot \boldsymbol{n}, \overbrace{\gamma_0 \psi(t)}^{\cdot} \rangle_{\Gamma} = l_t(\boldsymbol{v}), \tag{4.23}$$

$$\langle c^{-2} w, \ddot{\psi}(t) \rangle_{\Omega^{\mathrm{a}}} + (\operatorname{grad} \psi(t), \operatorname{grad} w)_{\Omega^{\mathrm{a}}} - \langle w, \overbrace{\gamma_0 \boldsymbol{u}(t) \cdot \boldsymbol{n}}^{\cdot} \rangle_{\Gamma} = 0. \tag{4.24}$$

Before we perform a domain discretization, we multiply (4.24) by $-\rho_{\mathrm{a}}$ in order to obtain in (4.24) a boundary integral similar to the one in (4.23). Thus, the matrices, occurring from an FE - discretization of these two boundary integrals, will be the transpose of each other and hence symmetry of the system matrices can be obtained. We finally arrive at the variational problem of finding $(\boldsymbol{u}, \psi) \in L^2(0, T;\, X^{\mathrm{e}} \times X^{\mathrm{a}})$ such that for all times $t \in (0, T)$

$$\langle \rho_{\mathrm{e}} \boldsymbol{v}, \ddot{\boldsymbol{u}}(t) \rangle_{\Omega^{\mathrm{e}}} + a_{\mathrm{e}}(\boldsymbol{u}(t), \boldsymbol{v}) + \langle \rho_{\mathrm{a}} \boldsymbol{v} \cdot \boldsymbol{n}, \overbrace{\gamma_0 \psi(t)}^{\cdot} \rangle_{\Gamma} = l_t(\boldsymbol{v}), \quad \boldsymbol{v} \in X^{\mathrm{e}}, \tag{4.25a}$$

$$\langle c^{-2} \rho_{\mathrm{a}} w, \ddot{\psi}(t) \rangle_{\Omega^{\mathrm{a}}} + a_{\mathrm{a}}(\rho_{\mathrm{a}} \psi(t), w) - \langle \rho_{\mathrm{a}} w, \overbrace{\gamma_0 \boldsymbol{u}(t) \cdot \boldsymbol{n}}^{\cdot} \rangle_{\Gamma} = 0, \qquad w \in X^{\mathrm{a}}. \tag{4.25b}$$

In contrast to the problem settings considered before, no additional Lagrange multiplier has to be introduced.

We remark that an alternative coupled problem can be derived, if, instead of the potential-based formulation, a displacement-based problem formulation is chosen also for the fluid domain. A rigorous mathematical error analysis is provided in [17] for the case of matching grids which could be extended to the non-matching situation. There, due to the displacement-based formulation, the weak form of the subproblem for the fluid is an H^{div}-problem requiring a non-standard discretization by means of Raviart–Thomas finite elements. Here, we are able to use standard Lagrangian nodal finite elements in both domains.

Spatial Discretization

For the spatial discretization, we use two independently generated triangulations $\mathcal{T}_{\mathrm{e}}$ and $\mathcal{T}_{\mathrm{a}}$ on Ω^{e} and Ω^{a}, respectively, and approximate the displacement $\boldsymbol{u}$ on $\mathcal{T}_{\mathrm{e}}$ and the potential ψ on $\mathcal{T}_{\mathrm{a}}$ by finite elements. The two triangulations inherit two $(d-1)$-dimensional grids $\mathcal{T}^{\mathrm{e}}$ and $\mathcal{T}^{\mathrm{a}}$ on Γ. Due to the flexible construction of both grids, the finite element nodes on $\mathcal{T}^{\mathrm{e}}$ and $\mathcal{T}^{\mathrm{a}}$ will in general not coincide. On the contrary, motivated by different spatial scales required for the resolution of the local subproblems, the difference in the mesh sizes can become quite large.

The discretized version of (4.23), (4.24) reads in matrix form

$$\begin{pmatrix} M_u & 0 \\ 0 & -M_\psi \end{pmatrix} \begin{pmatrix} \ddot{\boldsymbol{u}}_h \\ \ddot{\psi}_h \end{pmatrix} + \begin{pmatrix} 0 & C_{u\psi} \\ C_{u\psi}^T & -C_\psi \end{pmatrix} \begin{pmatrix} \dot{\boldsymbol{u}}_h \\ \dot{\psi}_h \end{pmatrix} + \begin{pmatrix} K_u & 0 \\ 0 & -K_\psi \end{pmatrix} \begin{pmatrix} \boldsymbol{u}_h \\ \psi_h \end{pmatrix} = \begin{pmatrix} \boldsymbol{f}_h \\ 0 \end{pmatrix}, \tag{4.26}$$

where the damping matrix C_ψ resulting from the absorbing boundary condition (4.14) has been included again. The block diagonal entries $M_u, M_\psi, C_\psi, K_u, K_\psi$ can be assembled locally without needing to transfer any information across the interface. The coupling between the two grids is represented by the matrices $C_{u\psi}$ and $C_{u\psi}^{\mathrm{T}}$ which realize the boundary integrals in (4.23) and (4.24). Their entries are given by

$$C_{u\psi} = [C_{pq}]; \quad C_{pq} = \int_{\Gamma_h^{\mathrm{a}}} \rho_{\mathrm{a}}\, \phi_p^{\mathrm{e}} \phi_q^{\mathrm{a}} \boldsymbol{n} \,\mathrm{d}\Gamma \;\in \mathbb{R}^d, \tag{4.27}$$

where ϕ_p^{e} is the scalar basis function associated with the node p on $\mathcal{T}^{\mathrm{e}}$, and ϕ_q^{a} is the one for node q on $\mathcal{T}^{\mathrm{a}}$. Thus, the same assembly procedures as in the case of the mortar coupling can be used. It should be emphasized that the coupled system of equations remains symmetric. This is not the case if instead of the acoustic velocity potential an acoustic pressure formulation is used.

4.2.2 Acoustic-Acoustic Coupling

For this type of coupled problem, we will use the framework of mortar methods as studied in the previous chapters. The global domain and its decomposition are again given in Figure 4.1, but this time both subdomains Ω^1 and Ω^2 (replacing Ω^{e} and Ω^{a}, respectively) are occupied by an acoustic fluid. Thus, in each subdomain we have to solve the wave equation for the velocity potentials $\psi_i : \Omega^i \times (0,T) \to \mathbb{R}$,

$$c^{-2}\,\ddot{\psi}_i - \operatorname{div}\operatorname{grad}\psi_i = f_i \quad \text{in } \Omega^i \times (0,T),\ i = 1,2, \tag{4.28}$$

again completed by appropriate initial conditions at time $t = 0$ and boundary conditions on the global boundary Γ^{a}. We emphasize that, in contrast to Section 4.2.1, all of the following considerations apply equally to the formulation of the linear acoustic equations in terms of the acoustic pressure.

Interface Condition

For simplicity, we use the same equation and primal variable in both subdomains, and the interface is just artificial, i.e., no material change occurs. We refer to [7, 79] for the treatment of more general situations. Therefore, in the strong setting, it is natural to impose continuity in the trace and flux of the velocity potential, i.e.,

$$\psi_1 = \psi_2 \quad \text{and} \quad \operatorname{grad}\psi_1 \cdot \boldsymbol{n} = \operatorname{grad}\psi_2 \cdot \boldsymbol{n} \quad \text{on} \quad \Gamma.$$

Analogous to the stationary case treated in Chapter 2, the flux coupling condition will be enforced in a strong sense by introducing the Lagrange multiplier

$$\lambda = -\operatorname{grad}\psi_1 \cdot \boldsymbol{n} = -\operatorname{grad}\psi_2 \cdot \boldsymbol{n}, \tag{4.29}$$

whereas the continuity in the trace will be understood in a weak sense as

$$b(\psi, \mu) = \langle \psi_1 - \psi_2,\ \mu \rangle_\Gamma = 0, \tag{4.30}$$

for all test functions μ out of the Lagrange multiplier space $M = H^{-1/2}(\Gamma)$.

Coupled Formulation

We proceed as in Section 4.2.1 and obtain from (4.28), again ignoring for the moment the boundary condition on Γ^{a},

$$\langle c^{-2} w_i,\, \ddot{\psi}_i(t)\rangle_{\Omega^i} + (\operatorname{grad}\psi_i(t),\, \operatorname{grad} w_i)_{\Omega^i} - \langle w_i,\, \operatorname{grad}\psi_i(t)\cdot \boldsymbol{n}_i\rangle_\Gamma = (f_i(t), w_i)_{\Omega^i},$$

for all test functions w_i, $i = 1, 2$. Inserting the definition of the Lagrange multiplier (4.29) and summing up, we obtain the symmetric evolutionary saddle point problem of finding $\psi = (\psi_1, \psi_2) \in L^2(0,T;\, X)$ and $\lambda \in L^2(0,T;\, M)$ such that for all times $t \in (0,T)$

$$\begin{aligned} \langle c^{-2} w, \ddot{\psi}(t)\rangle_\Omega \;+\; a(\psi(t), w) \;+\; b(w, \lambda(t)) \;&=\; (f(t), w)_\Omega, \qquad && w \in X, && \text{(4.31a)}\\ b(\psi(t), \mu) \;&=\; 0, && \mu \in M. && \text{(4.31b)} \end{aligned}$$

A suitable general functional framework for (4.31) is presented in [7], consisting of a combination of the theory of evolutionary variational equations, [34], and the theory of stationary saddle point problems, [27]. In particular, the same regularity (4.17) as for the purely primal formulation (4.16) can be established subdomain-wise for ψ. The Lagrange multiplier λ can be interpreted as a linear mapping from $H_0^1(0,T)$ to M. Both ψ and λ depend continuously on the data with respect to the corresponding canonical norms.

Spatial Discretization

Again switching to the algebraic formulation and assuming that we have chosen the Lagrange multipliers with respect to Ω^1, the discretization of (4.31a), (4.31b) yields

$$\begin{pmatrix} M_1 & 0 & 0 \\ 0 & M_2 & 0 \\ 0 & 0 & 0 \end{pmatrix} \begin{pmatrix} \ddot{\psi}_{1,h} \\ \ddot{\psi}_{2,h} \\ \ddot{\lambda}_h \end{pmatrix} + \begin{pmatrix} 0 & 0 & 0 \\ 0 & C_\psi & 0 \\ 0 & 0 & 0 \end{pmatrix} \begin{pmatrix} \dot{\psi}_{1,h} \\ \dot{\psi}_{2,h} \\ \dot{\lambda}_h \end{pmatrix} + \begin{pmatrix} K_1 & 0 & D \\ 0 & K_2 & M \\ D^{\mathrm{T}} & M^{\mathrm{T}} & 0 \end{pmatrix} \begin{pmatrix} \psi_{1,h} \\ \psi_{2,h} \\ \lambda_h \end{pmatrix} = \begin{pmatrix} f_{1,h} \\ f_{2,h} \\ 0 \end{pmatrix}.$$

The coupling matrices D, M are given by (1.23), the damping matrix C_ψ results from the absorbing boundary condition (4.14) on Γ^{a}. In [7], a rigorous error analysis is presented. Assuming enough smoothness of the potential ψ, namely, $\psi \in L^\infty(0,T;\, H^2(\Omega))$, $\dot{\psi} \in L^\infty(0,T;\, H^1(\Omega))$, $\ddot{\psi} \in L^2(0,T;\, L^2(\Omega))$, and of the Lagrange multiplier λ, namely, $\lambda \in L^\infty(0,T;\, H^1(\Gamma))$, $\dot{\lambda} \in L^2(0,T;\, L^2(\Gamma))$, it can be shown that the approximation error $e_h^{\mathrm{A}} = \Psi_h \psi - \psi_h$ can be bounded by

$$\begin{aligned} &\|e_h^{\mathrm{A}}\|^2_{C^0(X)} + \|\dot{e}_h^{\mathrm{A}}\|^2_{C^0(L^2(\Omega))} + \|\gamma_0 \dot{e}_h^{\mathrm{A}}\|^2_{L^2(L^2(\Gamma^{\mathrm{a}}))} \\ &\qquad\lesssim\; \|e_h^{\mathrm{A}}(0)\|_X^2 + \|\dot{e}_h^{\mathrm{A}}(0)\|^2_{0,\Omega} && \text{initial data approximation,} \\ &\qquad+\; \|\psi - \Psi_h\psi\|^2_{C^0(X)} + \|\ddot{\psi} - \Psi_h\ddot{\psi}\|^2_{L^2(L^2(\Omega))} && \text{projection error in } \psi, \\ &\qquad+\; \|\gamma_0\dot{\psi} - \gamma_0\Psi_h\dot{\psi}\|^2_{C^0(L^2(\Gamma))} + \|\gamma_0\ddot{\psi} - \gamma_0\Psi_h\ddot{\psi}\|^2_{L^2(L^2(\Gamma))} && \text{projection error in } \gamma_0\psi, \\ &\qquad+\; \|\lambda - \Phi_h\lambda\|^2_{L^\infty(M)} + \|\dot{\lambda} - \Phi_h\dot{\lambda}\|^2_{L^2(M)} && \text{projection error in } \lambda, \end{aligned}$$

with suitable projection operators Ψ_h and Φ_h.

4.3 Numerical Results

We present several numerical experiments for the elasto-acoustic and aero-acoustic coupling. In order to focus on the features of the nonconforming approach, many of the problem settings are kept quite simple. In particular, for the aero-acoustic coupling, we will not perform a numerical approximation of the fluid flow equations, and instead only consider the application of Lighthill's analogy, namely that a nonzero right hand side is entering the acoustic wave equation. Moreover, for the presented examples, it would often not be necessary to resolve the small subregion with a finer grid than the large one. However, as outlined in the introduction, we are interested in problem settings where it is mandatory that the mesh on the small subdomain is substantially finer than the one on the large subdomain. This may be due to the need for resolving small-scale nonlinear effects or complicated geometries.

In Section 4.3.1, we investigate the elasto-acoustic coupling, whereas results for the aero-acoustic coupling are presented in Section 4.3.2. In all numerical experiments, we use the Newmark scheme for time integration with parameters $\beta = 1/4$, $\gamma = 1/2$. In each time step, the resulting linear system is solved exactly. Since we do not have any moving bodies involved, the system matrix which has to be inverted is the same in each time step. Thus, it is possible to factor this system matrix only once, and then to reuse the factorization in each step.

4.3.1 Elasto-Acoustic-Coupling

Four examples for the mechanical-acoustic system are presented. First, a simple two-dimensional setting is considered in order to validate the nonconforming approach. Then, we demonstrate by means of an axisymmetric problem, how the numerical results may be of poor quality, if one has to employ distorted elements for achieving matching interface grids, in contrast to the use of structured grids made possible by dropping the matching requirement. Following this, we demonstrate the gain in flexibility for the nonconforming approach by investigating the emission of acoustic waves from several cylindrical structures. Finally, we present the simulation of a piezo-electric loudspeaker.

Two-dimensional Example

We start with a two-dimensional example. For the fluid domain $\Omega^{\mathrm{a}} = (-0.05, 0.06) \times (0.001, 0.1)\,\mathrm{m}^2$, the parameters of air are taken, $c = 343\,\mathrm{m/s}$, $\rho_{\mathrm{a}} = 1.205\,\mathrm{kg/m}^3$. On the lower edge of Ω^{a}, we append the structure $\Omega^{\mathrm{e}} = (0, 0.01) \times (0, 0.001)\,\mathrm{m}^2$ consisting of silicon, $E = 1.62{\cdot}10^{11}\,\mathrm{N/m}^2$, $\nu = 0.2$, $\rho_{\mathrm{e}} = 2.3{\cdot}10^3\,\mathrm{kg/m}^3$. The structure Ω^{e} is fixed on its left and right edge, on its lower edge a pressure force $\boldsymbol{g}$ is acting with a frequency $f = 1000\mathrm{Hz}$, $\boldsymbol{g}(t) = (0,\, 10^6 \sin(2\pi f t))^{\mathrm{T}}\,\mathrm{N/m}^2$. A time step size of $10\mu\mathrm{s}$ is used and we apply a plane strain formulation for the mechanical structure.

We compare the results obtained with conforming grids with the method using nonconforming grids. In Figure 4.2, a zoom of the computational grids is shown on the left. For both calculations, the grid on Ω^{e} consists of $64{\times}16$ uniform quadrilateral elements.

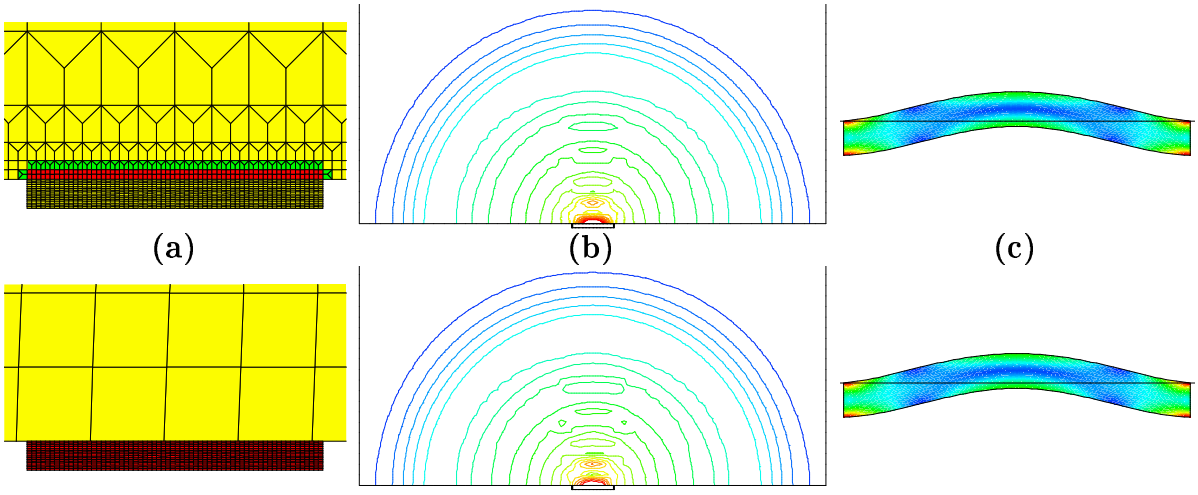

Figure 4.2: 2D example: (a) grid, (b) acoustic velocity potential, (c) deformed structure. Top row: conforming grids, bottom row: nonconforming grids.

For the nonconforming approach, the grid on Ω^a has 44×40 elements, yielding a ratio of the mesh size on Ω^a to the one on Ω^e of 16:1. In order to achieve a truly nonconforming situation, the nodes on the lower edge of Ω^a meeting Ω^e were also moved slightly to the left. For the conforming approach, the "unperturbed" grid on Ω^a was manually refined four times in the region meeting Ω^e. The pictures in the middle show the isolines of the acoustic velocity potentials after 15 time steps, the pictures on the right the von Mises stresses on the deformed structures with displacements magnified by a factor of 500. The results for both calculations behave equally well, no qualitative difference can be detected. This example reveals the clear advantages of the nonconforming approach. For the generation of a subdomain grid, no information from the other subdomain has to be used. We are able to use the grids which are best suited for the solution of the local subproblems. Moreover, if one attempted to move the structure Ω^e to the left or right, it would not be necessary to remesh the fluid Ω^a and to reassemble the corresponding mass and stiffness matrix. Only a reassembly of the coupling matrices would have to be performed.

Axisymmetric Problem

As a further test, we consider an axisymmetric problem. The structure Ω^e, a cylindrical plate of radius 0.2 m and height 0.01 m, is subject to a pressure force $\boldsymbol{g}(t) = (0,\, 0,\, 10^6 \sin 2\pi t)^{\mathrm{T}}\,\mathrm{N/m^2}$ acting on its bottom for the time interval $[0, 1\mathrm{ms}]$. For the acoustic fluid Ω^a, we choose the cylinder of radius 1.4 m and height 0.7 m, attached to Ω^e. Via transformation to cylindrical coordinates, we reduce the originally three-dimensional problem to a two-dimensional one. We compare the calculations for four different grids, as illustrated in Figure 4.3. For the structure Ω^e, we always use a grid consisting of 48×4 elements. In order to have a reference solution available, we choose a rather fine uniform grid of 11025 elements for the fluid Ω^a. For the other three grids, we choose

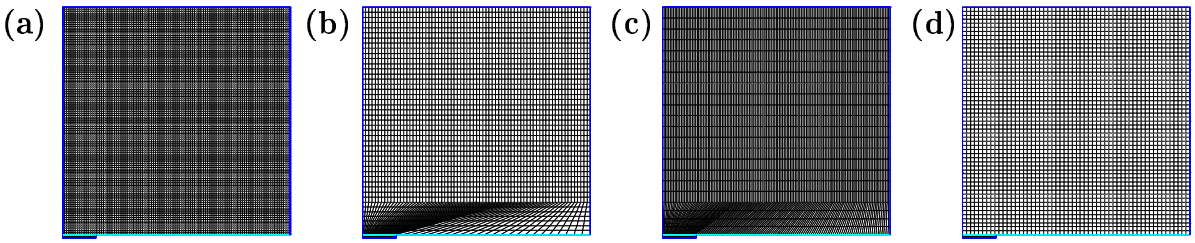

Figure 4.3: Axisymmetric example, computational grids: (a) reference, (b) and (c) matching, (d) non-matching.

roughly the same number of elements (around 3100), assuming that this is the maximum number because of memory restrictions. We test two situations with matching grids and one with non-matching grids. The isolines of the velocity potential at time $t = 1.3$ms for the four calculations are shown in Figure 4.4. The two conforming situations give

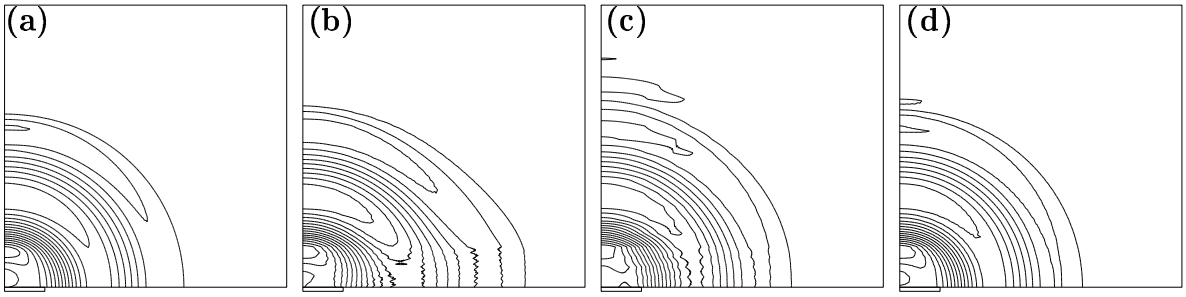

Figure 4.4: Axisymmetric example, isolines of the acoustic potential: (a) reference, (b) and (c) matching, (d) non-matching.

rather rough unphysical solutions, while the nonconforming one remains quite smooth. Of course, there might be matching grids yielding better results than the ones which are shown. But the advantage of the nonconforming approach is that the user does not have to worry about these issues and can choose optimal grids with respect to the subdomain geometry and the available computational resources.

Excitation by Multiple Structures

As a first real three-dimensional example, we present the emission of acoustic waves by multiple structures which admits the steering of the waves by exciting the structures in a specified chronological order. In particular, we use for the structure Ω^e 25 cylindrical silicon chips with diameter 50 µm and height 1 µm. They are placed as a (5×5)-array, each plate having a distance of 50 µm to its nearest neighbors. An excitation force with frequency $f = 1$ MHz is applied on their lower end. For the acoustic domain Ω^a which is assumed to be water, a cuboid of length and width 1200 µm and height 420 µm is chosen. Due to symmetry reasons, we use as computational domain one quarter of the original one. In Fig. 4.5(a), a part of the finite element meshes is shown, for

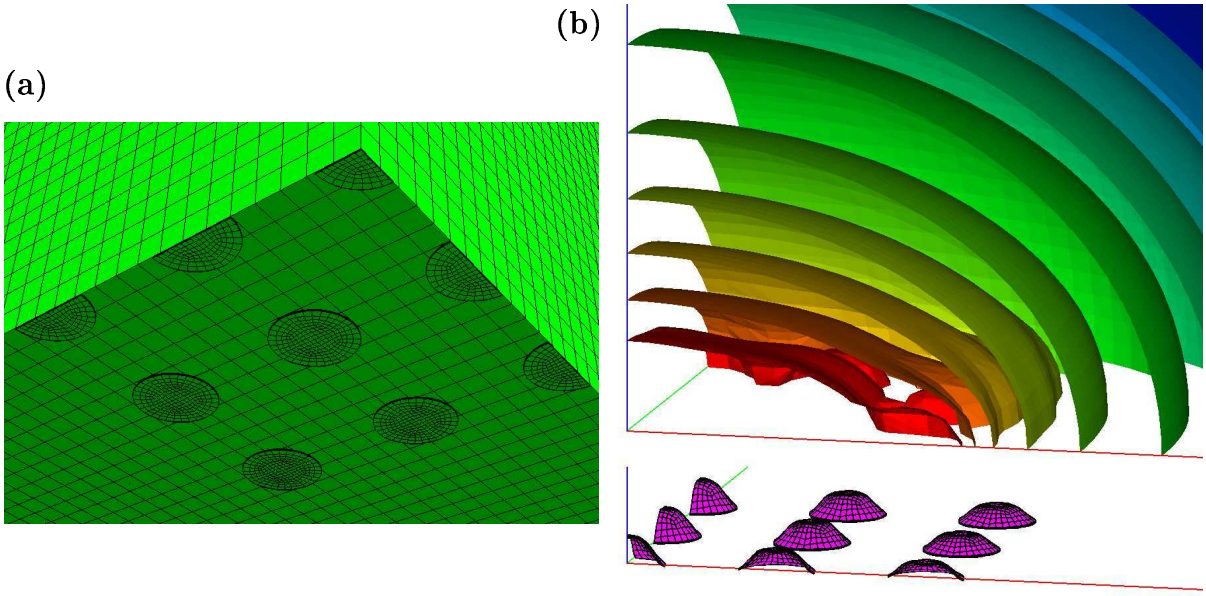

Figure 4.5: (a) cylindrical plates attached to the fluid domain, (b) isosurfaces of the acoustic potential, deformed plates

which a uniform grid of $40\times40\times28$ cubes is used to discretize the acoustic domain and a grid of 768 hexahedrons is employed for each full cylindrical chip. Thus, having a meshwidth of $h_{\mathrm{a}} = 600\,\mu\mathrm{m}/40 = 15\,\mu\mathrm{m}$, we use $c/(f h_{\mathrm{a}}) = 1500\mathrm{m\,s^{-1}}/(1\,\mathrm{MHz}\cdot h_{\mathrm{a}}) = 10$ elements per wavelength for Ω^{a}. If one had to employ matching grids, it would be quite difficult to generate them, and if the mesh-width could not be very small over the whole domain, the resulting element shapes would possibly result in a poor approximation of the solution. The nonconforming approach admits to use the grid desired for each subdomain regardless of the grids for the other subdomains. Moreover, it is very easy to add more plates or to change their position. Only the corresponding part of the coupling matrix would have to be (re-)calculated. Figures 4.6 and 4.7 show snapshots, taken every 10 time steps of 3.5 ns, of the evolution of the acoustic velocity potential ψ along with the deformation of the structures (magnified by a factor of 1000). For the results presented in Figure 4.6, the cylindrical plates are excited simultaneously, while for Figure 4.7, they are excited successively. For both calculations, the waves emitting from the structures add up as expected to constitute the superposed global sound beam. Given a target point, it is possible to optimally steer the acoustic wave towards this point by appropriately adjusting the chronological order of excitation of the silicon chips. This principle is used in so-called capacitive micro-machined ultrasound transducers (CMUTs), [76]. There, the deformation of the structure is induced by an electrostatic surface force acting on the boundary. We will address a similar electric-mechanical-acoustic system in the next example by means of a piezo-electric structure, where a volume coupling of the electric and the mechanical field is considered via the constitutive law.

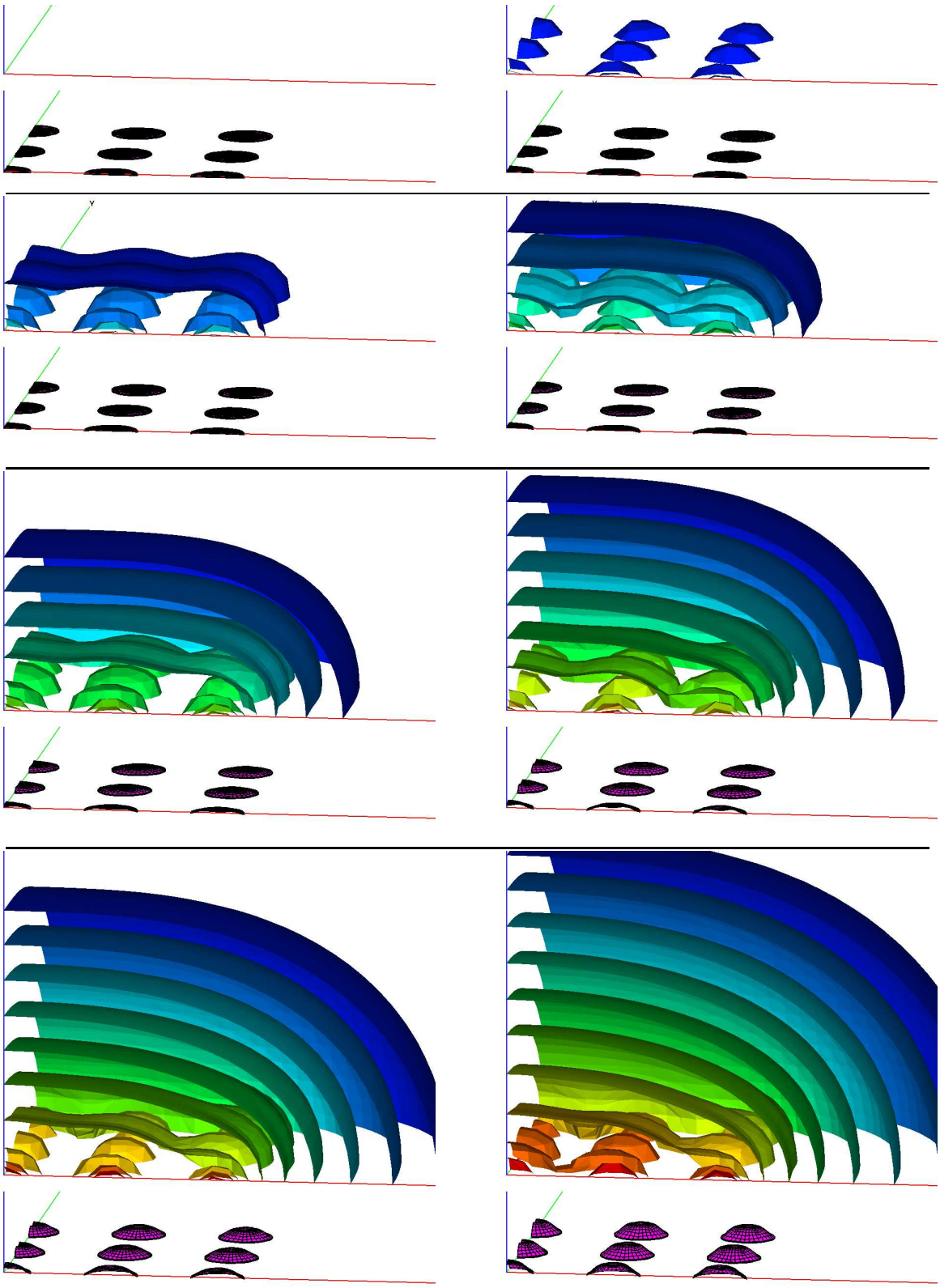

Figure 4.6: Evolution of the acoustic velocity potential and of the deformed structures, synchronous excitation: snapshots after $10, 20, \ldots, 80$ timesteps.

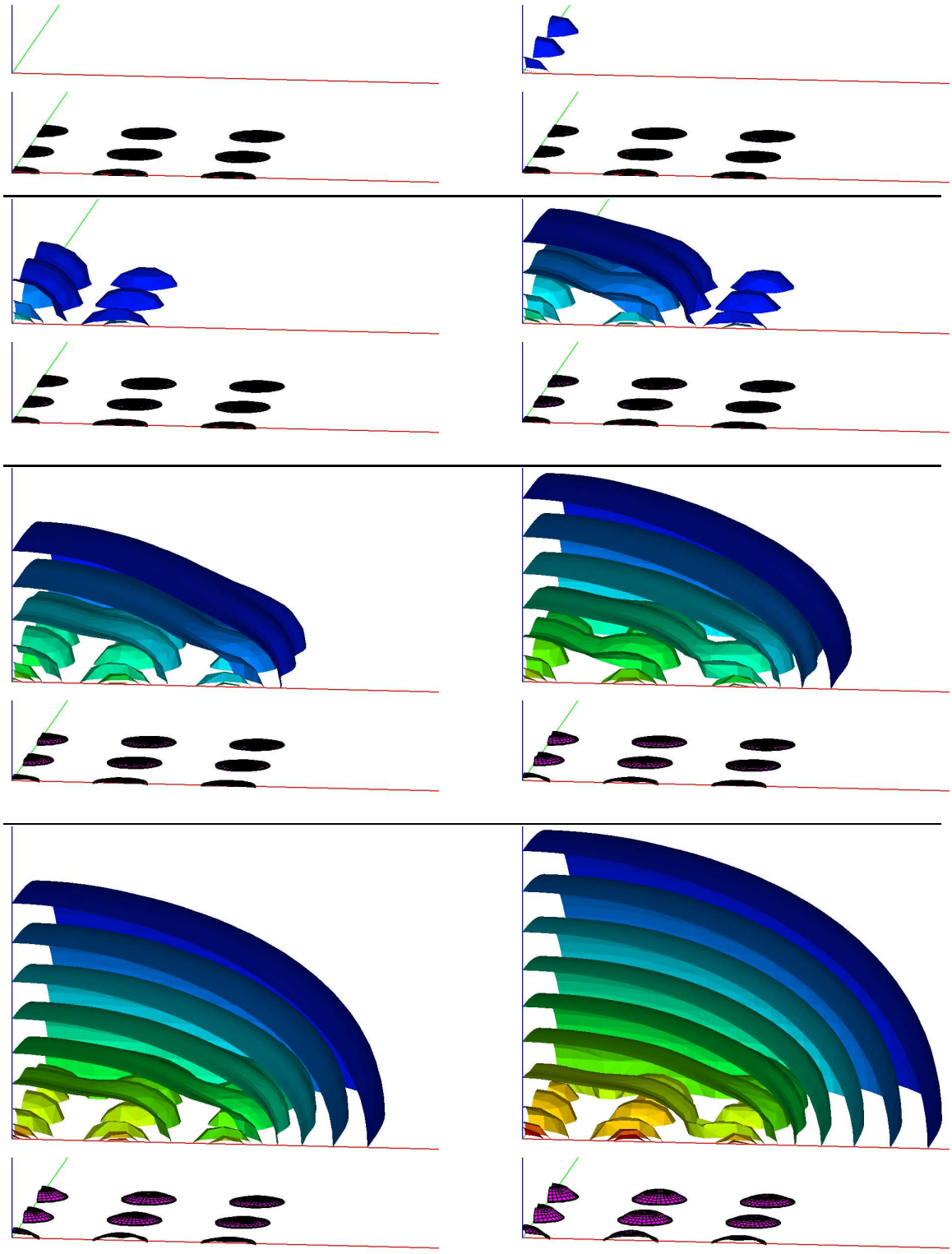

Figure 4.7: Evolution of the acoustic velocity potential and of the deformed structures, successive excitation: snapshots after $10, 20, \ldots, 80$ timesteps.

A Piezo-electric Loudspeaker

In our next example, we choose a piezo-electric material for a part Ω^{p} of the structure Ω^{e}, where mechanical quantities interact with an electric field. The new additional unknowns, namely, the electric potential φ, the flux density $\boldsymbol{d}$, and the electric field $\boldsymbol{e}$, correspond to the displacement $\boldsymbol{u}_{\mathrm{p}}$, the stress σ_{p}, and the strain ε_{p}, respectively. While the evolution of the mechanical displacement $\boldsymbol{u}_{\mathrm{p}}$ is still governed by the equilibrium of forces (4.1a), we have to satisfy a second partial differential equation realizing the conservation of electric charge. Moreover, the coupling between the electrical and the mechanical part takes place within the constitutive relations and is characterized by the elastic stiffness tensor $\mathcal{C}$, the piezo-electric tensor $\mathcal{B}$, and the dielectric permittivity tensor $\mathcal{E}$. Overall, the following coupled problem formulation is obtained: Find $(\boldsymbol{u}_{\mathrm{p}}, \varphi) : \Omega^{\mathrm{p}} \times (0,T) \to \mathbb{R}^{d+1}$ such that

$$\begin{aligned} \rho_{\mathrm{p}} \ddot{\boldsymbol{u}}_{\mathrm{p}} - \operatorname{div} \sigma_{\mathrm{p}}(\boldsymbol{u}_{\mathrm{p}}, \varphi) &= \boldsymbol{f}_{\mathrm{p}}, \\ \operatorname{div} \boldsymbol{d}(\boldsymbol{u}_{\mathrm{p}}, \varphi) &= q, \\ \sigma_{\mathrm{p}}(\boldsymbol{u}_{\mathrm{p}}, \varphi) &= \mathcal{C}\varepsilon_{\mathrm{p}}(\boldsymbol{u}_{\mathrm{p}}) + \mathcal{B}^{\mathrm{T}} \operatorname{grad} \varphi, \\ \boldsymbol{d}(\boldsymbol{u}_{\mathrm{p}}, \varphi) &= \mathcal{B}\varepsilon_{\mathrm{p}}(\boldsymbol{u}_{\mathrm{p}}) - \mathcal{E} \operatorname{grad} \varphi, \end{aligned}$$

where the strain $\varepsilon_{\mathrm{p}}(\boldsymbol{u}_{\mathrm{p}})$ is given by (1.5), complemented by appropriate boundary and initial conditions, [4]. The piezo-electric part Ω^{p} is attached to an aluminum part Ω^{q} such that $\overline{\Omega^{\mathrm{e}}} = \overline{\Omega^{\mathrm{p}} \cup \Omega^{\mathrm{q}}}$, as depicted in Figure 4.8. For Ω^{q}, we seek the displacement $\boldsymbol{u}_{\mathrm{q}}$

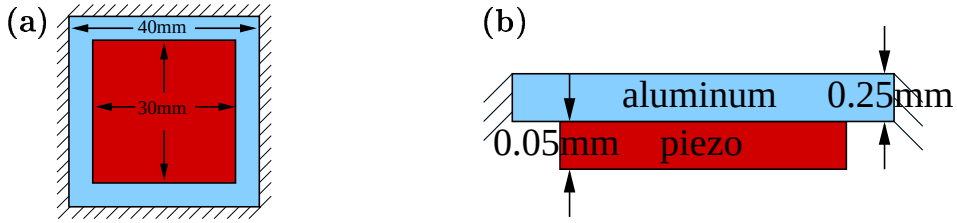

Figure 4.8: Piezo-electric loudspeaker: view of the (a) (x,y)-plane, (b) (x,z)-plane.

as solution of the standard model of linear elasto-dynamics (4.1a), (1.4), and (1.5). The coupling between Ω^{p} and Ω^{q} is again realized by the mortar approach as carried out in Chapter 3. For this particular example, the piezo-electric part Ω^{p} is chosen to be the lead titanate zirconate composition PZT-5 with density $\rho_{\mathrm{p}} = 7.75025{\cdot}10^{3}\,\mathrm{kg\,m^{-3}}$. The elastic stiffness tensor $\mathcal{C}$, the piezo-electric tensor $\mathcal{B}$, and the dielectric permittivity tensor $\mathcal{E}$ are given in Voigt notation [116] by

$$\mathcal{C} = \begin{pmatrix} c_{11} & c_{12} & c_{13} & 0 & 0 & 0 \\ c_{12} & c_{11} & c_{13} & 0 & 0 & 0 \\ c_{13} & c_{13} & c_{33} & 0 & 0 & 0 \\ 0 & 0 & 0 & c_{44} & 0 & 0 \\ 0 & 0 & 0 & 0 & c_{44} & 0 \\ 0 & 0 & 0 & 0 & 0 & (c_{11}-c_{22})/2 \end{pmatrix}, \quad \mathcal{B}^{\mathrm{T}} = \begin{pmatrix} 0 & 0 & b_{31} \\ 0 & 0 & b_{31} \\ 0 & 0 & b_{33} \\ 0 & b_{15} & 0 \\ b_{15} & 0 & 0 \\ 0 & 0 & 0 \end{pmatrix}, \quad \mathcal{E} = \begin{pmatrix} e_{11} & 0 & 0 \\ 0 & e_{11} & 0 \\ 0 & 0 & e_{33} \end{pmatrix},$$

where

$$c_{11} = 1.26{\cdot}10^{11}\,\mathrm{N\,m^{-2}}, \quad c_{12} = c_{13} = 8.41{\cdot}10^{10}\,\mathrm{N\,m^{-2}}, \quad c_{33} = 1.17{\cdot}10^{11}\,\mathrm{N\,m^{-2}},$$

$$c_{44} = 2.3{\cdot}10^{10}\,\mathrm{N\,m^{-2}}, \quad b_{31} = -6.5\,\mathrm{C\,m^{-2}}, \quad b_{33} = 23.3\,\mathrm{C\,m^{-2}},$$
$$b_{15} = 17\,\mathrm{C\,m^{-2}}, \quad e_{11} = 1.51{\cdot}10^{-8}\,\mathrm{C\,V^{-1}\,m^{-1}}, \quad e_{33} = 1.27{\cdot}10^{-8}\,\mathrm{C\,V^{-1}\,m^{-1}}.$$

For the aluminum membrane Ω^{q}, we have the density $\rho_{\mathrm{q}} = 8.4{\cdot}10^{3}\,\mathrm{kg\,m^{-3}}$ and the Lamé parameters $\lambda_{\mathrm{L}} = 2.30769{\cdot}10^{10}\,\mathrm{N\,m^{-2}}$, $\mu_{\mathrm{L}} = 1.53846{\cdot}10^{10}\,\mathrm{N\,m^{-2}}$. The membrane Ω^{q} is fixed at all of its thinner sides as visualized in Figure 4.8, while the remaining boundary of the composed structure Ω^{e} remains free. Between the lower and the upper end of the piezo Ω^{p}, a potential difference $\Delta\varphi(t) = \sin 2\pi f t$ of frequency f is applied by means of a Dirichlet boundary condition for the electric potential φ.

From the geometry dimensions given in Figure 4.8, it can be seen that the ratio of length to thickness is 160 for the aluminum part Ω^{q} and 600 for the piezo-electric part Ω^{p}. From this large ratio, a strong locking effect has to be expected. We investigate this locking effect by comparing the results of the motion under a constant potential difference $\Delta\varphi = 1$ obtained by using piecewise trilinear elements with the ones from employing Serendipity elements. In order to have a more uniform element quality in terms of the ratio h/d of length to thickness, we start with 2×2 elements in Ω^{q} and 4×4 elements in Ω^{p}, and perform a uniform refinement procedure only in (x, y)-direction, thus, always using only one element in z-direction. In Figure 4.9(a), the frequency of the resulting motion at the barycenter p_0 of the upper boundary of Ω^{q} is plotted, while in Figure 4.9(b), the maximum vertical displacement of the same point is visualized, both times against the maximum ratio h/d of the employed elements. The results for

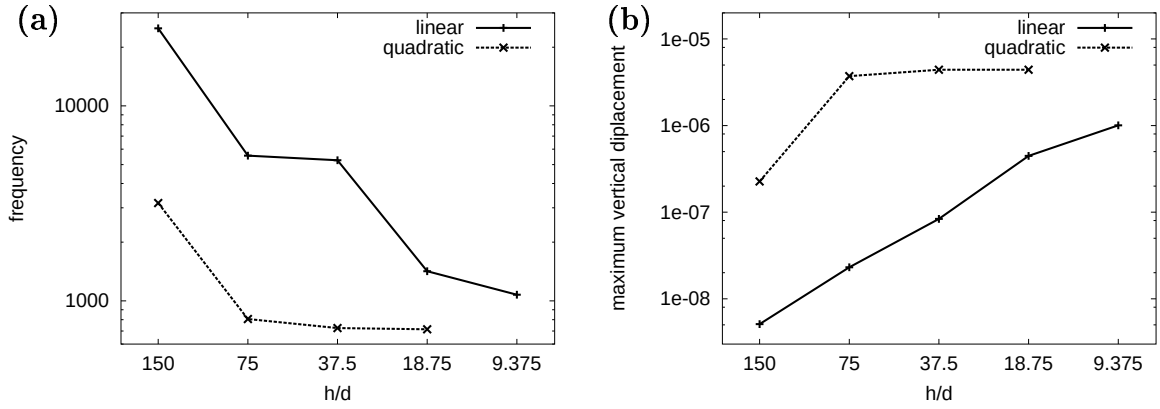

Figure 4.9: Comparison of linear with quadratic elements: (a) frequency, (b) vertical displacement in p_0 against the maximum ratio h/d of the elements.

trilinear elements clearly exhibit the typical signs of locking, namely, an overestimation of the frequency, an underestimation of the displacements, and a very slow convergence towards the correct values. In contrast, a rapid convergence can be observed if the quadratic Serendipity elements are used. Thus, in order to avoid locking, we discretize the structure by Serendipity elements in this example. We remark that there exist numerous alternatives for reducing locking effects for lowest order elements, [23, 112, 114].

In the following, we investigate the elastic response of the structure to applied potentials of the form $\Delta\varphi(t) = \sin(2\pi f t)$ with different frequencies f. The finite element mesh

is kept fixed at 16×16 elements in Ω^p and 8×8 elements in Ω^q, corresponding to the value $h/d = 37.5$ in Figure 4.9. In particular, we examine the applicability and the effect of introducing a damping matrix C_u in the formulation (4.5), which should be responsible for the damping of undesired eigenmodes. We use the easy model of Raleigh damping which is characterized by C_u being proportional to the mass and stiffness matrices, i.e., $C_u = \alpha M_u + \beta K_u$. At first, a low frequency $f = 50\,\text{Hz}$ is considered. Performing 200 time steps of size $\Delta t = 5{\cdot}10^{-4}$, the vertical displacement at p_0 is recorded and depicted in Figure 4.10(a). The dashed line corresponds to the undamped formulation. The applied

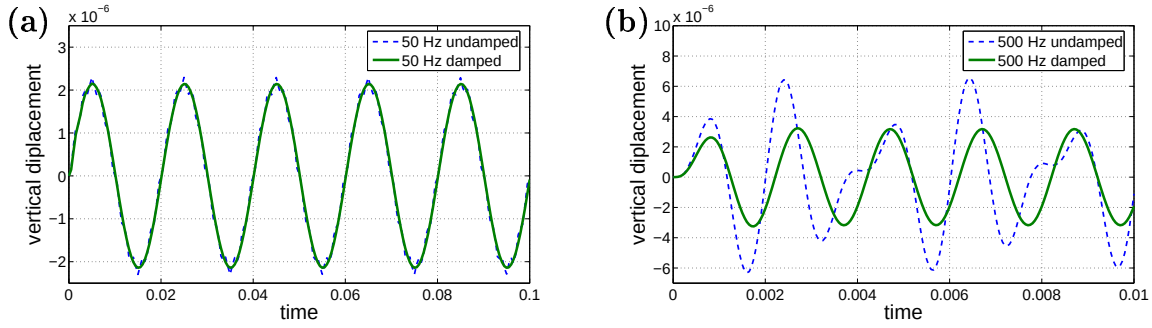

Figure 4.10: Vertical displacement at p_0 for different frequencies of excitation: (a) 50 Hz, (b) 500 Hz.

frequency is well below the first eigenfrequency which has been determined by the last test to be at roughly $f_0 = 720\,\text{Hz}$, as depicted in Figure 4.9(a). While the time step size is motivated by the applied frequency, it is too large to fully resolve the effects of the eigenmodes, a feature which is clearly desired in this particular context. The remaining influence can be easily damped out, resulting in the solid line exhibiting a stable sinusoidal motion. Here, the damping parameters are set to $\alpha = 2.51{\cdot}10^1$, $\beta = 1.59{\cdot}10^{-4}$ in Ω^p, and to $\alpha = 1.63{\cdot}10^1$, $\beta = 1.03{\cdot}10^{-4}$ in Ω^q. The influence of the eigenmodes increases considerably for the next applied frequency $f = 500\,\text{Hz}$, which is in the same range as f_0. As visualized in Figure 4.10(b), the undamped motion is clearly disturbed by the lowest eigenmode. Nevertheless, it is still feasible to extract a stable sinusoidal motion at the applied frequency by employing the Raleigh damping. While the parameter β has been left unchanged, the parameter α has been increased by a factor of 10.

The situation becomes more critical if f is chosen to be greater than f_0. As an example, we consider $f = 5000\,\text{Hz}$. The resulting vertical motion of p_0 is given in Figure 4.11. As before, the overall motion is a superposition of motions of different frequency. However, the frequency f we want to extract is now truly in between several eigenfrequencies, and not the lowest one like in the examples before. By manually adjusting the parameters α and β of the classical Raleigh damping, it seems impossible to extract a desired stable sinusoidal motion at the applied frequency. The solid line in Figure 4.11 corresponds to the result of the damped formulation with α once more increased by a factor of 10 and β decreased by a factor of 10. Obviously, a more sophisticated strategy is needed to damp out eigenfrequencies which are lower than the applied frequency. The development of such a strategy is clearly beyond the scope of this thesis.

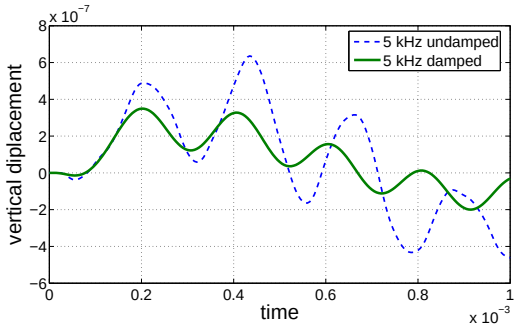

Figure 4.11: Vertical displacement at p_0 for an excitation of frequency 5000 Hz.

It remains to investigate the elasto-acoustic coupling. Since the acoustic medium is chosen to be air, we can neglect the influence of the acoustic field onto the structure. Thus, the system (4.26) is decoupled by setting $C_{u\psi}$ to zero in the first line of (4.26). In every time step, the structural equation is solved first, taking into account the changes in the applied electric potential. Afterwards, the acoustic response is calculated by imposing the normal velocity of the structure as inhomogeneous Neumann condition at the fluid-structure interface. For the solid, we use the same mesh as before: one layer in vertical direction of 16×16 elements in Ω^{p} and 8×8 elements in Ω^{q}, respectively, adding up to about 12000 degrees of freedom. The acoustic domain Ω^{a} is set to be a cuboid of 3 m width and depth, and of 1.5 m height, centered above the structure. On Ω^{a}, we also use quadratic Serendipity elements on a structured grid of meshsize 3/32 m, yielding 16384 hexahedrons and about 70000 degrees of freedom. The choice of the meshsize is motivated by the expected wavelength: since the excitation frequency is set to $f = 500$ Hz, we end up with roughly 7.3 quadratic elements per wavelength, which is enough to give reasonable results. A time step size $\Delta t = 5{\cdot}10^{-5}$s is used for performing 180 time steps. Figure 4.12 shows the resulting velocity potential in four nodes p_i at distances $i{\cdot}0.1875$ m, $i = 1, \ldots, 4$, located directly above the center of the solid. As expected, the frequency coincides with

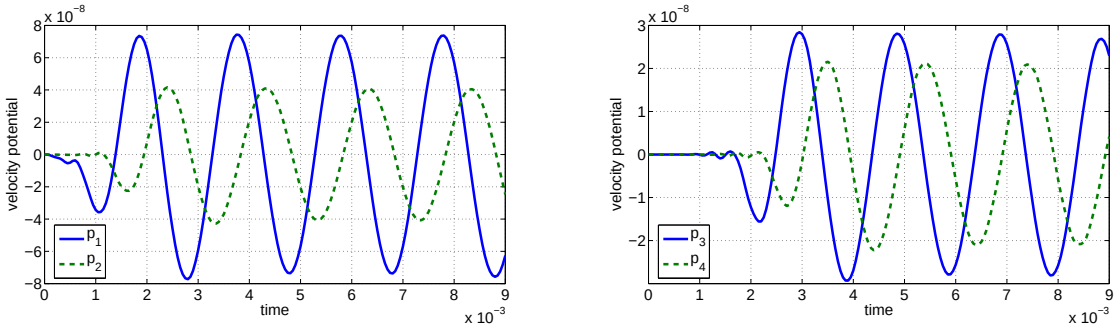

Figure 4.12: Velocity potential at p_i, $i = 1, \ldots, 4$, for an excitation of frequency 500 Hz.

the frequency of excitation by the structure. Moreover, the amplitude of the acoustic waves decreases as the distance to the vibrating structure increases. If we had to choose the meshsize conforming to the solid, namely 1/200 m, and did not want to distort the

elements by coarsening them, we would end up with $(3{\cdot}200/32)^3 = (75/4)^3 > 6000$ times the number of elements for the acoustic part, which would be clearly beyond the capability of present single processor architectures. This effect would become even stronger, if the wavelength increased and larger elements could be chosen to approximate the velocity potential.

4.3.2 Acoustic-Acoustic-Coupling

We present the results of several numerical examples. By means of the propagation of an acoustic wave emitted by a point source, the first one demonstrates that our approach is very robust with respect to a large difference in the grid sizes of two subdomains, and also with respect to the choice of the master and the slave side. We also study the convergence behavior by constructing the source term out of an exact solution. As for the elasto-acoustic problem, we again illustrate the negative effects of having to use distorted elements in order to obtain matching interface grids by investigating the numerical approximation of a single acoustic spherical pulse. Finally, we demonstrate the applicability of the nonconforming method to scattering problems, where once, the incoming wave is simply generated by a non-trivial boundary condition, and once, the source term is given by fluid flow data.

Point Source

In a first test, we choose the domain $\Omega = (-0.05, 0.05)\,\mathrm{m}^2$ and decompose it into $\Omega_1 = (-0.0125, 0.0125)\,\mathrm{m}^2$ and $\Omega_2 = \Omega \setminus \overline{\Omega_1}$. A point source is located at $(0, 0)$ and realized as a Dirichlet node dictating the solution to be $u(0, 0, t) = \sin(2\pi f t)$ with a frequency $f = 1000\,\mathrm{Hz}$. As medium, we choose air: $c = 343\mathrm{m/s}$. A time step size $\Delta t = 10\mu\mathrm{s}$ is used. Figure 4.13 shows the initial grid and two zooms towards the interface of the actual

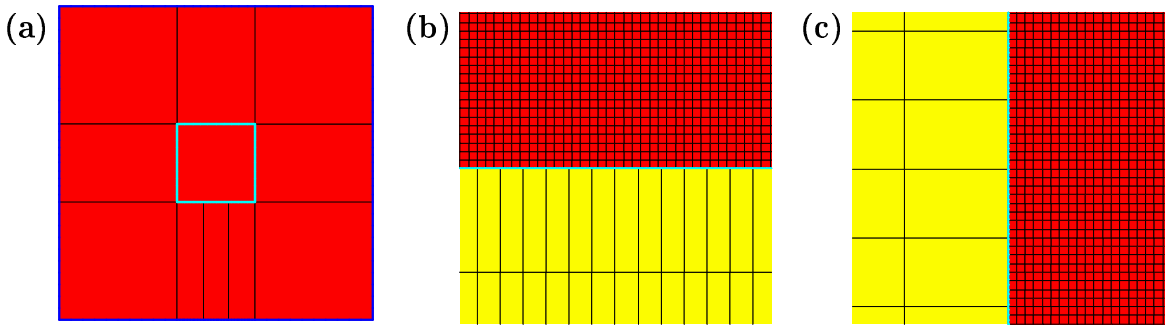

Figure 4.13: Acoustic point source: (a) initial grid, (b) and (c) two zooms into the computational grid.

computational grid, which was obtained by refining the grid on Ω_1 six times and the one on Ω_2 three times. Thus, on the lower interface side, we have a completely nonconforming situation, whereas on the other sides, the inner interface grid is a pure refinement of the outer one, with a mesh size ratio $h_1/h_2 = 1/8$. In Figure 4.14, the isolines of the solutions

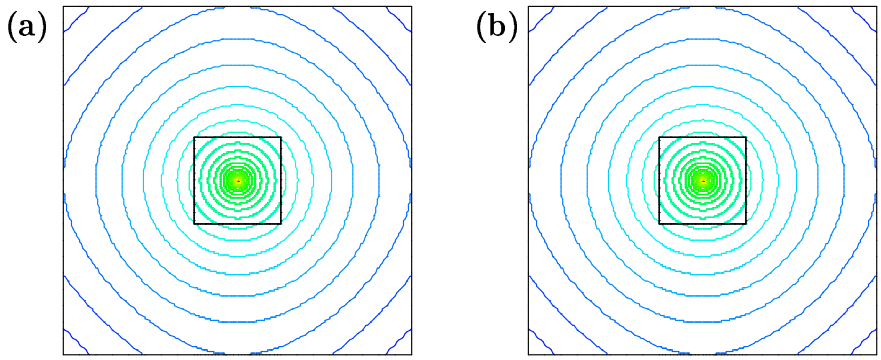

Figure 4.14: Solution at time $t = 280\mu s$, Lagrange multipliers defined with respect to the: (a) fine side, (b) coarse side.

for two settings after 28 time steps at $t = 280\mu s$ are plotted. For Figure 4.14(a), the discrete Lagrange multiplier space was chosen with respect to the fine grid on Ω_1, for Figure 4.14(b), it is defined on the coarse grid of Ω_2. There is no qualitative and no noteworthy quantitative difference between both solutions. Thus, for this example, the choice of the grid for the Lagrange multiplier space does not influence the numerical solution. More important, both solutions are well behaved near the interface and no artificial reflections occur despite the very large difference in the mesh sizes h_1 and h_2.

Convergence Behavior

We study the error decay with respect to a given analytic solution. The global domain is $\Omega = (-1, 1)^2$, with subdomains $\Omega_1 = (-1/3, 1/3)^2$ and $\Omega_2 = \Omega \setminus \overline{\Omega_1}$. In order to separately investigate the dependence of the error on the discretization parameters h and Δt, we perform two different tests. Once, we keep the time step size Δt fixed and perform a uniform refinement procedure of the grids on Ω_1 and Ω_2 starting from the initial triangulation plotted in Figure 4.15(a). The exact solution is set to $\psi(\boldsymbol{x}, t) =$

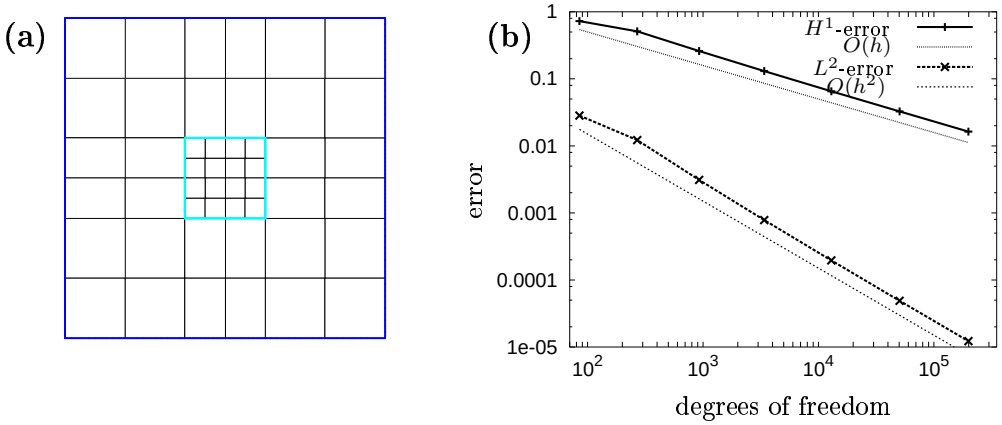

Figure 4.15: Investigation of spatial accuracy: (a) initial grid, (b) error decay.

$t^2 \exp(-50|\boldsymbol{x}|^2)$, which is quadratic in time. Thus, we do not expect to get any error due to time discretization. For the error decay visualized in Figure 4.15(b), the L^2-norm and the H^1-norm of the error after 10 time steps of size $\Delta t = 0.1$ have been calculated for each refinement step. As expected by the theory, the L^2-norm decay is $O(h^2)$, and the H^1-norm decay is $O(h)$. In order to investigate the dependence of the error on the time step size Δt, we set the exact solution to $\psi(\boldsymbol{x}, t) = \frac{1}{2}c^2t^3(x_1 - x_2)$. Thus, the spatial part $x_1 - x_2$ can be exactly interpolated on the initial grid from Figure 4.15(a), and we do not expect any error due to space discretization. Keeping this grid fixed, we record the discretization error at time $T = 4{\cdot}10^{-3}$ for varying time step sizes $\Delta t_k = 4{\cdot}10^{-4}{\cdot}2^{-k}$, $k = 0, \ldots, 9$. The result is given in Figure 4.16. As could be expected by the properties of the Newmark scheme, both the H^1- and the L^2-norm decay with order $O(\Delta t^2)$.

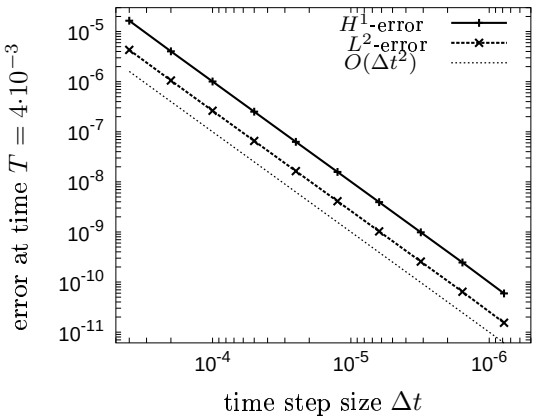

Figure 4.16: Investigation of temporal accuracy: discretization error at time $T = 4{\cdot}10^{-3}$ for varying time step sizes $\Delta t_k = 4{\cdot}10^{-4}{\cdot}2^{-k}$, $k = 0, \ldots, 9$.

Spherical Pulse

We furthermore investigate the numerical approximation of a single acoustic spherical pulse of frequency 1000 Hz and magnitude 1. The computational domain in the (r, z)-plane is shown in the left picture of Figure 4.17. The pulse is imposed in form of an essential boundary condition on $\Gamma_{\mathrm{D}} \subset \partial\Omega^1$. As before, we assume that the grid on Ω^1 has to be substantially finer than that required by the acoustic wavelength. Therefore, we use $2{\cdot}40{\cdot}40 = 3200$ elements on Ω^1, as depicted in the right picture of Figure 4.17. In order to compare the conforming method with the nonconforming one, we take 6400 elements on Ω^2 in both cases, choosing $n_x = 80$, $n_y = 40$ for the conforming and $n_x = 160$, $n_y = 20$ for the nonconforming case. In Figure 4.18, the isolines for the velocity potential at time $t = 1.6\,\mathrm{ms}$ are visualized. Whereas the conforming method exhibits numerical noise before and behind the pulse, the nonconforming approach is much closer to the expected solution. Inside the pulse, the radial symmetry of the isolines from the conforming method is observably disturbed. The poor quality of the conforming method can be easily explained by the fact, that, in order to obtain matching interface grids, the mesh on Ω^2

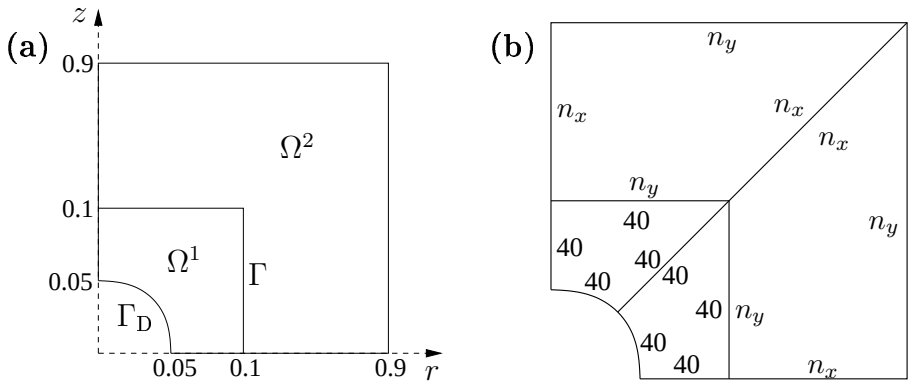

Figure 4.17: Spherical Pulse: (a) axisymmetric domain (dimensions in meter), (b) parameters for the computational grids.

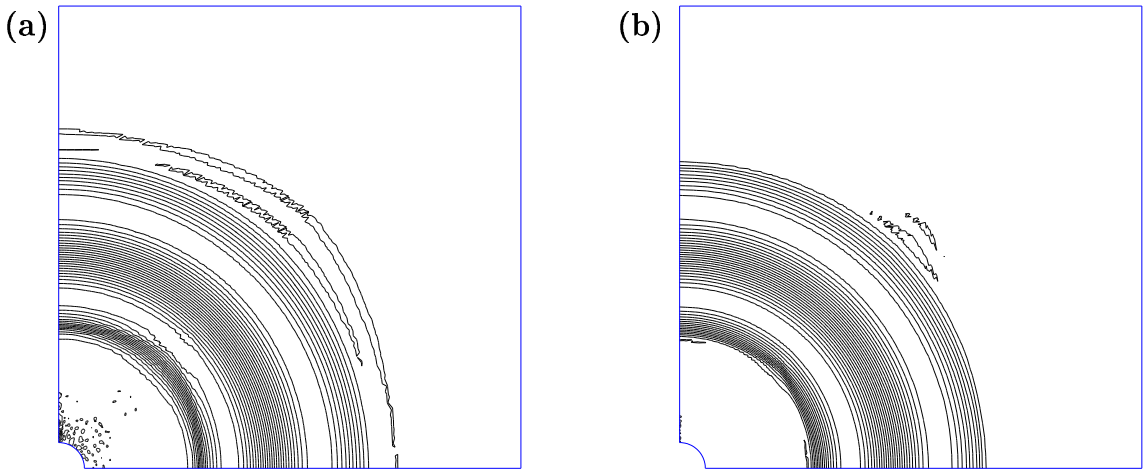

Figure 4.18: Isolines of the acoustic velocity potential at time $t = 1.6\,\mathrm{ms}$: (a) matching and (b) non-matching grids.

is simply too coarse to correctly resolve the solution. In order to examine the transient behavior more closely, we visualize the evolution of the acoustic potential at the point $(0, 0.1\,\mathrm{m})^{\mathrm{T}}$ in Figure 4.19. In addition to the comparison of both approaches, we employ a reference solution, obtained with a uniformly fine grid of 54500 elements. As expected from the observations above, the conforming approach exhibits quite strong oscillations, while the behavior of the nonconforming method is quite smooth and visually coinciding with the reference solution. We remark that even the reference solution is subject to small unphysical oscillations directly after the pulse.

Scattering of Planar Waves

In our next example, we examine the scattering of a wave by a rigid obstacle. As obstacle, a circle of radius 1 is chosen, which has perfectly reflecting walls realized by homogeneous Neumann boundary conditions. It is obvious that the close neighborhood of the circle can

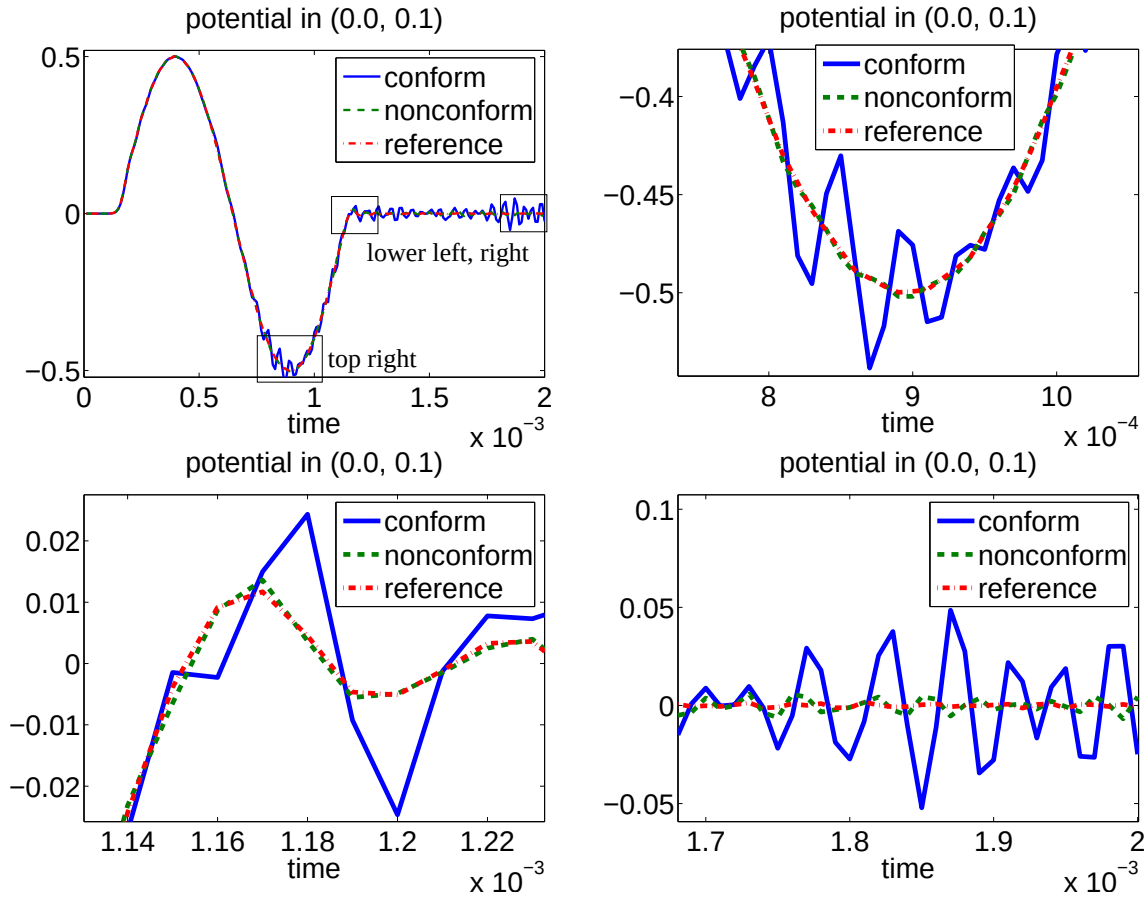

Figure 4.19: Evolution of the acoustic potential at the point $(0, 0.1)^{\mathrm{T}}$.

not be meshed by a uniform triangulation. Therefore, we choose a quadratic subdomain Ω^1 of side length $10/3$ which contains the scattering circle. Inside this subdomain, a unstructured mesh of relatively small meshwidth is used, while outside, it is now possible to employ a structured grid for obtaining an optimal quality of the solution with respect to the grid size. Figure 4.20(a) visualizes the initial grid which is refined three times more for the actual computation. On the left boundary of the computational domain, a Dirichlet boundary condition is imposed which realizes the inflow of a planar wave traveling in x_1-direction,

$$\psi_{\mathrm{i}}(\boldsymbol{x}, t) = \sin(x_1 - ct),$$

where the speed of sound is set to $c = 1$. On the upper and lower boundary, homogeneous Neumann conditions are used, while on the right boundary, we employ the first order local absorbing boundary conditions (4.14). For temporal integration, we choose a time step size of $\Delta t = 0.05$. Figure 4.20(b) shows the scattered waves at time $t = 13.5$. As expected, we can observe a superposition of incoming and reflected waves yielding amplifications as well as reductions depending on space and time. The presence of non-matching grids at the artificial interface does not produce any undesired effects.

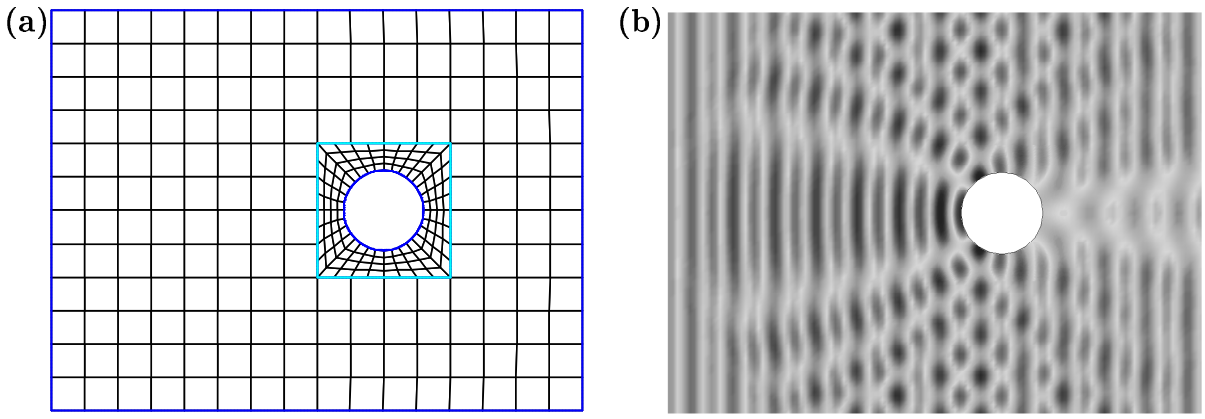

Figure 4.20: Scattering by an obstacle: (a) initial grid, (b) scattered waves at $t = 13.5$.

Flow Induced Noise

Our final example examines the sound generation due to airflow around an obstacle, [9]. In Figure 4.21(a), the situation in three dimensions is illustrated. A cuboidal block is

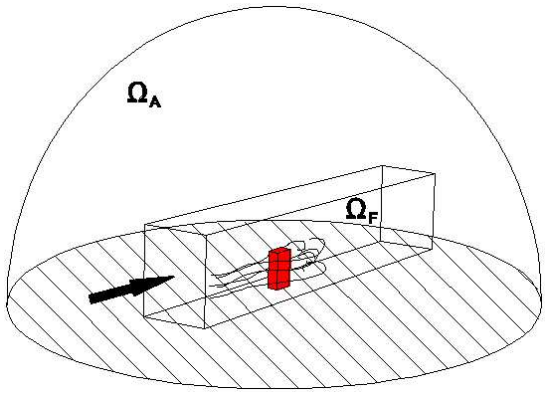

Figure 4.21: Flow induced noise: obstacle subject to airflow.

subject to an incoming airflow. The scattered fluid flow is responsible for the generation of acoustic waves. As carried out before, one often is interested in the sound field quite far away from the obstacle. Since the approximation of the full flow problem over the whole area of interest would be too time-consuming, the assumption is made that it is sufficient to solve the flow problem only in the subdomain $\Omega^1 = \Omega_F$, to calculate a source term for the acoustic wave equation according to Lighthill's analogy [82], and to solve the wave equation on both Ω^1 and on the exterior domain $\Omega^2 = \Omega_A$.

We restrict our example to a reduction of the problem to two dimensions. The obstacle is taken to be the square $\Omega^o = (-0.01\text{m}, 0.01\text{m})^2$, the fluid flow region is given by $\Omega^1 = (-0.2\text{m}, 0.6\text{m}) \times (-0.11\text{m}, 0.11\text{m}) \setminus \overline{\Omega^o}$, and the remaining purely acoustic region is set to $\Omega^2 = (-2.84\text{m}, 3.24\text{m}) \times (-2.75\text{m}, 2.75\text{m}) \setminus \overline{\Omega^o \cup \Omega^1}$. On both subdomains, we employ structured quadrilateral grids. On Ω^1, the grid size is $h_1 = 0.01$ as required by

the flow problem, while on Ω^2, a grid size $h_2 = 0.055$ is sufficient, as required by the acoustic wave length. We perform 60 time steps of size $\Delta t = 10^{-4}$ s. Figure 4.22 shows the isolines of the acoustic velocity potential close to the inner region Ω^1 after 60 time steps. The inflow is from left to right. Clearly, the highest values occur in the immediate

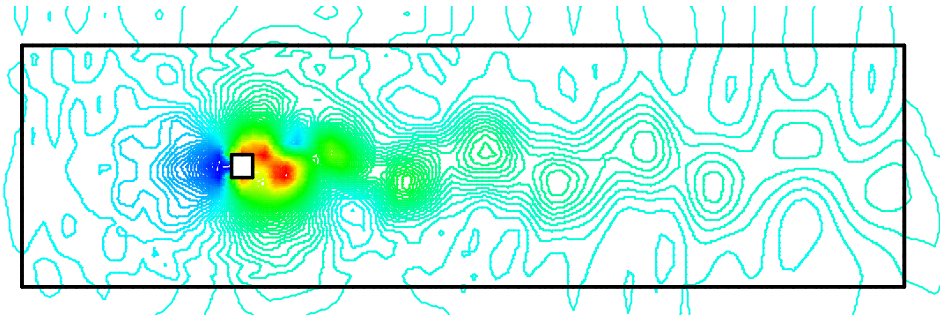

Figure 4.22: Flow induced noise: velocity potential close to the inner region Ω^1.

proximity of the obstacle. More important for demonstrating the applicability of our approach is the fact that the isolines cross the artificial interface in a reasonable way. Figure 4.23 visualizes the sound field further away from the obstacle.

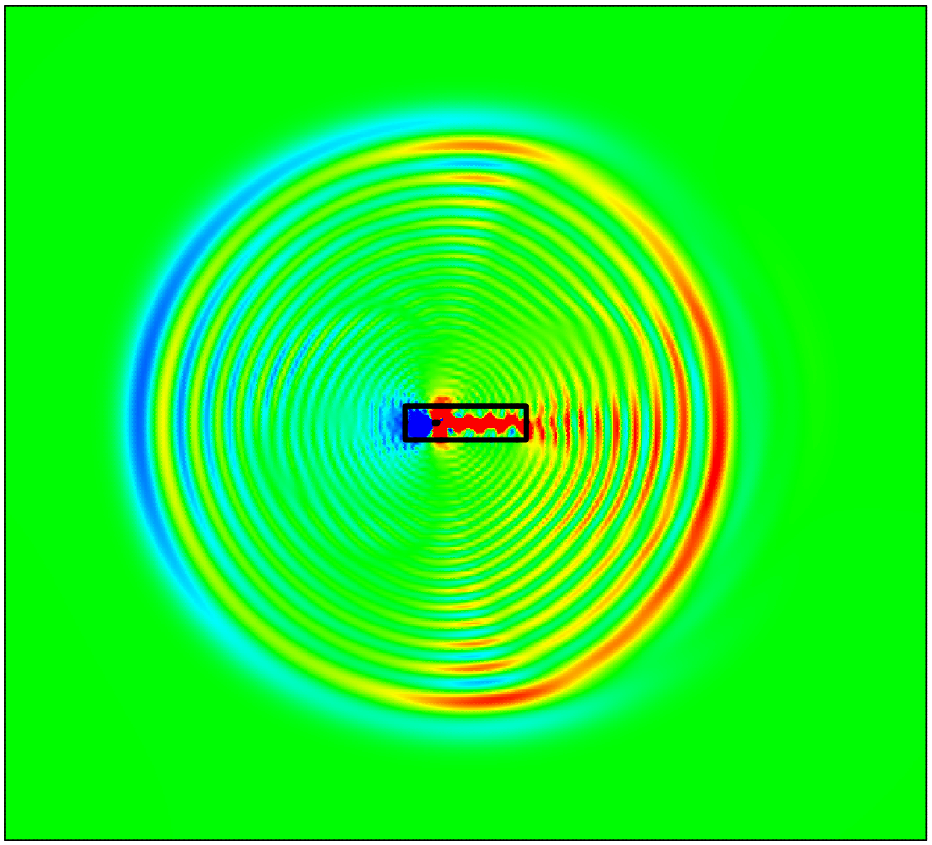

Figure 4.23: Flow induced noise: velocity potential in the whole computational domain.

4.4 Decoupling Nonlinearities

In this section, we extend the elasto-acoustic problem formulation (4.25) to geometrically nonlinear structures. The arising coupled system consists of nonlinear equations for the structural part, while for the acoustic part, we still obtain linear equations. We present an algorithm which takes into account this special structure and yields an efficient solver.

4.4.1 The Coupled System

We first present the discrete system arising from nonlinear structural mechanics after space and time discretization. After that, the corresponding system for linear acoustics is given. Finally, the fully coupled global system is introduced.

Nonlinear Structural Dynamics

The notation sets up on [78]. For the time integration of nonlinear structural dynamics, we will consider the generalized α-method, which extends Newmark's method by introducing two additional parameters $\alpha_m, \alpha_f \in [0,1]$ and setting

$$\ddot{\boldsymbol{u}}_{n+1-\alpha_m} = (1-\alpha_m)\ddot{\boldsymbol{u}}_{n+1} + \alpha_m \ddot{\boldsymbol{u}}_n, \quad \dot{\boldsymbol{u}}_{n+1-\alpha_f} = (1-\alpha_f)\dot{\boldsymbol{u}}_{n+1} + \alpha_f \dot{\boldsymbol{u}}_n, \tag{4.32a}$$

$$\boldsymbol{u}_{n+1-\alpha_f} = (1-\alpha_f)\boldsymbol{u}_{n+1} + \alpha_f \boldsymbol{u}_n, \quad \boldsymbol{f}_{n+1-\alpha_f} = (1-\alpha_f)\boldsymbol{f}_{n+1} + \alpha_f \boldsymbol{f}_n. \tag{4.32b}$$

Applying (4.32) to nonlinear structural dynamics on the spatially discrete level yields the system

$$M_u \ddot{\boldsymbol{u}}_{n+1-\alpha_m} + C_u \dot{\boldsymbol{u}}_{n+1-\alpha_f} + N(\boldsymbol{u}_{n+1-\alpha_f}) = \boldsymbol{f}_{n+1-\alpha_f}, \tag{4.33}$$

with the constant mass matrix M_u, the constant damping matrix C_u, the internal forces N and the external load $\boldsymbol{f}$.

Setting $a_1 = (1-\alpha_f)\gamma/(\beta\Delta t)$ and $a_2 = (1-\alpha_m)/(\beta\Delta t^2)$, the generalized mid-point velocities and accelerations can be given as functions of the end-point displacements $\boldsymbol{u}_{n+1}$ in analogy to (4.7) by

$$\dot{\boldsymbol{u}}_{n+1-\alpha_f}(\boldsymbol{u}_{n+1}) = a_1 \boldsymbol{u}_{n+1} - \widehat{\dot{\boldsymbol{u}}}_n, \tag{4.34a}$$

$$\widehat{\dot{\boldsymbol{u}}}_n = a_1 \boldsymbol{u}_n + \frac{(1-\alpha_f)\gamma - \beta}{\beta}\dot{\boldsymbol{u}}_n + \frac{(1-\alpha_f)(\gamma-2\beta)}{2\beta}\Delta t \ddot{\boldsymbol{u}}_n, \tag{4.34b}$$

$$\ddot{\boldsymbol{u}}_{n+1-\alpha_m}(\boldsymbol{u}_{n+1}) = a_2 \boldsymbol{u}_{n+1} - \widehat{\ddot{\boldsymbol{u}}}_n, \tag{4.34c}$$

$$\widehat{\ddot{\boldsymbol{u}}}_n = a_2 \boldsymbol{u}_n + \frac{1-\alpha_m}{\beta\Delta t}\dot{\boldsymbol{u}}_n + \frac{1-\alpha_m-2\beta}{2\beta}\ddot{\boldsymbol{u}}_n. \tag{4.34d}$$

This gives the effective structural equation

$$0 = G_u(\boldsymbol{u}_{n+1}) = N(\boldsymbol{u}_{n+1-\alpha_f}) - \boldsymbol{f}_{n+1-\alpha_f} + C_u \dot{\boldsymbol{u}}_{n+1-\alpha_f}(\boldsymbol{u}_{n+1}) + M_u \ddot{\boldsymbol{u}}_{n+1-\alpha_m}(\boldsymbol{u}_{n+1}). \tag{4.35}$$

The application of Newton's method to (4.35) amounts to solve in each iteration step q the linear system

$$K_u^*(\boldsymbol{u}_{n+1}^q)\Delta\boldsymbol{u} = -G_u(\boldsymbol{u}_{n+1}^q), \qquad \Delta\boldsymbol{u} = \boldsymbol{u}_{n+1}^{q+1} - \boldsymbol{u}_{n+1}^q, \tag{4.36}$$

with the deformation-dependent effective tangential matrix $K^*(\boldsymbol{u}^q_{n+1})$ given by

$$K^*_u(\boldsymbol{u}^q_{n+1}) = K^{\mathrm{t}}_{n+1-\alpha_m}(\boldsymbol{u}^q_{n+1}) + a_1 C_u + a_2 M_u, \tag{4.37}$$

where $K^{\mathrm{t}}_{n+1-\alpha_m}(\boldsymbol{u}^q_{n+1})$ denotes the tangential stiffness matrix

$$K^{\mathrm{t}}_{n+1-\alpha_m}(\boldsymbol{u}^q_{n+1}) = \frac{\partial N(\boldsymbol{u}^q_{n+1-\alpha_f})}{\partial \boldsymbol{u}_{n+1}}. \tag{4.38}$$

Linear Acoustics

The generalized α-method (4.32) applied to the weak form (4.16) of the wave equation (4.11a) for the acoustic velocity potential ψ gives

$$M_\psi \ddot{\psi}_{n+1-\alpha_m} + C_\psi \dot{\psi}_{n+1-\alpha_f} + K_\psi \psi_{n+1-\alpha_f} = 0, \tag{4.39}$$

with constant matrices M_ψ, C_ψ, K_ψ. Now, the consideration (4.34) yields a linear system to be solved at each time step,

$$K^*_\psi \psi_{n+1} = C_\psi \widehat{\dot{\psi}}_n + M_\psi \widehat{\ddot{\psi}}_n, \tag{4.40}$$

with the constant effective acoustic stiffness matrix

$$K^*_\psi = K_\psi + a_1 C_\psi + a_2 M_\psi. \tag{4.41}$$

The Global System

We set $\underline{u} = (\boldsymbol{u}, \psi)^{\mathrm{T}}$ and the matrices

$$C = \begin{pmatrix} \widetilde{C}_{u\cdot} \\ \widetilde{C}_{\psi\cdot} \end{pmatrix} = \begin{pmatrix} C_u & C_{u\psi} \\ C_{\psi u} & C_\psi \end{pmatrix}, \quad M = \begin{pmatrix} \widetilde{M}_{u\cdot} \\ \widetilde{M}_{\psi\cdot} \end{pmatrix} = \begin{pmatrix} M_u & 0 \\ 0 & M_\psi \end{pmatrix}. \tag{4.42}$$

The global system coupling structural dynamics with acoustics reads

$$G(\underline{u}_{n+1}) = 0, \tag{4.43a}$$
$$K^*_{\psi\cdot}\underline{u}_{n+1} = g_n, \tag{4.43b}$$

with

$$G(\underline{u}_{n+1}) = N(\boldsymbol{u}_{n+1-\alpha_f}) + \left(a_1 \widetilde{C}_{u\cdot} + a_2 \widetilde{M}_{u\cdot}\right)\underline{u}_{n+1} - \boldsymbol{f}_{n+1-\alpha_f} - \widetilde{\boldsymbol{u}}_n, \tag{4.44}$$
$$K^*_{\psi\cdot} = \begin{pmatrix} 0 & K_\psi \end{pmatrix} + a_1 \widetilde{C}_{\psi\cdot} + a_2 \widetilde{M}_{\psi\cdot}, \tag{4.45}$$
$$g_n = \widetilde{\psi}_n, \tag{4.46}$$

where we set

$$\underline{\widetilde{u}}_n = C\underline{\widehat{u}}_n + M\underline{\widehat{\ddot{u}}}_n. \tag{4.47}$$

4.4.2 Iterative Solution

We exploit the structure of the global system (4.43) by constructing iterative schemes, where the nonlinear equations (4.43a) are decoupled from the linear equations (4.43b) in each iteration step. We first present the most straightforward alternative by means of a non-overlapping block Gauß–Seidel scheme. Since this scheme turns out to be inefficient, we improve it by admitting the diagonal blocks to overlap. Finally, we investigate an inexact variant by fixing the maximum number of Newton steps.

Non-overlapping

Instead of applying Newton's method to the global system (4.43), we make use of the linearity of (4.43b) by employing the Gauß–Seidel scheme

$$G(\boldsymbol{u}^{k+1}, \psi^k) = 0, \tag{4.48a}$$

$$K_{\psi.}^{*}\underline{u}^{k+1} = g. \tag{4.48b}$$

We are now able to apply Newton's method only to (4.48a). The overall iterative solution procedure is given by Algorithm 2. We remark that most of the matrices only have to be assembled once in the very beginning, and only the relatively small tangential stiffness matrix $K^{\mathrm{t}}(\boldsymbol{u})$ has to be calculated in every Newton step. Unfortunately, the iteration count for the Gauß–Seidel scheme is far too high to yield an efficient algorithm, as we will show by a numerical example.

Algorithm 2 Iterative solution by a block Gauß–Seidel scheme

Set up the matrices M, C, K_ψ, K_ψ^*.	(4.42),(4.41)
for all time steps $n = 1, \ldots$ **do**	
Calculate $\boldsymbol{f}$, $\widehat{\underline{u}}$, $\widehat{\underline{\dot{u}}}$, $\widetilde{\underline{u}}$, g.	(4.34b),(4.34d),(4.47),(4.46)
for all Gauß–Seidel steps $k = 1, \ldots$ **do**	
for all Newton steps $q = 1, \ldots$ **do**	
Calculate $K^{\mathrm{t}}(\boldsymbol{u})$, $K_u^*(\boldsymbol{u})$, $G(\underline{u})$.	(4.38),(4.37),(4.44)
Solve $K_u^* \Delta\boldsymbol{u} = -G(\underline{u})$.	
Update $\boldsymbol{u} \leftarrow \boldsymbol{u} + \Delta\boldsymbol{u}$.	
Check for Newton convergence.	
end for	
Calculate $\widehat{g} = g - a_1 C_{\psi u}$.	(4.45)
Solve $K_\psi^* \psi = \widehat{g}$.	(4.45)
Update $\underline{u}$ (damping possible).	
Check for Gauß–Seidel convergence.	
end for	
Update $\underline{\dot{u}}$, $\underline{\ddot{u}}$.	(4.34a),(4.34c)
end for	

We investigate the sound emission of a vibrating structure in water. The structure Ω^{s} is of width 0.2 m and height 0.01 m and has the material parameters of silicon,

ρ_e=2.3·10^3 kg m^{-3}, E=1.62·10^{11} N m^{-2}, ν=0.2. It is fixed at its left and right boundary, and a surface traction of $10^8 \sin(2\pi 1000t)$ N m^{-2} is acting in vertical direction at its lower boundary. We assume the structure to behave geometrically nonlinear. The acoustic fluid domain Ω^a of width 1.4 m and height 0.7 m is centered above the structure. The mean density is $\rho_a = 10^3$ kg m^{-3}, the speed of sound is $c = 1.5 \cdot 10^3$ m s^{-1}. Due to symmetry reasons, we can set the computational domain to one half of the original one. In Figure 4.24(a), the computational grid is plotted, visualizing the structure in the lower

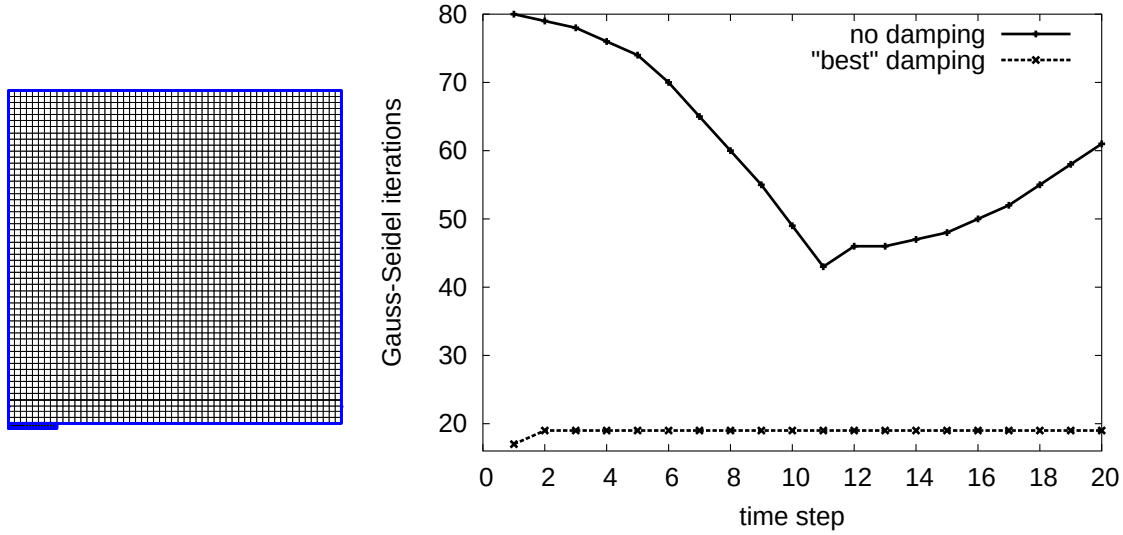

Figure 4.24: Test of Gauß-Seidel scheme: (a) computational grid, (b) iteration count versus time step

left part. Figure 4.24(b) shows the iteration count of the Gauß-Seidel scheme for the first 20 time steps. Depending on the time step, it ranges between 43 and 80 which is far too high for a block two-by-two system. Damping substantially improves the convergence behavior. At the end of each Gauß-Seidel step, we choose

$$\underline{u} = \omega \underline{u}^{\text{new}} + (1 - \omega)\underline{u}^{\text{old}}.$$

A quite good improvement is achieved for $\omega = 0.7$, as also shown in Figure 4.24(b). The iteration count is decreased to 19 and is very robust with respect to the solution behavior. However, it is still too high for obtaining numerical efficiency.

Overlapping

In order to improve the convergence behavior of the Gauß–Seidel method, we further decompose ψ into $(\psi_1, \psi_2, \lambda)$, where $\boldsymbol{u}$ couples with ψ_1 via $C_{u\psi}$ and $C_{\psi u}$, and ψ_1 with ψ_2 via the Lagrange multiplier λ in the same manner as in the preceding chapters. For the

matrices, we have

$$C = \begin{pmatrix} \widetilde{C}_{u\cdot} \\ \widetilde{C}_{1\cdot} \\ \widetilde{C}_{2\cdot} \\ \widetilde{C}_{\lambda\cdot} \end{pmatrix} = \begin{pmatrix} C_u & C_{u\psi} & 0 & 0 \\ C_{\psi u} & C_1 & 0 & 0 \\ 0 & 0 & C_2 & 0 \\ 0 & 0 & 0 & 0 \end{pmatrix}, \quad M = \begin{pmatrix} \widetilde{M}_{u\cdot} \\ \widetilde{M}_{1\cdot} \\ \widetilde{M}_{2\cdot} \\ \widetilde{M}_{\lambda\cdot} \end{pmatrix} = \begin{pmatrix} M_u & 0 & 0 & 0 \\ 0 & M_1 & 0 & 0 \\ 0 & 0 & M_2 & 0 \\ 0 & 0 & 0 & 0 \end{pmatrix}.$$

We modify (4.48) towards the overlapping scheme

$$G^{\mathrm{o}}(\boldsymbol{u}^{k+1}, \psi_1^{k+1}, \psi_2^k, \lambda^k) = 0, \tag{4.49a}$$

$$K^*_{\psi\cdot}\underline{u}^{k+1} = g, \tag{4.49b}$$

with

$$K^*_{\psi\cdot} = \begin{pmatrix} 0 & K_{11} & 0 & K_{1\lambda} \\ 0 & 0 & K_{22} & K_{2\lambda} \\ 0 & K_{\lambda 1} & K_{\lambda 2} & 0 \end{pmatrix} + a_1\widetilde{C}_{\psi\cdot} + a_2\widetilde{M}_{\psi\cdot}, \tag{4.50}$$

$$G^{\mathrm{o}}(\underline{u}) = \begin{pmatrix} N(\boldsymbol{u}) - \boldsymbol{f} \\ K_{11}\psi_1 + K_{1\lambda}\lambda \end{pmatrix} + \left(a_1 C_{u1,\cdot} + a_2 M_{u1,\cdot}\right)\underline{u} - \begin{pmatrix} \widetilde{\boldsymbol{u}} \\ \widetilde{\psi}_1 \end{pmatrix}, \tag{4.51}$$

$$g = \widetilde{\psi}. \tag{4.52}$$

For the resulting algorithm, only the Newton iteration has to be changed, i.e. the shaded region in Algorithm 2. The modified Newton scheme is given in Algorithm 3.

Algorithm 3 Newton iteration for overlapping scheme

for all Newton steps $q = 1, \ldots$ **do**
  Calculate $K^{\mathrm{t}}(\boldsymbol{u})$, $K^*_u(\boldsymbol{u})$, $G^{\mathrm{o}}(\underline{u})$. (4.38),(4.37),(4.51)
  Set up $K^*_{\mathrm{o}} = \begin{pmatrix} K^*_u(\boldsymbol{u}) & K^*_{u\psi} \\ K^*_{\psi u} & K^*_1 \end{pmatrix}$.
  Solve $K^*_{\mathrm{o}}\Delta \begin{pmatrix} \boldsymbol{u} \\ \psi_1 \end{pmatrix} = -G^{\mathrm{o}}(\underline{u})$.
  Update $\begin{pmatrix} \boldsymbol{u} \\ \psi_1 \end{pmatrix} \leftarrow \begin{pmatrix} \boldsymbol{u} \\ \psi_1 \end{pmatrix} + \Delta \begin{pmatrix} \boldsymbol{u} \\ \psi_1 \end{pmatrix}$.
  Check for Newton convergence.
end for

We use the same example as above to investigate the behavior of the overlapping method. In particular, we vary the thickness of the overlap. The thicker horizontal line inside the acoustic domain in Figure 4.25(a) indicates the upper boundary of the overlapping region. Thus, four element layers of overlap are used. In Figure 4.25(b), the iteration counts for different numbers of overlapping layers are visualized. Already a very small number of layers results in a strong improvement. With four or eight layers, the count is around 5 or 4, which is quite reasonable.

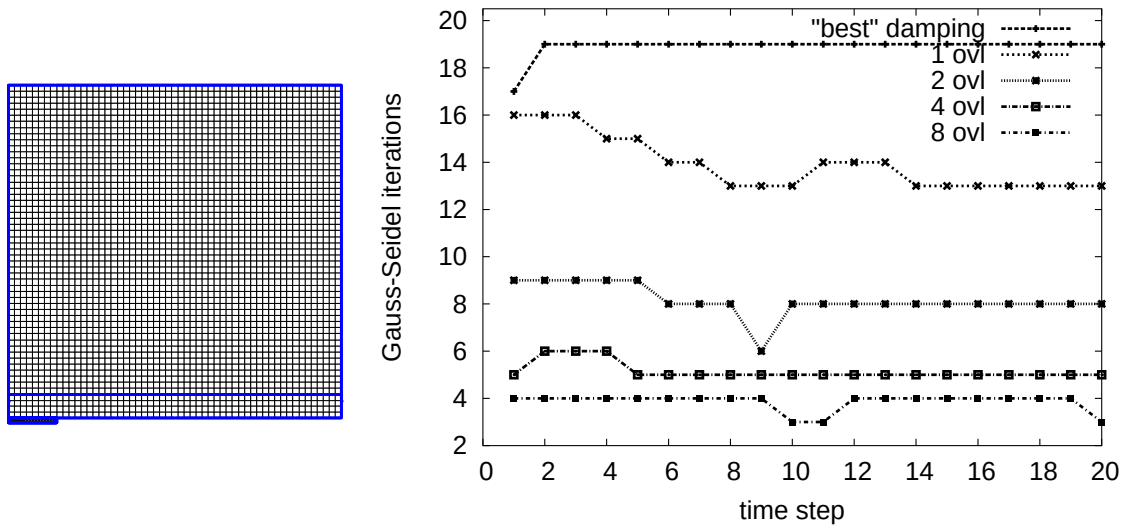

Figure 4.25: Test of overlapping scheme: (a) domain decomposition, (b) iteration count versus time step, varying the overlap

Inexact Strategy

So far, in each Gauß–Seidel step, there have been made so many Newton steps as necessary to meet the stopping criteria of the relative difference of two iterates to be below 10^{-10}. In Figure 4.26, the number of Newton iterations is plotted versus the time step

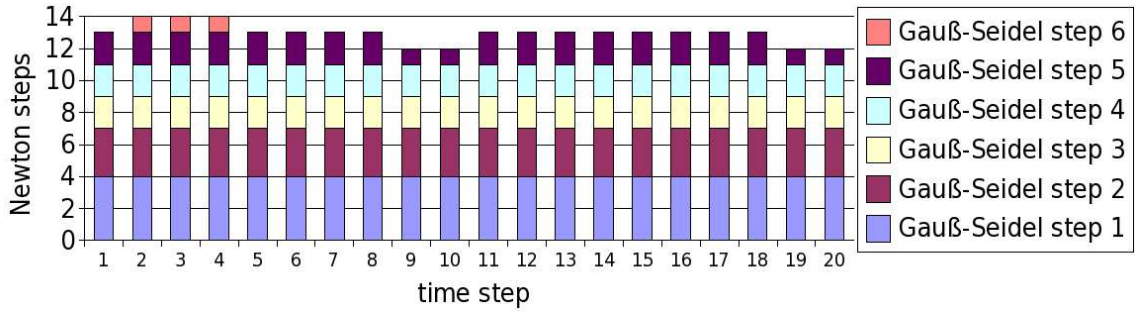

Figure 4.26: Overlapping Gauß–Seidel scheme, four layers of overlap: Newton iterations versus time step.

for the Gauß–Seidel scheme using four layers of overlap. In particular, the total number of Newton iterations per time step determines the height of the columns, whereas each column is subdivided to display the number of Newton iterations per Gauß–Seidel step within each time step. The first observation to be made is that the total number of Newton iterations per time step is almost constant, as already suggested by the stable behavior of the Gauß–Seidel scheme. Moreover, the number of Newton iterations in each Gauß–Seidel step is very low. Starting from the solution of the previous time step, it only takes four Newton iterations in the first Gauß–Seidel step, three in the second, and

between one and two in the subsequent steps. Nevertheless, the efficiency of the scheme can further be improved by employing an inexact strategy.

To this end, only one single Newton step is performed in each Gauß–Seidel step. Figure 4.27 shows the resulting iteration count for the Gauß–Seidel scheme versus the time steps for different numbers of overlapping layers. Up to eight layers, almost no difference

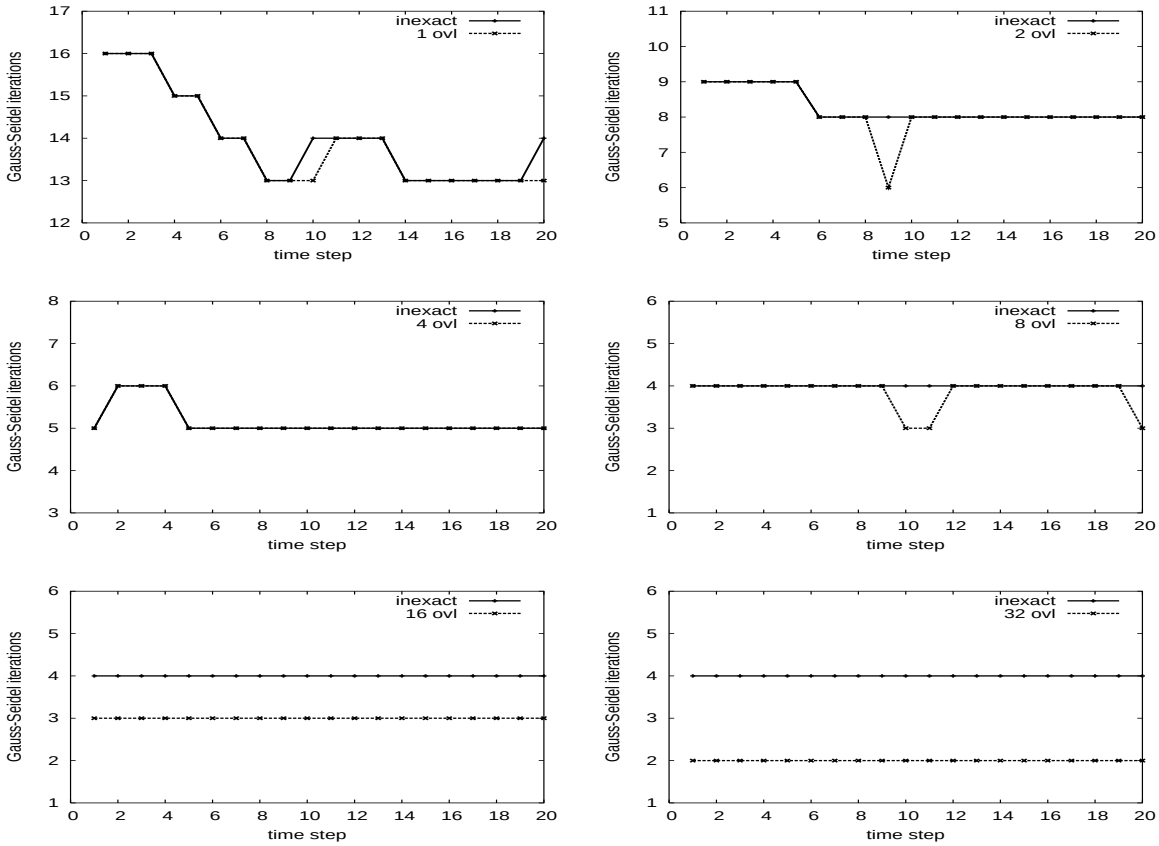

Figure 4.27: Overlapping Gauß–Seidel: inexact (solid line) vs. exact (dashed) strategy.

between the exact and the inexact method can be observed. This means that the number of Newton steps per time step reduces significantly to the number of Gauß–Seidel steps per time step. We remark that the resulting number of Newton steps per time step for the inexact strategy seems to be bounded from below by the number of Newton steps for the first Gauß–Seidel step of the exact strategy. Thus, if the size of the overlap further increases, the iteration count for the inexact method becomes worse than the one for the exact method. However, in the reasonable range between four and eight layers of overlap, the inexact strategy is clearly superior.

5 Overlap

In this chapter, we focus on overlapping domain decomposition methods, which have become an area of strong research over the past years [100, 113, 122, and the references therein]. As in the non-overlapping case, it is strongly desirable to keep as much flexibility as possible by discretizing the problems on non-matching grids. Again, the challenging task is to find suitable projection operators between the involved grids. Standard Lagrange interpolation operators often result in a loss of accuracy due to insufficient stability properties, while mortar techniques lead to optimal a priori error estimates also in the case of overlapping subdomains [2, 30]. However, the methods in the mentioned references applied to nested domains do not yield optimal results.

Problems involving nested domains have been extensively studied in the context of the Navier–Stokes equations. The region near the moving object of interest is discretized, and the resulting local grid moves together with the object through an underlying global grid. So-called Chimera methods are used to establish a bi-directionally coupled problem formulation by cutting out parts of the global grid, thereby creating an artificial boundary [68, 118]. An alternative approach to handle nested domains is provided by fictitious domain methods [53, 86].

In this chapter, we analyze the case of one subdomain which is nested inside the global domain of interest. Both the global domain and the subdomain are discretized by triangulations which may be completely independent of each other. The coupling between the two grids is managed by a projection operator onto the interface which has to satisfy certain stability and approximation properties. We lay special emphasis on the case of different meshwidths and different polynomial orders of the finite element spaces on the two grids. The developed method is ideally suited for transient problems, where the position of the subdomain may change during the computation. In this case, no remeshing will be necessary, and only the matrix responsible for the coupling has to be reassembled. In contrast to the above mentioned Chimera type methods, no elements of the grid on the global domain will be cut out in our approach. Moreover, unlike using a fictitious domain method, we calculate two solutions on two independent grids, and the values of the solution outside the subdomain are of physical relevance and interest.

We examine a one-directional coupling, where the solution on the global domain defines the boundary data for the problem on the subdomain. However, the presented coupling technique has been applied to several bi-directionally coupled problems, including the motion of a conductor through an electromagnetic field as carried out in Chapter 6, where different model equations and discretization techniques are coupled, demonstrating the flexibility of the approach.

Starting with the setup of the continuous model problem in Section 5.1, we introduce a discrete variational formulation, for which an a priori estimate is obtained in Section

5.2. The corresponding algebraic system is derived in Section 5.3. Section 5.4 is dedicated to the presentation of several numerical results, including a $\mathbb{P}_1$–$\mathbb{P}_2$ coupling and an application to a unilateral contact problem.

5.1 Continuous Setting and Discretization

5.1.1 Problem Description

We consider the model problem (1.1) with $\Gamma_{\mathrm{D}} = \partial\Omega$ and assume that Ω is an open bounded domain in $\mathbb{R}^d$, $d = 2, 3$, with polygonal boundary $\partial\Omega$. The corresponding variational problem consists of finding $u_\Omega \in H^1_0(\Omega)$ such that

$$a_\Omega(u_\Omega, v_\Omega) = (f, v_\Omega)_\Omega, \quad v_\Omega \in H^1_0(\Omega), \tag{5.1}$$

where $a_\Omega(w, v) = (\operatorname{grad} w, \operatorname{grad} v)_\Omega$ is the standard bilinear form.

As depicted in Figure 5.1(a), let $\omega \subset \Omega$ be a polygonal subdomain of Ω such that its distance to $\partial\Omega$ is bounded away from zero, and denote by $\omega^{\mathrm{c}} = \Omega \setminus \overline{\omega}$ its complement in Ω. We first solve Problem (5.1), and consecutively an additional problem in ω, taking as Dirichlet data the restriction of the solution u_Ω of (5.1) to the interface $\Gamma = \partial\omega$, in short: Find $(u_\Omega, u_\omega) \in H^1_0(\Omega) \times H^1_u(\omega)$ such that

$$\begin{aligned} a_\Omega(u_\Omega, v_\Omega) &= (f, v_\Omega)_\Omega, \quad v_\Omega \in H^1_0(\Omega), \\ a_\omega(u_\omega, v_\omega) &= (f, v_\omega)_\omega, \quad v_\omega \in H^1_0(\omega), \end{aligned} \tag{5.2}$$

where $H^1_u(\omega) = \{v_\omega \in H^1(\omega) : v_\omega|_\Gamma = u_\Omega|_\Gamma\}$ and $a_\omega(w, v) = (\operatorname{grad} w, \operatorname{grad} v)_\omega$. It is obvious that in the continuous setting Problem (5.2) yields $u_\omega = u_\Omega|_\omega$, but when we discretize the variational problem (5.2), the situation becomes more involved, see Figure 5.1(b).

5.1.2 Equivalent Generalized Saddle Point Problem

As has been carried out in [46], it is possible to derive an equivalent formulation of (5.2) in terms of a generalized saddle point problem. Starting from the strong form of the

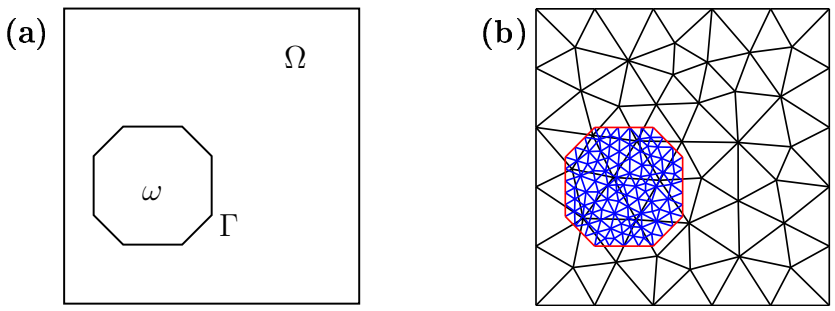

Figure 5.1: (a) nested domains, (b) overlapping non-matching grids.

additional problem on ω, namely,

$$-\operatorname{div}\operatorname{grad} u_\omega = f_\omega \text{ in } \omega, \quad u_\omega|_\Gamma = u_\Omega|_\Gamma, \tag{5.3}$$

we use Green's formula to obtain

$$a_\omega(u_\omega, v_\omega) + \langle v_\omega, \partial u_\omega/\partial \boldsymbol{n}\rangle_{M'\times M} = (f_\omega, v_\omega)_\omega, \quad v_\omega \in H^1(\omega),$$

with $\boldsymbol{n}$ denoting the unit outward normal on ω, and with $M = H^{-1/2}(\Gamma)$. Introducing the Lagrange multiplier $\lambda = \partial u_\omega/\partial \boldsymbol{n}$, we set

$$b_1(v,\mu) = \langle v_\omega, \mu\rangle_{M'\times M}, \quad v = (v_\Omega, v_\omega) \in X = H_0^1(\Omega)\times H^1(\omega),\ \mu \in M.$$

As usual for the non-overlapping case, we realize the continuity requirement along the boundary Γ in (5.3) by the bilinear form

$$b_2(v,\mu) = \langle v_\Omega - v_\omega, \mu\rangle_{M'\times M}, \quad v \in X,\ \mu \in M,$$

On the product space X, a composed bilinear form $a(\cdot,\cdot) : X\times X \to \mathbb{R}$ is obtained by

$$a(w,v) = a_\Omega(w_\Omega, v_\Omega) + a_\omega(w_\omega, v_\omega), \quad w, v \in X.$$

Proceeding like this, we have derived the following generalized saddle point problem: find $(u,\lambda) \in X\times M$ such that

$$a(u,v) \;+\; b_1(v,\lambda) = (f,v)_{\Omega\times\omega}, \quad v \in X, \tag{5.4a}$$

$$b_2(u,\mu) \qquad\quad = 0, \qquad\quad \mu \in M. \tag{5.4b}$$

As for standard saddle point problems, see Section A.2 in the appendix, the bilinear forms $b_i(\cdot,\cdot)$ define coupling operators $B_i : X \to M'$ and $B_i^{\mathrm{T}} : M \to X'$ by $\langle B_i v, \mu\rangle_{M'\times M} = \langle v, B_i^{\mathrm{T}}\mu\rangle_{X\times X'} = b_i(v,\mu)$ for $v \in X$ and $\mu \in M$. The validation of the following coercivity- and inf-sup-conditions guarantees the unique solvability of problem (5.4) in $X\times M/\operatorname{Ker} B_1^{\mathrm{T}}$, [27]:

$$\exists \alpha_0 > 0 : \sup_{v_0\in\operatorname{Ker} B_1} \frac{a(w_0,v_0)}{\|w_0\|_X\,\|v_0\|_X} \;\geq\; \alpha_0, \quad w_0 \in \operatorname{Ker} B_2, \tag{5.5}$$

$$\sup_{w_0\in\operatorname{Ker} B_2} \frac{a(w_0,v_0)}{\|w_0\|_X\,\|v_0\|_X} \;\geq\; \alpha_0, \quad v_0 \in \operatorname{Ker} B_1. \tag{5.6}$$

$$\exists k_0 > 0 : \inf_{\mu\in M}\sup_{v\in X} \frac{b_i(v,\mu)}{\|v\|_X \|\mu\|_{M/\operatorname{Ker} B_i^{\mathrm{T}}}} \;\geq\; k_0, \quad i = 1,2. \tag{5.7}$$

We note that the above conditions can be relaxed, [18, 31, 91].

It is obvious that problem (5.4) has a unique solution, since the problem on the global domain Ω is not influenced by the problem on the subdomain ω, and its solution u_Ω yields the boundary data for a well posed subdomain problem. Nevertheless, we provide a complete proof within the saddle point setting.

Theorem 5.1. *With the above definitions, problem (5.4) is uniquely solvable.*

Proof. We validate the conditions (5.5)–(5.7). Our main tool is the harmonic extension operator $\mathcal{H} : M' \to H^1(\omega)$, given by Definition A.25, i.e.,

$$a_\omega(\mathcal{H}w, v_\omega) = 0, \quad v_\omega \in H^1_0(\omega), \quad (\mathcal{H}w)|_\Gamma = w. \tag{5.8}$$

We observe that the trace of $H^1(\omega)$ onto Γ is the space M', and that

$$b_1((0,v),\mu) = b_2((0,-v),\mu), \qquad v \in M'.$$

Taking $v = (0, \pm\mathcal{H}w)$, $w \in M'$, condition (5.7) is a consequence of the definition of the $H^{-1/2}$-norm and of the fact that $\|\mathcal{H}w\|_{1,\omega} \le C\|w\|_{M'}$, see Theorem A.26.

Let us focus on condition (5.5). The kernels of the coupling operators are

$$\operatorname{Ker} B_1 = H^1_0(\Omega) \times H^1_0(\omega), \quad \text{and} \quad \operatorname{Ker} B_2 = \{v \in X : v_\Omega|_\Gamma = v_\omega|_\Gamma\}.$$

We uniquely decompose $v_\omega \in H^1(\omega)$ into $v_B + v_I$ such that $v_B = \mathcal{H}(v_\omega|_\Gamma)$ and $v_I \in H^1_0(\omega)$. For an arbitrary $w_0 = (w_\Omega, w_B + w_I) \in \operatorname{Ker} B_2$, we consider $v_0 = (w_\Omega, w_I) \in \operatorname{Ker} B_1$. By using the properties of the harmonic extension and the Poincaré–Friedrichs type inequality (A.12), we get

$$\|w_\Omega\|^2_{1,\Omega} \ge c\left(\int_\Gamma w_\Omega \,\mathrm{d}\Gamma\right)^2 + c|w_\Omega|^2_{1,\Omega} \ge c\left(\int_\Gamma w_B \,\mathrm{d}\Gamma\right)^2 + c|w_B|^2_{1,\omega} \ge c\|w_B\|^2_{1,\omega}. \tag{5.9}$$

Condition (5.5) follows from (5.9), using the ellipticity of $a(\cdot,\cdot)$ on $\operatorname{Ker} B_1$:

$$\begin{aligned} a(w_0, v_0) &= a_\Omega(w_\Omega, w_\Omega) + a_\omega(w_I, w_I) \ge c\|w_\Omega\|^2_{1,\Omega} + c\|w_I\|^2_{1,\omega} \\ &\ge c\|w_\Omega\|^2_{1,\Omega} + c\|w_B + w_I\|^2_{1,\Omega} + c\|w_I\|^2_{1,\omega} \\ &\ge c\|w_0\|^2_X + c\|v_0\|^2_X \ge c\|w_0\|_X\|v_0\|_X. \end{aligned} \tag{5.10}$$

The proof of condition (5.6) is similar. For an arbitrary $v_0 = (v_\Omega, v_I) \in \operatorname{Ker} B_1$, we set $w_0 = (v_\Omega, \mathcal{H}(\operatorname{tr} v_\Omega) + v_I) \in \operatorname{Ker} B_2$, and obtain (5.10). □

5.1.3 Discretization

The discretization and the derivation of a priori error estimates is carried out for the purely primal problem (5.2). If no ambiguity can occur, we write $u = u_\Omega$ for the global solution. We use two different shape regular triangulations $\mathcal{T}_H$ on Ω and $\mathcal{T}_h$ on ω, with H and h indicating the maximum element diameters, respectively. These overlapping triangulations may be completely independent of each other, hence, in general, they do not match on ω. Moreover, the edges and faces of the triangulation $\mathcal{T}_h$ on the interface Γ also do not coincide with edges and faces of $\mathcal{T}_H$, see Figure 5.1(b). We use standard conforming finite elements of order p and q on $\mathcal{T}_H$ and $\mathcal{T}_h$, respectively. The associated discrete spaces with no boundary conditions are denoted by $S^p_H(\Omega)$ and $S^q_h(\omega)$, respectively, and we set $S^p_{0,H}(\Omega) = S^p_H(\Omega) \cap H^1_0(\Omega)$ and $S^q_{0,h}(\omega) = S^q_h(\omega) \cap H^1_0(\omega)$ to be the

spaces taking into account homogeneous Dirichlet conditions on $\partial\Omega$ and Γ, respectively. The trace space of $S_h^q(\omega)$ on Γ is indicated by W_h^q.

We note that the restriction of a function $v_H \in S_H^p(\Omega)$ onto the interface Γ is, in general, not an element of W_h^q. Thus, the Dirichlet problem on $S_h^q(\omega)$ cannot be solved directly, and a suitable projection operator Π_h from $S_H^p(\Omega)$ onto W_h^q is required. In order to get an optimal a priori error estimate, the projection Π_h has to satisfy the stability property stated in the following assumption, which is the analog of Assumption 2.1(c) from the non-overlapping setting.

Assumption 5.2. *The operator $\Pi_h : H^1(\Omega) \to W_h^q$ is a projection onto W_h^q, i.e., $\Pi_h v_h = v_h$, $v_h \in W_h^q$, and satisfies*

$$\|\Pi_h v\|_{1/2,\Gamma} \leq C\|v\|_{1/2,\Gamma}, \quad v \in H^1(\Omega), \tag{5.11}$$

with a constant C independent of the meshsize h.

Such projection operators are well-known from the preceding chapters and play an important role within the framework of mortar finite elements. We note that Assumption 5.2 implies that the operator Π_h satisfies an approximation property on $H^{1/2}(\Gamma)$, i.e., $\|v - \Pi_h v\|_{1/2,\Gamma} \leq Ch^q |v|_{q+1/2,\Gamma}$, $v \in H^{1+q}(\Omega)$.

We are now able to formulate the discrete variational problem. Find $(u_H, u_h) \in S_{0,H}^p(\Omega) \times S_{u,h}^q(\omega)$ such that

$$\begin{aligned} a_\Omega(u_H, v_H) &= (f, v_H)_\Omega, \quad v_H \in S_{0,H}^p(\Omega), \\ a_\omega(u_h, v_h) &= (f, v_h)_\omega, \quad v_h \in S_{0,h}^q(\omega), \end{aligned} \tag{5.12}$$

where $S_{u,h}^q(\omega) = \{v \in S_h^q(\omega) : v|_\Gamma = \Pi_h u_H\}$. In contrast to the continuous formulation (5.2), it is obvious that the discrete solution u_h on the patch cannot simply be the restriction of the global discrete solution u_H, due to the nonconforming setting. Of course, this is also not intended by the approach, and u_h should rather give a better approximation than u_H to the exact solution u.

5.2 A Priori Error Estimate

Expecting that u_h is closer to u on ω, the finite element solution u_{FE} is defined by

$$u_{\mathrm{FE}} = \begin{cases} u_H & \text{in } \omega^{\mathrm{c}}, \\ u_h & \text{in } \omega. \end{cases} \tag{5.13}$$

We note that, in general, $u_{\mathrm{FE}} \notin H_0^1(\Omega)$. The error $e = u - u_{\mathrm{FE}}$ measured in the broken H^1-norm $\|\cdot\|_{1,\mathrm{b},\Omega}$ is split up into the error in ω^{c} and ω:

$$\|e\|_{1,\mathrm{b},\Omega}^2 = \|u - u_H\|_{1,\omega^{\mathrm{c}}}^2 + \|u - u_h\|_{1,\omega}^2. \tag{5.14}$$

It is obvious that, e.g., for orders $p = q = 1$ and $u \in H^2(\Omega)$, the norm $\|e\|_{1,\mathrm{b},\Omega}$ is bounded by $C \max(h, H)|u|_{2,\Omega}$. In what follows we establish a more accurate and more local upper

bound, which is especially useful when the parameter pairs (H,p) and (h,q) become quite different.

To estimate the second term of the right hand side in (5.14), we employ a Scott–Zhang type projection operator of order q denoted by P_h, [109]. We will make use of the approximation property of P_h, namely

$$\|v - P_h v\|_{1,T} \leq c h_T^q |v|_{q+1,\omega_T}, \quad T \in \mathcal{T}_k,\ v \in H^{q+1}(\omega_T),\ k = h, H, \tag{5.15}$$

where ω_T indicates the set of elements in $\mathcal{T}_k$ sharing at least one vertex with T.

Let $z_h \in S_h^q(\omega)$ be the finite element solution satisfying

$$\begin{aligned} a_\omega(z_h, v_h) &= (f, v_h)_\omega, \quad v_h \in S_{0,h}^q(\omega), \\ z_h &= P_h u, \quad \text{on } \Gamma. \end{aligned}$$

The following result is well-known, we give a proof for completeness.

Lemma 5.3. *There exists a constant C independent of the meshsizes such that*

$$\|u - z_h\|_{1,\omega} \leq C h^q |u|_{1+q,\omega}, \quad u \in H^{1+q}(\omega). \tag{5.16}$$

Proof. Using the triangle inequality and P_h, we get

$$\|u - z_h\|_{1,\omega} \leq \|u - P_h u\|_{1,\omega} + \|z_h - P_h u\|_{1,\omega}. \tag{5.17}$$

In terms of the coercivity and the continuity of the bilinear form $a_\omega(\cdot,\cdot)$ on $H_0^1(\omega)\times H_0^1(\omega)$, and the Galerkin orthogonality, the second term of the right hand side in (5.17) is bounded as follows:

$$\begin{aligned} \|z_h - P_h u\|_{1,\omega}^2 &\leq C a_\omega(z_h - P_h u, z_h - P_h u) = C a_\omega(u - P_h u, z_h - P_h u) \\ &\leq C \|u - P_h u\|_{1,\omega} \|z_h - P_h u\|_{1,\omega}. \end{aligned}$$

Using this upper bound in (5.17) and applying the approximation property (5.15), we obtain (5.16). □

The next lemma estimates the difference $u_h - z_h$ using the stability property of the projection Π_h given in Assumption 5.2.

Lemma 5.4. *There exists a constant C independent of the meshsizes H, h such that for u sufficiently regular*

$$\|z_h - u_h\|_{1,\omega} \leq C \left(h^q |u|_{1+q,\omega} + \|u - u_H\|_{1,\omega^c} \right). \tag{5.18}$$

Proof. The difference $z_h - u_h$ is discrete harmonic on ω with respect to test functions in $S_{0,h}^q(\omega)$. Using this fact and the resulting norm equivalence (A.25), together with the stability property (5.11) of the projection operator Π_h, we obtain

$$\begin{aligned} \|z_h - u_h\|_{1,\omega} &\leq C \|z_h - u_h\|_{1/2,\Gamma} = C \|P_h u - \Pi_h u_H\|_{1/2,\Gamma} \\ &\leq C \left(\|\Pi_h P_h u - \Pi_h u\|_{1/2,\Gamma} + \|\Pi_h u - \Pi_h u_H\|_{1/2,\Gamma} \right) \\ &\leq C \left(\|P_h u - u\|_{1/2,\Gamma} + \|u - u_H\|_{1/2,\Gamma} \right). \end{aligned}$$

The rest follows from the trace theorem A.13 and the approximation property (5.15) of the Scott–Zhang projection operator P_h. □

To obtain a more local a priori estimate for $\|e\|_{1,\mathrm{b},\Omega}$, the remaining term $\|u - u_H\|_{1,\omega^c}$ has to be considered in more detail. We apply a modified version of [117, Theorem 9.1] to derive an upper bound in terms of the best approximation and the error in the L^2-norm on a larger subdomain $B \supset \omega^c$. Let us first introduce some notation. With $A_0 \subset A_1 \subset \Omega$, set

$$\partial_<(A_0, A_1) = \operatorname{dist}(\partial A_0 \setminus \partial\Omega,\, \partial A_1 \setminus \partial\Omega),$$

and further, $C^\infty_<(A) = \{v \in C^\infty(A) : \partial_<(\operatorname{supp} v, A) > 0\}$ and $S^p_{0,H}(A) = S^p_H(\Omega) \cap H^1_0(A)$ for an arbitrary subdomain $A \subset \Omega$. We can now state our main result. The proof is based on the techniques given in [117].

Theorem 5.5. *Let $B \supset \omega^c$ such that $\partial_<(\omega^c, B) > 0$. Then for H sufficiently small, there exists $B_H \subset B$, which can be written as a union of elements of the triangulation $\mathcal{T}_H$, and it holds that*

$$|u - u_H|_{1,\omega^c} \le C \min_{v_H \in S^p_H(\Omega)} \|u - v_H\|_{1,B_H} + C\|u - u_H\|_{0,B_H}, \tag{5.19}$$

where $C < \infty$ depends on $\partial_<(\omega^c, B)$.

Proof. We choose subdomains A_1, A_2, B_H which can be written as unions of elements of the triangulation $\mathcal{T}_H$ such that $\omega^c \subset A_1 \subset A_2 \subset B_H \subset B$ and $\partial_<(\omega^c, A_1)$, $\partial_<(A_1, A_2)$, $\partial_<(A_2, B_H) > 0$. The situation is illustrated in Figure 5.2(a). Note that the meshwidth

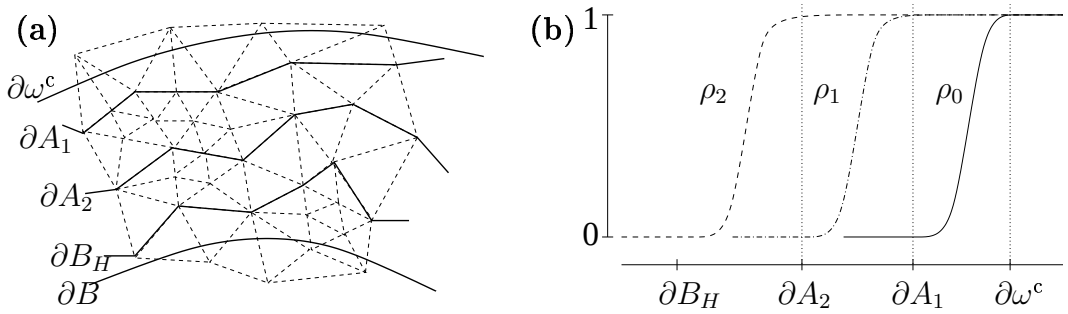

Figure 5.2: (a) nested subdomains, (b) support of ρ_i.

H has to be sufficiently small to guarantee the existence of the domains A_1, A_2, B_H. Let $\rho_i : C^\infty(\Omega) \to [0,1], i = 1,2,3$, satisfy

$$\rho_0 \in C^\infty_<(A_1),\ \rho_{0|\omega^c} = 1, \quad \rho_1 \in C^\infty_<(A_2),\ \rho_{1|A_1} = 1, \quad \rho_2 \in C^\infty_<(B_H),\ \rho_{2|A_2} = 1,$$

as depicted in Figure 5.2(b). On A_2, we can write

$$u - u_H = \rho_2(u - v_H) - P_1(\rho_2(u - v_H)) + P_1(\rho_2(u - v_H)) - (u_H - v_H),$$

where $v_H \in S^p_H(\Omega)$, and P_1 denotes the projection from $H^1(\Omega)$ into $S^p_{0,H}(\Omega)$ with respect to the H^1-semi-norm $|\cdot|_{1,\Omega}$, namely,

$$(\operatorname{grad} P_1 w, \operatorname{grad} v_H)_\Omega = (\operatorname{grad} w, \operatorname{grad} v_H)_\Omega, \quad w \in H^1(\Omega),\ v \in S^p_{0,H}(\Omega).$$

The stability of P_1 with respect to the H^1-semi-norm is immediately given by

$$|P_1 w|^2_{1,\Omega} = (\operatorname{grad} P_1 w, \operatorname{grad} P_1 w)_\Omega = (\operatorname{grad} w, \operatorname{grad} P_1 w)_\Omega \leq |w|_{1,\Omega} |P_1 w|_{1,\Omega}.$$

We get

$$\begin{aligned} |u - u_H|_{1,\omega^c} \leq\ & |\rho_2(u - v_H) - P_1(\rho_2(u - v_H))|_{1,\omega^c} \\ & + |P_1(\rho_2(u - v_H)) - (u_H - v_H)|_{1,\omega^c}. \end{aligned} \tag{5.20}$$

The first term on the right hand side of (5.20) is bounded by

$$\begin{aligned} |\rho_2(u - v_H)|_{1,\Omega} &\leq \|\rho_2 \operatorname{grad}(u - v_H)\|_{0,\Omega} + \|(u - v_H) \operatorname{grad} \rho_2\|_{0,\Omega} \\ &\leq C \|u - v_H\|_{1,B_H}, \end{aligned} \tag{5.21}$$

due to the stability of the projection P_1 and since $\rho_2 \in C^\infty_<(B_H)$. Note that the constant C in (5.21) becomes large in case of a small distance $\partial_<(A_2, B_H)$.

Let us consider the second term on the right hand side of (5.20) and define

$$z_H = P_1(\rho_2(u - v_H)) - (u_H - v_H).$$

Note that z_H is discrete harmonic on A_2, since for $w_H \in S^p_{0,H}(A_2)$,

$$(z_H, w_H)_{1,\Omega} = (\rho_2(u - v_H) - (u_H - v_H), w_H)_{1,\Omega} = (u - u_H, w_H)_{1,\Omega} = 0. \tag{5.22}$$

We will derive an upper bound for $|z_H|_{1,\omega^c}$ by estimating it by the L^2-norm of z_H on A_2. Let $\mathcal{I}_H : H^1_0(\Omega) \to S^p_{0,H}(\Omega)$ denote the Lagrangian interpolation operator of degree p on $\mathcal{T}_H$. We use the identity

$$\operatorname{div}(z_H \operatorname{grad} \rho_0) = \operatorname{grad} \rho_0 \operatorname{grad} z_H + z_H \operatorname{div} \operatorname{grad} \rho_0,$$

and apply integration by parts to obtain

$$\begin{aligned} (z_H, z_H \operatorname{div} \operatorname{grad} \rho_0)_\Omega &= (z_h, \operatorname{div}(z_H \operatorname{grad} \rho_0))_\Omega - (z_h, \operatorname{grad} \rho_0 \operatorname{grad} z_H)_\Omega \\ &= -2(\operatorname{grad} z_H, z_H \operatorname{grad} \rho_0)_\Omega \end{aligned}$$

Using this observation yields

$$\begin{aligned} |z_H|^2_{1,\omega^c} &\leq (\operatorname{grad} z_H, \rho_0 \operatorname{grad} z_H)_\Omega \\ &= (\operatorname{grad} z_H, \operatorname{grad}(\rho_0 z_H))_\Omega - (\operatorname{grad} z_H, z_H \operatorname{grad} \rho_0)_\Omega \\ &= (\operatorname{grad} z_H, \operatorname{grad}(\rho_0 z_H))_\Omega + \tfrac{1}{2}(z_H, z_H \operatorname{div} \operatorname{grad} \rho_0)_\Omega. \end{aligned}$$

Since by construction $\mathcal{I}_H(\rho_0 z_H) \in S^p_{0,H}(A_2)$, we can make use of (5.22), and derive

$$\begin{aligned} |z_H|^2_{1,\omega^c} &\leq (z_H, \rho_0 z_H - \mathcal{I}_H(\rho_0 z_H))_{1,\Omega} + C \|z_H\|^2_{0,A_1} \\ &\leq |z_H|_{1,A_1} |\rho_0 z_H - \mathcal{I}_H(\rho_0 z_H)|_{1,A_1} + C \|z_H\|^2_{0,A_1}, \end{aligned} \tag{5.23}$$

where the constant C depends on $\partial_<(\omega^c, A_1)$. Let us focus on the term $|\rho_0 z_H - \mathcal{I}_H(\rho_0 z_H)|_{1,A_1}$. Since A_1 is the union of elements, we derive, using the Bramble–Hilbert lemma,

$$|\rho_0 z_H - \mathcal{I}_H(\rho_0 z_H)|^2_{1,A_1} \leq C H^{2p} \sum_{T \subset A_1} |\rho_0 z_H|^2_{p+1,T}. \tag{5.24}$$

Since $D^\alpha z_H = 0$ for $|\alpha| = p+1$ on each element T, the right hand side of (5.24) can be estimated by a sum of terms of the form

$$CH^{2p}\|(D^\alpha\rho_0)(D^\beta z_H)\|^2_{0,T}, \quad |\alpha|+|\beta| = p+1,\ |\alpha| \geq 1.$$

Using the smoothness of ρ_0 and the standard inverse assumption on T (A.27), each term is bounded by

$$CH^{2(p+1-|\beta|)}\|z_H\|^2_{1,T}, \quad |\beta| \geq 1,$$

where the constant C depends on $\partial_<(\omega^c, A_1)$. Since $p+1-|\beta| = |\alpha| \geq 1$, this can be estimated by

$$CH^2\|z_H\|^2_{1,T}.$$

Summation over all $T \subset A_1$ gives

$$|\rho_0 z_H - \mathcal{I}_H(\rho_0 z_H)|_{1,A_1} \leq CH\|z_H\|_{1,A_1}.$$

Using this upper bound in (5.23), we obtain

$$|z_H|_{1,\omega^c} \leq C(\|z_H\|_{0,A_1} + H^{1/2}|z_H|_{1,A_1}). \tag{5.25}$$

Thus, a factor of $H^{1/2}$ in the H^1-semi-norm is gained by considering the larger subdomain A_1. We intend to apply the standard inverse estimate (A.28) on the H^1-semi-norm of z_H, hence one more factor of $H^{1/2}$ is necessary to get rid of the dependence on negative powers of H. This can be achieved by moving on to the next larger subdomain A_2. Note that $\operatorname{supp}\rho_1 \subset A_2$ and therefore $\mathcal{I}_H(\rho_1 z_H) \in S^p_{0,H}(A_2)$. Replacing ω^c, A_1, and ρ_0 by A_1, A_2, and ρ_1, respectively, the same arguments as before yield

$$|z_H|_{1,A_1} \leq C(\|z_H\|_{0,A_2} + H^{1/2}|z_H|_{1,A_2}), \tag{5.26}$$

with C now depending on $\partial_<(A_1, A_2)$. Combining (5.25), (5.26), and using (A.28), we derive

$$|z_H|_{1,\omega^c} \leq C(\|z_H\|_{0,A_2} + H|z_H|_{1,A_2}) \leq C\|z_H\|_{0,A_2}. \tag{5.27}$$

With the definition of z_H, this gives

$$\begin{aligned} |z_H|_{1,\omega^c} &\leq C\|P_1(\rho_2(u-v_H)) - (u_H - v_H)\|_{0,A_2} \\ &\leq C\|u-u_H\|_{0,A_2} + C\|P_1(\rho_2(u-v_H)) - \rho_2(u-v_H)\|_{0,A_2}. \end{aligned}$$

Using a Poincaré–Friedrichs type inequality and the fact that $\operatorname{supp}\rho_2 \subset B_H$, we obtain

$$\begin{aligned} |z_H|_{1,\omega^c} &\leq C\|u-u_H\|_{0,A_2} + C|P_1(\rho_2(u-v_H)) - \rho_2(u-v_H)|_{1,\Omega} \\ &\leq C\|u-u_H\|_{0,A_2} + C|\rho_2(u-v_H)|_{1,\Omega} \\ &\leq C\|u-u_H\|_{0,A_2} + C\|u-v_H\|_{1,B_H}. \end{aligned} \tag{5.28}$$

Combining (5.20), (5.21), and (5.28) yields the desired estimate (5.19). □

Estimating (5.19) by $C(H^p|u|_{p+1,B} + H^{p+1}|u|_{p+1,\Omega})$, the following global a priori estimate is an immediate consequence of Lemmas 5.3, 5.4, and Theorem 5.5.

Theorem 5.6. *Let $B \supset \omega^c$ such that $\partial_<(\omega^c, B) > 0$. Then for H sufficiently small and u regular enough,*

$$\|u - u_{FE}\|_{1,b,\Omega} \leq Ch^q |u|_{q+1,\omega} + CH^p |u|_{p+1,B} + CH^{p+1} |u|_{p+1,\Omega}. \tag{5.29}$$

Once the derivatives of u on the subdomain ω are large compared to the derivatives on ω^c, the quality of the finite element solution u_{FE} may be improved by considering meshwidths $h < H$ and orders $q > p$. We point out that in order to achieve this improvement, the approximate solution u_H has to be good enough in accordance with the term $CH^{p+1}|u|_{p+1,\Omega}$ in (5.29). This term is the fundamental difference of our approach to the estimates obtained by standard adaptive finite element methods. It is due to the fact that in our one-directionally coupled approach no pollution effect is taken into account. If the nature of the considered problem is such that the L^2-term $C\|u - u_H\|_{0,B_H}$ in (5.19) dominates the upper bound in (5.29), it is necessary to involve a bi-directionally coupled approach, i.e., to give a feedback from the subdomain ω to the global domain Ω. This has been investigated in the recent work [52]. At the expense of a bi-directional volume coupling, the last term in (5.29) vanishes.

5.3 Algebraic System

In this section, the algebraic form of the coupled problem (5.12) is considered. We decompose the nodes of $\mathcal{T}_h$ into inner and boundary nodes, and write $v_h = (v_I, v_B) \in S_h^q(\omega)$, again not distinguishing our notation between a finite element function and its coefficient vector. The matrix A_h associated with the Dirichlet problem on $S_{0,h}^q(\omega)$ in terms of the bilinear form $a_\omega(\cdot,\cdot)$ reads

$$A_h = \begin{pmatrix} A_{II} & A_{I\Gamma} \\ 0 & \mathrm{Id} \end{pmatrix}.$$

Denoting by Q the matrix corresponding to the projection operator Π_h, the coupled algebraic system reads

$$\begin{pmatrix} A_H & 0 & 0 \\ 0 & A_{II} & A_{I\Gamma} \\ -Q & 0 & \mathrm{Id} \end{pmatrix} \begin{pmatrix} u_H \\ u_I \\ u_\Gamma \end{pmatrix} = \begin{pmatrix} f_H \\ f_I \\ 0 \end{pmatrix}, \tag{5.30}$$

where A_H is the global stiffness matrix associated with the Dirichlet problem on $S_{0,H}^p(\Omega)$. Since the first line of system (5.30) is decoupled from the rest, we solve (5.30) in two successive steps, i.e.,

$$u_H = A_H^{-1} f_H, \quad u_I = A_{II}^{-1}(f_I - A_{I\Gamma} Q u_H). \tag{5.31}$$

For the solution of (5.31), we can use standard multigrid or domain decomposition techniques. We note that the stiffness matrices A_H and A_h do not change if the position of the subdomain ω changes inside the global domain Ω. Moreover, no remeshing is

necessary. Thus, the introduced technique is ideally suited for transient problems with moving subdomains. However, the matrix Q, which represents the projection operator Π_h, has to be reassembled whenever the subdomain ω changes its position. Therefore, an adequate choice of Π_h is important in order to obtain efficient algorithms of optimal complexity.

We propose to use as operator Π_h the extension of the mortar projection from the non-overlapping setting treated in the preceding chapters. Thus, it is defined using test functions out of a Lagrange multiplier space M_h^q,

$$\Pi_h : H^1(\Omega) \to W_h^q, \quad (\Pi_h v, \nu)_\Gamma = (v, \nu)_\Gamma, \quad \nu \in M_h^q. \tag{5.32}$$

The Lagrange multiplier space M_h^q is of crucial importance to obtain a well defined operator Π_h for which Assumption 5.2 holds. One approach is to take the trace space W_h^q, [21]. As an alternative, we propose that M_h^q consists of dual basis functions as introduced in Section 2.4.1, [120]. Both approaches have the advantage that the mass matrix system resulting from (5.32) is easy to assemble due to the locality of the support of all involved basis functions. For the dual basis functions, the required spaces for higher orders $q > 1$ are constructed and analyzed in two dimensions in [80, 94]. In three dimensions, no general results for unstructured grids and arbitrary high order q dual Lagrange multiplier spaces, having a reproduction property for $\mathbb{P}_{q-1}$, are available. However, in contrast to the mortar setting, here the Lagrange multiplier space does not have to satisfy this reproduction property. Thus, we can always work with a dual Lagrange multiplier space defined on a reference element, by gluing the local pieces together.

Denoting by D and M the mass matrices corresponding to the left and right hand side of (5.32), respectively, we derive the algebraic system

$$\begin{pmatrix} A_H & 0 & 0 \\ 0 & A_{II} & A_{I\Gamma} \\ -M & 0 & D \end{pmatrix} \begin{pmatrix} u_H \\ u_I \\ u_\Gamma \end{pmatrix} = \begin{pmatrix} f_H \\ f_I \\ 0 \end{pmatrix}, \tag{5.33}$$

The last equation of system (5.33) implies that $u_\Gamma = D^{-1} M u_H$. Denoting by Q the product $D^{-1}M$, system (5.30) is obtained. Due to the reduced number of nodes on the interface Γ, the inversion of D is computationally cheap compared to the complexity of the global algorithm. Moreover, the use of dual Lagrange multipliers yields a diagonal and trivial to invert mass matrix D. We note that, in contrast to standard mortar element methods, no modifications of the Lagrange multiplier basis functions in the neighborhood of the corners of Γ are required.

For the element-wise assembly of the mass matrix M, integrals of the form

$$(\phi_H, \mu_h)_{T^s} \tag{5.34}$$

have to be computed, where T^s is again the side of an element of the triangulation $\mathcal{T}_h$ meeting the interface Γ, ϕ_H is a basis function of the finite element space $S_{0,H}^p(\Omega)$, and μ_h is a basis function of the Lagrange multiplier space M_h^q. We point out the close similarity

of (5.34) with (1.23). However, in contrast to the non-overlapping situation, now the area of intersection of the $(d-1)$-dimensional side T^s with the d-dimensional support of ϕ_H has to be calculated. This is fairly feasible in two dimensions, but may become rather challenging on unstructured grids in three dimensions. It can be circumvented by using higher order quadrature formulas, reducing the task to the calculation of products of the form $\phi_H(s)\mu_h(s)$ at some quadrature points s. Nevertheless, fast algorithms are required to detect the functions ϕ_H whose supports contain these quadrature points, in order to preserve optimal complexity. We propose recursive searching algorithms by using a possibly available grid hierarchy or a quad-/octree type organization of the triangulation $\mathcal{T}_H$. The assembly of the second mass matrix D poses no difficulty, since the involved basis functions ϕ_h and μ_h are defined with respect to the same triangulation $\mathcal{T}_h \cap \Gamma$.

5.4 Numerical Results

We show several numerical results illustrating the performance of the algorithm. In particular, five test examples are chosen. The first two couple piecewise linear finite elements on both grids, whereas the third deals with piecewise linear elements on $\mathcal{T}_H$ and piecewise quadratic elements on $\mathcal{T}_h$. The fourth example deals with a 3D problem, and the last provides an application to a unilateral contact problem in 3D.

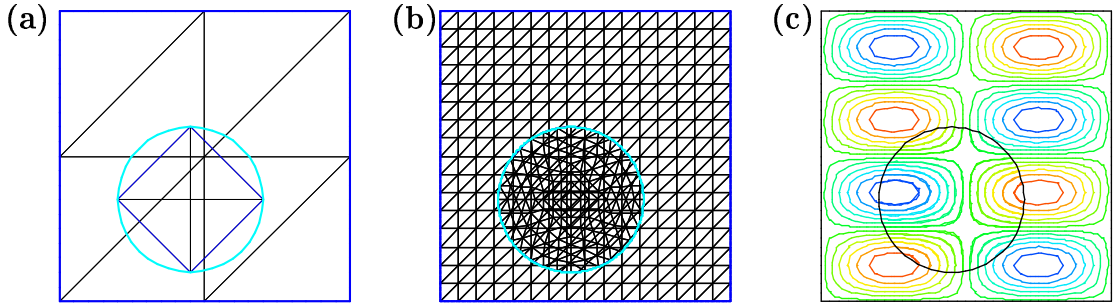

Figure 5.3: Numerical Test 1: overlapping triangulations: (a) initial, (b) after three uniform refinement steps, (c) isolines of the finite element solution u_{FE}.

Consider the model problem (1.1) on $\Omega = (0,1)^2$ with source term f derived from the exact solution $u(x,y) = \sin(2\pi x)\sin(4\pi y)$. A circular patch of radius 0.25 is placed in the domain Ω with its center at $(0.45, 0.35)$. The left picture in Figure 5.3 shows the initial overlapping triangulations $\mathcal{T}_H$ and $\mathcal{T}_h$. Piecewise linear finite elements are used on both grids, thus, $p = q = 1$. We consecutively solve the problem by means of Equation (5.31) and perform a uniform refinement step. The finite element solution u_{FE} which is defined by (5.13) is visualized in the right picture of Figure 5.3. At each step, the errors $e_H = u - u_H$, $e_h = u|_\omega - u_h$, and $e_{\mathrm{FE}} = u - u_{\mathrm{FE}}$, are calculated in the L^2-norm and the H^1-norm, documented in Tables 5.1 and 5.2.

For comparison, we also include the error $\tilde{e}_h$ calculated from the finite element solution $\tilde{u}_h \in S_h^q(\omega)$, where the values of the exact solution u are imposed as Dirichlet boundary

# elements	$\|e_H\|_{0,\Omega}$	$\|e_h\|_{0,\omega}$	$\|e_{\mathrm{FE}}\|_{0,\Omega}$	$\|\tilde{e}_h\|_{0,\omega}$
192	$2.01{\cdot}10^{-1}$	$5.97{\cdot}10^{-2}$	$1.91{\cdot}10^{-1}$	$2.56{\cdot}10^{-2}$
768	$5.81{\cdot}10^{-2}(3.46)$	$1.66{\cdot}10^{-2}(3.60)$	$5.48{\cdot}10^{-2}(3.49)$	$6.86{\cdot}10^{-3}(3.73)$
3072	$1.51{\cdot}10^{-2}(3.85)$	$4.19{\cdot}10^{-3}(3.96)$	$1.42{\cdot}10^{-2}(3.86)$	$1.75{\cdot}10^{-3}(3.92)$
12288	$3.81{\cdot}10^{-3}(3.96)$	$1.04{\cdot}10^{-3}(4.03)$	$3.57{\cdot}10^{-3}(3.98)$	$4.40{\cdot}10^{-4}(3.98)$
49152	$9.54{\cdot}10^{-4}(3.99)$	$2.63{\cdot}10^{-4}(3.96)$	$8.95{\cdot}10^{-4}(3.99)$	$1.10{\cdot}10^{-4}(4.00)$

Table 5.1: Numerical Test 1: L^2-norm of the error.

# elements	$\|e_H\|_{1,\Omega}$	$\|e_h\|_{1,\omega}$	$\|e_{\mathrm{FE}}\|_{1,\mathrm{b},\Omega}$	$\|\tilde{e}_h\|_{1,\omega}$
192	$3.81{\cdot}10^{0}$	$1.25{\cdot}10^{0}$	$3.65{\cdot}10^{0}$	$9.95{\cdot}10^{-1}$
768	$2.01{\cdot}10^{0}$ (1.90)	$5.66{\cdot}10^{-1}(2.21)$	$1.89{\cdot}10^{0}$ (1.93)	$5.11{\cdot}10^{-1}(1.95)$
3072	$1.02{\cdot}10^{0}$ (1.97)	$2.67{\cdot}10^{-1}(2.12)$	$9.51{\cdot}10^{-1}(1.99)$	$2.58{\cdot}10^{-1}(1.98)$
12288	$5.11{\cdot}10^{-1}(2.00)$	$1.31{\cdot}10^{-1}(2.04)$	$4.77{\cdot}10^{-1}(1.99)$	$1.29{\cdot}10^{-1}(2.00)$
49152	$2.56{\cdot}10^{-1}(2.00)$	$6.50{\cdot}10^{-2}(2.02)$	$2.38{\cdot}10^{-1}(2.00)$	$6.46{\cdot}10^{-2}(2.00)$

Table 5.2: Numerical Test 1: H^1-norm of the error.

data, i.e.,

$$\tilde{u}_{h|\Gamma} = \mathcal{I}_h u|_\Gamma, \qquad a_\omega(\tilde{u}_h, v) = (f, v)_\omega, \quad v \in S^q_{0,h}(\omega).$$

In the parentheses, the factor of error reduction from the last refinement step to the actual one is given. The error e_H of the standard FE method decreases in the expected way. The solutions u_h and u_{FE} obtained by the overlapping method confirm the theoretical results obtained in Section 5.2. In particular, this example illustrates nicely the stability of the interface coupling. On the subdomain ω, the errors e_h and $\tilde{e}_h$ measured in the L^2-norm differ by a factor of 2.5, whereas there is almost no difference in the H^1-norms, which demonstrates the quality of the approach. Because of the solution behavior, we cannot expect to profit from choosing $h \ll H$ or $q > p$.

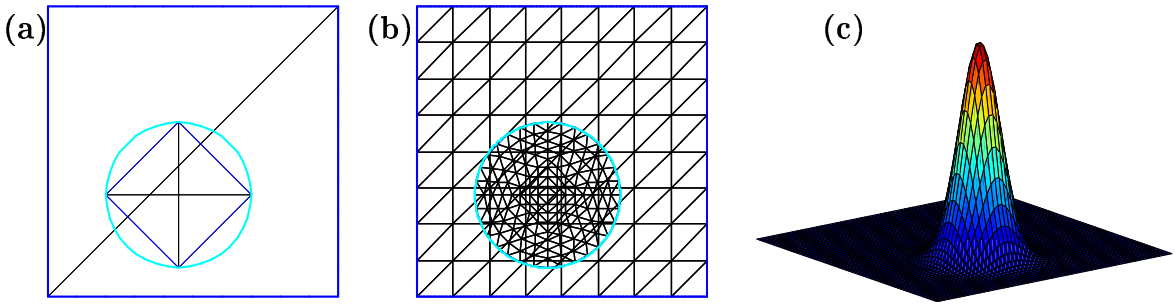

Figure 5.4: Numerical Test 2: overlapping triangulations. Initial (left), after three uniform refinement steps (middle). Peak structure of solution u (right).

In a second test, we consider the exact solution $u(x, y) = \exp(-100((x - 0.45)^2 + (y - 0.35)^2))$. Again, a circular patch of radius 0.25 is placed in the domain Ω with its center

at $(0.45, 0.35)$. Since the solution tends to zero with an exponential decay, we may have a coarser triangulation far enough away from $(0.45, 0.35)$, see Figure 5.4. Therefore, we choose an initial triangulation with $h/H = 1/4$. Again, $\mathbb{P}_1$ elements are used on both grids. For comparison we also solve only the global problem. Figure 5.5 shows the decay of the errors e_H and e_{FE} in the L^2- and H^1-norm under uniform refinement.

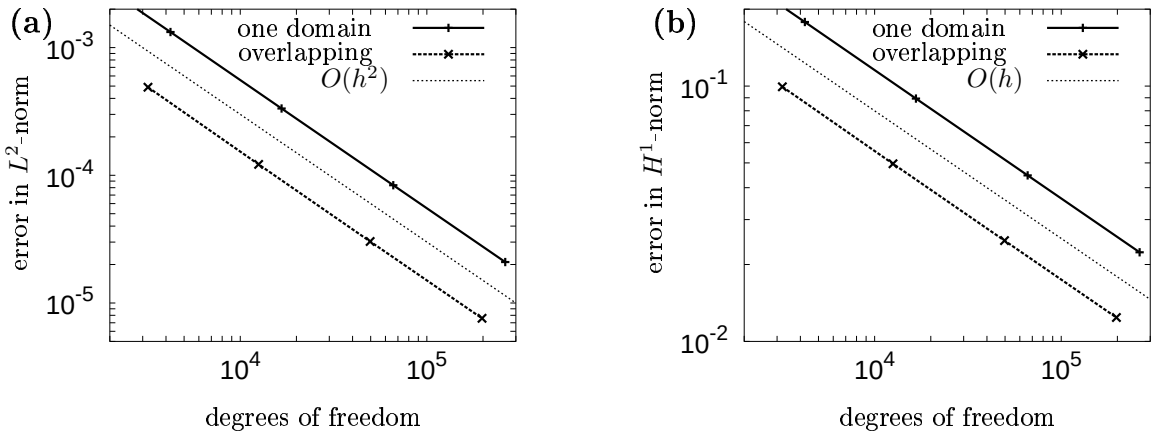

Figure 5.5: Numerical Test 2: error decay in the (a) L^2-norm and (b) H^1-norm.

As before, the errors e_H and e_{FE} both satisfy the a priori estimates. Moreover, choosing the same number of unknowns for the standard and the overlapping method, the solution u_{FE} obtained by the overlapping method is significantly better than the solution u_H obtained by the standard method. Of course, similar results can also be obtained by using adaptive refinement strategies on Ω. However, in case of a moving time dependent source term, this results in a time consuming remeshing and reassembly procedure at the beginning of each time step, which is not necessary for the overlapping method.

We keep the setting of the last test, and now use $\mathbb{P}_1$ elements on $\mathcal{T}_H$ and $\mathbb{P}_2$ elements on $\mathcal{T}_h$. In Figure 5.6, the error e_h on ω measured in the L^2- and H^1-norm is compared with the $\mathbb{P}_1 - \mathbb{P}_1$ coupling from the previous example. In the case of the L^2-error, there is no improvement in the asymptotic behavior, and the values of the error are even higher for the same number of degrees of freedom. In contrast, for the H^1-norm, the error decay on the subdomain ω is almost optimal with respect to the piecewise quadratic finite elements used on $\mathcal{T}_h$. In agreement with (5.29), the error e_h behaves like $c_1 h^2 + c_2 H$, and, moreover, $c_2 \ll c_1$.

For a first 3D example, we set the global domain $\Omega = (0,1)^3$ and the solution $u(x,y,z) = \sin(2\pi x)\sin(3\pi y)\sin(4\pi z)$. The subdomain ω now is a spherical patch of radius 0.25 with its center at $(0.6, 0.4, 0.6)$. The triangulation $\mathcal{T}_H$ of the global domain Ω consists of hexahedrons, whereas $\mathcal{T}_h$ is composed of tetrahedrons. Consequently, piecewise trilinear $\mathbb{Q}_1$ elements are used on $\mathcal{T}_H$, coupled with $\mathbb{P}_1$ elements on $\mathcal{T}_h$. The assembly of the coupling matrices is performed by the use of quadrature formulas. The left picture of Figure 5.7 shows, on a cutting plane through the domain Ω, the isolines of the composed finite element solution u_{FE}, smoothly crossing the interface Γ. The decay of the error e_{FE}, which is illustrated in the right picture of Figure 5.7, agrees with (5.29).

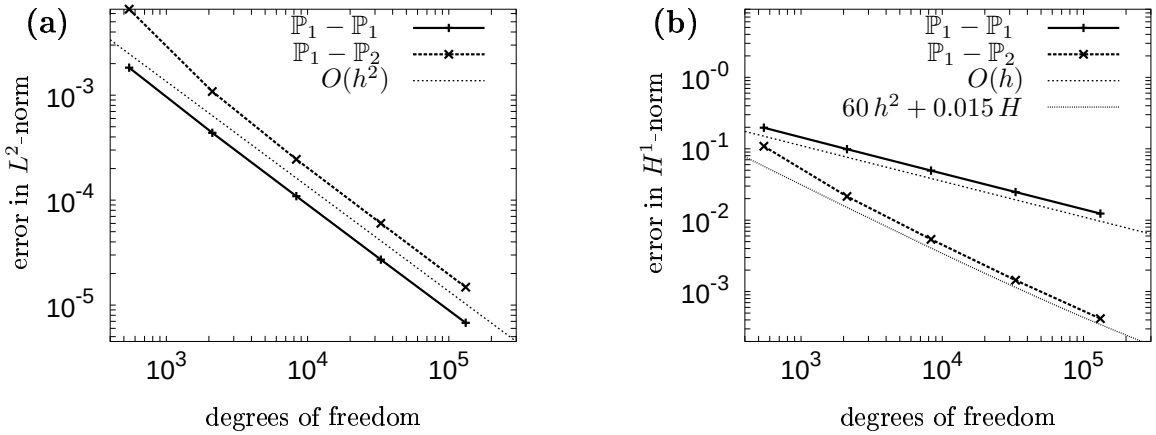

Figure 5.6: Numerical Test 3: error decay in the (a) L^2-norm and (b) H^1-norm.

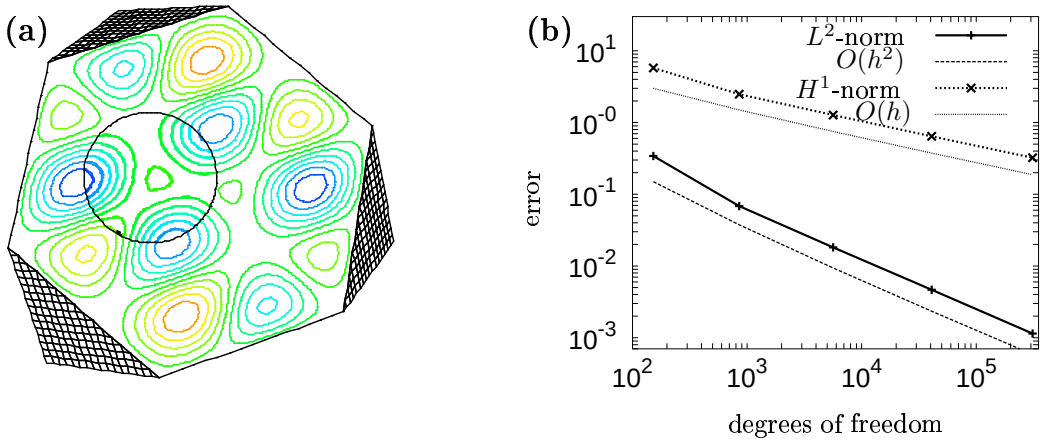

Figure 5.7: Numerical Test 4: (a) isolines, (b) error decay.

For the following example, we apply our approach to the solution of a unilateral frictional contact problem, as illustrated in Figure 5.8. A cylindrical ring Ω of outer radius 0.4, inner radius 0.3, and height 0.25 is subject to a surface traction concentrated on a small part of its inner boundary. It is pressed against a planar obstacle which constitutes a tangent plane prior to the contact. On Ω, we have to solve a variational inequality of the following form: find $(\boldsymbol{u}_H, \boldsymbol{\lambda}_H) \in X_H \times M_H^+$ such that

$$a_H(\boldsymbol{u}_H, \boldsymbol{v}_H) + b_H(\boldsymbol{v}_H, \boldsymbol{\lambda}_H) = f(\boldsymbol{v}_H)\,, \qquad \boldsymbol{v}_H \in X_H\,, \tag{5.35a}$$

$$b_H^{\mathrm{n}}(\boldsymbol{u}_H, \boldsymbol{\mu}_H - \boldsymbol{\lambda}_H) \leq \langle d, (\boldsymbol{\mu}_H - \boldsymbol{\lambda}_H)\,\boldsymbol{n}\rangle_{\Gamma_{\mathrm{C}}^{\mathrm{s}}}\,, \qquad \boldsymbol{\mu}_H \in M_H^+\,, \tag{5.35b}$$

$$b_H^{\mathrm{t}}(\boldsymbol{u}_H, \boldsymbol{\nu}_H - \boldsymbol{\lambda}_H) \leq 0\,, \qquad \boldsymbol{\nu}_H \in \Lambda_H(\boldsymbol{\lambda}_H)\,. \tag{5.35c}$$

In (5.35), the bilinear form $a_H(\cdot,\cdot)$ and the space X_H are obtained from (1.3)–(1.5) with corresponding boundary conditions, whereas the bilinear form $b_H(\cdot,\cdot) = b_H^{\mathrm{n}}(\cdot,\cdot) + b_H^{\mathrm{t}}(\cdot,\cdot)$ and the spaces M_H^+, Λ_H are responsible for incorporating the contact conditions. A close account and discussion of these contact conditions is given in [36]. There, we also show

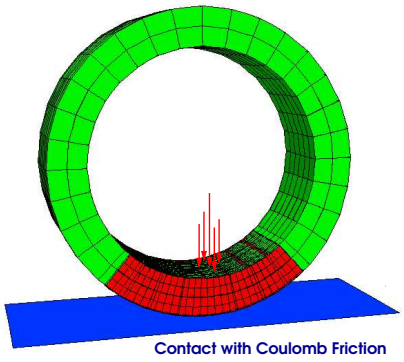

Figure 5.8: Unilateral contact problem: global domain Ω, overlapping patch ω.

how the advantages of the dual approach can be fully exploited for the efficient solution of (5.35).

In order to improve the solution $\boldsymbol{u}_H$ of (5.35), we solve on the patch ω problem (5.35) with H replaced by h, where the elements of the solution space X_h respect the boundary condition $\boldsymbol{u}_h = \Pi_h \boldsymbol{u}_H$ with Π_h denoting the mortar projection onto Γ. In Fig. 5.9, we demonstrate the effect of our approach, (a) visualizes a reference solution obtained on

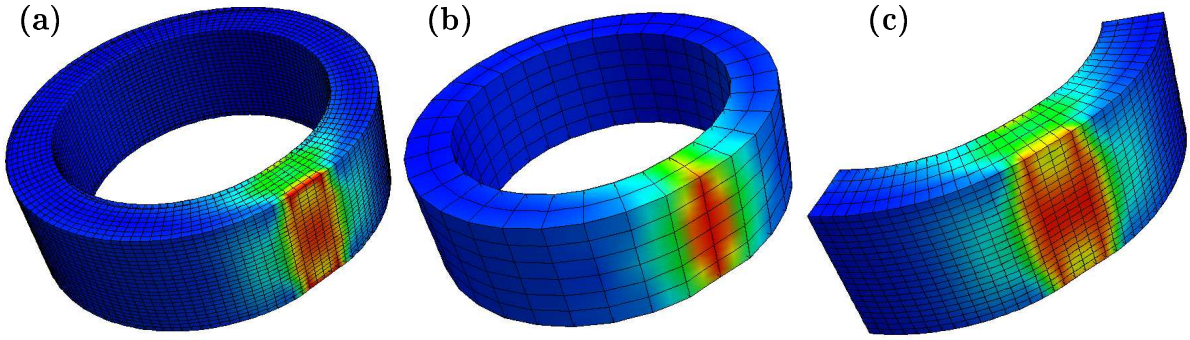

Figure 5.9: (a) reference solution, (b) solution $\boldsymbol{u}_H$, (c) solution $\boldsymbol{u}_h$

a quite fine global grid, (b) shows the solution $\boldsymbol{u}_H$ calculated on a coarse global grid. Comparing with the reference solution, we observe that $\boldsymbol{u}_H$ does not approximate the solution very well. In Fig. 5.9(c), the improved solution $\boldsymbol{u}_h$ is plotted on the patch ω. It is obvious that $\boldsymbol{u}_h$ resolves the characteristics of the reference solution much better.

6 Application to Electro-Mechanical Problems

In this chapter, we present an application of overlapping domain decomposition techniques to an electro-mechanical problem. The great flexibility of the approach enables us to deal with different model equations and discretizations on the two subdomains of interest. Especially in the presence of a moving subdomain, the method is very appealing. We start with the problem setting in Section 6.1, and continue to the variational formulation in Section 6.2. After introducing the discretization in Section 6.3, we focus on the details of the numerical solution algorithm in Section 6.4. First numerical results are given in Section 6.5, and the final Section 6.6 is dedicated to present the simulation of an electromagnetic brake.

6.1 Problem Setting

Low frequency electromagnetic devices are often modeled numerically on the basis of the eddy current formulation [5]. Two main families of formulations are widely used, the one based on magnetic and the one based on electric fields. In this paper, we restrict ourselves to the magnetic field approach. The space $\mathbb{R}^3$ is decomposed in the conducting region ω and the external region $\mathbb{R}^3 \setminus \omega$. Denoting by $\boldsymbol{h}$, $\boldsymbol{b}$, $\boldsymbol{\iota}$ and $\boldsymbol{e}$ the magnetic field, the magnetic flux density, the current density and the electric field, respectively, the quasi-stationary Maxwell equations restricted to the conducting region ω read as follows:

$$\operatorname{curl} \boldsymbol{h} = \boldsymbol{\iota}, \qquad \operatorname{curl} \boldsymbol{e} = -\dot{\boldsymbol{b}}, \qquad \operatorname{div} \boldsymbol{b} = 0\,. \tag{6.1}$$

The densities and the fields are linked by constitutive equations, namely,

$$\boldsymbol{b} = \mu \boldsymbol{h}, \qquad \boldsymbol{\iota} = \sigma \boldsymbol{e} \qquad \text{in } \omega, \tag{6.2}$$

where $\mu = \mu_0 \mu_r > 0$ is the magnetic permeability (the symbol μ_0 denotes the magnetic permeability of the air while $\mu_r > 1$ is the relative permeability of the medium), and $\sigma > 0$ stands for the electric conductivity. Moreover, we assume that the material parameters are time independent and associated with linear isotropic media, and that the external source $\boldsymbol{\iota}_s$ is zero within the conducting regions. As a result, we obtain the following field equations in $\mathbb{R}^3 \setminus \omega$:

$$\operatorname{curl} \boldsymbol{h} = \boldsymbol{\iota}_s, \qquad \operatorname{div} \boldsymbol{b} = 0, \qquad \boldsymbol{b} = \mu \boldsymbol{h}\,. \tag{6.3}$$

The problem is well posed by adding regularity conditions at infinity and suitable interface conditions on $\Gamma = \partial\omega$. In particular, $[\boldsymbol{h}] \times \boldsymbol{n} = 0$, $[\boldsymbol{b}] \cdot \boldsymbol{n} = 0$, $\boldsymbol{e} \times \boldsymbol{n} = 0$ and $\boldsymbol{\iota} \cdot \boldsymbol{n} =$

0, where $\boldsymbol{n}$ is the outer normal on Γ, and $[v]$ stands for the jump of v on Γ. These interface conditions have also to be verified at any surface where σ or μ is discontinuous. Additionally to the boundary conditions, we have to impose suitable initial values for the vector fields at a given time t_0. In particular, the initial condition on $\boldsymbol{b}$ has to satisfy $\operatorname{div} \boldsymbol{b} = 0$ and $[\boldsymbol{b}] \cdot \boldsymbol{n} = 0$ at any interface. The condition $\operatorname{div} \boldsymbol{b} = 0$ is satisfied at any time provided that it is verified by the initial condition. We point out the fact that the vector fields $\boldsymbol{\iota}$ and $\dot{\boldsymbol{b}}$ are automatically forced to be solenoidal by (6.1). By introducing artificial boundary conditions, we can work on a bounded domain Ω. Furthermore, we consider the same geometrical setting as in Chapter 5, namely, that ω is a simply connected polyhedral subdomain of Ω and $\overline{\omega} \subset \Omega$, and set $\omega^{\mathrm{c}} = \Omega \setminus \overline{\omega}$.

From (6.1)–(6.3), we see that the solenoidality $\operatorname{div} \boldsymbol{b} = 0$ and the constitutive law $\boldsymbol{b} = \mu \boldsymbol{h}$ are satisfied in the whole global domain Ω, yielding

$$\operatorname{div} \mu \boldsymbol{h} = 0 \quad \text{in } \Omega. \tag{6.4}$$

In a weak form, this reads

$$(\mu \boldsymbol{h},\, \operatorname{grad} v)_\Omega = 0\,, \qquad v \in H_0^1(\Omega). \tag{6.5}$$

Inside the conductor ω, we can combine the first two equations of (6.1) and the constitutive laws (6.2) to eliminate all unknown quantities but the magnetic field $\boldsymbol{h}$, and obtain

$$\operatorname{curl} \operatorname{curl} \boldsymbol{h} + \sigma \mu \dot{\boldsymbol{h}} = 0 \quad \text{in } \omega. \tag{6.6}$$

Transforming to the variational form, this yields by the partial integration formula (A.9) that

$$(\operatorname{curl} \boldsymbol{h},\, \operatorname{curl} \boldsymbol{w})_\omega + (\sigma \mu \dot{\boldsymbol{h}},\, \boldsymbol{w})_\omega = 0\,, \qquad \boldsymbol{w} \in H_0^{\mathrm{curl}}(\omega)\,, \tag{6.7}$$

where $H_0^{\mathrm{curl}}(\omega) = \{ \boldsymbol{w} \in (L^2(\omega))^3 \mid \operatorname{curl} \boldsymbol{w} \in (L^2(\omega))^3,\, (\boldsymbol{w} \times \boldsymbol{n})|_\Gamma = 0 \}$.

For the current density $\boldsymbol{\iota}$, the solenoidality condition $\operatorname{div} \boldsymbol{\iota} = 0$ admits the introduction of a vector potential $\tilde{\boldsymbol{t}}$ such that $\boldsymbol{\iota} = \operatorname{curl} \tilde{\boldsymbol{t}}$. Then in ω, the difference between the vector potential $\tilde{\boldsymbol{t}}$ and the magnetic field $\boldsymbol{h}$ is irrotational by the first equation of (6.1), thus, it can be written as the gradient of a scalar function $\tilde{\varphi}$, i.e., $\boldsymbol{h} = \tilde{\boldsymbol{t}} - \operatorname{grad} \tilde{\varphi}$. A similar argument holds for the insulating region, where we assume knowing a vector potential $\boldsymbol{t}_s$ such that $\boldsymbol{\iota}_s = \operatorname{curl} \boldsymbol{t}_s$. Combining external and conducting regions, we write $\boldsymbol{h}$ as

$$\boldsymbol{h} = \begin{cases} \tilde{\boldsymbol{t}} - \operatorname{grad} \tilde{\varphi} & \text{in } \omega, \\ \boldsymbol{t}_s - \operatorname{grad} \tilde{\varphi} & \text{in } \omega^{\mathrm{c}}. \end{cases} \tag{6.8}$$

By inserting (6.8) in (6.5) and (6.7), we obtain a coupled eddy current problem in terms of the vector potential $\tilde{\boldsymbol{t}}$ defined only in the conducting region ω and the scalar potential $\tilde{\varphi}$ defined everywhere in Ω, as will be carried out in the next section. This system is completed with appropriate interface conditions on $\partial\omega$ stating, e.g., that $\tilde{\varphi}$ is continuous. This is nevertheless not enough to define $\tilde{\varphi}$ and $\tilde{\boldsymbol{t}}$ uniquely. In fact $\operatorname{div} \tilde{\boldsymbol{t}}$ is not specified, and thus there are many different gauge possibilities. One of them is to require that $\tilde{\boldsymbol{t}}$ has the same divergence as $\boldsymbol{h}$ in ω but this eliminates $\tilde{\varphi}$ on ω. We prefer another condition, given in the next section.

Remark 6.1. In the considered configuration, the conductor ω can freely move in Ω. In presence of moving conductors, we have to choose the reference system with respect to which we write the eddy current problem. Let $\mathcal{R}_\Omega$ be a reference system linked to Ω and $\mathcal{R}_\omega$ be a reference system linked to ω. If $\boldsymbol{v}$ is the conductor velocity, the appropriate form of Ohm's law in the reference system $\mathcal{R}_\Omega$ reads

$$\boldsymbol{\iota} = \sigma(\boldsymbol{e} + \boldsymbol{v} \times \boldsymbol{b}) \text{ in } \omega, \qquad \text{and} \qquad \boldsymbol{\iota} = \sigma\, \boldsymbol{e} \text{ in } \Omega.$$

The motion of ω is directly considered in the convective term $\boldsymbol{v} \times \boldsymbol{b}$. This is a typical feature of the Eulerian description, i.e., the use of a single reference system for both parts Ω and ω. To get rid of the explicit velocity term, it is advisable to use as many different frames as the number of parts, that is, in our case, to reformulate with respect to $\mathcal{R}_\Omega$ the equations in Ω and with respect to $\mathcal{R}_\omega$ the equations in ω. This is the Lagrangian description, where the spectator is attached to the considered part and describes the events from his material point of view. This approach makes disappear the explicit velocity term from Ohm's law, provided that each part is treated in its own "co-moving" frame ($\mathcal{R}_\Omega$ with Ω and $\mathcal{R}_\omega$ co-moving with ω). If two different reference systems are used, one has to couple both by suitable transmission conditions at the conductor boundary. We stress the fact that for the analysis of eddy current problems in domains with moving parts, there is some freedom in the choice of the reference frame, provided that the motion can be regarded as quasi-stationary with respect to electro-dynamics. This freedom is a consequence of the low frequency limit. However, this is not possible for the full set of Maxwell's equations, where already a small acceleration can have a significant effect (see [37] and the references therein). For a convenient Lagrangian description of electro-dynamics in the language of differential forms, we refer to [43]. Thanks to the characteristic of the eddy current model, we can adopt the "piecewise Lagrangian approach" (a Lagrangian approach on each part). This allows us to work with independent meshes and discretizations. To do so, we use mortar techniques realizing the coupling of scalar and vector potentials on non-matching grids. This approach has been introduced in [85] and analyzed in [84]. Classical techniques often rely on the use of boundary elements [89], or on the fictitious domain approach [65].

6.2 Variational Problem

In this section, we define a variational formulation based on the decomposition (6.8). We restrict ourselves to the system obtained after time discretization of (6.5) and (6.7). Using an implicit Euler scheme with time step size Δt, we approximate $\dot{\boldsymbol{h}}$ by $(\Delta t)^{-1}(\boldsymbol{h} - \boldsymbol{h}_{\text{old}})$. Inserting this approximation and the decomposition (6.8) into (6.7), we obtain

$$(\alpha \operatorname{curl} \tilde{\boldsymbol{t}},\, \operatorname{curl} \boldsymbol{w})_\omega + (\tilde{\boldsymbol{t}},\, \boldsymbol{w})_\omega - (\operatorname{grad} \tilde{\varphi},\, \boldsymbol{w})_\omega = (\boldsymbol{h}_{\text{old}}, \boldsymbol{w})_\omega, \qquad \boldsymbol{w} \in H_0^{\text{curl}}(\omega),$$

with $\alpha = \Delta t/(\sigma\mu)$. Applying (6.8) to (6.5) amounts to

$$(\beta \operatorname{grad} \tilde{\varphi},\, \operatorname{grad} v)_\Omega - (\tilde{\boldsymbol{t}},\, \operatorname{grad} v)_\omega = (\beta \boldsymbol{t}_s,\, \operatorname{grad} v)_{\omega^c}, \quad v \in H_0^1(\Omega),$$

with β depending on μ. Thus, we have to face a variational problem at each time step: find $(\tilde{\boldsymbol{t}}, \tilde{\varphi}) \in H_0^{\mathrm{curl}}(\omega) \times H_0^1(\Omega)$ such that

$$\begin{aligned} a_\Omega(\tilde{\varphi}, v) \; + \; \tilde{b}(\tilde{\boldsymbol{t}}, v) \quad &= (\boldsymbol{f}, \operatorname{grad} v)_{\omega^{\mathrm{c}}}, \qquad v \in H_0^1(\Omega), && \text{(6.9a)} \\ \tilde{b}(\boldsymbol{w}, \tilde{\varphi}) \; + \; a_\omega(\tilde{\boldsymbol{t}}, \boldsymbol{w}) &= (\boldsymbol{f}_{\mathrm{c}}, \boldsymbol{w})_\omega, \qquad \boldsymbol{w} \in H_0^{\mathrm{curl}}(\omega). && \text{(6.9b)} \end{aligned}$$

Here, the continuous bilinear forms are defined by

$$\begin{aligned} \tilde{b}(\boldsymbol{w}, v) &= -(\boldsymbol{w}, \operatorname{grad} v)_\omega\,, \quad \boldsymbol{w} \in H_0^{\mathrm{curl}}(\omega), \quad v \in H_0^1(\Omega)\,, \\ a_\Omega(\tilde{\varphi}, v) &= (\beta \operatorname{grad} \tilde{\varphi}, \operatorname{grad} v)_\Omega, \quad \tilde{\varphi},\, v \in H_0^1(\Omega)\,, \\ a_\omega(\tilde{\boldsymbol{t}}, \boldsymbol{w}) &= (\alpha \operatorname{curl} \tilde{\boldsymbol{t}}, \operatorname{curl} \boldsymbol{w})_\omega + (\tilde{\boldsymbol{t}}, \boldsymbol{w})_\omega, \quad \tilde{\boldsymbol{t}},\, \boldsymbol{w} \in H_0^{\mathrm{curl}}(\omega), \end{aligned}$$

where the coefficients $\alpha, \beta > 0$ are assumed to be piecewise constant. In a more general approach, they would still be uniformly positive definite. Note that the unknowns $\tilde{\boldsymbol{t}}$ and $\tilde{\varphi}$ denote the approximations at the current time step, $\boldsymbol{f}_{\mathrm{c}}$ depends on the approximations of $\tilde{\boldsymbol{t}}$ and $\tilde{\varphi}$ at the previous time step, and $\boldsymbol{f}$ denotes the scaled source term depending on $\boldsymbol{t}_s$. Choosing $\tilde{\boldsymbol{t}} \in H_0^{\mathrm{curl}}(\omega)$ and $\tilde{\varphi} \in H_0^1(\Omega)$, $\tilde{\boldsymbol{t}}$ and $\tilde{\varphi}$ satisfy at each time step the interface conditions, namely, $\tilde{\varphi}$ is continuous at Γ and $[\boldsymbol{t}] \times \boldsymbol{n} = 0$. In our approach, the strong coupling between $\tilde{\boldsymbol{t}}$ and $\tilde{\varphi}$ at the interface is replaced by a weak one.

It is easy to see that if $(\tilde{\boldsymbol{t}}, \tilde{\varphi})$ is a solution of (6.9), then $(\tilde{\boldsymbol{t}} + \operatorname{grad} \chi, \tilde{\varphi} + \chi)$, $\chi \in H_0^1(\omega)$, is a solution as well. In order to get uniqueness, we choose χ such that $\varphi = \tilde{\varphi} + \chi$ is harmonic on ω. Using the harmonic extension operator $\mathcal{H} : H^{1/2}(\Gamma) \longrightarrow H^1(\omega)$, see (A.22), we can state the modified variational problem: find $(\boldsymbol{t}, \varphi) \in H_0^{\mathrm{curl}}(\omega) \times H_0^1(\Omega)$ such that

$$\begin{aligned} a_\Omega(\varphi, v) \; + \; b(\boldsymbol{t}, v) \quad &= (\boldsymbol{f}, \operatorname{grad} v)_{\omega^{\mathrm{c}}}, \qquad v \in H_0^1(\Omega), && \text{(6.10a)} \\ b(\boldsymbol{w}, \varphi) \; + \; a_\omega(\boldsymbol{t}, \boldsymbol{w}) &= (\boldsymbol{f}_{\mathrm{c}}, \boldsymbol{w})_\omega, \qquad \boldsymbol{w} \in H_0^{\mathrm{curl}}(\omega), && \text{(6.10b)} \end{aligned}$$

where $b(\boldsymbol{w}, v) = -(\boldsymbol{w}, \operatorname{grad} \mathcal{H} v|_\Gamma)_\omega$, for $v \in H_0^1(\Omega)$ and $\boldsymbol{w} \in H_0^{\mathrm{curl}}(\omega)$. The bilinear form given by

$$a((\boldsymbol{w}, w), (\boldsymbol{v}, v)) = a_\omega(\boldsymbol{w}, \boldsymbol{v}) + b(\boldsymbol{w}, v) + b(\boldsymbol{v}, w) + a_\Omega(w, v),$$

where $\boldsymbol{v}, \boldsymbol{w} \in H_0^{\mathrm{curl}}(\omega)$ and $v, w \in H_0^1(\Omega)$, is elliptic on $H_0^{\mathrm{curl}}(\omega) \times H_0^1(\Omega)$; see [84]. Consequently, the variational problem (6.10) has a unique solution. The first line (6.10a) and the definition (A.22) of the harmonic extension yield $b(\boldsymbol{t}, v) = 0,\ v \in H_0^1(\omega)$. Using $\boldsymbol{w} = \operatorname{grad} v$, $v \in H_0^1(\omega)$, in the second line (6.10b), we find that $\boldsymbol{t}$ is divergence free if $\boldsymbol{f}_{\mathrm{c}}$ is divergence free. Hence, $\boldsymbol{t}$ is implicitly gauged, and φ restricted to ω is harmonic.

As for the model problem in Chapter 5, we can again derive a saddle point formulation which is equivalent to (6.10). In order to see, this we start from the strong formulation (6.4), (6.6) for the magnetic field $\boldsymbol{h}$ and its decomposition into $\boldsymbol{t} - \operatorname{grad} \varphi$ on ω and $\boldsymbol{t}_s - \operatorname{grad} \varphi$ on ω^{c}. We now assume the just validated gauging condition on $\boldsymbol{t}$, namely, we use the Coulomb gauge, and $\boldsymbol{t}$ is chosen to be solenoidal. From (6.4), we obtain

$$a_\Omega(\varphi, v) \; - \; (\boldsymbol{t}, v\boldsymbol{n})_\Gamma = (\beta \boldsymbol{t}_s, \operatorname{grad} v)_{\omega^{\mathrm{c}}}, \quad v \in V_\Omega = H_0^1(\Omega). \qquad \text{(6.11)}$$

Taking $v \in H_0^1(\omega)$, this implies that φ is harmonic on ω, thus, there exists $\gamma = \varphi|_\Gamma \in H^{1/2}(\Gamma)$ such that $\varphi|_\omega = \mathcal{H}\gamma$. Furthermore, due to the solenoidality of $\boldsymbol{t}$, it holds that

$$(\boldsymbol{t},\, \delta \boldsymbol{n})_\Gamma - (\boldsymbol{t},\, \operatorname{grad} \mathcal{H}\delta)_\omega = 0, \qquad \delta \in H^{1/2}(\Gamma).$$

After time discretization, we obtain from (6.6) at each time step:

$$\widehat{a}_\omega((\gamma, \boldsymbol{t}), (\delta, \boldsymbol{w})) + (\boldsymbol{t},\, \delta \boldsymbol{n})_\Gamma = (\boldsymbol{f}_c,\, \boldsymbol{w})_\omega, \quad (\delta, \boldsymbol{w}) \in V_\omega = H^{1/2}(\Gamma) \times H_0^{\mathrm{curl}}(\omega), \tag{6.12}$$

with

$$\widehat{a}_\omega((\gamma, \boldsymbol{t}), (\delta, \boldsymbol{w})) = (\alpha \operatorname{curl} \boldsymbol{t},\, \operatorname{curl} \boldsymbol{w})_\omega + (\boldsymbol{t},\, \boldsymbol{w})_\omega - (\boldsymbol{w},\, \operatorname{grad} \mathcal{H}\gamma)_\omega - (\boldsymbol{t},\, \operatorname{grad} \mathcal{H}\delta)_\omega. \tag{6.13}$$

This suggests the introduction of the Lagrange multiplier $\lambda = \boldsymbol{t} \cdot \boldsymbol{n} \in M = H^{-1/2}(\Gamma)$, and of the coupling bilinear form

$$\widehat{b}((v, \delta, \boldsymbol{w}), \mu) = \langle \delta - v, \mu \rangle_{M' \times M}, \quad (v, \delta, \boldsymbol{w}) \in X = V_\Omega \times V_\omega,\ \mu \in M.$$

yielding the saddle point formulation (1.16) with $\widehat{a}(\cdot,\cdot) = a_\Omega(\cdot,\cdot) + \widehat{a}_\omega(\cdot,\cdot)$ and $\widehat{b}(\cdot,\cdot)$ replacing $a(\cdot,\cdot)$ and $b(\cdot,\cdot)$, respectively.

6.3 Discretization

As in Chapter 5, we use two different quasi-uniform triangulations $\mathcal{T}_H$ on Ω and $\mathcal{T}_h$ on ω. On $\mathcal{T}_H$, we use standard conforming finite elements of lowest order for the approximation of the scalar potential φ. The associated discrete space having zero boundary conditions on $\partial\Omega$ is called $S_{0,H}(\Omega) = S^1_{0,H}(\Omega)$. For the discretization of the vector field $\boldsymbol{t}$, we use lowest order curl-conforming Nédélec finite elements on $\mathcal{T}_h$. The basis functions $\boldsymbol{w}_e$ are associated with the edges e of the triangulation $\mathcal{T}_h$ and are also known as edge elements, [88]. They can be defined in terms of the standard H^1-conforming nodal basis functions ϕ_p by

$$\boldsymbol{w}_e = \phi_p \operatorname{grad} \phi_q \,-\, \phi_q \operatorname{grad} \phi_p,$$

where the edge $e = \{p, q\}$ is oriented from node p to node q. The orientation of the edges can be chosen arbitrarily. We set $E_h(\omega) = \operatorname{span}\{\boldsymbol{w}_e \,|\, e \,\text{edge} \in \mathcal{T}_h\}$ and $E_{0,h}(\omega) = E_h(\omega) \cap H_0^{\mathrm{curl}}(\omega)$. Note that the elements $\boldsymbol{t} \in E_{0,h}(\omega)$ have vanishing tangential components on Γ. Finally, we denote by $S_h(\omega)$ the space of standard conforming finite elements of lowest order associated with $\mathcal{T}_h$ on ω, and its trace space on Γ is called $W_h(\Gamma)$. We remark that no boundary conditions are imposed on $S_h(\omega)$.

In order to formulate the discrete version of the variational problem (6.10), we have to replace the harmonic extension $\mathcal{H}$ in the definition of the bilinear form $b(\cdot,\cdot)$. A natural choice is to involve the discrete harmonic extension $\mathcal{H}_h : W_h(\Gamma) \to S_h(\omega)$ defined by (A.23). The restriction of $v \in S_{0,H}(\Omega)$ on Γ is, in general, not an element in $W_h(\Gamma)$. Thus, we cannot apply directly the discrete harmonic extension to the restriction of $v \in S_{0,H}(\Omega)$ on Γ. To overcome this difficulty, we use the mortar projection operator

Π_h as defined in (5.32). In terms of the operators $\mathcal{H}_h$ and Π_h, we formulate the discrete variational problem: find $(\boldsymbol{t}_h, \varphi_H) \in E_{0,h}(\omega) \times S_{0,H}(\Omega)$ such that

$$a_\Omega(\varphi_H, v) \; + \; b_h(\boldsymbol{t}_h, v) \;\; = (\boldsymbol{f},\, \operatorname{grad} v)_{\omega^c}, \qquad v \in S_{0,H}(\Omega)\,, \tag{6.14a}$$

$$b_h(\boldsymbol{w}, \varphi_H) \; + \; a_\omega(\boldsymbol{t}_h, \boldsymbol{w}) = (\boldsymbol{f}_c,\, \boldsymbol{w})_\omega, \qquad \boldsymbol{w} \in E_{0,h}(\omega)\,, \tag{6.14b}$$

where $b_h(\boldsymbol{w}, v) = -(\boldsymbol{w},\, \operatorname{grad} \mathcal{H}_h \Pi_h v)_\omega$ for $v \in S_{0,H}(\Omega)$ and $\boldsymbol{w} \in E_{0,h}(\omega)$. This approach is characterized by an optimal error estimate, as stated in the next lemma which is proved in [84].

Lemma 6.2. *For h/H small enough, the discrete variational problem (6.14) has a unique solution and there exists a constant C independent of the meshsize such that, for $\boldsymbol{t} \in (H^1(\omega))^3$ with $\operatorname{curl} \boldsymbol{t} \in (H^1(\omega))^3$ and $\varphi \in H^\beta(\Omega)$, $1 < \beta \leq 2$, we have*

$$|||\boldsymbol{t} - \boldsymbol{t}_h|||_\omega + ||\varphi - \varphi_H||_{1;\Omega} \leq C\Big(h(||\boldsymbol{t}||_{1;\omega} + ||\operatorname{curl} \boldsymbol{t}||_{1;\omega}) + H^{\beta-1}||\varphi||_{\beta;\Omega}\Big),$$

where $|||\boldsymbol{t}|||_\omega = (||\boldsymbol{t}||^2_{0,\omega} + \alpha||\operatorname{curl} \boldsymbol{t}||^2_{0,\omega})^{1/2}$ is a norm which is equivalent to the standard Hilbert space norm on $H_0^{\operatorname{curl}}(\omega)$.

6.4 Implementation and Algorithmic Details

We carry out some details on the implementation of the coupling bilinear form $b_h(\cdot, \cdot)$. In particular, we have to apply the operators Π_h, $\mathcal{H}_h$, and grad to a function $v \in S_{0,H}(\Omega)$, and the result should be given in terms of coefficients for the edge element basis functions in $E_h(\omega)$. For the realization of Π_h yielding the matrix $Q = D^{-1}M$, we refer to Section 5.3 for a detailed account. The second step of the coupling is the definition of the discrete harmonic extension $\mathcal{H}_h v$. This corresponds to solve a Dirichlet boundary problem in ω for the Laplace operator with a zero source term and given boundary data on Γ. We denote by S the matrix associated with the harmonic extension $\mathcal{H}_h$ from $W_h(\Gamma)$ to $S_h(\omega)$. Finally, we have to realize the coupling between the global scalar potential and the local vector one. We remark that the values of $\boldsymbol{w}_h \in E_{0,h}(\omega)$ on the boundary edges are zero due to the homogeneous boundary condition on Γ. As it is classical, the vector $\operatorname{grad} \mathcal{H}_h v$ can be decomposed in terms of the same edge element basis as $\boldsymbol{w}_h$; the coefficients of the decomposition are circulations along the considered edges defined from nodal values at the end points of the edge. The passage from the nodal values to the associated circulation can be done efficiently by introducing the incidence matrix G, see also [22]. As we have seen, an edge is not only a two-node subset of the set of all mesh nodes, but an ordered subset where the order implies an orientation. Let $e = \{p, q\}$ be an edge of the mesh oriented from node p to node q. Then, we can define the incidence numbers $G(e, q) = 1$, $G(e, p) = -1$ and $G(e, r) = 0$ for all other nodes r. These numbers form a rectangular matrix G which describes how edges connect to nodes.

According to the example given in Figure 6.1 where $\{\alpha, \beta, \delta, \chi, \epsilon\}$ are the mesh nodes and $\{a, b, c, d, e, f, g, h\}$ the mesh edges, the node-to-edge operator is represented by the

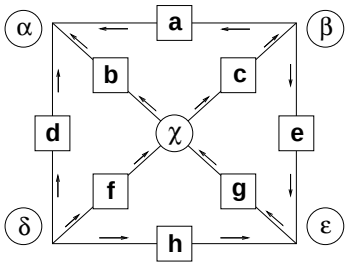

Figure 6.1: Computing the node-to-edge incident matrix G in two dimensions.

8×5 matrix G that reads

$$G = \begin{pmatrix} 1 & -1 & 0 & 0 & 0 \\ 1 & 0 & 0 & -1 & 0 \\ 0 & 1 & 0 & -1 & 0 \\ 1 & 0 & -1 & 0 & 0 \\ 0 & -1 & 0 & 0 & 1 \\ 0 & 0 & -1 & 1 & 0 \\ 0 & 0 & 0 & 1 & -1 \\ 0 & 0 & -1 & 0 & 1 \end{pmatrix}.$$

Let $v \in S_h(\omega)$, then $\boldsymbol{w} = \operatorname{grad} v \in E_h(\omega)$. Using the node-to-edge incidence matrix G, the algebraic representation has the form $\boldsymbol{w} = Gv$. Figure 6.2 illustrates the action of the node-to-edge and edge-to-node operators G and G^{T}.

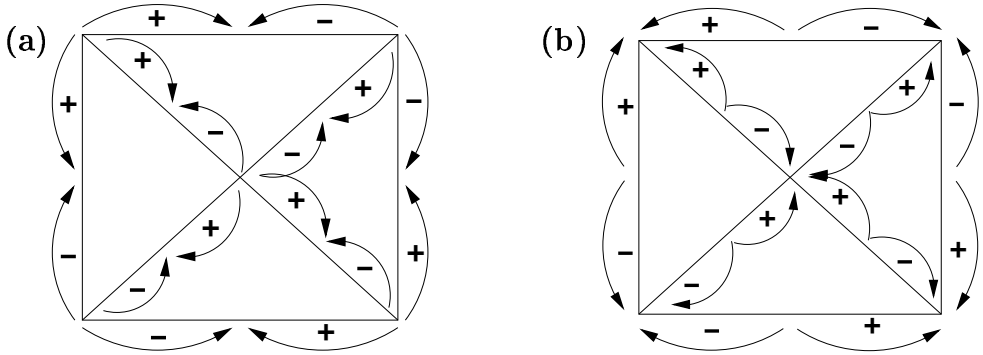

Figure 6.2: The action of the (a) node-to-edge and (b) edge-to-node operators G and G^{T}, respectively.

We associate with $-(\boldsymbol{w}, \operatorname{grad} v)_\omega$, $\boldsymbol{w} \in E_h(\omega)$ and $v \in S_h(\omega)$, the rectangular matrix B. It can be written as $B = -M_e\, G$, where M_e is the edge element mass matrix on ω. The stiffness matrix A associated with the bilinear form $a_\omega(\cdot,\cdot)$ on $E_h(\omega)\times E_h(\omega)$ can be decomposed in $A = M_e + C$ where C is associated with the curl part of $a_\omega(\cdot,\cdot)$, i.e., the elements of C are given by $(C)_{ee'} = (\alpha \operatorname{curl} \boldsymbol{w}_e, \operatorname{curl} \boldsymbol{w}_{e'})_\omega$, for all edges e, e' of $\mathcal{T}_h$. Observing that $C\,G = 0$, due to the fact that $\operatorname{curl}\operatorname{grad}(\cdot) = 0$, we find $B = -A\,G$. If

we now decompose the edges into boundary and interior edges, we can write A as a 2×2 block matrix

$$A = \begin{pmatrix} A_{II} & A_{I\Gamma} \\ A_{\Gamma I} & A_{\Gamma\Gamma} \end{pmatrix} \quad \text{and} \quad A_0 = \begin{pmatrix} A_{II} & A_{I\Gamma} \\ 0 & \mathrm{Id} \end{pmatrix},$$

where A_0 is the matrix associated with the Dirichlet problem on $E_{0,h}(\omega)$ defined in terms of the same bilinear form $a_\omega(\cdot,\cdot)$.

We finally present a numerical algorithm to solve the discrete problem (6.14). Let us denote by $K_{0,\Omega}$ the standard stiffness matrix associated with the bilinear form $a_\Omega(\cdot,\cdot)$ on $H_0^1(\Omega)\times H_0^1(\Omega)$. The algebraic form of the discrete problem (6.14) reads: find two vectors $\boldsymbol{t}_h$ and φ_H solving the linear system

$$A_0\boldsymbol{t}_h + PBSQ\varphi_H = F_{\mathrm{c}}\,, \qquad K_{0,\Omega}\varphi_H + Q^{\mathrm{T}}S^{\mathrm{T}}B^{\mathrm{T}}\boldsymbol{t}_h = F\,. \tag{6.15}$$

The right hand side vectors take into account the homogeneous Dirichlet boundary conditions, and P is a cut off matrix; i.e., $P(v_I, v_\Gamma)^{\mathrm{T}} = (v_I, 0)^{\mathrm{T}}$. The application of P is necessary to guarantee the homogeneous Dirichlet boundary condition of $\boldsymbol{t}_h$ on Γ.

As iterative solver for (6.15), we propose a block Gauß–Seidel method. Starting from φ_H^n, we first compute $\boldsymbol{t}_h^{n+1}$ and then φ_H^{n+1} by

$$A_0\boldsymbol{t}_h^{n+1} + PBSQ\varphi_H^{n} = F_{\mathrm{c}}\,, \qquad K_{0,\Omega}\varphi_H^{n+1} + Q^{\mathrm{T}}S^{\mathrm{T}}B^{\mathrm{T}}\boldsymbol{t}_h^{n+1} = F\,. \tag{6.16}$$

The following lemma guarantees the convergence of the algorithm, see [84].

Lemma 6.3. *Let $e^n = \varphi_H - \varphi_H^n$ be the iteration error in the n-th step, then there exists a constant $0 < \theta < 1$ not depending on H and h such that*

$$a_\Omega(e^{n+1}, e^{n+1}) < \theta\, a_\Omega(e^n, e^n)\,.$$

The convergence of φ_H^n to φ_H yields the one of $\boldsymbol{t}_h^n$ to $\boldsymbol{t}_h$.

Figure 6.3 illustrates the algorithm. It is compatible with the presence of a conductor ω that can move inside Ω. The construction of the mortar projection Π_h is the only part of the algorithm that is influenced by the motion of ω. Thus, only the matrix Q has to be reassembled whenever the conductor ω changes its position in Ω.

In the rest of this section, we present an equivalent formulation of (6.16). In particular, we show that (6.16) is equivalent to a preconditioned Richardson iteration only involving three solves per iteration step in contrast to four in case of (6.16). We denote by K_ω the standard stiffness matrix associated with the Laplace operator on ω corresponding to the bilinear form $(\operatorname{grad} v, \operatorname{grad} v')_\omega$.

Lemma 6.4. *The following identity holds*

$$S^T B^T A_0^{-1} PBS = \mathcal{S}_K - G_{\Gamma\Gamma}^T \mathcal{S}_A G_{\Gamma\Gamma}\,,$$

where $\mathcal{S}_A$ and $\mathcal{S}_{K_\omega}$ is the Schur complement of A and K_ω, respectively, i.e., $\mathcal{S}_A = A_{\Gamma\Gamma} - A_{\Gamma I}A_{II}^{-1}A_{I\Gamma}$.

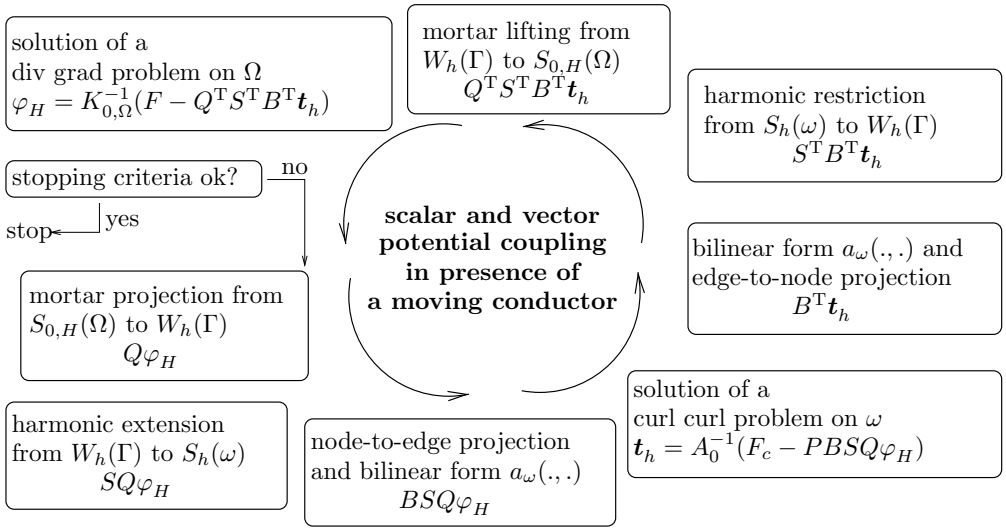

Figure 6.3: Numerical algorithm for the scalar and vector potentials coupling.

Proof We start by rewriting

$$\begin{aligned} AA_0^{-1}PA &= \begin{pmatrix} A_{II} & A_{I\Gamma} \\ A_{\Gamma I} & A_{\Gamma\Gamma} \end{pmatrix} \begin{pmatrix} A_{II}^{-1} & -A_{II}^{-1}A_{I\Gamma} \\ 0 & \mathrm{Id} \end{pmatrix} \begin{pmatrix} \mathrm{Id} & 0 \\ 0 & 0 \end{pmatrix} \begin{pmatrix} A_{II} & A_{I\Gamma} \\ A_{\Gamma I} & A_{\Gamma\Gamma} \end{pmatrix} \\ &= \begin{pmatrix} \mathrm{Id} & 0 \\ A_{\Gamma I}A_{II}^{-1} & \mathcal{S}_A \end{pmatrix} \begin{pmatrix} A_{II} & A_{I\Gamma} \\ 0 & 0 \end{pmatrix} = \begin{pmatrix} A_{II} & A_{I\Gamma} \\ A_{\Gamma I} & A_{\Gamma I}A_{II}^{-1}A_{I\Gamma} \end{pmatrix} \\ &= \begin{pmatrix} A_{II} & A_{I\Gamma} \\ A_{\Gamma I} & A_{\Gamma\Gamma} \end{pmatrix} - \begin{pmatrix} 0 & 0 \\ 0 & \mathcal{S}_A \end{pmatrix} = A - \begin{pmatrix} 0 & 0 \\ 0 & \mathcal{S}_A \end{pmatrix}. \end{aligned} \tag{6.17}$$

Recalling that $-B = AG = M_eG$ and thus $G^{\mathrm{T}}AG = G^{\mathrm{T}}M_eG = K_\omega$, we find

$$S^{\mathrm{T}}G^{\mathrm{T}}AGS = S^{\mathrm{T}}K_\omega S = \left(-K_{\Gamma I}K_{II}^{-1}, \mathrm{Id}\right) \begin{pmatrix} K_{II} & K_{I\Gamma} \\ K_{\Gamma I} & K_{\Gamma\Gamma} \end{pmatrix} \begin{pmatrix} -K_{II}^{-1}K_{I\Gamma} \\ \mathrm{Id} \end{pmatrix} = \mathcal{S}_{K_\omega},$$

where we have used another 2×2 block decomposition into interior and boundary vertices.

Finally, we have to consider the second term on the right hand side of (6.17) in more detail. To do so, we use the block decomposition

$$G = \begin{pmatrix} G_{II} & G_{I\Gamma} \\ 0 & G_{\Gamma\Gamma} \end{pmatrix},$$

noting that $G_{\Gamma I} = 0$ since an interior vertex cannot be an endpoint of an edge on the boundary. The block decomposition of G yields

$$S^{\mathrm{T}}G^{\mathrm{T}} \begin{pmatrix} 0 & 0 \\ 0 & \mathcal{S}_A \end{pmatrix} GS = (*, \mathrm{Id}) \begin{pmatrix} 0 & 0 \\ 0 & G_{\Gamma\Gamma}^{\mathrm{T}}\mathcal{S}_A G_{\Gamma\Gamma} \end{pmatrix} \begin{pmatrix} * \\ \mathrm{Id} \end{pmatrix} = G_{\Gamma\Gamma}^{\mathrm{T}}\mathcal{S}_A G_{\Gamma\Gamma}.$$

Summarizing the results, we find

$$S^{\mathrm{T}}B^{\mathrm{T}}A_0^{-1}PBS = S^{\mathrm{T}}G^{\mathrm{T}}AA_0^{-1}PAGS = \mathcal{S}_{K_\omega} - G_{\Gamma\Gamma}^{\mathrm{T}}\mathcal{S}_A G_{\Gamma\Gamma}\,. \qquad \square$$

Using the first equation in (6.15), we find $\boldsymbol{t}_h = A_0^{-1}(F_{\mathrm{c}} - PBSQ\varphi_H)$. Then, the elimination of $\boldsymbol{t}_h$ in (6.15) and Lemma 6.4 yield a linear system for φ_H:

$$(K_{0,\Omega} - Q^{\mathrm{T}}(\mathcal{S}_{K_\omega} - G_{\Gamma\Gamma}^{\mathrm{T}}\mathcal{S}_A G_{\Gamma\Gamma})\,Q)\varphi_H = F - Q^{\mathrm{T}}S^{\mathrm{T}}B^{\mathrm{T}}A_0^{-1}F_{\mathrm{c}} = F_H\,. \tag{6.18}$$

If h/H is small enough, the matrix $K_{0,\Omega} - Q^{\mathrm{T}}(\mathcal{S}_{K_\omega} - G_{\Gamma\Gamma}^{\mathrm{T}}\mathcal{S}_A G_{\Gamma\Gamma})Q$ is symmetric and positive definite, see [84]. Applying to (6.18) a Richardson iteration (see [103] for more details) with $K_{0,\Omega}^{-1}$ as preconditioner yields

$$\begin{aligned}\varphi_H^{n+1} &= \varphi_H^n + K_{0,\Omega}^{-1}(F_H - (K_{0,\Omega} - Q^{\mathrm{T}}(\mathcal{S}_{K_\omega} - G_{\Gamma\Gamma}^{\mathrm{T}}\mathcal{S}_A G_{\Gamma\Gamma})Q)\varphi_H^n)\\ &= K_{0,\Omega}^{-1}(F_H + Q^{\mathrm{T}}(\mathcal{S}_{K_\omega} - G_{\Gamma\Gamma}^{\mathrm{T}}\mathcal{S}_A G_{\Gamma\Gamma})Q\varphi_H^n)\,.\end{aligned} \tag{6.19}$$

Lemma 6.5. *The block Gauß–Seidel method (6.16) with $\varphi_H^0 = K_{0,\Omega}^{-1}F_H$ is equivalent to the preconditioned Richardson iteration (6.19) with the same φ_H^0.*

Proof The block Gauß–Seidel method yields the following recursive definition of $\boldsymbol{t}_h^{n+1}$

$$\begin{aligned}\boldsymbol{t}_h^{n+1} &= A_0^{-1}(F_{\mathrm{c}} - PBSQ\varphi_H^n) = A_0^{-1}(F_{\mathrm{c}} - PBSQ\varphi_H^{n-1} + PBSQ(\varphi_H^{n-1} - \varphi_H^n))\\ &= \boldsymbol{t}_h^n - A_0^{-1}PBSQ(\varphi_H^n - \varphi_H^{n-1})\,,\end{aligned}$$

where we set $\varphi_H^{-1} = 0$ and $\boldsymbol{t}_h^0 = A_0^{-1}F_{\mathrm{c}}$. Using $\varphi_H^0 = K_{0,\Omega}^{-1}F_H$, we find for the block Gauß–Seidel method

$$\begin{pmatrix} K_{0,\Omega}\varphi_H^{n+1} = F - Q^{\mathrm{T}}S^{\mathrm{T}}B^{\mathrm{T}}\boldsymbol{t}_h^n + Q^{\mathrm{T}}S^{\mathrm{T}}B^{\mathrm{T}}A_0^{-1}PBSQ(\varphi_H^n - \varphi_H^{n-1}) \\ \varphi_H^{n+1} = \varphi_H^n + K_{0,\Omega}^{-1}Q^{\mathrm{T}}S^{\mathrm{T}}B^{\mathrm{T}}A_0^{-1}PBSQ(\varphi_H^n - \varphi_H^{n-1})\,. \end{pmatrix}$$

By means of Lemma 6.4, we get that the Gauß–Seidel method (6.16) is equivalent to

$$\varphi_H^{n+1} = \varphi_H^n + K_{0,\Omega}^{-1}Q^{\mathrm{T}}(\mathcal{S}_{K_\omega} - G_{\Gamma\Gamma}^{\mathrm{T}}\mathcal{S}_A G_{\Gamma\Gamma})Q(\varphi_H^n - \varphi_H^{n-1})\,. \tag{6.20}$$

Comparing (6.19) and (6.20), the assertion can be easily shown by induction. $\square$

Due to Lemmas 6.3 and 6.5, the convergence rate of (6.19) does not depend on the meshsize and can be improved by applying a Krylov subspace method. When the difference between two successive iterations φ_H^{n+1} and φ_H^n satisfies a stopping criteria, then we can compute $\boldsymbol{t}_h^{n+1}$ by means of the first equation in (6.16). At this point, the moving conductor reaches its new position, and the algorithm (6.19) starts again.

The preconditioned Richardson iteration to obtain φ_H^{n+1} is illustrated in Figure 6.4. In each iteration step, we have to solve one Dirichlet problem on ω associated with the Laplace operator, one Dirichlet problem on ω associated with the curl operator, and one Dirichlet problem associated with the Laplace operator on Ω.

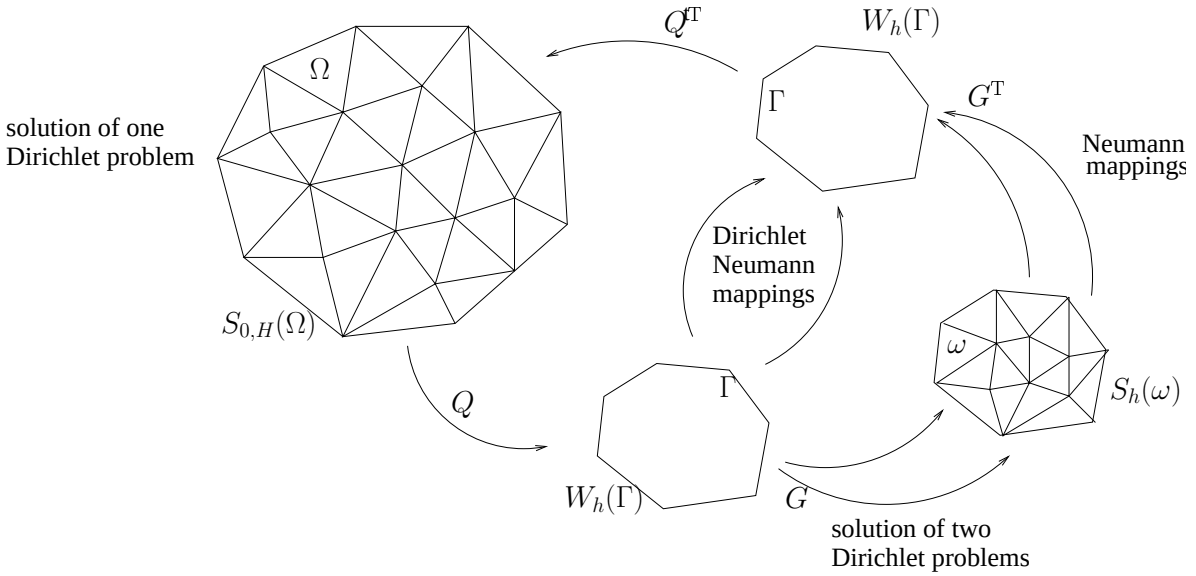

Figure 6.4: Illustration of the preconditioned Richardson iteration.

6.5 Numerical Results

We apply the block Gauß–Seidel method (6.16) in two dimensions to the example shown in Figure 6.5. The computational domain Ω is the square $(-0.1\mathrm{m}, 0.1\mathrm{m})^2$ containing a ferromagnet of permeability $\mu = 5{\cdot}10^{-4}\mathrm{H/m}$. Two coils generating the source field $\boldsymbol{t}_s$ are located on a part of the ferromagnet (shadowed part of Figure 6.5, left). The conductor ω of width 0.012m and height 0.09m moves with the constant velocity $v = -0.2\vec{e}_y\mathrm{m/s}$, its barycenter having the initial position $x_0 = (0, 0.01\mathrm{m})^{\mathrm{T}}$. The conductivity σ of ω is set to be $10^6\mathrm{S/m}$, its magnetic permeability is the same as the one of the surrounding air, $\mu_0 = 4\pi 10^{-7}\mathrm{H/m}$. The used time step is $\Delta t = 0.00625\mathrm{s}$.

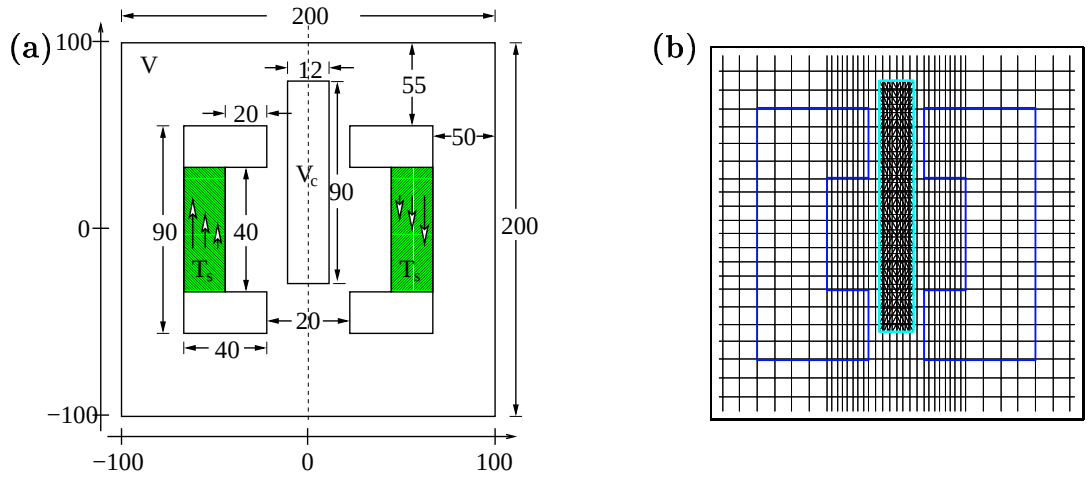

Figure 6.5: (a) conductor ω moving through the magnetic field induced by $\boldsymbol{t}_s$ (dimensions are given in millimeters), (b) overlapping non-matching grids (zoom).

The triangulation $\mathcal{T}_H$ of the domain Ω consists of 1536 quadrilateral elements sharing 1616 nodes. The conductor ω is discretized by means of 512 triangles yielding 808 edge element unknowns. We remark that the motion of the conductor is performed without involving any remeshing procedure. Moreover, since $K_{0,\Omega}^{-1}$, $\mathcal{S}_{K_\omega}$, and $\mathcal{S}_A$ stay constant during the whole simulation, it is sufficient to carry out the corresponding LU-decompositions only once. The presented algorithm consists of two nested iterative schemes. An implicit Euler scheme is used for the outer iteration with zero initial condition. The inner iteration is the preconditioned Richardson method given in (6.19). We use $\|\varphi_H^{n+1} - \varphi_H^n\|/\|\varphi_H^n\| < 10^{-4}$ as stopping criteria for our inner iteration scheme. For the considered example, the number of iterations is between 5 and 11 for all time steps. Figure 6.6 illustrates the preconditioned Richardson iteration for a fixed time step. To support the theoretical result of Lemma 6.3, we consider different meshsizes and show the number of required iteration steps versus the number of unknowns. We observe convergence rates which are independent of the meshsizes.

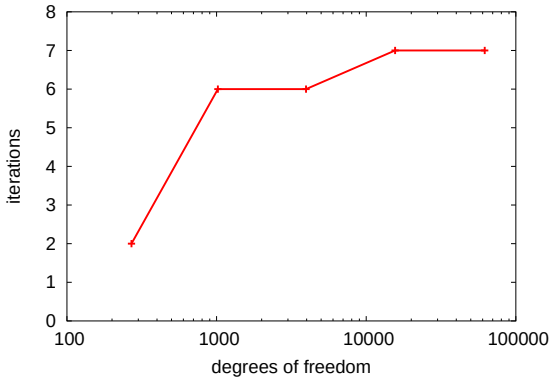

Figure 6.6: Time step 8. Number of iteration steps with respect to the number of unknowns

Figures 6.7 and 6.8 show the distribution of the magnetic field outside and inside the conductor ω corresponding to two different positions of the moving part ω. The distribution of the induced field in the conductor is in agreement with that predicted by the Lenz law, i.e., the induced currents create a field which contrasts the one generated by the sources in order to give a zero total magnetic field in ω.

In Figure 6.9, the components of the magnetic field in horizontal direction are plotted along the vertical axis of symmetry, which is indicated by the dashed line in Figure 6.5, left. The inducing component $-\partial_x\varphi$ generates a reaction field $\boldsymbol{t}_x$ in ω trying to compensate the first one. Thus these two components have opposite signs. After the first time step, the resulting total field $(\boldsymbol{t} - \operatorname{grad}\varphi)_x$ inside the conductor is almost completely suppressed because of the instantaneous penetration by the inducing field, as shown in Figure 6.9(a). As the conductor moves along, this effect becomes less intense. Moreover even when the barycenter of ω is exactly at the origin of the system, the field distribution in ω is not symmetric with respect to the horizontal axis, as illustrated in Figure 6.9(b). This is due to the motion of the conductor towards the bottom.

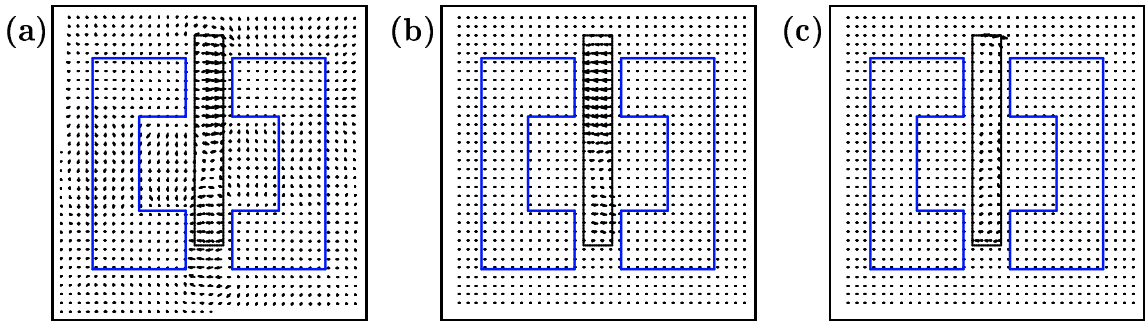

Figure 6.7: Time step 1: (a) generated field $-\operatorname{grad}\varphi$ in Ω between the poles, (b) induced vector potential $\boldsymbol{t}$ on ω, (c) magnetic field $\boldsymbol{h} = \boldsymbol{t} - \operatorname{grad}\varphi$ on ω.

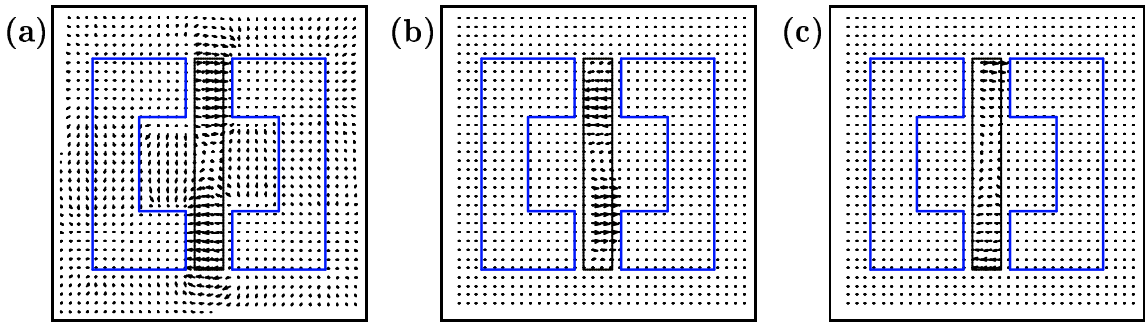

Figure 6.8: Time step 8: (a) generated field $-\operatorname{grad}\varphi$ in Ω between the poles, (b) induced vector potential $\boldsymbol{t}$ on ω, (c) magnetic field $\boldsymbol{h} = \boldsymbol{t} - \operatorname{grad}\varphi$ on ω.

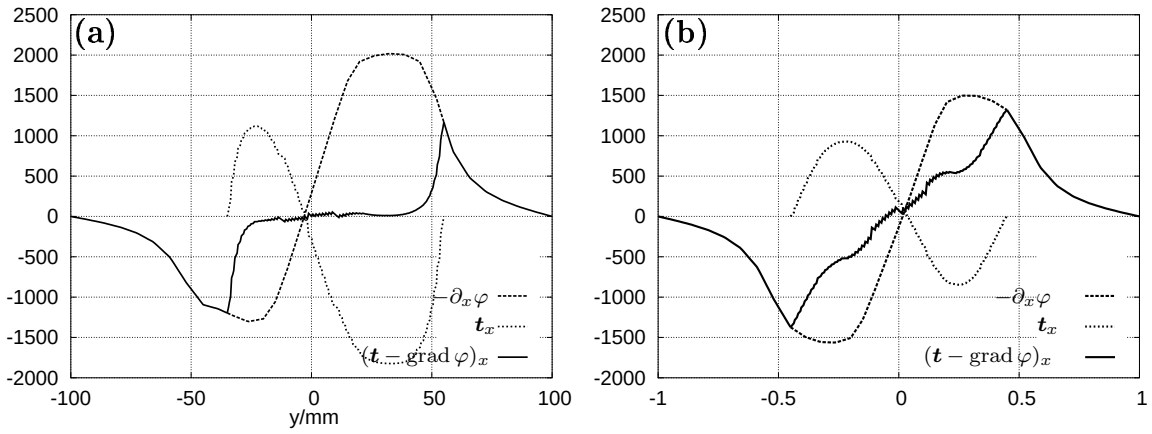

Figure 6.9: Field intensity in horizontal direction along the vertical axis of symmetry: (a) time step 1, (b) time step 8.

6.6 An Electromagnetic Brake

So far, the motion of the conductor was given in advance. In general, this motion is influenced by the electromagnetic forces acting on ω. In order to account for this effect, we use the simple model of a damped harmonic oscillator for the mechanical part. Let ℓ be the distance between the two equilibrium positions of ω which correspond to take or not to take into account the gravity force, respectively. We denote by m the mass of ω and by z the vertical position of the center of ω at time t, with the initial conditions $z(0)$, $\dot{z}(0)$. Then at any given time, there are four forces acting on m: the gravity force $-mg$ pulling downward, the spring force $k(\ell - z)$, the damping force $-b\dot{z}$ and the external magnetic force $(F_m)_z$. Neglecting any motion parallel to the (x, y)-plane, the Newton's law of motion for a point mass (the center of ω) reads:

$$m\ddot{z} = -mg + k(\ell - z) - b\dot{z} + (\int_\omega (\operatorname{curl} H) \times \mu\, H)_z, \tag{6.21}$$

where we assume that ω has free space permeability μ_0, and, therefore, no forces due to magnetization need to be taken into account. If we write (6.21) at the equilibrium position, i.e. $z = 0$ and $F_m = 0$, we get $mg = k\ell$. Then, (6.21) simplifies into

$$m\ddot{z} + b\dot{z} + kz = (\int_\omega (\operatorname{curl} H) \times \mu\, H)_z\,. \tag{6.22}$$

To discretize (6.22), we apply a second order explicit finite difference scheme of time step size Δt.

In the following, we present some numerical results for problem (6.14) explicitly coupled with the discrete form of (6.22). The considered domain Ω is the cube $(-0.1\mathrm{m}, 0.1\mathrm{m})^3$ containing a ferromagnet of relative magnetic permeability $\mu_r = 1000$, and a cylindrical conductor ω having permeability $\mu_0 = 4\pi 10^{-7}\mathrm{H/m}$. The geometry parameters are illustrated in Fig. 6.10. The ferromagnet contains a coil (shadowed part in the right picture of Fig. 6.10) consisting of 500 windings each of which carries a constant current of 50A, which yields a source current density $\boldsymbol{\iota}_s = 41.67\,\mathrm{A/mm^2}$. The conductor ω moves with a velocity $v \parallel \vec{e}_z$ determined by the solution of the coupled problem. Its barycenter has the initial position $\vec{x}_0 = (0, 0, 0.02\mathrm{m})^\mathrm{T}$.

Both the geometry and the source term are axisymmetric with respect to the vertical axis. Therefore, by transformation to cylindrical coordinates, we can reduce the problem dimension and choose the right half of the (x, z)-plane as computational domain [66]. The left picture of Fig. 6.11 shows a zoom of the computational grids, being quadrilateral in Ω and triangular in ω. The mechanical parameters are chosen to give a damped oscillating system (i.e., $b^2 - 4km < 0$). Here, $m = 0.1\mathrm{kg}$, $b = 0.05\mathrm{Ns/m}$, and $k = 20\mathrm{N/m}$. Using as initial conditions $z(0) = 0.02\mathrm{m}$ and $\dot{z}(0) = 0$, we perform 200 time iterations of step size $\Delta t = 0.01\mathrm{s}$. We run five different tests, thereby varying the conductivity σ of ω from 10^6 to $10^8\mathrm{S/m}$.

The results are illustrated in the right picture of Fig. 6.11, plotting the vertical position z of the center of the conductor against the time t. We observe that, for $\sigma = 10^6\,\mathrm{S/m}$, the

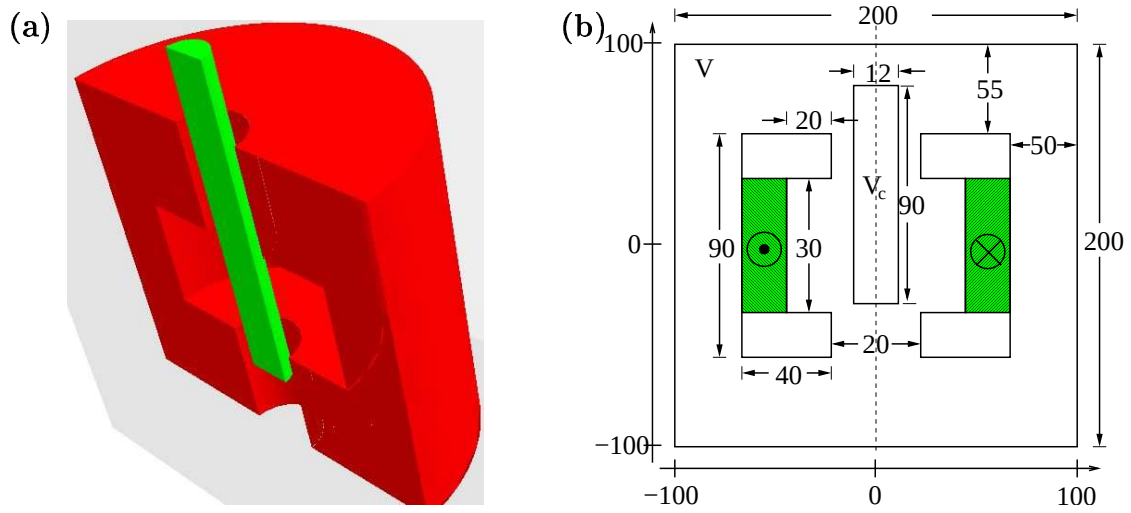

Figure 6.10: (a) domain geometry, (b) (x, z)-plane, dimensions in mm.

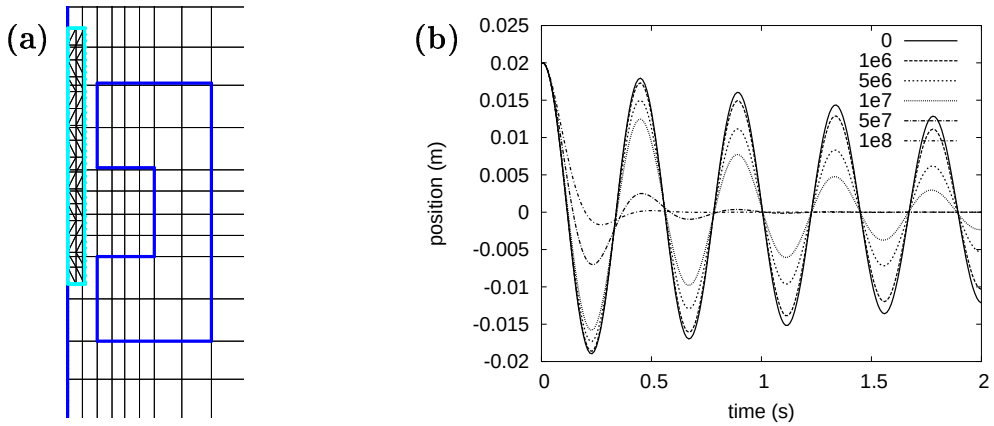

Figure 6.11: (a) overlapping grids (zoom), (b) vertical position y of ω with respect to time for different values of σ (given in S/m).

motion almost coincides with that described by the homogeneous form of (6.22). In this case, the magnetic force related to the induced currents in ω is rather weak and within the computational time interval, the conductor cannot hold the equilibrium position. As soon as $\sigma \geq 5{\cdot}10^6\,\mathrm{S/m}$, the contrasting effect of the eddy currents to the motion is more visible and the amplitude of the oscillation decreases. For the large conductivities $5{\cdot}10^7$ and $10^8\,\mathrm{S/m}$, the conductor stays within equilibrium position after roughly 1 and 0.5 seconds, respectively.

7 Concluding Remarks

This thesis is devoted to the development and analysis of nonconforming discretization schemes for coupled problems. In order to be able to deal with the naturally arising non-matching interface grids, the framework of mortar finite elements in combination with dual Lagrange multipliers has been chosen, which guarantees the stability, optimality and efficiency of the resulting numerical algorithms. Some extensions to the original approach have been proposed, and their validation has been performed both theoretically and by means of several non-trivial applications.

A large part has been dedicated to the extension of the mortar method to the case of curvilinear interfaces. For a scalar model equation, a rigorous convergence analysis in the spirit of variational crimes has been carried out. Reformulating the discrete problem formulation on affine elements as a perturbation of a blending element approach, optimal a priori error estimates have been derived, based on abstract assumptions for the discrete Lagrange multiplier space. The analysis has been expanded to the linear elasticity setting by investigating modifications for dual Lagrange multipliers necessary to ensure stability.

Moreover, the extension of lowest order dual Lagrange multipliers from simplicial or parallelogram-shaped surface elements to arbitrary quadrilateral elements has been proposed by means of two alternatives. For both possibilities, the optimality of the approach has been shown by validating the reproduction property for constants which immediately implies the approximation property, while the stability already follows from the biorthogonality of the dual basis functions.

In addition, the use of non-matching grids for coupled problems in computational acoustics has been studied. Two settings have been examined, the first one considering an aero-acoustic problem given by the wave equation for the acoustic velocity potential in both regions, the second one realizing a fluid-structure coupling of a displacement based formulation for an excited elastic structure with the wave equation for the surrounding acoustic fluid. The advantages of being able to deal with non-matching grids in both settings have been clarified by several applications. Moreover, a solution method for the case of nonlinear structures has been introduced and tested.

Whenever moving subdomains are involved, it is very appealing to use an overlapping decomposition. The mortar framework has been extended to the case of nested domains. For a simple one-directionally coupled model problem, a detailed error analysis incorporating the use of different meshwidths and finite element spaces has been carried out. Moreover, an equivalent formulation as a generalized saddle point problem has been presented.

As a particular application of an overlapping decomposition of nested domains, the eddy currents resulting from the motion of a conductor through an electromagnetic field have been investigated. The unknown magnetic field has been decomposed into the dif-

ference of a local vector potential and the gradient of a global scalar potential. According to the different model equations, different discretization schemes have been used which were successfully coupled by weak matching conditions. The simulation of an electromagnetic brake has been considered as an example clearly depicting the advantage of using an overlapping decomposition.

Overall, this thesis is intended to contribute to the evolution of mathematically sound and numerically efficient algorithms from purely academic examples towards the simulation of real-life problems. Increasing the complexity of coupled problem settings further and further, the issue of robust data transmission between the decoupled subproblems becomes more and more important. The construction of the required projection operators by naturally adapting the continuous variational formulations, like it is done within the mortar framework, is very promising and worth to be considered for industrial applications.

A Appendix

A.1 Functional Analysis

We follow closely the presentation in [39]. Henceforth, Ω is a measurable open set of $\mathbb{R}^d$ with boundary $\partial\Omega$. Whenever it is well-defined, its outward normal is denoted by $\boldsymbol{n}$.

Definition A.1 (L^p-spaces). Let $\mathbb{M}(\Omega)$ be the space of (equivalence classes of) scalar-valued functions on Ω that are Lebesgue-measurable. For $1 \leq p \leq \infty$, set

$$L^p(\Omega) = \{f \in \mathbb{M}(\Omega) : \|f\|_{0,p,\Omega} < \infty\}, \tag{A.1}$$

where

$$\begin{aligned} \|f\|_{0,p,\Omega} &= \left(\int_\Omega |f|^p \,\mathrm{d}\Omega\right)^{1/p}, \quad 1 \leq p < \infty, \\ \|f\|_{0,\infty,\Omega} &= \operatorname*{ess\,sup}_{x\in\Omega} |f(x)| = \inf\{M \geq 0; |f(x)| \leq M \text{ a.e. on } \Omega\}. \end{aligned}$$

Definition A.2 (locally integrable). The space of locally integrable functions is denoted by $L^1_{\mathrm{loc}}(\Omega)$ and is defined as

$$L^1_{\mathrm{loc}}(\Omega) = \{f \in \mathbb{M}(\Omega) : \text{ for all compact } K \subset \Omega,\ f \in L^1(K)\}.$$

Theorem A.3 (L^2-inner product). *The space $L^2(\Omega)$ is a Hilbert space when equipped with the scalar product*

$$(f, g)_\Omega = \int_\Omega fg \,\mathrm{d}\Omega. \tag{A.2}$$

The corresponding norm is denoted by

$$\|f\|_{0,\Omega} = \|f\|_{0,2,\Omega} = \left(\int_\Omega |f|^2 \,\mathrm{d}\Omega\right)^{1/2}. \tag{A.3}$$

Definition A.4 (distribution). Let $\mathcal{D}(\Omega)$ denote the vector space of infinitely often differentiable functions whose support in Ω is compact. A linear mapping

$$v : \mathcal{D}(\Omega) \ni \varphi \mapsto \langle v, \varphi\rangle_{\mathcal{D}',\mathcal{D}} \in \mathbb{R},$$

is said to be a distribution on Ω if and only if the following property holds: For all compact K in Ω, there is an integer p and a constant C such that

$$|\langle v, \varphi\rangle_{\mathcal{D}',\mathcal{D}}| \leq C \sup_{x\in K, |\alpha|\leq p} |\partial^\alpha \varphi(x)|, \qquad \varphi \in \mathcal{D}(\Omega),\ \operatorname{supp}(\varphi) \subset K.$$

Every function $f \in L^1_{\text{loc}}(\Omega)$ can be identified with the distribution

$$\tilde{f} : \mathcal{D}(\Omega) \ni \varphi \mapsto \langle \tilde{f}, \varphi \rangle_{\mathcal{D}',\mathcal{D}} = \int_\Omega f\varphi \, \mathrm{d}\Omega.$$

Definition A.5 (distributional derivative). Let $v \in \mathcal{D}'(\Omega)$ be a distribution. For a multi-index α, the α-th distributional (or weak) derivative $\partial^\alpha v$ is defined such that

$$\partial^\alpha v : \mathcal{D}(\Omega) \ni \varphi \mapsto \langle \partial^\alpha v, \varphi \rangle_{\mathcal{D}',\mathcal{D}} = (-1)^{|\alpha|} \langle v, \partial^\alpha \varphi \rangle_{\mathcal{D}',\mathcal{D}}.$$

Definition A.6 (Sobolev spaces). Let s and p be two integers with $s \geq 0$ and $1 \leq p \leq \infty$. The Sobolev space $W^{s,p}(\Omega)$ is defined as

$$W^{s,p}(\Omega) = \{v \in \mathcal{D}'(\Omega) : \partial^\alpha v \in L^p(\Omega),\ |\alpha| \leq s\}, \tag{A.4}$$

a Banach space equipped with the norm

$$\|v\|_{s,p,\Omega} = \sum_{|\alpha| \leq s} \|\partial^\alpha v\|_{L^p(\Omega)}.$$

Theorem A.7 (Hilbert Sobolev spaces). *Let $s \geq 0$. The space $H^s(\Omega) = W^{s,2}(\Omega)$ is a Hilbert space when equipped with the scalar product*

$$(v, w)_{s,\Omega} = \sum_{|\alpha| \leq s} (\partial^\alpha v, \partial^\alpha w)_\Omega. \tag{A.5}$$

The associated norm is denoted by $\| \cdot \|_{s,\Omega}$.

Definition A.8 (Lipschitz continuous). Let D be a subset of $\overline{\Omega}$ and $\mathcal{C}^0(D)$ denote the space of functions that are continuous on D. Then $\mathcal{C}^{0,1}(D)$ is the space of functions that are Lipschitz continuous on D, namely,

$$\mathcal{C}^{0,1}(D) = \left\{ f \in \mathcal{C}^0(D) : \sup_{x,y \in D} \frac{|f(x) - f(y)|}{|x - y|} < \infty \right\}. \tag{A.6}$$

Definition A.9 (Lipschitz domain). We say that Ω is a Lipschitz domain, if in a neighborhood U_x of any point $x \in \partial\Omega$, the boundary $\partial\Omega$ may be represented as a hypersurface $y_d = \theta(y_1, \ldots, y_{d-1})$, where θ is a Lipschitz function in $\mathcal{C}^{0,1}(U_x)$, and $(y_1, \ldots, y_d)$ are rectangular coordinates in $\mathbb{R}^d$ that may be different from the canonical basis.

Theorem A.10 (density). *Let Ω be a Lipschitz domain. The restriction of functions in $\mathcal{D}(\mathbb{R}^d)$ to Ω span a dense subspace of $W^{1,p}(\Omega)$.*

Definition A.11 (fractional Sobolev spaces). For $0 < s < 1$ and $1 \leq p < \infty$, the Sobolev space with fractional exponent is defined as

$$W^{s,p}(\Omega) = \{v \in L^p(\Omega) : \frac{v(x) - v(y)}{|x - y|^{s+d/p}} \in L^p(\Omega \times \Omega)\}. \tag{A.7}$$

When $s > 1$ is not integer, letting $\sigma = s - [s]$ with $[s]$ being the integer part of s, $W^{s,p}(\Omega)$ is defined as

$$W^{s,p}(\Omega) = \{v \in W^{[s],p}(\Omega) : \partial^\alpha v \in W^{\sigma,p}(\Omega), |\alpha| = s\}.$$

For $p = 2$, we denote $H^s(\Omega) = W^{s,2}(\Omega)$.

Definition A.12 ($W_0^{s,p}(\Omega)$ and its dual). For $1 \le p < \infty$ and $s \ge 0$, set

$$W_0^{s,p}(\Omega) = \overline{\mathcal{D}(\Omega)},$$

where the closure is taken with respect to $\|\cdot\|_{s,p,\Omega}$, and let $W^{-s,p'}(\Omega) = (W_0^{s,p}(\Omega))'$ be the dual of $W_0^{s,p}(\Omega)$ with the norm

$$\|f\|_{-s,p',\Omega} = \sup_{v \in W_0^{s,p}(\Omega)} \frac{\langle f, v\rangle_{W^{-s,p'} \times W_0^{s,p}}}{\|v\|_{s,p,\Omega}}. \tag{A.8}$$

For $p = 2$, we denote $H_0^s(\Omega) = W_0^{s,2}(\Omega)$ and $H^{-s}(\Omega) = W^{-s,2}(\Omega)$.

Theorem A.13 (trace theorem). *Let $\gamma_0 : \mathcal{C}^0(\overline{\Omega}) \to \mathcal{C}^0(\partial\Omega)$ map functions in $\mathcal{C}^0(\overline{\Omega})$ to their trace on $\partial\Omega$. If Ω is a Lipschitz domain, γ_0 can be continuously extended to $H^1(\Omega)$, $1 \le p < \infty$. Moreover, it holds that*

(i) The extension $\gamma_0 : H^1(\Omega) \to H^{1/2}(\partial\Omega)$ is surjective.

(ii) The kernel of γ_0 is $H_0^1(\Omega)$.

We often write $v|_{\partial\Omega}$ instead of $\gamma_0 v$.

Lemma A.14. *Let Ω be a Lipschitz bounded open set, and $\boldsymbol{u} \in (L^2(\Omega))^3$ such that $\operatorname{curl} \boldsymbol{u} \in (L^2(\Omega))^3$. Then, $\boldsymbol{u} \times \boldsymbol{n} \in (H^{-1/2}(\partial\Omega))^3$, and*

$$(\operatorname{curl} \boldsymbol{u},\, \boldsymbol{v})_\Omega = (\boldsymbol{u},\, \operatorname{curl} \boldsymbol{v})_\Omega - \langle \boldsymbol{u} \times \boldsymbol{n},\, v\rangle_{H^{-1/2} \times H^{1/2}}. \tag{A.9}$$

Lemma A.15 (Green's formula). *Let Ω be a Lipschitz bounded open set, $\sigma \in (L^\infty(\Omega))^{d\times d}$, and $u \in H^1(\Omega)$ such that $\operatorname{div}(\sigma \operatorname{grad} u) \in L^2(\Omega)$. Then, $\boldsymbol{n} \cdot \sigma \operatorname{grad} u \in H^{-1/2}(\partial\Omega)$, and*

$$-(\operatorname{div}(\sigma \operatorname{grad} u),\, v)_\Omega = (\operatorname{grad} v,\, \sigma \operatorname{grad} u)_\Omega - \langle \boldsymbol{n} \cdot \sigma \operatorname{grad} u,\, v\rangle_{H^{-1/2} \times H^{1/2}}. \tag{A.10}$$

Lemma A.16 (Poincaré). *Let Ω be a bounded open set. Then, there exists C_Ω such that*

$$\|v\|_{0,\Omega} \le C_\Omega \|\operatorname{grad} v\|_{0,\Omega}, \quad v \in H_0^1(\Omega).$$

Lemma A.17. *Let Ω be a Lipschitz domain. Let f be a linear form on $H^1(\Omega)$ whose restriction on constant functions is not zero. Then, there exists C_Ω such that*

$$\|v\|_{1,\Omega} \le C_\Omega \left(\|\operatorname{grad} v\|_{0,\Omega} + |f(v)|\right), \quad v \in H^1(\Omega).$$

Lemma A.18. *Let Ω be a Lipschitz domain. Let D be a subset of Ω of non-zero measure, and Γ be a subset of $\partial\Omega$ of non-zero $(d-1)$-measure. By Lemma A.17, we have that*

$$\|v\|_{1,\Omega} \le C_\Omega \left(\|\operatorname{grad} v\|_{0,\Omega} + |D|^{-1} \int_D v \,\mathrm{d}\Omega\right), \quad v \in H^1(\Omega), \tag{A.11}$$

$$\|v\|_{1,\Omega} \le C_\Omega \left(\|\operatorname{grad} v\|_{0,\Omega} + |\Gamma|^{-1} \int_\Gamma v \,\mathrm{d}\Gamma\right), \quad v \in H^1(\Omega). \tag{A.12}$$

Lemma A.19 (Korn's second inequality). *Let Ω be a Lipschitz domain. Then, there exists C_Ω such that*

$$\|\boldsymbol{v}\|_{1,\Omega} \leq C_\Omega \left(\|\varepsilon(\boldsymbol{v})\|_{0,\Omega} + \|\boldsymbol{v}\|_{0,\Omega} \right), \quad \boldsymbol{v} \in (H^1(\Omega))^d.$$

Corollary A.20. *Let Ω be a Lipschitz domain and let $\Gamma_D \subset \partial\Omega$ be of non-zero measure. Then, there exists C such that*

$$\|\boldsymbol{v}\|_{1,\Omega} \leq C \|\varepsilon(\boldsymbol{v})\|_{0,\Omega}, \quad \boldsymbol{v} \in \{\boldsymbol{w} \in (H^1(\Omega))^d : \boldsymbol{w}|_{\Gamma_D} = 0\}.$$

Lemma A.21 (Lax–Milgram). *Let V be a Hilbert space, let $a \in \mathcal{L}(V \times V; \mathbb{R})$, and let $f \in V'$. Assume that the bilinear form is V-elliptic, i.e., there exists a constant $\alpha > 0$ such that*

$$a(v, v) \geq \alpha \|v\|_V^2, \qquad v \in V.$$

Then, the problem of seeking $u \in V$ such that $a(u, v) = f(v)$ for all $v \in V$ is well-posed with the a priori-estimate

$$\|u\|_V \leq \frac{1}{\alpha} \|f\|_{V'}.$$

Definition A.22 ($L^p(0,T;X)$). For $p \in [1, \infty)$, the space $L^p(0,T;X)$ consists of functions $t \mapsto v(t)$ which are Lebesgue-mesuarable on $(0,T)$ with respect to the measure $\mathrm{d}t$, such that

$$\|v\|_{L^p(0,T;X)} = \left(\int_0^T \|v(t)\|_X^p \, \mathrm{d}t \right)^{1/p} < \infty.$$

A.2 Saddle Point Problems

Let X and M be two reflexive Banach spaces, $f \in X'$, $g \in M'$, and consider two bilinear forms $a \in \mathcal{L}(X \times X; \mathbb{R})$ and $b \in \mathcal{L}(X \times M; \mathbb{R})$, where $\mathcal{L}(E; F)$ denotes the vector space of bounded linear operators from E to F. The saddle point problem to be investigated is given by: Find $(u, \lambda) \in X \times M$ such that

$$a(u, v) + b(v, \lambda) = f(v), \qquad v \in X, \tag{A.13a}$$
$$b(u, \mu) = g(\mu), \qquad \mu \in M. \tag{A.13b}$$

We usually refer to M as Lagrange multiplier space. Introduce the operators A and B such that $A : X \to X'$ with $\langle Aw, v \rangle_{X',X} = a(w, v)$, and $B : X \to M'$ (and $B^{\mathrm{T}} : M = M'' \to X'$) with $\langle Bv, \mu \rangle_{M',M} = b(v, \mu)$. Problem (A.13) is equivalent to: Find $(u, \lambda) \in X \times M$ such that

$$Au + B^{\mathrm{T}}\lambda = f, \tag{A.14a}$$
$$Bu = g. \tag{A.14b}$$

Let $\operatorname{Ker} B = \{v \in X : b(v, \mu) = 0, \ \mu \in M\}$ be the null space of B.

Theorem A.23 (SPP). *Under the above framework, problem* (A.13) *is well-posed if and only if*

$$\begin{cases} \exists \alpha > 0 \text{ such that } \inf\limits_{w \in Ker\, B} \sup\limits_{v \in Ker\, B} \dfrac{a(w,v)}{\|w\|_X \|v\|_X} \ \geq \ \alpha, \\ \forall v \in Ker\, B,\ (a(w,v) = 0,\ w \in Ker\, B) \ \Rightarrow \ (v = 0), \end{cases} \tag{A.15}$$

and

$$\exists \beta > 0 \text{ such that } \inf_{\mu \in M} \sup_{v \in X} \frac{b(v,\mu)}{\|v\|_X \|\mu\|_M} \ \geq \ \beta. \tag{A.16}$$

Furthermore, the following a priori estimates hold:

$$\begin{cases} \|u\|_X \ \leq \ c_1 \|f\|_{X'} + c_2 \|g\|_{M'}, \\ \|\lambda\|_X \ \leq \ c_3 \|f\|_{X'} + c_4 \|g\|_{M'}, \end{cases} \tag{A.17}$$

with $c_1 = 1/\alpha$, $c_2 = c_3 = (1 + \|a\|/\alpha)/\beta$, *and* $c_4 = \|a\|(1 + \|a\|/\alpha)/\beta^2$.

Let X_h and M_h be finite-dimensional conformal approximations of X and M, respectively. Consider the approximate problem: Find $(u_h, \lambda_h) \in X_h \times M_h$ such that

$$a(u_h, v_h) \ + \ b(v_h, \lambda_h) = f(v_h), \qquad v_h \in X_h, \tag{A.18a}$$

$$b(u_h, \mu_h) \qquad\qquad = g(\mu_h), \qquad \mu_h \in M_h. \tag{A.18b}$$

Let $B_h : X_h \to M_h'$ be the operator induced by b such that $\langle B_h v_h, \mu_h \rangle_{M_h', M_h} = b(v_h, \mu_h)$. Let $\mathrm{Ker}\, B_h = \{v_h \in X_h : b(v_h, \mu_h) = 0,\ \mu_h \in M_h\}$ be the null space of B_h.

Theorem A.24 (discrete SPP). *Problem* (A.18) *is well-posed if and only if*

$$\exists \alpha_h > 0 \text{ such that } \inf_{w_h \in Ker\, B_h} \sup_{v_h \in Ker\, B_h} \frac{a(w_h, v_h)}{\|w_h\|_X \|v_h\|_X} \geq \ \alpha_h, \tag{A.19}$$

$$\exists \beta_h > 0 \text{ such that } \inf_{\mu_h \in M_h} \sup_{v_h \in X_h} \frac{b(v_h, \mu_h)}{\|v_h\|_X \|\mu_h\|_M} \qquad \geq \ \beta_h. \tag{A.20}$$

Under assumptions (A.19) *and* (A.20), *the solution* (u_h, λ_h) *to* (A.18) *satisfies*

$$\begin{cases} \|u - u_h\|_X \ \leq \ c_{1h} \inf\limits_{v_h \in X_h} \|u - v_h\|_X + c_{2h} \inf\limits_{\mu_h \in M_h} \|\lambda - \mu_h\|_M, \\ \|\lambda - \lambda_h\|_M \ \leq \ c_{3h} \inf\limits_{v_h \in X_h} \|u - v_h\|_X + c_{4h} \inf\limits_{\mu_h \in M_h} \|\lambda - \mu_h\|_M, \end{cases} \tag{A.21}$$

with $c_{1h} = (1 + \|a\|/\alpha_h)(1 + \|b\|/\beta_h)$, $c_{2h} = \|b\|/\alpha_h$ *if* $Ker\, B_h \not\subset Ker\, B$ *and* $c_{2h} = 0$ *otherwise,* $c_{3h} = c_{1h}\|b\|/\alpha_h$, *and* $c_{4h} = 1 + \|b\|/\beta_h + c_{2h}\|a\|/\beta_h$.

A.3 Preliminaries for Finite Element Spaces

We recall some often needed properties of finite element spaces, as presented for example in [127]. Given a quasi-uniform triangulation $\mathcal{T}_h$ of the domain Ω, we indicate by X_h the corresponding space of piecewise linear finite elements on $\mathcal{T}_h$, and set $X_{h,0} = X_h \cap H_0^1(\Omega)$.

Definition A.25 (harmonic). A function $v \in H^1(\Omega)$ is called harmonic, if

$$(\operatorname{grad} v, \operatorname{grad} w)_\Omega = 0, \qquad w \in H^1_0(\Omega).$$

Given $v \in H^{1/2}(\partial\Omega)$, the harmonic extension $\mathcal{H}v \in H^1(\Omega)$ is defined by

$$\begin{aligned} (\operatorname{grad} \mathcal{H}v, \operatorname{grad} w)_\Omega &= 0, \qquad w \in H^1_0(\Omega), \\ (\mathcal{H}v)|_{\partial\Omega} &= v, \end{aligned} \tag{A.22}$$

Theorem A.26 (harmonic). *For any harmonic function $v \in H^1(\Omega)$, it holds that*

$$|v|_{1,\Omega} \sim |v|_{1/2,\partial\Omega},$$

Definition A.27 (discrete harmonic). A finite element function $v_h \in X_h$ is called discrete harmonic, if

$$(\operatorname{grad} v_h, \operatorname{grad} w_h)_\Omega = 0, \qquad w_h \in X_{h,0}.$$

Considering the full inner product $(\cdot,\cdot)_{1,\Omega}$ given by (A.5), a function $v_h \in X_h$ is called generalized discrete harmonic, if

$$(v_h, w_h)_{1,\Omega} = 0, \qquad w_h \in X_{h,0}.$$

Given $v_h \in X_h|_{\partial\Omega}$, the discrete harmonic extension $\mathcal{H}_h v_h \in X_h$ is defined by

$$\begin{aligned} (\operatorname{grad} \mathcal{H}_h v_h, \operatorname{grad} w_h)_\Omega &= 0, \qquad w_h \in X_{h,0}, \\ (\mathcal{H}_h v_h)|_{\partial\Omega} &= v_h, \end{aligned} \tag{A.23}$$

while the generalized discrete harmonic extension $\mathcal{H}^{\mathrm{g}}_h v_h \in X_h$ is given by

$$(\mathcal{H}^{\mathrm{g}}_h v_h, w_h)_{1,\Omega} = 0, \qquad w_h \in X_{h,0}, \tag{A.24a}$$

$$(\mathcal{H}^{\mathrm{g}}_h v_h)|_{\partial\Omega} = v_h. \tag{A.24b}$$

Theorem A.28 (discrete harmonic). *For any discrete harmonic function $v_h \in X_h$, it holds that*

$$|v_h|_{1,\Omega} \sim |v_h|_{1/2,\partial\Omega},$$

with equivalence constants independent of the meshwidth h. If v_h is generalized discrete harmonic, then

$$\|v_h\|_{1,\Omega} \sim \|v_h\|_{1/2,\partial\Omega}, \tag{A.25}$$

Theorem A.29 (norm equivalence). *Let $\mathcal{V}_h$ indicate the finite element nodes of the triangulation $\mathcal{T}_h$. It holds that*

$$\|v_h\|^2_{0,\Omega} \sim h^d \sum_{p \in \mathcal{V}_h} (v_h(p))^2, \qquad v_h \in X_h. \tag{A.26}$$

Theorem A.30 (local inverse inequality). *Let $\{\widehat{T}, \widehat{\mathbb{P}}, \widehat{\Sigma}\}$ be a finite element, $l \geq 0$ be such that $\widehat{\mathbb{P}} \subset W^{l,\infty}(\widehat{T})$, and $\{\mathcal{T}_h\}_{h>0}$ be a shape-regular family of affine meshes in $\mathbb{R}^d$ with $h \leq 1$. For $0 \leq m \leq l$, there exists a constant C independent of h and T such that*

$$\|v_h\|_{l,T} \leq C h_T^{m-l} \|v_h\|_{m,T}, \qquad v_h \in \mathbb{P}_T = \{\widehat{p} \circ F_T^{-1} : \widehat{p} \in \widehat{\mathbb{P}}\}. \tag{A.27}$$

Theorem A.31 (global inverse inequality). *It holds that*

$$\|v_h\|_{1,\Omega} \leq C h^{-1} \|v_h\|_{0,\Omega}, \qquad v_h \in X_h. \tag{A.28}$$

Assumption A.32 (Strang). *Let V, W be Hilbert spaces, $a(\cdot,\cdot)$ a continuous bilinear form on $W \times V$, and $l(\cdot)$ a continuous linear form on V. Assume that $u \in W$ is the unique solution satisfying $a(u,v) = l(v)$ for all $v \in V$. Let W_h, V_h be finite-dimensional spaces equipped with norms $\|\cdot\|_{W_h}, \|\cdot\|_{V_h}$, respectively. Assume that $W(h) = W + W_h$ can be equipped with a norm $\|\cdot\|_{W(h)}$ such that*

$$\|w_h\|_{W(h)} = \|w_h\|_{W_h}, \quad w_h \in W_h, \qquad \text{and} \qquad \|w\|_{W(h)} \leq C\|w\|_W, \quad w \in W.$$

Construct an approximation of u by solving the problem of finding $u_h \in W_h$ such that $a_h(u_h, v_h) = l_h(v_h)$ for all $v_h \in V_h$ with approximations $a_h(\cdot,\cdot)$ and $l_h(\cdot)$ to $a(\cdot,\cdot)$ and $l(\cdot)$, respectively. Assume that $\dim(W_h) = \dim(V_h)$, and that there exists a constant $\alpha_h > 0$ such that

$$\inf_{w_h \in W_h} \sup_{v_h \in V_h} \frac{a_h(w_h, v_h)}{\|w_h\|_{W_h} \|v_h\|_{V_h}} \geq \alpha_h.$$

Lemma A.33 (Strang 1). *Let Assumption A.32 hold. Moreover, assume that $W_h \subset W$ and $V_h \subset V$, that the bilinear form $a_h(\cdot,\cdot)$ is bounded on $W_h \times V_h$, and that $a(\cdot,\cdot)$ is bounded on $W \times V_h$ when W is equipped with the extended norm $\|\cdot\|_{W(h)}$. Then, it holds that*

$$\begin{aligned}\|u - u_h\|_{W(h)} \leq \left(1 + \frac{\|a\|_{W(h),V_h}}{\alpha_h}\right) \inf_{w_h \in W_h} \|u - w_h\|_{W(h)} + \frac{1}{\alpha_h} \sup_{v_h \in V_h} \frac{|l_h(v_h) - l(v_h)|}{\|v_h\|_{V_h}} \\ + \frac{1}{\alpha_h} \inf_{w_h \in W_h} \sup_{v_h \in V_h} \frac{|a_h(w_h, v_h) - a(w_h, v_h)|}{\|v_h\|_{V_h}}.\end{aligned}$$

Lemma A.34 (Strang 2). *Let Assumption A.32 hold. Moreover, assume that the bilinear form $a_h(\cdot,\cdot)$ can be extended to $W(h) \times V_h$ and that it is bounded on $W(h) \times V_h$. Then, it holds that*

$$\|u - u_h\|_{W(h)} \leq \left(1 + \frac{\|a_h\|_{W(h),V_h}}{\alpha_h}\right) \inf_{w_h \in W_h} \|u - w_h\|_{W(h)} + \frac{1}{\alpha_h} \sup_{v_h \in V_h} \frac{|l_h(v_h) - a_h(u, v_h)|}{\|v_h\|_{V_h}}.$$

Bibliography

[1] Proceedings of the annual international domain decomposition meetings, `http://www.ddm.org`. 1987–2006. 1

[2] Y. Achdou and Y. Maday. The mortar element method with overlapping subdomains. *SIAM J. Numer. Anal.*, 40(2):601–628, 2002. 117

[3] R. A. Adams. *Sobolev Spaces.* Academic Press, 1975. 16

[4] M. Akamatsu and G. Nakamura. Well-posedness of initial-boundary value problems for piezoelectric equations. *Appl. Anal.*, 81(1):129–141, 2002. 99

[5] R. Albanese and G. Rubinacci. Formulation of the eddy-current problem. *IEE Proc. A*, 137(1):16–22, 1990. 133

[6] D. N. Arnold, D. Boffi, and R. S. Falk. Approximation by quadrilateral finite elements. *Math. Comp.*, 71(239):909–922, 2002. 53

[7] A. Bamberger, R. Glowinski, and Q. H. Tran. A domain decomposition method for the acoustic wave equation with discontinuous coefficients and grid change. *SIAM J. Numer. Anal.*, 34(2):603–639, 1997. 83, 88, 91, 92

[8] P. Bastian, K. Birken, K. Johannsen, S. Lang, N. Neuß, H. Rentz-Reichert, and C. Wieners. UG – a flexible software toolbox for solving partial differential equations. *Comput. Vis. Sci.*, 1(1):27–40, 1997. 4

[9] S. Becker, M. Kaltenbacher, I. Ali, M. Escobar, and C. Hahn. Sound generation by flow around simple geometries: Simulation and experiment. In *Proceedings of the 12th AIAA/CEAS Aeroacoustics Conference, number 2699 in AIAA-2006, 2006. 08.-10.05.2006, Cambridge, Massachusetts, CD-ROM Proceedings.* 108

[10] F. Ben Belgacem. The mortar finite element method with Lagrange multipliers. *Numer. Math.*, 84(2):173–197, 1999. 2, 15, 28

[11] F. Ben Belgacem. The mixed mortar finite element method for the incompressible Stokes problem: convergence analysis. *SIAM J. Numer. Anal.*, 37(4):1085–1100, 2000. 2

[12] F. Ben Belgacem. A stabilized domain decomposition method with nonmatching grids for the Stokes problem in three dimensions. *SIAM J. Numer. Anal.*, 42(2):667–685, 2004. 2

[13] F. Ben Belgacem, P. Hild, and P. Laborde. The mortar finite element method for contact problems. *Math. Comput. Modelling*, 28(4-8):263–271, 1998. Recent advances in contact mechanics. 2

[14] F. Ben Belgacem, P. Hild, and P. Laborde. Extension of the mortar finite element method to a variational inequality modeling unilateral contact. *Math. Models Methods Appl. Sci.*, 9(2):287–303, 1999. 2

[15] F. Ben Belgacem and Y. Maday. The mortar element method for three-dimensional finite elements. *RAIRO Modél. Math. Anal. Numér.*, 31(2):289–302, 1997. 2

[16] F. Ben Belgacem, P. Seshaiyer, and M. Suri. Optimal convergence rates of *hp* mortar finite element methods for second-order elliptic problems. *M2AN Math. Model. Numer. Anal.*, 34(3):591–608, 2000. 2

[17] A. Bermúdez, R. Rodríguez, and D. Santamarina. Finite element approximation of a displacement formulation for time-domain elastoacoustic vibrations. *J. Comput. Appl. Math.*, 152(1-2):17–34, 2003. 83, 90

[18] C. Bernardi, C. Canuto, and Y. Maday. Generalized inf-sup conditions for Chebyshev spectral approximation of the Stokes problem. *SIAM J. Numer. Anal.*, 25(6):1237–1271, 1988. 119

[19] C. Bernardi, N. Debit, and Y. Maday. Coupling finite element and spectral methods: first results. *Math. Comp.*, 54(189):21–39, 1990. 2

[20] C. Bernardi, Y. Maday, and A. T. Patera. Domain decomposition by the mortar element method. In *Asymptotic and numerical methods for partial differential equations with critical parameters (Beaune, 1992)*, volume 384 of *NATO Adv. Sci. Inst. Ser. C Math. Phys. Sci.*, pages 269–286. Kluwer Acad. Publ., Dordrecht, 1993. 2, 15, 16, 18, 25

[21] C. Bernardi, Y. Maday, and A. T. Patera. A new nonconforming approach to domain decomposition: the mortar element method. In *Nonlinear partial differential equations and their applications. Collège de France Seminar, Vol. XI (Paris, 1989–1991)*, volume 299 of *Pitman Res. Notes Math. Ser.*, pages 13–51. Longman Sci. Tech., Harlow, 1994. 2, 15, 16, 18, 127

[22] A. Bossavit. *Computational electromagnetism.* Electromagnetism. Academic Press Inc., San Diego, CA, 1998. Variational formulations, complementarity, edge elements. 138

[23] D. Braess. Enhanced assumed strain elements and locking in membrane problems. *Comput. Methods Appl. Mech. Engrg.*, 165(1-4):155–174, 1998. 100

[24] D. Braess and W. Dahmen. Stability estimates of the mortar finite element method for 3-dimensional problems. *East-West J. Numer. Math.*, 6(4):249–263, 1998. 2, 16, 18

[25] D. Braess, W. Dahmen, and C. Wieners. A multigrid algorithm for the mortar finite element method. *SIAM J. Numer. Anal.*, 37(1):48–69, 1999. 2

[26] S. Brenner and L. Scott. *The Mathematical Theory of Finite Element Methods.* Springer–Verlag, New York, 1994. 43, 64

[27] F. Brezzi and M. Fortin. *Mixed and Hybrid Finite Element Methods.* Springer Verlag, 1991. 7, 26, 92, 119

[28] F. Brezzi and D. Marini. Error estimates for the three-field formulation with bubble stabilization. *Math. Comp*, 70:911–934, 2001. 71

[29] I. Bronstein, K. Semendjajew, G. Musiol, and H. Mühlig. *Taschenbuch der Mathematik. 4., überarb. und erweit. Aufl. der Neubearbeitung.* Harri Deutsch, Frankfurt/Main, 1999. 40

[30] X.-C. Cai, M. Dryja, and M. Sarkis. Overlapping nonmatching grid mortar element methods for elliptic problems. *SIAM J. Numer. Anal.*, 36(2):581–606, 1999. 117

[31] P. Ciarlet, Jr., J. Huang, and J. Zou. Some observations on generalized saddle-point problems. *SIAM J. Matrix Anal. Appl.*, 25(1):224–236, 2003. 119

[32] P. G. Ciarlet. *Mathematical elasticity. Vol. I*, volume 20 of *Studies in Mathematics and its Applications.* North-Holland Publishing Co., Amsterdam, 1988. Three-dimensional elasticity. 5, 6

[33] R. Clayton and B. Engquist. Absorbing boundary conditions for acoustic and elastic wave equations. *Bulletin of the Seismological Society of America*, 67:1529–1540, 1977. 87

[34] R. Dautray and J.-L. Lions. *Mathematical analysis and numerical methods for science and technology. Vol. 5: Evolution problems I.* Springer-Verlag, Berlin, 1992. 84, 92

[35] C. Dohrmann, S. Key, and M. Heinstein. A method for connecting dissimilar finite element meshes in two dimensions. *Int. J. Numer. Methods Eng.*, 48(5):655–678, 2000. 12

[36] P. Eberhard, S. Hüeber, Y. Jiang, and B. Wohlmuth. Multilevel numerical algorithms and experiments for contact dynamics. In R. Helmig, A. Mielke, and B. Wohlmuth, editors, *Multifield problems in solid and fluid mechanics*, volume 28 of *Lecture notes in applied and computational mechanics*, pages 272–319. Springer, 2006. 131

[37] C. Emson, C. Riley, D. Walsh, K. Ueda, and T. Kumano. Modelling eddy currents induced in rotating systems. *IEEE Trans. on Magn.*, 34(5):2593–2596, 1998. 135

[38] B. Engquist and A. Majda. Absorbing boundary conditions for the numerical simulation of waves. *Math. Comp.*, 31(139):629–651, 1977. 87

[39] A. Ern and J.-L. Guermond. *Theory and practice of finite elements*, volume 159 of *Applied Mathematical Sciences*. Springer-Verlag, New York, 2004. 74, 151

[40] L. C. Evans. *Partial differential equations*, volume 19 of *Graduate Studies in Mathematics*. American Mathematical Society, Providence, RI, 1998. 84

[41] M. Fischer and L. Gaul. Application of the fast multipole BEM for structural-acoustic simulations. *J. Comput. Acoust.*, 13(1):87–98, 2005. 84

[42] B. Flemisch, M. Kaltenbacher, and B. I. Wohlmuth. Elasto-acoustic and acoustic-acoustic coupling on non-matching grids. *Internat. J. Numer. Methods Engrg.*, 67(13):1791–1810, 2006. 3

[43] B. Flemisch, S. Kurz, and B. I. Wohlmuth. A framework for Maxwell's equations in non-inertial frames based on differential forms, IANS preprint 2006/011. Technical report, University of Stuttgart, 2006. 135

[44] B. Flemisch, Y. Maday, F. Rapetti, and B. I. Wohlmuth. Coupling scalar and vector potentials on nonmatching grids for eddy currents in a moving conductor. *J. Comput. Appl. Math.*, 168(1-2):191–205, 2004. 4

[45] B. Flemisch, Y. Maday, F. Rapetti, and B. I. Wohlmuth. Scalar and vector potentials' coupling on nonmatching grids for the simulation of an electromagnetic brake. *COMPEL*, 24(3):1061–1070, 2005. 4

[46] B. Flemisch, M. Mair, and B. I. Wohlmuth. Nonconforming discretization techniques for overlapping domain decompositions. In *Feistauer, M. (ed.) et al., Numerical mathematics and advanced applications. Proceedings of ENUMATH 2003, the 5th European conference on numerical mathematics and advanced applications, Prague, Czech Republic, August 18-22, 2003*, pages 316–325. Springer, Berlin, 2004. 4, 118

[47] B. Flemisch, J. Melenk, and B. I. Wohlmuth. Mortar methods with curved interfaces. *Appl. Numer. Math.*, 54(3-4):339–361, 2005. 3

[48] B. Flemisch, M. A. Puso, and B. I. Wohlmuth. A new dual mortar method for curved interfaces: 2D elasticity. *Internat. J. Numer. Methods Engrg.*, 63(6):813–832, 2005. 3

[49] B. Flemisch and B. I. Wohlmuth. A domain decomposition method on nested domains and nonmatching grids. *Numer. Methods Partial Differential Equations*, 20(3):374–387, 2004. 4

[50] B. Flemisch and B. I. Wohlmuth. Nonconforming methods for nonlinear elasticity problems. In O. B. Widlund and D. E. Keyes, editors, *Domain Decomposition Methods in Science and Engineering XVI*, volume 55 of *Lecture notes in Computational Science and Engineering*. Springer, 2007. 78

[51] B. Flemisch and B. I. Wohlmuth. Stable Lagrange multipliers for quadrilateral meshes of curved interfaces in 3D. *Comput. Methods Appl. Mech. Engrg.*, 196(8):1589–1602, 2007. 3

[52] R. Glowinski, J. He, A. Lozinski, J. Rappaz, and J. Wagner. Finite element approximation of multi-scale elliptic problems using patches of elements. *Numer. Math.*, 101(4):663–687, 2005. 126

[53] R. Glowinski, T. Pan, and J. Periaux. Fictitious domain methods for incompressible viscous flow around moving rigid bodies. In *Whiteman, J. R. (ed.), The mathematics of finite elements and applications. Highlights 1996. Proceedings of the 9th conference, MAFELAP 1996, Uxbridge, GB, June 25–28, 1996, Chichester: Wiley. 155-173* . 1997. 117

[54] J. Gopalakrishnan. *On the mortar finite element method.* PhD thesis, Texas A&M University, 1999. 8, 25

[55] J. Gopalakrishnan. Mortar estimates independent of number of subdomains. *East-West J. Numer. Math.*, 8(2):111–125, 2000. 2

[56] W. Gordon. Blending-function methods of bivariate and multivariate interpolation and approximation. *SIAM J. Numer. Anal.*, 8:158–177, 1973. 15

[57] W. Gordon and C. Hall. Construction of curvilinear co-ordinate systems and applications to mesh generation. *Internat. J. Numer. Meths. Engrg.*, 7:461–477, 1973. 15, 22

[58] W. Gordon and C. Hall. Transfinite element methods: Blending function interpolation over arbitrary curved element domains. *Numer. Math.*, 21:109–129, 1973. 15, 22

[59] P. Grisvard. *Elliptic Problems in Nonsmooth Domains.* Pitman, 1985. 25

[60] P. Hansbo, J. Hermansson, and T. Svedberg. Nitsche's method combined with space-time finite elements for ALE fluid-structure interaction problems. *Comput. Methods Appl. Mech. Engrg.*, 193(39-41):4195–4206, 2004. 83

[61] P. Hauret. *Numerical methods for the dynamic analysis of twoscale incompressible nonlinear structures.* PhD thesis, Ecole Polytechnique, Paris, 2004. 8

[62] P. Hauret and P. Le Tallec. Dirichlet– Neumann preconditioners for elliptic problems with small disjoint geometric refinements on the boundary. Technical Report 552, CMAP - Ecole Polytechnique, 2004. 10

[63] P. Hauret and P. Le Tallec. A stabilized discontinuous mortar formulation for elastostatics and elastodynamics. Part I: Formulation and analysis. Technical Report 553, Ecole Polytechnique CMAP, 2004. 2

[64] P. Hauret and P. Le Tallec. A stabilized discontinuous mortar formulation for elastostatics and elastodynamics. Part II: Discontinuous lagrange multipliers. Technical Report 554, Ecole Polytechnique CMAP, 2004. 2

[65] E. Heikkola, Y. A. Kuznetsov, P. Neittaanmäki, and J. Toivanen. Fictitious domain methods for the numerical solution of two-dimensional scattering problems. *J. Comput. Phys.*, 145(1):89–109, 1998. 135

[66] F. Henrotte, B. Meys, H. Hedia, P. Dular, and W. Legros. Finite element modelling with transformation techniques. *IEEE Trans. on Magn.*, 35(3):1434–1437, 1999. 146

[67] M. Hofer. *Finite-Elemente-Berechnung von periodischen Oberflächenwellen-Strukturen.* PhD-thesis, Universität Erlangen, 2003. 87

[68] G. Houzeaux and R. Codina. A chimera method based on a Dirichlet/Neumann(Robin) coupling for the Navier-Stokes equations. *Comput. Methods Appl. Mech. Engrg.*, 192(31-32):3343–3377, 2003. 117

[69] J. Huang and J. Zou. A mortar element method for elliptic problems with discontinuous coefficients. *IMA J. Numer. Anal.*, 22:549–576, 2002. 15

[70] S. Hüeber, M. Mair, and B. I. Wohlmuth. A priori error estimates and an inexact primal-dual active set strategy for linear and quadratic finite elements applied to multibody contact problems. *Appl. Numer. Math.*, 54(3-4):555–576, 2005. 2

[71] S. Hüeber and B. I. Wohlmuth. An optimal a priori error estimate for nonlinear multibody contact problems. *SIAM J. Numer. Anal.*, 43(1):156–173, 2005. 8

[72] S. Hüeber and B. I. Wohlmuth. A primal-dual active set strategy for non–linear multibody contact problems. *Comput. Methods Appl. Mech. Engrg.*, 194:3147–3166, 2005. 2, 10, 81

[73] T. Hughes. *The Finite Element Method.* Prentice-Hall, New Jersey, 1987. 85

[74] M. Kaltenbacher. *Numerical Simulation of Mechatronic Sensors and Actuators.* Springer Berlin-Heidelberg-New York, 2004. ISBN: 3-540-20458-X. 83

[75] M. Kaltenbacher, M. Escobar, I. Ali, and S. Becker. Finite Element Method Formulation of Lighthill's Analogy. *JSV*, 2005. (submitted). 83

[76] M. Kaltenbacher, R. Lerch, and G. Link. Numerical modeling of capacitive micromachined transducers. In *Computational Methods for Coupled Problems in Science and Engineering. CD-ROM Proceedings, ECCOMAS Santorini, Greece; 25.-27.05.2005.* 96

[77] C. Kim, R. D. Lazarov, J. E. Pasciak, and P. S. Vassilevski. Multiplier spaces for the mortar finite element method in three dimensions. *SIAM J. Numer. Anal.*, 39(2):519–538, 2001. 2, 16, 18

[78] D. Kuhl and M. A. Crisfield. Energy-conserving and decaying algorithms in non-linear structural dynamics. *Internat. J. Numer. Methods Engrg.*, 45(5):569–599, 1999. 110

[79] D. J. P. Lahaye, F. Maggio, and A. Quarteroni. Hybrid finite element–spectral element approximation of wave propagation problems. *East-West J. Numer. Math.*, 5(4):265–289, 1997. 83, 91

[80] B. P. Lamichhane. *Higher Order Mortar Finite Elements with Dual Lagrange Multiplier Spaces and Applications.* PhD thesis, Universität Stuttgart, 2006. 19, 39, 42, 127

[81] P. Le Tallec and S. Mani. Numerical analysis of a linearised fluid-structure interaction problem. *Numer. Math.*, 87(2):317–354, 2000. 83

[82] M. J. Lighthill. On sound generated aerodynamically. I. General theory. *Proc. Roy. Soc. London. Ser. A.*, 211:564–587, 1952. 83, 108

[83] J.-L. Lions and E. Magenes. *Non-homogeneous boundary value problems and applications. Vol. I.* Springer-Verlag, New York, 1972. Translated from the French by P. Kenneth, Die Grundlehren der mathematischen Wissenschaften, Band 181. 84

[84] Y. Maday, F. Rapetti, and B. Wohlmuth. Mortar element coupling between global scalar and local vector potentials to solve eddy current problems. In *Brezzi, Franco (ed.) et al., Numerical mathematics and advanced applications. Proceedings of ENUMATH 2001, the 4th European conference, Ischia, July 2001*, pages 847–865. Springer, Berlin, 2003. 135, 136, 138, 140, 142

[85] Y. Maday, F. Rapetti, and B. I. Wohlmuth. Coupling between scalar and vector potentials by the mortar element method. *C. R. Math. Acad. Sci. Paris*, 334(10):933–938, 2002. 135

[86] G. I. Marchuk, Y. A. Kuznetsov, and A. M. Matsokin. Fictitious domain and domain decomposition methods. *Soviet J. Numer. Anal. Math. Modelling*, 1(1):3–35, 1986. 117

[87] T. W. McDevitt and T. A. Laursen. A mortar-finite element formulation for frictional contact problems. *Internat. J. Numer. Methods Engrg.*, 48(10):1525–1547, 2000. 2

[88] J.-C. Nédélec. Mixed finite elements in $\mathbb{R}^3$. *Numer. Math.*, 35:315–341, 1980. 137

[89] J.-C. Nédélec. *Acoustic and electromagnetic equations. Integral representations for harmonic problems.* Springer, New York, 2001. 135

[90] N. M. Newmark. A method of computation for structural dynamics. *J. Engng. Mech. Div., Proc. ASCE*, 85(EM3):67–94, 1959. 85

[91] R. A. Nicolaides. Existence, uniqueness and approximation for generalized saddle point problems. *SIAM J. Numer. Anal.*, 19(2):349–357, 1982. 119

[92] R. W. Ogden. *Nonlinear elastic deformations.* Ellis Horwood Series: Mathematics and its Applications. Ellis Horwood Ltd., Chichester, 1984. 6

[93] F. A. Ortega. General mesh viewer (gmv) user's manual. Technical Report LA-UR-95-2986, Los Alamos National Laboratory, 1995. 4

[94] P. Oswald and B. I. Wohlmuth. On polynomial reproduction of dual FE bases. In *Domain decomposition methods in science and engineering (Lyon, 2000)*, Theory Eng. Appl. Comput. Methods, pages 85–96. Internat. Center Numer. Methods Eng. (CIMNE), Barcelona, 2002. 127

[95] M. Peszyńska. Mortar adaptivity in mixed methods for flow in porous media. *Int. J. Numer. Anal. Model.*, 2(3):241–282, 2005. 2

[96] M. Peszyńska, M. F. Wheeler, and I. Yotov. Mortar upscaling for multiphase flow in porous media. *Comput. Geosci.*, 6(1):73–100, 2002. 2

[97] M. Puso. A 3D mortar method for solid mechanics. *Internat. J. Numer. Methods Engrg.*, 59(3):315–336, 2004. 48, 57

[98] M. A. Puso and T. A. Laursen. A mortar segment-to-segment frictional contact method for large deformations. *Comput. Methods Appl. Mech. Engrg.*, 193(45-47):4891–4913, 2004. 2

[99] A. Quarteroni. Domain decomposition methods for wave propagation problems. In *Domain-based parallelism and problem decomposition methods in computational science and engineering*, pages 21–38. SIAM, Philadelphia, PA, 1995. 83

[100] A. Quarteroni and A. Valli. *Domain decomposition methods for partial differential equations.* Numerical Mathematics and Scientific Computation. The Clarendon Press Oxford University Press, New York, 1999. Oxford Science Publications. 1, 117

[101] P.-A. Raviart and J. M. Thomas. Primal hybrid finite element methods for 2nd order elliptic equations. *Math. Comp.*, 31(138):391–413, 1977. 26

[102] P.-A. Raviart and J.-M. Thomas. *Introduction à l'analyse numérique des équations aux dérivées partielles.* Collection Mathématiques Appliquées pour la Maîtrise. Masson, Paris, 1983. 84, 85, 86

[103] Y. Saad. *Iterative methods for sparse linear systems.* PWS Publishing Company, Boston, 1996. 142

[104] A.-M. Sändig. Nichtlineare Funktionalanalysis mit Anwendungen auf partielle Differentialgleichungen. Vorlesung im Sommersemester 2006, IANS preprint 2006/012. Technical report, University of Stuttgart, 2006. 6

[105] O. Schenk and K. Gärtner. Solving unsymmetric sparse systems of linear equations with PARDISO. *Journal of Future Generation Computer Systems*, 20(3):475–487, 2004. 4

[106] O. Schenk and K. Gärtner. On fast factorization pivoting methods for symmetric indefinite systems. *Elec. Trans. Numer. Anal.*, 23:158–179, 2006. 4

[107] T. Schwartzkopff and C.-D. Munz. Direct simulation of aeroacoustics. In *Wendland, Wolfgang (ed.) et al., Analysis and simulation of multifield problems. Selected papers of the international conference on multifield problems, Stuttgart, Germany, April 8-10, 2002. Berlin: Springer. Lect. Notes Appl. Comput. Mech. 12, 337-342* . 2003. 83

[108] J. Schöberl. NETGEN: An advancing front 2D/3D-mesh generator based on abstract rules. *Comput. Vis. Sci.*, 1(1):41–52, 1997. 4

[109] L. R. Scott and S. Zhang. Finite element interpolation of nonsmooth functions satisfying boundary conditions. *Math. Comp.*, 54(190):483–493, 1990. 43, 122

[110] P. Seshaiyer and M. Suri. Convergence results for non-conforming *hp* methods: the mortar finite element method. In *Domain decomposition methods, 10 (Boulder, CO, 1997)*, volume 218 of *Contemp. Math.*, pages 453–459. Amer. Math. Soc., Providence, RI, 1998. 2

[111] P. Seshaiyer and M. Suri. *hp* submeshing via non-conforming finite element methods. *Comput. Methods Appl. Mech. Engrg.*, 189(3):1011–1030, 2000. 2

[112] J. C. Simo and T. J. R. Hughes. On the variational foundations of assumed strain methods. *Trans. ASME J. Appl. Mech.*, 53(1):51–54, 1986. 100

[113] B. F. Smith, P. E. Bjørstad, and W. D. Gropp. *Domain decomposition*. Cambridge University Press, Cambridge, 1996. Parallel multilevel methods for elliptic partial differential equations. 1, 117

[114] R. L. Taylor. A mixed-enhanced formulation for tetrahedral finite elements. *Internat. J. Numer. Methods Engrg.*, 47(1-3):205–227, 2000. Richard H. Gallagher Memorial Issue. 100

[115] A. Toselli and O. Widlund. *Domain decomposition methods—algorithms and theory*, volume 34 of *Springer Series in Computational Mathematics*. Springer-Verlag, Berlin, 2005. 1

[116] W. Voigt. *Lehrbuch der Kristallphysik*. Teubner, 1910. 99

[117] L. B. Wahlbin. Local behavior in finite element methods. In *Handbook of numerical analysis, Vol. II*, Handb. Numer. Anal., II, pages 353–522. North-Holland, Amsterdam, 1991. 123

[118] Z. Wang and V. Parthasarathy. A fully automated Chimera methodology for multiple moving body problems. *Int. J. Numer. Methods Fluids*, 33(7):919–938, 2000. 117

[119] C. Wieners and B. I. Wohlmuth. Duality estimates and multigrid analysis for saddle point problems arising from mortar discretizations. *SIAM J. Sci. Comput.*, 24(6):2163–2184 (electronic), 2003. 2

[120] B. I. Wohlmuth. A mortar finite element method using dual spaces for the Lagrange multiplier. *SIAM J. Numer. Anal.*, 38(3):989–1012, 2000. 2, 39, 58, 59, 127

[121] B. I. Wohlmuth. A multigrid method for saddle point problems arising from mortar finite element discretizations. *Electron. Trans. Numer. Anal.*, 11:43–54 (electronic), 2000. 2

[122] B. I. Wohlmuth. *Discretization methods and iterative solvers based on domain decomposition*, volume 17 of *Lecture Notes in Computational Science and Engineering*. Springer, 2001. 16, 18, 41, 117

[123] B. I. Wohlmuth. A comparison of dual Lagrange multiplier spaces for mortar finite element discretizations. *M2AN Math. Model. Numer. Anal.*, 36(6):995–1012, 2002. 59

[124] B. I. Wohlmuth. A $\mathcal{V}$-cycle multigrid approach for mortar finite elements. *SIAM J. Numer. Anal.*, 42(6):2476–2495, 2004. 10

[125] B. I. Wohlmuth and R. H. Krause. A multigrid method based on the unconstrained product space for mortar finite element discretizations. *SIAM J. Numer. Anal.*, 39(1):192–213, 2001. 2

[126] B. I. Wohlmuth and R. H. Krause. Monotone multigrid methods on nonmatching grids for nonlinear multibody contact problems. *SIAM J. Sci. Comput.*, 25(1):324–347, 2003. 2

[127] J. Xu and J. Zou. Some nonoverlapping domain decomposition methods. *SIAM Rev.*, 40(4):857–914, 1998. 155